Design, Analysis and Implementation of Bridge Configured Winding in Switched Reluctance Motor for Self-Bearing Operation

A thesis submitted in partial fulfilment of the requirements

for the degree of Doctor of Philosophy

by

Firdausa Ahmed

CENTRE FOR ENERGY
INDIAN INSTITUTE OF TECHNOLOGY GUWAHATI,
GUWAHATI - 781039

March 2020

CERTIFICATE

This is to certify that the thesis entitled **"Design, Analysis and Implementation of Bridge Configured Winding in Switched Reluctance Motor for Self-Bearing Operation,"** submitted by **Firdausa Ahmed (136151008)**, a research scholar in the *Centre for Energy, Indian Institute of Technology Guwahati*, for the award of **Doctor of Philosophy** is a record of an original research work carried out by her under our supervision and guidance. The results embodied in this thesis have not been submitted to any other University or Institute for the award of any degree or diploma.

Prof. Karuna Kalita
Professor
Department of Mechanical Engineering
Indian Institute of Technology Guwahati
Guwahati-781039, Assam, India

Prof. H. B. Nemade
Professor
Department of Electronics and Electrical Engineering
Indian Institute of Technology Guwahati
Guwahati-781039, Assam, India

Date:
Guwahati

To

My Grandmother

Mrs. Saleha Khatun

&

My parents, my brother and my husband

Mr. Islam Ahmed, Mrs. Hasina Ahmed, Ashique Elahi and Mr. Shahaduj Jaman

Acknowledgements

The work presented in this thesis would not have been possible without my close association with many people. I take this opportunity to extend my sincere gratitude and appreciation to all those who made this Ph.D thesis possible. My sincere gratitude goes to my advisors Prof. Karuna Kalita and Prof. H. B. Nemade for their continuous support of my Ph.D study and related research, for their patience, motivation, and immense knowledge. Their unwavering enthusiasm for innovative researches kept me constantly engaged with my research work. Without them, it would have not been possible for me to give a structured and concrete form to my research study and complete my thesis.

Besides my supervisors, I would like to thank the members of my doctoral committee: Prof. Praveen Kumar, Prof. B. Baruah, and Dr. Atanu Banerjee, for their insightful suggestions and encouragement, and also for the inquisitive questions which incented me to widen my research from various perspectives.

My sincere thanks also goes to Non-Ferrous Materials Technology Development Centre (NFTDC) R & D centre, who extended their help in the fabrication of the experimental test rigs and also gave an access to their laboratory and research facilities. I would also like to thank the members of Centre for Energy and Dept. of Mechanical Engineering for their precious support and help to conduct this research.

My appreciation also extends to my fellow Ph.D students and labmates, Dr. K. Basumatary, Dr. G. Kumar, Dr. S. K. Natesan, M. D. Choudhury, J. Choudhury, Ashim Kalita, S. Dutta and M. Sheikh for their constant help and support through out my journey of Ph.D. I would also like to thank Dr. Mridul Kanti Malakar and Dr. Ankit Dalal for all the technical discussions and help while conducting the experimental works.

I am again thankful to my friends within the institute : Dr. Shyamali Sarma, Hirak J. Basumatary, Dudul Das, Samar Das, Devarshi Kashyap, Dr. Anupam Alok, Sangjukta Devi, Paban Bujorbaruah, Nilakshi Sharma, Dr. Needhi Kotoky and Dr. Binita Nath, and outside the institute : Tapashi Kalita, Dhritika Saikia, Chinmoy Bordoloi and Sumit Deb for their constant support and motivation during my Ph.D journey.

Last but not the least, I am extremely grateful to my parents for their love, care and sacrifices in educating me and preparing me for the future. Also I express my thanks to my brother Ashique Elahi, my uncle Sahadat Ali, my mother in law and every members of my family for their forever support and love. At last, I owe my deepest gratitude to my husband Mr. Shahaduj Jaman for his constant love, care and support in this journey of Ph.D.

Firdausa Ahmed

भारतीय प्रौद्योगिकी संस्थान गुवाहाटी
Indian Institute of Technology Guwahati

Abstract

With the advancement of science and technology, the demand for rotating electrical machines with a compact drive system has been on the rise. The electrical motors, which are of wide applications are induction motors, permanent magnet synchronous motors, switched reluctance motors (SRMs) etc. Recently, SRMs have become a major contribution in areas where high starting torque and high rotational speed are required at a low cost. However, a higher rotational speed often shortens the life of mechanical bearings and limits the high speed ability of such motors. Such a situation demands an electrical motor, which can avoid contact between the bearings and shaft to reduce the wear and tear of the mechanical bearings. One such effort by researchers has been made by introducing magnetic bearing in electrical machines and another is the integration of bearingless technology with machines. Various researchers have contributed to integrate bearingless operation in switched reluctance motors. One such technique is a specialized stator winding scheme called Bridge Configured Winding (BCW) which can be used to generate transverse force or radial force efficiently in electrical motors. The radial forces produced, when controlled accurately can suspend the rotor in its position thus reducing the use of mechanical bearing and avoid the frictional losses incurred. This controllable radial force can also be used to mitigate the vibration and acoustic noises that arise inherently in a SRMs.

BCW is a specialized single set of stator winding containing a double layer of coils in each stator slot. The bridge connection does not require any special structure to house the windings and can be implemented in motors just as conventional windings. The principal advantage of this technique is the impetus on designing bearingless switched reluctance motor (BSRM) to utilize a combined stator winding system for both torque and radial force production and thus provide a cost-saving solution. This winding scheme forms two sets of terminals in each phase, one for the supply of voltage to produce torque and the other for the supply of voltage to produce controllable radial force. It provides the flexibility to operate as a normal motor when the bridge terminals are not used.

The radial force and torque characteristics of the proposed motor have been investigated by developing a Finite Element Model (FEM) using Ansoft Maxwell 2D. The force generation in BCW is related with the torque producing current which is named as the main current and the levitation current which are named as the bridge currents. A mathematical model is developed which gives the relation of torque and radial forces with the main current and the bridge currents respectively. The mathematical model is used in developing a control algorithm for the drive system of the proposed motor. The bridge currents have been further explored considering static rotor eccentricity and are utilized in positioning of the rotor towards the centre.

A SRM normally requires a power converter system for the production of positive torque. This thesis presents the modelling and simulation of an asymmetric bridge power

converter with a speed-current control drive for both motoring and radial force production in BCW SRM. For radial force production in SRMs, it has to be kept in mind that the normal torque production of the motor is not compromised and no negative torque is produced. Owing to this condition, a switching topology has been proposed for producing positive torque as well as radial force for the bridge winding scheme. Further, in order to demonstrate the control of the radial force and radial displacement using the bridge currents, a simulation model is developed in MATLAB/SIMULINK and the conventional closed loop control mechanism called the proportional integral derivative (PID) controller is used to minimize the displacement error.

Two test rigs have been designed and fabricated for carrying out experiments on conventional SRM and a BCW SRM. Two 12/8 SRMs have been fabricated, one with the conventional winding and the other with BCW. An asymmetric bridge power converter has been practically implemented for the rotational drive system of the prototype. A real-time closed loop control of radial displacement using PID has been implemented and the capability of the BCW for both torque and radial displacement control has been experimentally validated.

Contents

List of Figures

List of Tables

भारतीय प्रौद्योगिकी संस्थान गुवाहाटी
Indian Institute of Technology Guwahati

List of Acronyms

AWG American Wire Gauge

BCW Bridge Configured Winding

BSRM Bearingless Switched Reluctance Motor

DC Direct Current

DAQ Data Acquisition

FEA Finite Element Analysis

FEM Finite Element Model

IEC International Electrotechnical Commission

KCL Kirchoff's Current Law

MEC Magnetic Equivalent Circuit

NEMA National Electrical Manufacturers Association

PID Proportional Integral Derivative

PI Proportional Integral

PWM Pulse Width Modulation

SRM Switched Reluctance Motor

UMP Unbalanced Magnetic Pull

CAD Computer aided design

भारतीय प्रौद्योगिकी संस्थान गुवाहाटी
Indian Institute of Technology Guwahati

Nomenclature

β_r	Rotor pole arc angle
β_s	Stator pole arc angle
λ	Flux linkage
λ_a, λ_b, λ_c	Flux linkages in windings of phase-a, phase-b and phase-c
μ_0	Magnetic permeability of vacuum or air
ω	Rated speed of the motor
ϕ_{a1}, ϕ_{a2}, ϕ_{a3}, ϕ_{a4}	Magnetic fluxes in airgap 1, airgap 2, airgap 3 and airgap 4 of phase-A
$\Re_{sp}$, $\Re_g$, $\Re_{rc}$, $\Re_y$	Reluctances of stator pole, airgap, rotor core, and stator yoke
ρ	Resistivity of copper
τ	Magnetomotive force
θ	Rotor angle
θ_a, θ_b, θ_c	Rotor angle for phase-A, phase-B and phase-C
θ_d	Dwell angle or conduction angle
θ_{max}	Complete overlap angle of stator and rotor tooth
$A1$, $A2$, $A3$, $A4$	Airgap 1, airgap 2, airgap 3 and airgap 4 of phase-A
A_c	Area of coil
a_c	Area of conductor

A_g	Area of air gap
A_r	Area of rotor pole
A_{rc}	Area of rotor core
A_s	Area of stator pole
a_s	Area of stator slot
A_y	Area of stator yoke
A_y	Area of yoke
B	Magnetic field density
B_{f1}, B_{f2}	Fringing flux densities
B_m	Main flux density
B_{max}	Maximum flux density
B_r	Flux density in rotor pole
B_{rc}	Flux density in rotor core
B_y	Flux density in stator yoke
C_r	Back of core thickness of rotor
C_s	Back of core thickness of stator
D	Bore diameter or frame size
D_o	Outer diameter of stator
D_{sh}	Diameter of the shaft
d_w	Diameter of conducting wire
F_l	Lifting force
F_r	Radial force component
F_t	Tangential force component

F_x	Radial force component in x - axis direction
F_y	Radial force component in y - axis direction
h	Length of the rotor stack
H_g	Magnetic field intensity of airgap
H_r	Magnetic field intensity of rotor pole
H_{rc}	Magnetic field intensity of rotor core
H_s	Magnetic field intensity of stator pole
h_s	Height of stator tooth
h_w	Height of the winding per slot
H_y	Magnetic field intensity of stator yoke
i	Total current per phase
i_a, i_b, i_c	Phase currents in normal SRM
i_{b1a}, i_{b1b}, i_{b1c}	Bridge current for radial force along x-axis direction of phase-A, phase-B and phase-C
i_{b2a}, i_{b2b}, i_{b2c}	Bridge current for radial force along y-axis direction of phase-A, phase-B and phase-C
I_m	Main current in dual set of winding
i_{ma}, i_{mb}, i_{mc}	Main current in phase-A, phase-B and phase-C of bridge configured winding
i_p	Peak current
i_p	Rated current of the motor
I_s	Suspension currents in dual set of winding
J_c	Current density
k	Variable for shape of flux path

K_i	Force current factor
K_x	Translational stiffness factor
L	Inductance
l	Average length of the magnetic path
L_a	Aligned inductance
l_g	Air gap length
l_r	Length of flux path in rotor pole
l_{rc}	Length of flux path in rotor core
l_s	Length of flux path in stator pole
L_u	Unaligned inductance
l_y	Length of flux path in stator yoke
N	Total number of turns in per phase winding
P	Total permeance
P_{a1}, P_{a2}, P_{a3}, P_{a4}	Magnetic permeances in airgap 1, airgap 2, airgap 3 and airgap 4 of phase-A
$P_{cu(ph)}$	Copper loss per phase
r	Outer radius of the rotor
$R_{s(ph)}$	Equivalent resistance per phase
T	Electromagnetic torque
t	Position on the rotor circular face
W_f	Magnetic field co-energy
w_{sp}	Width of stator pole
x, y	Horizontal and vertical axes cartesian co-ordinates

Chapter 1

Introduction

Contents

1.1 Background

An electrical machine is an integral component of industry and society. In power sector industry, rotating electrical machines dominates large scale power generation, for efficiency, reliability and cost reasons. Electrical machines are widely used in various applications, such as centrifugal pumps, compressors, elevators, electricity generation and many other industrial applications. Therefore, the efficiency of the electrical machine is also a major environmental factor. Besides, there is also a strong industrial demand for reliable and safe operation of the rotating machine. An electrical machine is normally divided into two applications such as, electrical generator and electrical motor. In the emerging industrial applications, rotating electrical motors have made wide contributions. An electric motor normally comprises of a stator, a rotor and a shaft, where the rotor of the motor is supported by two mechanical bearings through a shaft.

Modern electric motors with conventional bearings are usually employed for high-speed applications which often shorten the overall life span of the motor due to continuous friction. The load capacity of the bearings in electric motor drives further reduces when exposed to harsh conditions. Study shows that nearly 40-50 % of motor failure occurs due to bearing failure [1]. Hence, magnetic suspension in electrical motors can enlarge the possible application areas of motor drives. In order to overcome this limitation, a technology has been developed for bearingless operation, which avoids contact of bearing and shaft, thus integrating the function of magnetic bearing with an electric motor and making it suitable to operate as a conventional motor but with the shaft magnetically levitated. This is basically done by using separate winding system called suspension windings which share the same stator slot with the torque producing main windings [**?**]. Radial forces are produced by perturbation in the currents flowing through the main winding and creating an unbalance in the magnetic field. The radial forces which are produced should be controlled effectively in order to suspend the rotor in its centre, and thus reduce the use of mechanical bearing to avoid the frictional losses. Such bearingless motors offer a technically attractive alternative to conventional motors and in drive systems which require maintenance free operation for a lifetime and in contamination free transportation of fluids or gases [2].

A switched reluctance motor (SRM) is a robust motor and appropriate for applications with high external impact and is well suited for bearingless motors. The SRM is an electrical motor having doubly salient poles where torque is produced due to the tendency of the rotor pole to achieve a position of minimum reluctance. It has one of the simplest mechanical constructions among all the electrical machines with only the stator

poles having windings. The rotor poles contain no conductors or permanent magnets. Therefore inherent advantages like rigid construction, low cost, less weight and high reliability along with its superior performance have motivated a large amount of research on SRMs over the last few decades. However due to its doubly salient geometry, high acoustic noise and vibrations are produced [3]. In addition, the non-uniformity of the air gap in SRM generates radial magnetic forcesand leads to vibration and noise. As the torque is produced by a sequential switching of the stator winding currents, a large ripple is also generated in the torque. A viable solution for mitigating such mechanical vibration and noise is to suspend the rotor magnetically i.e.to convert the motor into a self-bearing or bearingless motor. The SRMs offer a good prospect for bearingless operation. In the process of torque generation, a significant amount of radial force is also generated in SRMs due to their double salient pole structures and very small air gap between the rotor and the stator. Thus, it is possible to take advantage of this inherent feature for magnetic suspension of the rotor-shaft.

The present work is about design and analysis of a BSRM using a step by step procedure by applying the basic principles of electromagnetics. The thesis focuses on the design of a combined stator winding which can accomplish the tasks of both torque and controllable radial force production, thus avoiding additional stator winding for radial forces. This bridge winding scheme certain advantages such as i) single power supply for torque production, ii) low voltage supply for radial force production, iii) relatively less copper losses as the number of winding in each phase is reduced to one single set and iv) utilization of entire slot area for torque production as currents for both torque and levitation can flow through the same winding, taking full advantage of the available number of turns in the stator slot. This characteristic is true in case of other combined winding schemes too [4].

1.1.1 Principle of radial force generation in SRM

An asymmetric air gap magnetic field is the reason behind the generation of radial force or magnetic pull in electrical machines. There are various factors which lead to asymmetry in the air gap magnetic field. It may be either present in electrical machines or can be created by regulating the coil currents.

The SRMs are doubly salient pole motors and whenever a phase winding of an SRM is energized a magnetic pull is generated. This pull can be distributed into a tangential component and radial component. In normal motors, this tangential component is responsible for the rotation of the motor while the radial component is neutralized due

to the balanced current in the windings and uniform flux distribution in the air gaps. It transpires that a relatively small amount of additional flux introduced can create an asymmetry in the distribution of magnetic flux in the air gap, resulting in significant net radial forces. In BSRMs these radial force components are utilized for levitation of the rotor by creating an unbalance in the magnetic field through perturbation in the winding currents. This radial force can suspend the rotor in its position when controlled accurately, thus reducing the use of mechanical bearing and avoid frictional losses. Figure 1.1 shows the principle of radial force generation in SRMs for bearingless operation. The stator and rotor are magnetized with currents in windings W1, W2, W3 and W4 such that four magnetic poles in north, south, north, south sequence are formed in the air gaps *A1*, *A2*, *A3* and *A4* respectively. In Figure 1.1 (a), these four magnetic poles have equal flux density and equal attractive force magnitudes. Thus, the net sum of the four radial forces is zero. This configuration indicates a motor with a four-pole magnetic field motor winding for torque generation. However, if the current in W1 is more than W3, it results in an increase of magnetic field density in air gap *A1* and decrease in *A3* as shown in Figure 1.1 (b) and hence, a radial force F_x is generated in the x direction. A negative radial force along the x-axis can be generated by decreasing the current in W1 and increasing the current in W3. The radial force increases as the difference in the currents increases. Similarly, radial force F_y in y direction can be generated by controlling the currents in W2 and W4 as shown in Figure 1.1 (c). Thus, the above explanation describes the principle of radial force generation in x and y directions. This methodology of radial force generation is generally done using separate winding called suspension winding which occupies the same slots with the torque winding [5]. The same method of radial force production has been used by researchers using a single set of stator winding called combined winding. In combined winding scheme both torque and force production functionalities are combined into the same stator winding for bearingless motors [6].

The nature of such type of machines demands that the development of SRM as bearingless motors requires accurate design of the machine and its control, unlike other conventional machines. The design procedure of conventional SRM has been extensively explored by Krishnan in 2001 [3]. Vijayraghavan in 2001 [7] developed a design procedure for SRM and discussed the factors affecting the selection of the various geometrical parameters of the motor. However, a BSRM differs from a conventional SRM as more focus is directed towards the generation of the suspension force. Several bearingless structures of SRMs have been recently studied and proposed. There are several methodologies to generate radial suspension force. Various design methodologies of winding schemes have

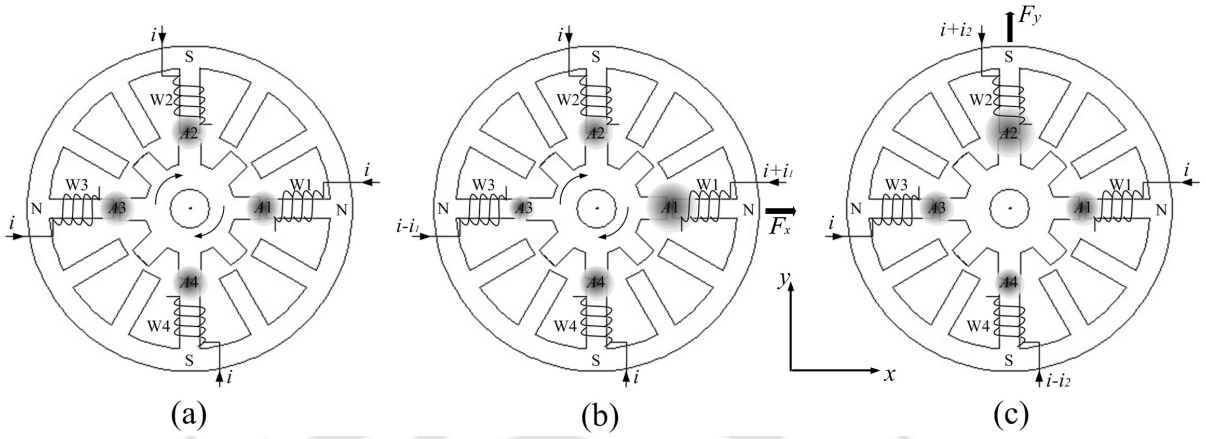

Figure 1.1: (a) Balanced magnetic field density. Unbalanced magnetic field density in air gaps with radial force generation in (b) x direction, (c) y direction.

been introduced by researchers to produce radial force, which can be utilized for the self-bearing operation of an SRM [5], [8–11]. Differential stator winding configurations have been implemented by Takemoto *et al*. [9] where the motor winding and radial force windings are wound on the same stator slot in order to produce a force for the suspension of the rotor and shaft. Some researchers have focused on wide rotor structures, however the excitation scheme in such cases are slightly different where two phases are excited simultaneously [12]. One phase is excited for torque and the adjacent phase for radial force. Such schemes introduces negative torque production and hampers the normal motoring operation of the machine. Again, some methodologies included separate excitation of the winding which again required high power sources and complex control algorithm [13].

In this thesis, a special combined winding scheme, called Bridge Configured Winding (BCW), has been proposed for SRM which has the ability to generate both torque and radial forces using the same set of motor winding and help the motor to operate as a bearingless machine [14], [15]. Unlike conventional BSRMs, where the main windings in each phase contains four coils connected in series, the BCW has four coils connected in bridge configuration where the main power supply is connected between two opposite terminals for the main current and an isolated power supply is connected between the other two terminals for injecting bridge current to generate the radial forces as shown in Figure 1.2(a) and in Figure 1.2(b). The BCW is an elegant development where no additional windings are necessary to produce the net radial forces as done in conventional BSRMs [14], [15], [16]. The present work is about the study and implementation

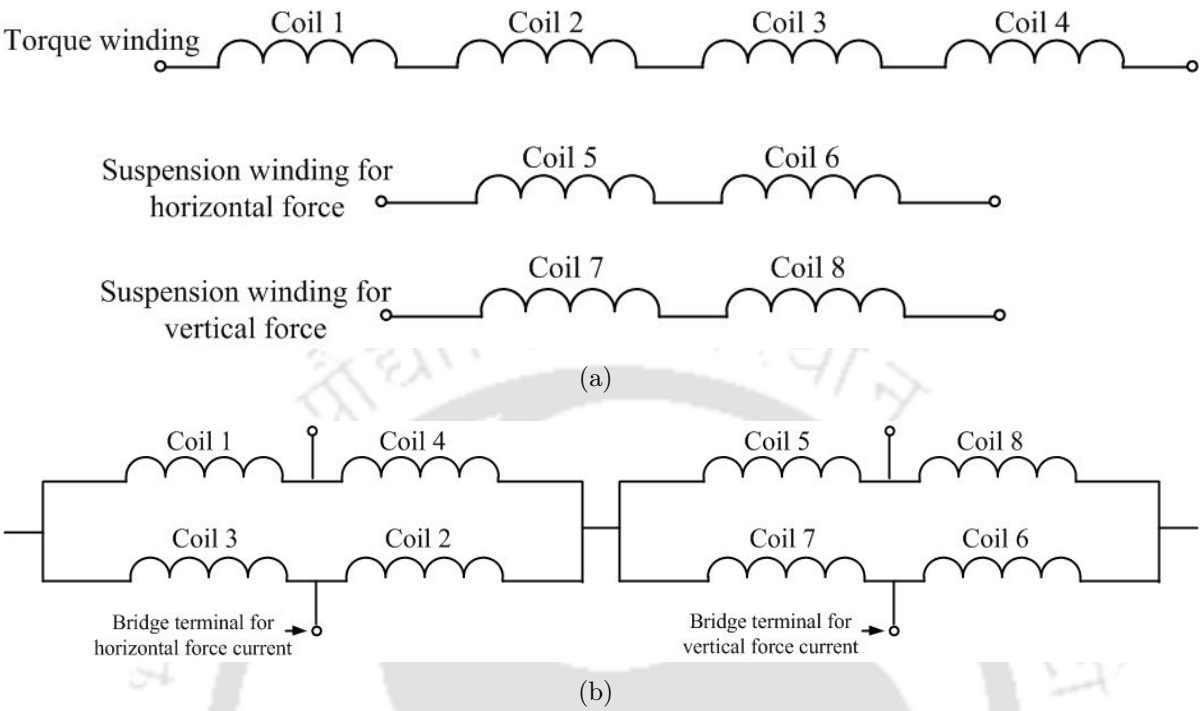

Figure 1.2: Schematic of coil connection per phase in (a) conventional separate winding scheme and (b) BCW scheme.

of controllable radial force generation using BCW in SRM which can help in self-bearing operation of the motor. These controllable radial forces can be used for various purposes such as active vibration control, rotor eccentricity control and noise reduction. Considering the characteristics and advantages of BSRM for maintenance-free high-speed drive applications, the design methodology is of utmost importance to design engineers. The present work focuses on a step by step design procedure of a 12/8 SRM with BCW for torque and radial force production using the same winding. A trade-off is maintained with the proposed design such that the torque of the motor is not compromised. A detailed discussion is given in the literature review in Chapter 2 of the thesis.

1.2 Motivation

The motivation behind this work is to design an efficient electrical machine, viz. SRM and develop a system which can contribute to low power losses incurred due to friction. Electrical bearingless machines offer great opportunities through their ability to provide radial suspension force without any significant losses. Bearingless motors have been

widely and significantly developed in permanent magnet synchronous motors, induction motors, switched reluctance motors and also in ac homopolar motors [17–19], [5], [15]. Such machines have already found its application in low speed machines like in bioreactors, centrifugal pumps and artificial heart and also in high speed machines like flywheel, spindle tools, and turbomachinery [20–27]. Some of the existing designs of bearingless motors affects the normal torque production as well as incurs copper losses due to the additional suspension winding configuration. Such drawback can be overcome by a novel design methodology which can provide a better torque in such motors and focus on a winding scheme which can contribute in lower copper loss. Such development can be a good contribution to the power industry if it can be achieved with low inverter power requirement for radial force production. Combining these functions into one device has the benefit of simplifying the machine, reducing the amount of raw materials needed, and reducing the manufacturing cost. In addition to the advantages of obtaining high speed as bearingless motors, this would also add to vibration and noise reduction in SRMs due to unbalanced forces caused by manufacturing error. Bridge configured winding (BCW) scheme is one such novel stator winding scheme which can be installed in an electrical machine to control rotor radial displacement with a low power inverter requirement along with its primary function as a motor or generator. There is an ample scope of obtaining both rotation and self-bearing operation in SRM using a combined winding (BCW) set in order to reduce the complexities of using additional windings for producing suspension forces. This winding is a novel approach which can be used to transform an existing motor to produce both torque and control radial displacement by modifying the end winding connection. From the design front, it can be stated that with the selection of proper geometrical dimensions and an appropriate switching strategy of SRMs, both torque and force profiles can be obtained. With this motive, an effort has been made to develop an SRM and demonstrate torque and radial displacement control of the rotor using a combined winding set.

1.3 Aim of the research

Wear and tear of mechanical bearing in a motor have always been a major issue caused by friction. Frictional losses proves to be a major hindrance in the high-speed performance of electrical machines. This can be overcome by replacing conventional motors with bearingless or self-bearing motors. A bridge configured winding scheme has been proposed for the development of an SRM which is capable of producing controllable

radial displacements in the motor. However, the implementation of the BCW scheme in SRM production offers certain challenges which need to be addressed. The work in this thesis aims to address certain challenges by setting up the following objectives:

- Development of a mathematical model of the proposed BCW scheme to understand the characteristics of torque and radial force with the winding currents. Derivation of the relationships of torque and radial forces with the rotor radial displacement and winding currents for every change in rotor position.
- An analytical procedure is presented for the design of a SRM configurable for bridge winding scheme applying the basic principles of electromagnetics. In this thesis, the design procedure is described in a methodical manner for the development of the prototype for the proposed motor.
- Development of a finite element based simulation model using finite element analysis (FEA) tool in order to verify the design procedure and the mathematical model of the BSRM with BCW.
- Analysis and simulation of a speed-current controlled drive system is presented for both torque and radial force generation in BSRM with BCW. The effects and capability of the bridge currents and the motor main current to produce radial force in the motor are analyzed.
- Implementation of the proposed BCW scheme in a 750 W, 12/8 SRM. An experimental set up is developed and the hardwares of asymmetric bridge power converters are fabricated. A real-time controller is developed to practically demonstrate the BCW SRM for both rotating and radial displacement control by injecting controlled bridge currents in the bridge terminals.

1.4 Organization of the thesis

The thesis is organized into six chapters. The brief descriptions of each chapter are as follows.

Chapter 1 describes the background of the study along with the motivation and aim of the research.

Chapter 2 introduces the fundamentals of SRM and the principles of torque and radial force production in it. An exhaustive literature review involving various mathematical methods of modeling of BSRMs, numerical modeling, various winding structures, and

design methodologies are discussed in this chapter to understand the state of art in this area. A further literature review involves various converter topologies for the conventional SRM drive system and for bearingless drives. The different control methods of torque and radial force in BSRMs are also included in the chapter.

Chapter 3 introduces the concept of BCW for the self-bearing operation of a 12/8 SRM. The theory is explained for a generic combined winding for one phase of a 4-pole self-bearing motor with bridge winding scheme. The effects of the bridge current supply and its contribution in producing radial forces are explained in details. A reluctance network model is developed for the proposed 12/8 BSRM with BCW using a magnetic equivalent circuit method. For effective radial force production in SRM in case of both aligned and unaligned positions, the effects of the main flux and fringing flux paths are modeled analytically to obtain an accurate model of radial force control. The relationship of torque and radial forces with winding currents with respect to rotational position is derived using the Maxwell stress tensor method. Further, a step by step design procedure is followed for the development of a prototype of a 12/8 SRM with BCW for self-bearing purpose. The analysis is verified with a numerical model developed using FEA in the software Ansoft Maxwell 2D. A parametric based analysis, focusing on the geometrical parameters is done using FEA and an optimized model suitable for bridge winding scheme is developed. Further, the analytical relationships between radial force, torque and current are verified with the FE model.

Chapter 4 describes the principle of asymmetric bridge power converter along with its modes of operation for the proposed motor. The chapter also outlines the design topology of the drive system of the motor for both torque and radial force production. Simulation results of the drive system are described in this chapter using co-simulation of FE model with a closed loop drive system developed in the commercial software package Ansoft Simplorer. Later part of the chapter deals with a radial force control method using a simple PID controller developed in Matlab SIMULINK© for the proposed configuration.

Chapter 5 presents the practical development and implementation of the proposed SRM with BCW to investigate the effect of the bridge current supply in radial displacement control. An asymmetric bridge converter is implemented and tested for the motoring operation. A real-time closed loop system is developed using a PID controller for the radial displacement control of the motor. The experimental results demonstrate the capability and flexibility of the combined stator winding called BCW for both torque and radial displacement control.

Chapter 6 presents the conclusion of the current research and outlines the directions

for future work.

Chapter 2

Literature Review

Contents

This chapter presents a brief introduction to the origin of switched reluctance motor (SRM) and its features. A literature review is initially presented on the design of SRM and drives. Literature involving the origin of SRM as bearingless motors has been highlighted. Various methods of radial force and torque calculation for bearingless switched reluctance motor (BSRM) using analytical and numerical methods are discussed in this chapter. The study of the literature review is divided into the following main sections:

- Background of switched reluctance motors and drives.

  -Principle of operation of SRM.

  -Power converter for SRM drives.

- Methods of radial force calculation and control.

  -Analytical and numerical methods for radial force calculation.

  -Radial force control methods and bearingless drives.

- Winding topologies in BSRMs.

  - Separate set of winding.

  - Combined set of winding.

- Structural modifications in BSRMs.

2.1 Background of design of SRM and drives

The concept of reluctance motor can be dated back to 1842, when a locomotive was propelled by a reluctance motor in Scotland [28]. In 1969, S. A. Nasar [29] introduced the basic concepts of modern SRMs. The reinvention of this motor has been possible with the advent of modern, inexpensive and high-power switching devices. The SRM is a type of special motor which runs by reluctance torque with certain novel features. SRMs have doubly salient pole structures, with field coils wound on the stator as a DC motor and has no coils or magnets on its rotor. Each stator pole carries a coil for excitation and the opposite coils are connected to form one phase winding. The excitation of coils is controlled using power electronic converters to achieve sequential phase excitation and continuous torque. Depending on their applications, SRMs are produced within a wide range of structural configurations, viz. 6/4, 8/6, 12/8, 18/12 etc. The number of phases

of SRM converter is generally determined from the number of stator pole numbers (N_s) and rotor pole numbers (N_r) as

$$q = \frac{N_s}{N_s - N_r} \tag{2.1}$$

where q is the number of phases [3]. In case of a 12/8 SRM configuration, the number of converter phases is three. Figure 2.1 shows the cross-section of a 12/8 SRM with its coil excitation using a three phase power converter circuit, where A, B and C represent coils in each phase winding.

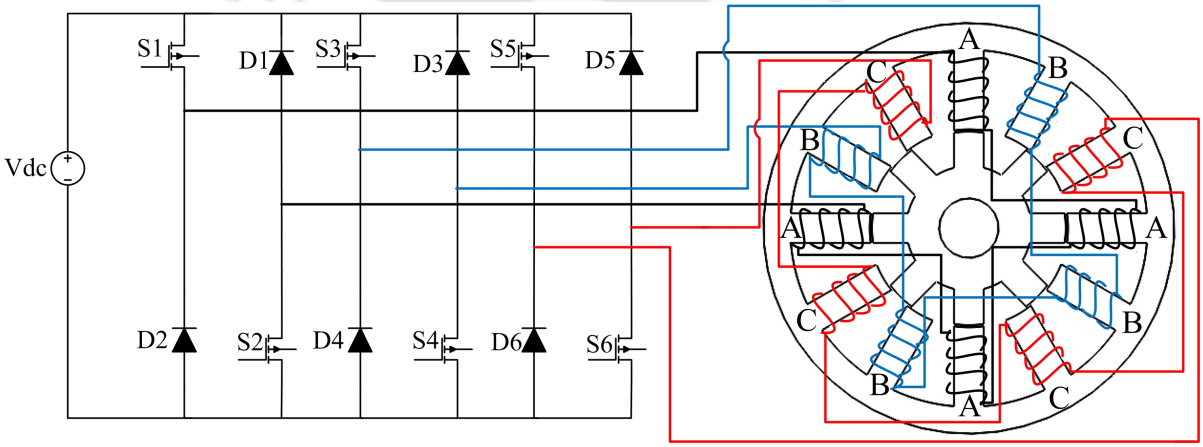

Figure 2.1: Cross-section of 12/8 SRM with a three phase power converter where $N_s = 12$ and N_r=8

2.1.1 Principle of operation of SRMs

The theory of torque production is best explained using the principle of electromechanical energy conversion in a solenoid. If a coils of solenoid is excited with a current then a coils sets up a flux and as the current increases, the armature moves towards the fixed yoke. Similarly in case of SRM, whenever the coils in the diametrically opposite stator poles are excited, the rotor poles tend to attain minimum reluctance position and get aligned with the stator poles, causing the rotor to turn. When two rotor poles are aligned the next set of rotor poles is out of alignment. Consequently, the next set of stator poles is excited to bring the corresponding set of rotor poles into alignment. Thus, by sequential switching of currents into the stator coils, the rotor is set into continuous rotation. A notable feature of SRM is that in case of open circuit, uninterrupted operation with reduced power output is possible [3].

Generally, electromechanical energy conversion may be considered as consecutive transformation of electrical energy into magnetic energy and of magnetic energy to mechanical energy. The transformation of electrical energy to magnetic energy can be best described by the differential equation as

$$\frac{\partial \Psi}{\partial t} = V - iR. \tag{2.2}$$

The co-energy W_c of the magnetic field is obtained as an integral of flux linkage at constant rotor position θ as

$$W_c(\theta, i) = \int_0^i \Psi(\theta, i) di. \tag{2.3}$$

Transformation of magnetic co-energy into mechanical energy without exchange between the winding and the electrical supply at constant current generates torque and is determined by differentiating the co-energy function W_c with respect to θ at constant current, i.e.

$$T_e(\theta, i) = \left.\frac{\partial W_c}{\partial \theta}\right|_{i=\text{constant}}. \tag{2.4}$$

Sustained rotating motion is achieved by sequentially energizing the appropriate phases according to the rotor position as the rotor rotates. The flux linkage can be expressed as a product of inductance and winding current.The magnetic saturation is neglected as the system is assumed to operate in a linear region. For simplicity, the linear variation of the inductance for every change in rotor position is considered. The flux-linkage can be expressed as

$$\Psi(\theta, i) = iL(\theta, i), \tag{2.5}$$

where L is the phase inductance and i is the phase winding current. The inductance is a function of rotor position and current. Thus, from the above expressions of flux linkage and co-energy, the torque equation can be written as

$$T_e(\theta, i) = \frac{1}{2} i^2 \frac{\partial L(\theta, i)}{\partial \theta}. \tag{2.6}$$

From Equation 2.6, it is understood that the generated torque is independent of the direction of current flow. Hence, unidirectional currents are generally used, thereby, greatly simplifying the design of the power converter.

The period of the late 70s was a time of development of concepts of the SRM along with the development of fast switching devices culminating in the work by Byrne [30] and Lawrenson *et al*. [31]. The very nature of the machine demands that the development of the switched reluctance motor drive requires the design of the machine and control to go hand in hand unlike any other machine. While the work by Lawrenson [31] *et al*. stands out in the development of the concepts of the machine as well as the fundamentals of control, the paper by Krishnan *et al*. [32] stands out in the development of a design procedure from an analytical stand point because it helps equate the design of the machine in terms of machine dimensions.

There are several publications that rely heavily on the design process solely based on finite element analysis, but this thesis will demonstrate that the design of the machine is rooted in the analytical relationships that govern the machine, followed by finite element analysis for verification. Finite element analysis of switched reluctance machines has been described in detail first in 1985 by Arumugam *et al*. [33] in a step by step design process applying the basic principles of electromagnetics. The analytical procedure of design of a normal switched reluctance machine with the selection of frame size and various dimensions in a methodical manner was initially developed by Corda and Stephenson [34]. After the selection of dimensions, they described a procedure to calculate the inductance in the aligned and unaligned position. Some authors have used analytical methods to derive the performance characteristics of SRM by calculating the relationships between flux linkages and rotor position as function of phase currents [35] and [36]. The flux maps are usually derived analytically by using various techniques, however they are fine-tuned with finite element analysis tool to improve accuracy of the flux paths. A 2-D magnetic field analysis using finite element software is sufficient for most applications. The procedure followed in the thesis for the design of the conventional SRM has been described in [3]. The development of converters and design of SRMs have been in existence since the development of the modern switched reluctance machine [37]. A number of configurations have been described and suitably summarized in [3] and [38]. The power converters normally studied and used are the asymmetric bridge converter which consists of two switches, viz. MOSFETs or IGBTs in one leg of the bridge and two freewheeling diodes across the winding. Figure 2.2 shows an asymmetric bridge converter with one phase leg, where S_1 and S_2 are two switches and D_1 and D_2 are the two

freewheeling diodes across the winding phase-a.

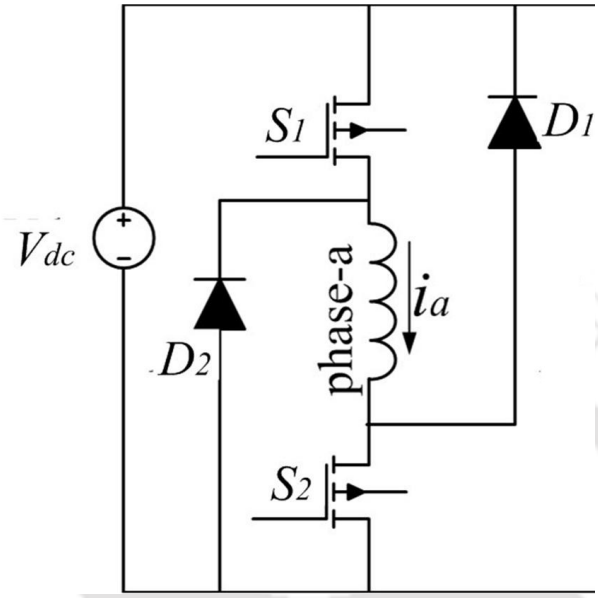

Figure 2.2: An asymmetric bridge converter with one phase leg

2.1.2 Power converters for SRM drives

SRMs can operate with unipolar current, i.e. the current flowing only in one direction in the windings, regardless of whether positive or negative torque is required. Since the reversal of current is not required, the converter consists of only one or two switches to be in series with each phase winding. The turning on or off of this switch regulates the flow of current in the phase. Different topologies of converters have been described in [3]. One of the most popular converters, viz. asymmetric bridge converter is discussed in this section as it has been implemented in the experimental part of this research work. The number of phases, q in SRM converters is decided based on the number of stator-rotor pole configuration of the motor as given in Equation 2.1. The asymmetric bridge converter uses two power semiconductor switches for each phase winding, each switch rated to withstand the dc supply voltage. Figure 2.3 shows the asymmetric bridge converter considering three single phase legs of the SRM. Each phase leg consists of two switches and two freewheeling diodes, where each phase winding of the motor is connected in series with the two switches. These switches are basically IGBTs or MOSFETs and the diodes used are fast recovery diodes. Each phase is excited sequentially in accordance with the rotor position. For instance, considering the first leg as phase-A of the SRM, turning on switches S_1 and S_2 will circulate a current i_a through the winding of phase-A

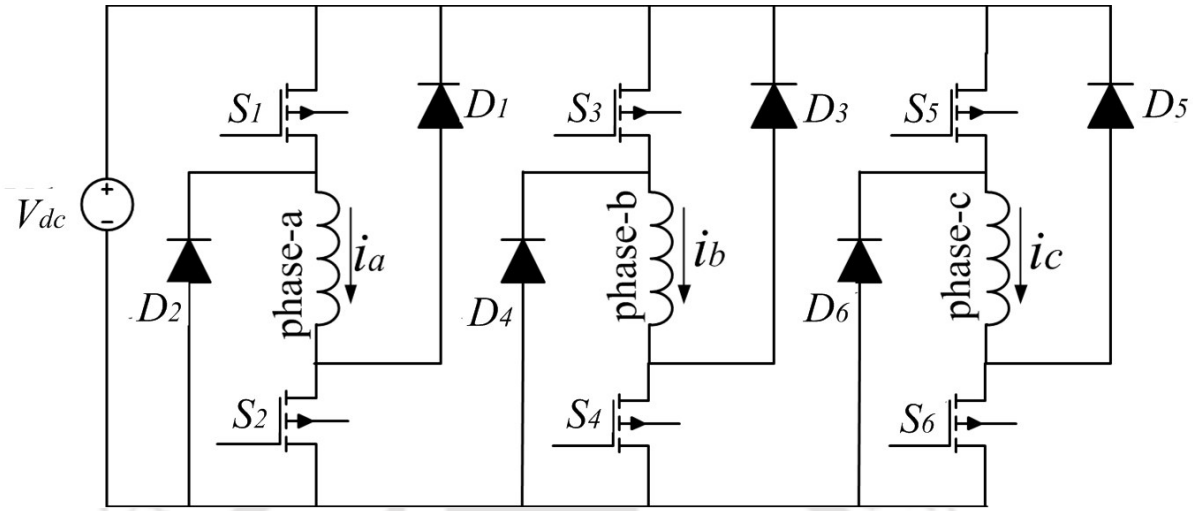

Figure 2.3: Basic configuration of an asymmetric bridge converter with three phase legs

as shown in Figure 2.3. The switching on and off of the switches S_1 and S_2 are governed by a hysteresis current controller to maintain the desired current with reference to a current feedback loop in the phase winding. The commutation of the phase current in the circuit is controlled by the duty cycle of the control signals fed to the gates of the switches based on the rotor position. When S_1 and S_2 are on during excitation of phase-A, if the current in the winding rises above the commanded value then the switches S_1 and S_2 turns off and the current freewheels through the diodes D_1 and D_2. The energy stored in the phase winding will keep the current in the same direction until it is exhausted. This leads to recharging of the DC source through the diodes D_1 and D_2. Similarly, the rest of the phases are controlled sequentially.

The operational waveform of current and its commutation in a particular phase-A can be explained with the help of Figure 2.4. Suppose a current of I_p is desired during the rising inductance region, i.e. from unaligned inductance (L_u) to aligned inductance (L_a) region for motoring action. Phase-a current is generated by turning on the switches S_1 and S_2. A current command i_a* is enforced with a current feedback loop where it is compared with the phase current i_a. Generally, a hysteresis current controller window is used which processes the current error with a current window of Δi. When the current error exceeds $I_p + \Delta i$, the switches S_1 and S_2 are turned off and the phase current i_a starts decreasing. When the current error drops below I_p - Δi, the switches S_1 and S_2 are turned on again maintaining the current error within the limits of $\pm \Delta i$. This process is maintained as long as the rotor is in the rising inductance region and as the rotor reaches the aligned position, the control signal of the gates commutates the phase

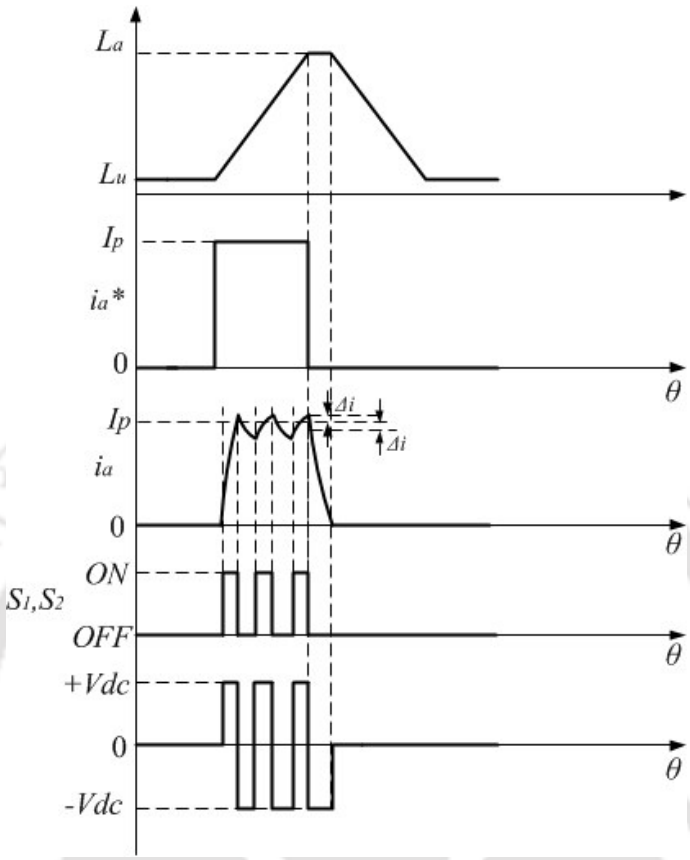

Figure 2.4: Operational waveform of the asymmetric bridge converter using hard chopping strategy

winding current allowing the phase-A circuit to turn off. S_1 and S_2 are completely turned off and the current completes its path through D_1 and D_2 and the DC source. This method of current chopping is known as hard chopping. This logic has an advantage of being simple and easy to implement. Hence this converter topology has been proposed in the experimental set up in this thesis, though various other switching strategies have been proposed by Krishnan in [3].

Another method of current chopping is the soft chopping method. In this method, by turning on the switches S_1 and S_2, current flows through the winding and it gets energized. The energy stored in phase-A can be effectively circulated by turning off, say, S_2 only. In that case, the current will continue to flow through S_1, phase-A winding and D_1. As soon as S_2 is turned off, diode D_1 gets forward biased and the voltage across the winding becomes zero if the voltage drops of the diode and the switches are neglected as shown in Figure 2.5. The phase current goes from $I_p + \Delta i$ to I_p - Δi in a time greater than the hard chopping strategy. When the current command goes to zero, both S_1 and

S_2 are turned off simultaneously. During this interval, the voltage across the phase-a winding is $-V_{dc}$ as long as D_1 and D_2 conducts after which the winding voltage becomes zero. The voltage across S_2 during its off time and when S_1 is on is equal to the source voltage V_{dc}. Hence, the power switches and diodes have to be rated to a minimum of source voltage [3].

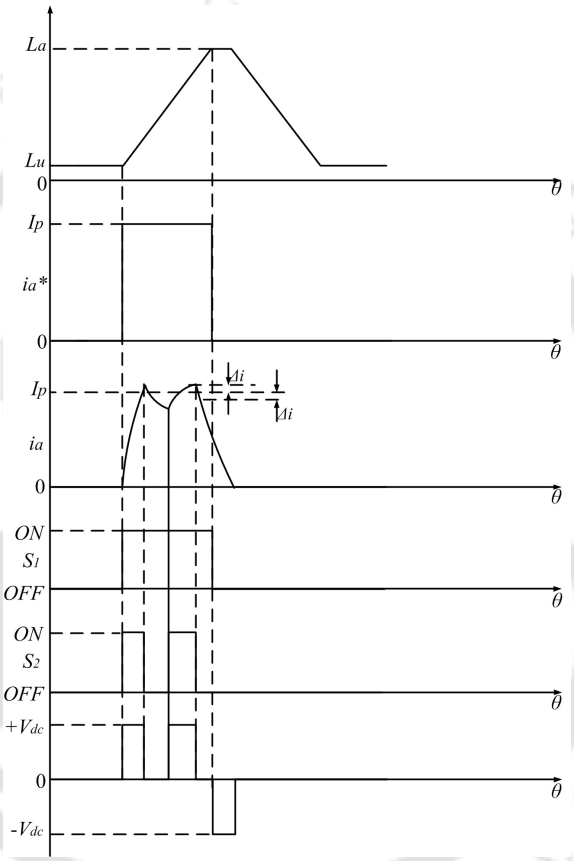

Figure 2.5: Waveform of asymmetric bridge converter for soft chopping strategy

The design of a novel converter drive based on the power requirement of the SRM has been reported in [28], [39]. Mahmoud *et al.* [40] have given comparison between various converter topologies, viz. C-Dump converter, R-Dump converter, C-Dump with freewheeling converter, asymmetric bridge converter, series passive converter etc. By comparing various converter topologies, it is found that the asymmetric converter with MOSFETs is suitable for high-speed operation at low power due to the fast fall and rise time of current and also prevent shoot-through fault. However, IGBTs power switches are preferable for medium speed operation at high power due to their high input impedance and low conduction losses.

The salient structure of the rotor and stator of SRMs brings along unbalanced radial

forces due to varying air-gap and under eccentric condition, causes vibration and noise in SRMs. To overcome this, several researchers proposed solution to produce controllable radial forces to reduce vibration and in addition, take advantage of this inherent radial force for rotor-shaft magnetic suspension. The following section focuses on the literature comprising various methods of analytical and numerical approaches of modelling controllable radial forces for bearingless operation of SRMs. An extensive literature review is also done considering various winding configurations for bearingless operation of SRM and different design methodologies of the geometrical structure of the motor. The literature review is also done on the various drive systems and control schemes of the BSRMs.

2.2 Methods to calculate radial force and torque in BSRMs

One of the primary disadvantages of SRM is its high acoustic noise and vibration as compared to other AC machines. The possible sources of vibration and noise may be magnetic field related, mechanical structure related or due to the power converters. The salient pole features and varying air-gap length produce radial forces in SRMs. It results in an unbalanced magnetic force on the rotor and causes rotor and shaft to vibrate and produce acoustic noises. These motor vibrations can be reduced by intentionally producing radial forces to cancel the unbalanced radial forces. It is also possible to take advantage of this inherent radial force and use it for magnetic suspension of the rotor-shaft. The literature shows that study related to the characteristics of radial forces in SRMs has started as early as in 1989. SRMs have a stator with concentrated windings around salient stator poles. Thus, if currents in the windings of each stator pole are controlled independently, both radial force and torque can be controlled. It has been found that this idea was originally proposed by Higuchi in 1989 [8].

The study of radial force and torque generation and its control for self-bearing operation and vibration reduction has been classified into two sub-sections:

(i) Analytical and numerical methods for radial force and torque calculation.

(ii)Radial force and drive control methods in BSRMs.

2.2.1 Analytical and numerical methods for radial force and torque calculation

For the calculation of electromagnetic forces acting between the stator and rotor, two methods are popular, i.e. principle of virtual work method and Maxwell Stress Tensor method. In case of reluctance machines, the electromagnetic force is based on the concept of the stored magnetic energy in the system. In some cases, researchers use the air-gap permeance method, where the permeance at each air-gap is modelled and based on it, the torque and force components are derived. For example, if we consider an electromagnetic core with air-gap length as l_g, number of coil turns as N, excitation current as i and permeability of the air as μ_0, the reluctance is given as

$$\Re = \frac{\mu_0 A}{l_g}. \tag{2.7}$$

The magnetic field energy is given as

$$W = \frac{1}{2}\frac{N^2 i^2}{\Re}. \tag{2.8}$$

Thus, the electromagnetic torque and radial force are given as

$$T_e = \frac{dW}{d\theta}, \tag{2.9}$$

$$F_x = \frac{dW}{dx}, \tag{2.10}$$

where θ is the rotor angle and x is the radial displacement of the rotor. The Maxwell stress method on the other hand, provides flexibility that yields an access to tangential and radial local force densities (stresses) at every point located on a closed contour in the air-gap. Local tangential and radial stresses in terms of components of the flux density at the respective location are given as

$$F_t = \frac{1}{\mu_0} B_n B_t, \tag{2.11}$$

$$F_n = \frac{1}{2\mu_0}(B_n^2 - B_t^2), \tag{2.12}$$

where B_n and B_t are the normal (radial) and tangential components of magnetic flux densities. Once normal and tangential stresses are calculated at every position on the

integration contour, one may calculate the net electromagnetic force using the following integration

$$F = \oint_c \overrightarrow{F_n} ds.\overrightarrow{n} + \oint_c \overrightarrow{F_t} ds.\overrightarrow{t}, \tag{2.13}$$

where, F is the net electromagnetic force, $\vec{t}$ and $\vec{n}$ denotes the unit vectors in the tangential and normal direction and c is the integration contour, respectively. This method has been successfully applied for predicting electromagnetic torque and radial forces in SRM and other types of electric machinery.

Several authors have used analytical approach to calculate the radial forces acting on the rotor. For the derivation of radial force model, the initial step is the calculation of the magnetic field distribution in the air-gap. Several authors have used the air-gap permeance method and have modelled the flux path in between the stator-rotor poles considering the main flux and the fringing flux paths. From the permeance model, the inductances are obtained and the radial force relationships are then derived from the inductances using the principle of virtual work energy method. Some authors have calculated magnetic radial force based on the assumption of independent pole pair using an analytical model which combines Maxwell stress tensor method with magnetic equivalent circuit method considering rotor displacement.

Takemoto *et al.* [9] have developed a differential stator winding which comprises of two sets of stator windings, one for torque production (main winding) and the other set of windings for radial force production (suspension windings). Figure 3.46 shows the two sets of windings for the phase-A configuration in BSRM. In this paper, the authors have developed a magnetic equivalent circuit for the differential stator winding and derived theoretical formulae for radial forces based on permeances in the air-gaps of the stator and rotor poles. They have assumed the fringing flux paths as elliptical lines and calculated the permeances in the air-gaps. From the permeances, the self and mutual inductances have been derived in order to obtain the stored magnetic energy in each phase.

By using virtual work method, the radial forces have been obtained as a derivative of the stored magnetic energy as

$$F_\alpha = \frac{\partial W}{\partial \alpha} = N_m N_{sa1}[\frac{\mu_0 hr(\pi - 12\theta_a)}{6l_o^2} + \frac{32\mu_0 hrc\theta_a}{\pi(4cr\theta_a(l_o+\alpha)+\pi l_o^2}]i_{ma}i_{sa1}, \tag{2.14}$$

$$F_\beta = \frac{\partial W}{\partial \beta} = N_m N_{sa2}[\frac{\mu_0 hr(\pi - 12\theta_a)}{6l_o^2} + \frac{32\mu_0 hrc\theta_a}{\pi(4cr\theta_a(l_o+\beta)+\pi l_o^2}]i_{ma}i_{sa2}, \tag{2.15}$$

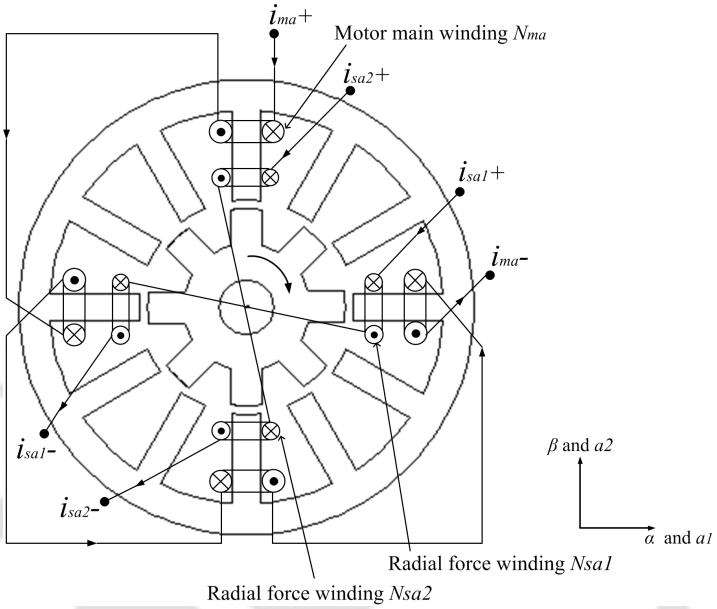

Figure 2.6: Phase-A winding configuration for the two sets of windings [9].

where, N_m, N_{sa1} and N_{sa2} are the number of turns of the main winding and the suspension windings, i_{ma} is the main current in phase-A, i_{sa1} is the current in suspension winding for radial force in α-direction and i_{sa2} is the current in suspension winding for radial force in β-direction, θ_a is the rotor angle, μ_0 is the permeability of air, h is the stack length of the motor, l_o is the length of the air-gap, r is the radius of the rotor and c is a constant value obtained from the flux paths.

In this method, the authors have assumed that the magnetic paths are composed of elliptical lines. The magnetic paths comprises of main flux lines and fringing flux lines. The fringing flux path is assumed to have an infinitesimal width 'dt' and 'kdt' at the rotor and stator surface. A constant 'k' is used to determine the shape of the ellipse. A position 't' is considered on the rotor circular surface which varies as the rotor angle changes. A relationship is obtained between the average length of the magnetic path, l with l_g, k and t as

$$\frac{l}{l_g} = \frac{\pi}{4}\left(1 + \frac{t}{l_g}(1+k)\right) \tag{2.16}$$

Equation 2.16 is simplified and written as

$$\frac{l}{l_g} = c\frac{t}{l_g} + \frac{\pi}{4} \tag{2.17}$$

From Equation 2.17 the term 'c' is obtained which is a constant value and has to be

determined from FEM results. This value 'c' helps in calculating the radial forces as given in Equations 2.14 and 2.15. The authors have used a finite element (FE) modeling approach of the proposed motor and determined the value of the variable 'c' based on the shape of the flux path. The shape of the flux path obtained from FE model is further used in the analytical model to validate the derived mathematical relations. Takemoto *et al.* [10] further considered the cross-coupling between the α and β directions and gave an improved analytical relation between radial forces and phase winding currents as

$$\begin{bmatrix} F_\alpha \\ F_\beta \end{bmatrix} = i_{ma} \begin{bmatrix} K_{f1} & -K_{f2} \\ K_{f2} & K_{f1} \end{bmatrix} \begin{bmatrix} i_{sa1} \\ i_{sa2} \end{bmatrix} \tag{2.18}$$

where,

$$K_{f_1} = N_m N_{sa1} \left(\frac{\mu_0 hr(\pi - 12\,|\theta_e|)}{6l_0^2} + \frac{32\mu_0 hrc\,|\theta_e|}{\pi(4rc\,|\theta_e|\,l_0 + \pi l_0^2}} \right)$$

and

$$K_{f_2} = N_m N_{sa2} \left(\frac{\mu_0 hr(\pi - 12\,|\theta_e|)\,|\theta_e|}{12l_0^2} - \frac{2\mu_0 h}{l_0} + \frac{16\mu_0 hc|\theta_e|^2 + 2l_0}{\pi(4rc\,|\theta_e|\,l_0 + \pi l_0^2}}. \right)$$

where, N_m, N_{sa1} and N_{sa2} are the number of turns of main winding and suspension windings, i_{ma} is the main current in phase-A, i_{sa1} is the current in suspension winding for radial force in α-direction, i_{sa2} is the current in suspension winding for radial force in β-direction, and θ_e is the rotor position. In this paper, the authors have used FE analysis to predict the shape of the magnetic flux paths by determining the value of 'c' as given in Equation 2.17. However, this method could not invariably give a relation between the radial forces and the phase current unless the value of the variable 'c' is predicted from FE analysis. Takemoto *et al.* [11] proposed a method for fast calculation of the radial force and torque for 12/8 BSRM with separate winding operating in a state of magnetic saturation. They predicted the influence of saturation on the fringing flux paths. They gave the formula for radial force as

$$F_{a1} = \frac{\partial W_{a1}}{\partial \alpha} = \frac{1}{2} \frac{\partial P_{ga1}}{\partial \alpha} U_{ga1}^2 = K_f(\theta) U_{ga1}^2, \tag{2.19}$$

where P_{ga1} is the permeance in air-gap $a1$ of phase-A, U_{ga1} is the magnetic potential difference in the air-gap of phase-A.

Finally, the expression of torque has been derived as

$$T_{a1} = \frac{\partial W}{\partial \theta} = \frac{1}{2} \frac{\partial P_{ga1}}{\partial \theta} U_{ga1}^2 = G_t(\theta) U_{ga1}^2. \tag{2.20}$$

In this paper, the authors gave theoretical relations of radial force and torque with respect to phase currents and used them to build a real-time control system for the machine. They have considered axial permeance in the air-gaps and have modified the equation of the magnetic potential as

$$U_g = \frac{\Psi_{ma}}{4N_m(P_g + P_L)} \tag{2.21}$$

where ψ_{ma} is the flux linkage in phase-A winding, N_m is the number of turns of phase-A, P_g is the air-gap permeance and P_L is the axial permeance. The axial permeance is basically due to the flux path which go out from the rotor in an axial way. In this case, the authors have assumed the axial permeance in parallel with the air-gap permeance. The authors have not considered the axial permeances in three dimensions, but have assumed the axial permeance on a condition that the measured values of the magnetic potential difference correspond to the ideal linearity of magnetic potential difference equal to the magnetomotive force in a region of no saturation. This paper could provide an effective method to derive the fringing fluxes assumed to be distributed as elliptical lines. The analytical derivations provided an effective way to control the dual winding BSRM at a normal operating point as well as at its maximum operating region in a real-time system. However, FE analysis needs considerable time for calculation, hence being not suitable for real time control. It has been shown experimentally in this paper that the proposed analytical method of calculating the radial forces and the torque under conditions of magnetic saturation could provide a stable operation.

Garrigan *et al.* [41] gave an analytical approach of radial force characteristics and examined the dynamic radial force behavior in SRM associated with eccentric rotor positioning. They have used the Maxwell Stress Tensor method by taking integration of flux paths around the pole faces and provided a straight forward calculation of the radial forces as

$$\begin{aligned} F_{radial} &= \tfrac{L_{stack}}{2\mu_0}\left(\int_1^2 B_{f1}^2 dl + \int_2^3 B_m^2 dl + \int_4^5 B_m^2 dl + \int_5^6 B_{f2}^2 dl\right) \\ &= \tfrac{L_{stack}}{2\mu_0}\left(B_{f1}^2 l_{12} + B_m^2(l_{23} + l_{45}) + B_{f2}^2 l_{56}\right), \end{aligned} \tag{2.22}$$

where B_m is the main flux density in the air-gap, B_{f1} and B_{f2} are the fringing flux densities in the air-gap, and L_{stack} is the stack length of the rotor. Thus, the radial force is equivalent to integration of magnetic flux densities over the surface area of the air-gap. The authors have characterized the radial force properties with eccentric rotor positioning and have established a way of predicting the radial forces under both static

and dynamic conditions.

Lin and Yang [42] gave an approach to produce controllable radial forces to compensate vibration caused due to unbalance radial forces in the motor. They have used different excitation procedure in the stator poles to produce controllable radial forces. The analytical model has been verified using FE analysis and also with experimental results.

Morrison *et al.* [43] performed analysis and experimental measurement of the electromagnetic force loads on a hybrid rotor in a novel hybrid magnetic-bearing switched-reluctance motor (MBSRM). They employed two magnetic circuit geometries, approximating the complex topology of the magnetic fields in and around the hybrid rotor, in formulating the electromagnetic radial force equations. The circular lamination stack and the scalloped lamination stack were treated as independent entities, and one-dimensional magnetic force equations were developed for each stack. The researchers used magnetic equivalent circuit for modelling the motor and derived the radial force model using virtual work method.

Takahashi *et al.* [44] gave a mathematical model of a 12/8 BSRM having the stator modified to facilitate two suspension windings, each coil occupying three adjacent stator poles. The magnetic equivalent circuit method is employed to obtain the self-inductances and mutual inductances of the motor torque windings (main windings) and suspension windings (control windings). The motor is analyzed using an analytical model and finite element model. Takemoto's approach is used to calculate the air-gap permeance. Though only two suspension windings are required for generating the radial forces, the structure of the stator poles is asymmetric and complicated. Similarly, Chen *et al.* [45] worked on combined winding hybrid structures of BSRM and developed mathematical model based on virtual work method and deduced its mathematical model of suspending force. A mathematical model using two phase excitation and a control strategy has been developed. Though this method could establish a decoupled control method for torque and suspension forces, occurrence of fluctuation in suspension forces were visible in the unaligned position from the simulation results. Moreover, the authors have not verified the proposed methodology experimentally. Yuan *et al.* [46] gave an accurate mathematical model of suspension force using Maxwell stress tensor method for a 8/14 pole BSRM structure which consisted of permanent magnets in the rotor. However, this work is only limited to analytical and finite element verification.

Various scholars have investigated on the mathematical modelling of radial forces considering eccentric rotor in SRMs and have studied the effects of eccentric rotor. Hus-

sain *et al.* [47] gave a detailed analytical model of computing radial forces in SRMs, occurring due to the displacements of the rotor from the centre. The authors have provided analytical expressions for the unbalanced force for the rotor positions where the rotor and stator poles are aligned and unaligned. The net radial forces have been derived as the sum of the two forces acting between two diametrically opposite poles considering different currents in the two poles. However, this method has been considered for individual current in the stator pole and the radial forces have been calculated considering individual pole current and net phase current. The authors have used finite-element analysis to validate the detailed analytical model. Dorell *et al.* [48] studied the effects of torque and radial forces due to rotor eccentricity in SRMs. This was illustrated using finite element analysis by consideration of the current/flux linkage loops for each phase and verified on an experimental four-phase SRM. Chen and Hoffmann [49] developed a mathematical model to calculate the forces based on rotor eccentricity. They gave the assumptions that the eccentric forces on different turn angles will be different because inductance of air-gap changes on each turn angle. With a mathematical model they gave the relations of the changing air-gap and the eccentric forces and the maximum winding currents required for levitation. Wang *et al.* [50] studied the effect of rotor eccentricity on suspension forces and developed an analytical model using the virtual work method for deriving the radial force model. They have used FEM to verify the analytical model. Wang *et al.* [51] further gave an improved analytical model for an eccentric rotor with a dual stator winding structure. The analytical model has been developed using the air-gap permeance method. The feasibility of proposed model was verified by FEM under dynamic conditions. The analytic model in this paper provided a control strategy to implement suspension control of the BSRM.

Ji *et al.* [52] studied the flux distributions and radial force of BSRM based on FEM. The authors could give relation curves between the radial force and the rotor position and the currents, obtained from the FE analysis. With the analysis, the magnetic characteristics of the motor at various rotor position was obtained. The authors could also predict the region effective for radial force production at different conditions of magnetic flux distributions in the air-gap.

Zhang *et al.* [53] built a nonlinear electromagnetic radial force model and designed a skewed rotor slot structure for reduction of radial forces and vibration. They defined radial force as a nonlinear function of rotor position θ and current i as

$$F_r = -\frac{1}{2}i^2\frac{L(\theta, i)}{r(1-\cos\theta)}, \tag{2.23}$$

Their observations were based on a FE model of the skewed rotor slot structure and no experimental investigations were done to validate the model. A rapid change of current, particularly associated with a declined range of inductance, produces vibration. In addition, vibrations increase as the rotor pole approaches alignment with a stator pole for a given current magnitude. Considering only finite element analysis, a nonlinear static radial force model has been developed by Zhang *et al.* [54]. They derived the radial forces at different rotor positions and different phase current excitations by using FE analysis. The FE model has been developed using ANSYS and the simulation has been carried out in MATLAB/SIMULINK. Zhang *et al.* [55] further developed a 3D FE model to calculate the electromagnetic radial forces and vibration modes for obtaining the periodic excitation and natural frequencies of stator. FFT has been used to analyse the dynamic vibration response of the SRM drive system with the radial force controller under the environment of SIMULINK.

2.2.2 Radial force and drive control methods for BSRMs

The generation of controllable radial forces is accompanied with various control methods. Several methods have been proposed to produce controlled radial force for BSRM. Takemoto *et al.* [5], [9] derived the mathematical model about the relationship between radial force, torque and winding currents to implement the levitation control strategy. Figure 2.7 shows the control drive system for BSRM having separate set of windings [10]. Figure 2.7 shows that the radial position control is operated with a negative feedback loop. The information of the rotor displacement is provided by the gap sensors placed on the shaft with respect to α and β axis. An encoder gives the rotor position and the derivative of the position gives the speed which is used as a negative feedback loop in the speed controller. The calculator in the radial position control block, calculates the suspension winding currents using the force equations from the mathematical model. The required suspension currents and the main current are then fed to the motor to generate the radial force required to bring the rotor back to the centre.

The same authors developed a feed-forward compensator for radial force control drive as shown in Figure 2.8. In order to suppress the radial vibration it is necessary to compensate the magnetic attractive force by cancelling the magnetic force caused by the rotor eccentricity or the circular movement of the rotor centre around the stator centre. For this purpose, the locus of the rotor radial position is traced in both the reference axes and the relation of the magnetic attraction force with the radius of the locus, winding current and the rotor position are determined. Using this feed-forward compensator, if

the locus of the rotor centre is not a circle it is still possible to compensate the magnetic attraction force without time delay by means of accurately measuring the locus. As shown in Figure 2.8 the output of the feed-forward compensator is then compared with the radial force's reference and fed to the controller for the suspending winding currents. The inverter generates the currents required to produce the desired radial force to bring back the rotor to its centre position. The authors have also proposed a square wave current topology for the main winding, in order to obtain a stable levitation of the motor. They gave an optimum value of the current pulse width [56]. The motor main winding current with square waveform is used in simplifying the drive system. The authors have derived relationship of the torque and radial forces with the main current and the suspension currents. As such by keeping the main current as constant, the suspension current for every rotational position can be evaluated. This helps in realizing a non-zero torque and sufficient radial forces can be generated at no load condition. The relationship between torque and radial force is controlled by the pulse width of the main winding current. The same authors further gave a control scheme to determine an advance angle for square wave current control method in BSRMs for stable operation of the motor [57], [58]. They derived an algorithm to calculate the advance angle by deriving relationship between average torque and radial force. They deduced the operating area for both radial force and average torque and could verify experimentally and conclude that the operating area can be controlled by fixing the commutation period in each phase and varying the advanced angle or firing angle to change the commutation position. The currents and the firing angle determine the values of radial force and torque.

Table 2.1: Description of symbols in Figure 2.7

Symbols	**Description**
1A'	Calculator (Inverse function of force equations)
2A'	Gate pulse controller
3A'	Phase detector
4A'	Inverter for suspension current, i_{sa1}
5A'	Inverter for suspension current, i_{sa2}
6A'	Inverter for motor current, i_m
7A'	Gap sensor for x-directional displacement
8A'	Gap sensor for y-directional displacement

Another control scheme based on the currents distribution is reported in [59]. In this scheme, the required main winding and auxiliary winding currents are summed and fed into a single motor coil per pole. However, the current and firing angle calculating

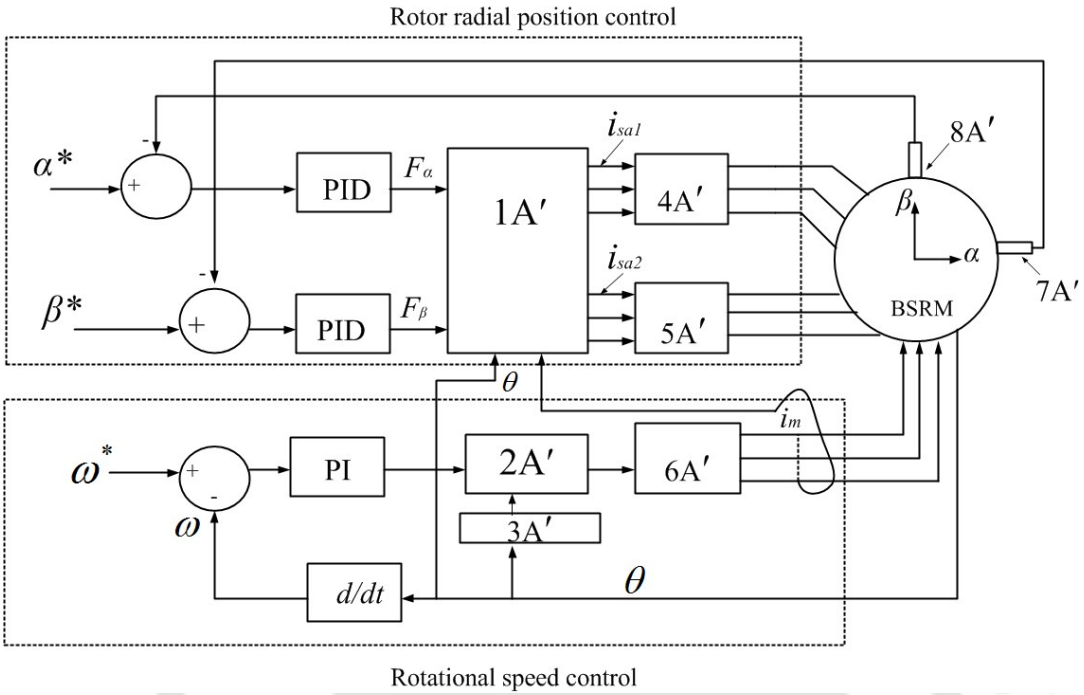

Figure 2.7: Control drive system of BSRM with separate set of winding [10]

.

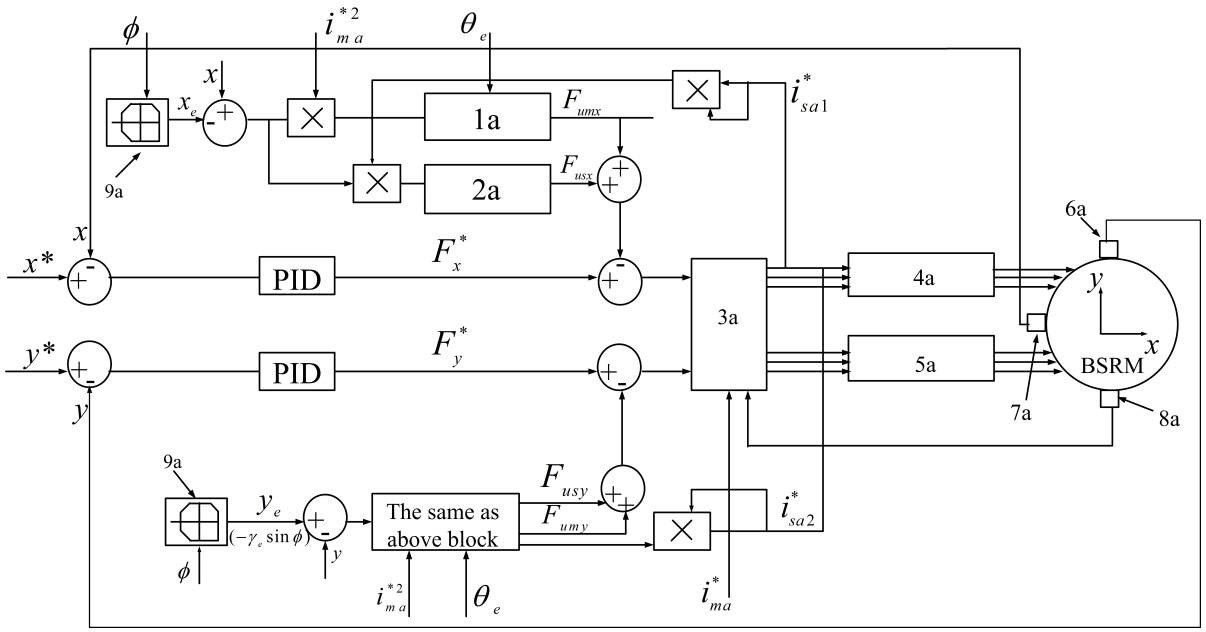

Figure 2.8: Rotor radial position controller with a feed-forward compensator [5]

.

processes in these schemes are sophisticated and for a good performance of the motor,

Table 2.2: Description of symbols in Figure 2.8

Symbols	Description
1a	$K_{um}(\theta_e)4N_m^2$
2a	$K_{us}(\theta_e)N_s^2$
3a	Controller for suspension winding currents
4a	Inverter for suspension current, i_{sa1}
5a	Inverter for suspension current, i_{sa1}
6a	Gap sensor for y-directional displacement
7a	Gap sensor for x-directional displacement
8a	Rotary encoder

large memory in digital signal processor is required to store the look up tables. Some researchers have focused on novel control algorithms to obtain independent control strategy.

Lin and Yang [60] gave an approach for separate control of radial force and torque by independent pole selection for excitation. They have proposed that, if SRM is controlled with the selected sinusoidal currents, it can produce the desired shaft radial force in any direction of the rotational plane without disrupting the rotational torque. However, in this scheme the phase current commutation strategy is complex and a sophisticated DSP controller is required for this purpose. Lin and Yang [61] proposed an approach of controllable radial force in SRMs using sinusoidal excitations. The researchers have used a technique of independent pole current control. They have used single phase excitation and two phase excitation methods based on the required torque and radial forces in each position. Two phase excitation improves the radial force production in the region of unalignment. In addition to the conducting phase in which the inductance is rising, the adjacent phase which lies in the descending inductance region, is also excited. However, such control scheme generated negative torque production because the descending inductance region is used for force control. Similar control technique has been observed in [62].

Cao *et al.* [63] gave an independent control strategy for torque and radial force using hybrid excitation in the main winding and levitation windings. The proposed control scheme has been derived by developing relation between the radial force and currents using Maxwell's Stress Tensor method. A current calculating algorithm has been developed to minimize the magnitude of the instantaneous torque in the levitation region. The scheme uses hybrid excitation of current in the main winding and single phase excitation in the levitation winding. In this paper, the authors have used PID controller to regulate the radial displacements. But, this control scheme has its disadvantage of

producing negative torque because the descending inductance region is used for levitation control. However, this problem has not been hlinvestigated by the authors. Yang *et al.* [64] developed a control strategy to calculate the control parameters based on least difference in the magnetomotive force of the main winding and radial force winding. The authors have analyzed the different magnetomotive forces on the radial force and torque, and the optimal combination of mmf is obtained. Based on the mmf required the winding currents are calculated. However, this control scheme required large memory resource in the controller for the calculation of the algorithms in real time.

Lee *et al.* [65] proposed a decoupling control strategy for torque and radial force control. A 8/10 pole SRM has been proposed where four diametrically opposite poles are used for radial force control and four successive stator poles for torque control. The radial force producing stator pole arc larger than the torque producing stator pole is proposed. In order to realize steady suspension, a model for radial force is introduced and used to design the controller. In the control scheme, a simple PID compensator and hysteresis current controllers are employed. Winding currents on the suspension poles are independently controlled to construct four radial force windings in x and y directions. The suspension winding currents could provide a steady levitation force in the motor. Though this scheme provides a simpler control algorithm and easier implementation, there is a probability of negative torque production owing to the excitation scheme of the torque winding. Park *et al.* [66] worked on similar hybrid pole BSRM and developed a control algorithm. The proposed algorithm has been tested and verified under loaded condition. Yang *et al.* [12] used wider rotor pole arc for suspension force windings. In this paper, the authors have used combined set winding in a 12/4 BSRM and dual windings in 12/8 BSRM. The authors have analysed the principle of operation for torque and levitation force by applying different modes of excitation and have developed a current control scheme by fixing the width of the conducting current accordingly. However, to avoid the problem of poor suspension force performance caused by current delay when switching the main winding current from torque production region to suspension force production region, it is necessary to add a compulsive excitation unit into the converter of the main winding. Decoupling strategy using wider rotor pole arc structure has further been investigated by Yang *et al.* [64] with a slightly modified control scheme. They shaped the conduction width of the current according to the current required in the torque region and the suspension force region.

Wang *et al.* [67] worked on decoupling torque and force strategy in BSRM with a biased permanent magnet (PM). In this paper, the proposed bearingless SRM consists

of two motors, in which each motor has two radial control degrees of freedom. In order to realize decoupling control, torque flux is completely independent from radial force flux. When the rotor center is eccentric, suspending force is generated by the control flux from the suspending force pole and the torque flux from the PM. Huang *et al.* developed a Hybrid Stator Bearingless Switched Reluctance Motor (HBSRM). A direct suspension force control strategy under the third-order sliding mode based on quasi-continuous algorithm is proposed for the HSBSRM to maintain the stability of suspension system [68]. Another decoupling control strategy of torque and suspension has been proposed and implemented by [69] where the authors have developed a single winding structure of 12/4 BSRM. A PWM control strategy has been used to control the speed and the current in the winding and obtain a simple levitation/suspension control of the motor. However, due to the wide rotor tooth structure, the motor provided a dead zone area during the torque production which introduces a zero or low torque in the motor.

Apart from the drive systems and control of BSRMs, a literature survey has been conducted on some effective and recently developed control schemes of bearingless motors. An effective controller for bearingless motor composed of a combined winding set has been proposed by [15] which has been termed as a dual purpose no-voltage winding drive to reduce the number of required hardware components of the parallel drive compared to a separate winding drive of traditional bearingless AC homopolar motors. The author has proposed a novel circuit topology using a floating capacitor inverter to implement a parallel dual purpose no-voltage winding. The paper presents a theoretical derivation for why the cross-coupling degrades the torque inverter's control performance while having no impact on the suspension performance. The dual-purpose no-voltage winding drive has been further investigated considering the cross-coupling effects between the suspension and torque operation [70]. The authors have explained the nature of the coupling in relation to the machine and the control parameters to provide an inception for the bearingless controller design. Jiang *et al.* [71] further experimentally validated this control strategy by using feed-forward compensation method and resonant compensation. The feed-forward method is effective when real-time communication is provided between the motor and suspension controllers. However, this method is not possible to be implemented with commercial motor drive products. On the other hand, the resonant controller approach requires no communication between the suspension and motor controllers and therefore can be implemented on a commercial motor drive via a firmware update and is also effective at suppressing steady-state disturbances.

2.3 Winding topologies in BSRMs

One of the primary focus of this thesis is the geometrical structure of the motor along with the winding methodology for controllable radial force production in BSRM. From the windings perspective, self-bearing or bearingless motors can be broadly categorized into two distinctive groups, namely, separate set of winding configurations and combined set of winding configurations. The former category refers to any self-bearing machine that incorporates two separate sets of winding, where the primary set of winding carries the motor currents while the secondary set carries levitation currents. While these machines operate successfully, they inherently suffer from poor power rating. For a self-bearing machine to fall in the latter category, however, all its windings must carry motor currents at any operating cycle. These machines are very expensive because they employ a number of high rating power supplies and the manner in which they are controlled as a motor is somewhat unusual. Magnetic bearing action was first integrated using dual set of stator windings of switched reluctance motor by Mark *et al* [72]. Takemoto *et al*. proposed a bearingless structure of a 12/8 SRM using two sets of winding. In this design, one set of winding called the main winding is responsible for the torque production and an auxiliary set of windings called the radial force windings is responsible for providing suspension forces to the rotor. The configuration of the dual set of windings is shown in Figure 3.46. Dual winding scheme has been applied by various researchers using different modes of configuration and winding arrangements [73]. Wang *et al*. [44] have used dual winding scheme with modification in the suspension winding arrangement. The torque windings of the motor are similar to that of the conventional structure, but there are only two sets of suspension windings used to control the rotor radial suspending force, rather than six sets of suspension windings in the conventional BSRM. Dual winding has also been applied using wider rotor pole arc by Yang *et al*. [12] where the authors have developed the mathematical model along with decoupling control strategy. However, this dual winding configuration occupies additional space in the stator slot, which could have been otherwise used for optimum torque production. As such, researchers have further focused on single winding schemes for generation of both torque and radial forces. Higuchi *et al*. [8] first proposed the idea of single set winding for both torque and radial force production in 1989. In 1995, Preston [72] applied single set winding in a 12/8 BSRM, however they did not publish any literature on its successful operation. Liu and Yang proposed a single winding structure, where they have used the conventional excitation scheme for the torque production but two additional poles in the descending inductance are excited to produce the required radial force for rotor

balancing. Lin and Yang [60] have proposed a single winding structure where they have used one-phase and two-phase sinusoidal excitation to control SRM radial force. The main drawback of this scheme is that the maximum attainable radial force is limited by motor torque. In particular, only small radial force can be produced when the motor is lightly loaded. The control scheme is based on the scheme presented in [62] but with the addition of a two-phase control mode to increase the radial force operating range. However, such scheme produces negative torque and in order to compensate the negative torque, more current has to be supplied in the region of unaligned inductance.

Chen and Hofmann [13,49,74–76] proposed an analytical model, described the design procedure and later implemented experimentally the idea of utilising a simpler single set of stator winding for an 8/6 bearingless structure. The major contribution of this study is that it proposes a method where the total number of windings of the motor is decreased from eight to six in order to produce the same force and torque. They proposed a special motor driving theory and speed regulation technique where three phase windings are initially energised by different currents in each commutation period in order to produce the required force and torque. However, the method proposed by Chen and Hofmann comprises of complex control strategies and proper excitation scheme of the various stator pole windings. Zhao *et al.* [77] proposed a model of a single winding structure for BSRM which is suitable for both single-phase and two phase excitation modes. Though this method could give a substantial amount of levitation force, it resulted in negative torque production. Cao *et al.* [78] further gave a novel control strategy for torque ripple reduction and radial displacement control. The authors have introduced a solution for direct torque control (DTC) and direct force control (DFC) by using space vector formulation. This method is basically implemented by controlling the flux linkages. This method could minimize the torque ripple and radial displacement, but negative torque is produced since the excitation scheme consists of two phase excitation simultaneously. Single winding scheme with wider rotor pole arc has been proposed by various researchers and could provide a decoupled control strategy between torque and radial force [12], [79].

Xiang *et al.* [80] have also focused on single winding using hybrid permananent magnet (PM) excitation, which combines conventional double-stator bearingless switched reluctance motor (DSBSRM) with rare-earth permanent magnetic materials of high performance. In this work, the proposed hybrid excitation in DSBSRM could improve the radial suspension force and decrease the required suspension current when the same radial force is produced. Xiang *et al.* [81] further proposed a 24/16/8 Hybrid Excitation

Double Stator Bearingless Switched Reluctance Motor. This method could improve the radial force profile along with simpler controls strategy, however such method increased the overall size of the motor structure which does not provide a cost effective solution.

Raggl *et al*. [82] gave a comparative analysis between separate winding and combined winding for bearingless pumps where the copper losses, coil volume, power electronics requirements and achievable rotational speed are evaluated. The authors concluded that with combined winding scheme the reduction in copper loss and copper volume is achieved. Dietz and Binder [83] gave a comparative study between separate winding and combined winding in a bearingless permanent magnet synchronous machines. The authors concluded that the bearingless drives with combined winding for torque and lateral force generation exhibited higher electromagnetic utilization than a bearingless motor with separate suspension winding for the same thermal utilization under condition of the same inverter voltage limit. In this paper, the authors have shown that the copper losses were effectively less than the separate winding and also the manufacturing effort reduces in combined winding scheme. Holenstein *et al*. [84] introduced bearingless six-slot, four-pole synchronous reluctance slice motor with rotor flux barriers and six concentrated motor windings for combined torque and radial force generation. The six motor windings are connected as two three-phase systems with a floating star point each and are powered by a six-phase inverter. This topology could generate both torque and radial force by controlling only four currents instead of six independent currents in the winding.

However, in 2005, a novel winding scheme called bridge configured winding was proposed by Khoo [14] for polyphase permanent magnet synchronous self-bearing machines. The speciality of the winding is that, the same winding is responsible for both torque and levitation force generation using low value of excitation current. BCW is a specialized single set of stator winding containing double layer of coils in each stator tooth. One special feature of BCW is that, the bridge structure contains eight bridge terminals per phase winding, where four terminals can be utilized for connecting the motoring current supply and remaining four terminals for connecting the current supply for radial forces. The bridge connection does not require any special structure to house the windings and can be implemented in motors just as conventional windings are done. Khoo gave a general representation of the scheme for both concentrated winding and distributed winding in a polyphase machine and can also be extended to machines like induction motor, SRM, polyphase synchronous motor to name a few.

Figure 2.9 shows the coils connection of a single phase BCW incorporated by Khoo

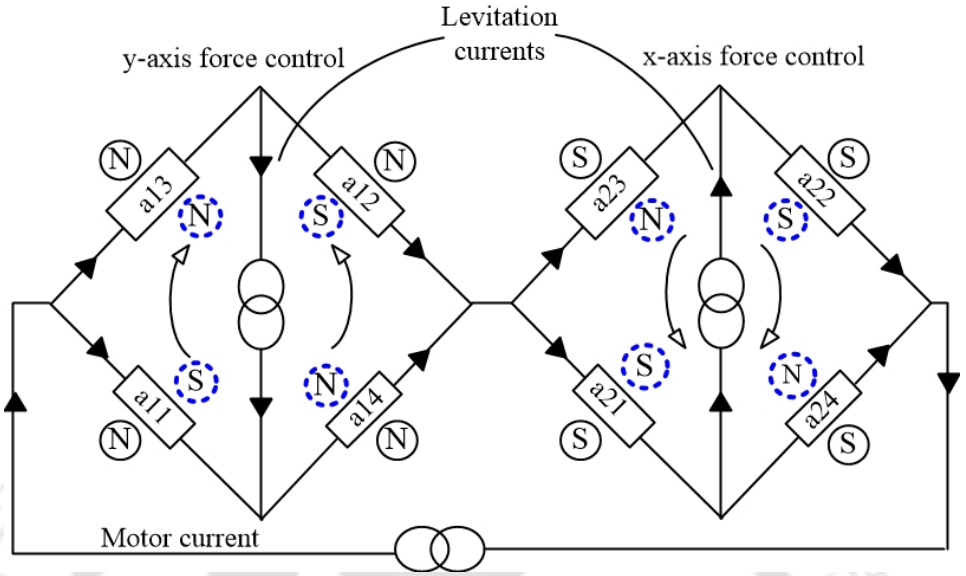

Figure 2.9: Coils connection of a single-phase BCW for self-bearing PMSM [14].

in a permanent magnet synchronous (PMSM) self-bearing machine. As shown in Figure 2.9, in BCW, the motor current gets divided into two parallel paths which results in the formation of a four pole magnetic field. This four pole magnetic field produces torque in the motor. When a positive motor current (solid arrow) flows in the direction as shown Figure 2.9, the coils in the first bridge i.e. (a11-a12-a13-a14) gives a north polarity while the other set of coils in the second bridge i.e. (a21-a22-a23-a24) gives a south polarity. The two levitation currents (hollow arrows) in Figure 2.9 drive the two bridges, one generates levitation force in y-axis and the other in x-axis. Two separate isolated low power current sources inject levitation currents in the bridge terminals. With the injection of these levitation currents, the balanced magnetic field generated by both permanent magnet and motor current gets perturbed resulting in the formation of a net magnetic field as explained in Figure 2.10. With no bridge current supply, the motor could operate as a normal torque producing machine as shown in Figure 2.10 (a). The figure also shows the plot of magnetic flux density with respect to the rotor position, θ. The plot can be obtained by considering a fixed rotor and relatively rotating the magnetic field. Figure 2.10 (b) and (c) show the flux distribution for only the y-axis and x-axis levitation currents respectively. Figure 2.10 (d) shows the flux due to motor current and y-axis levitation current superimposed, resulting in a force in the y-axis. Similarly, a force in x-axis can be obtained as shown in Figure 2.10 (e). Figure 2.10 (f) shows the resultant force obtained due to superimposition of flux for motor current and both the levitation currents. This resultant force can be generated in any desired

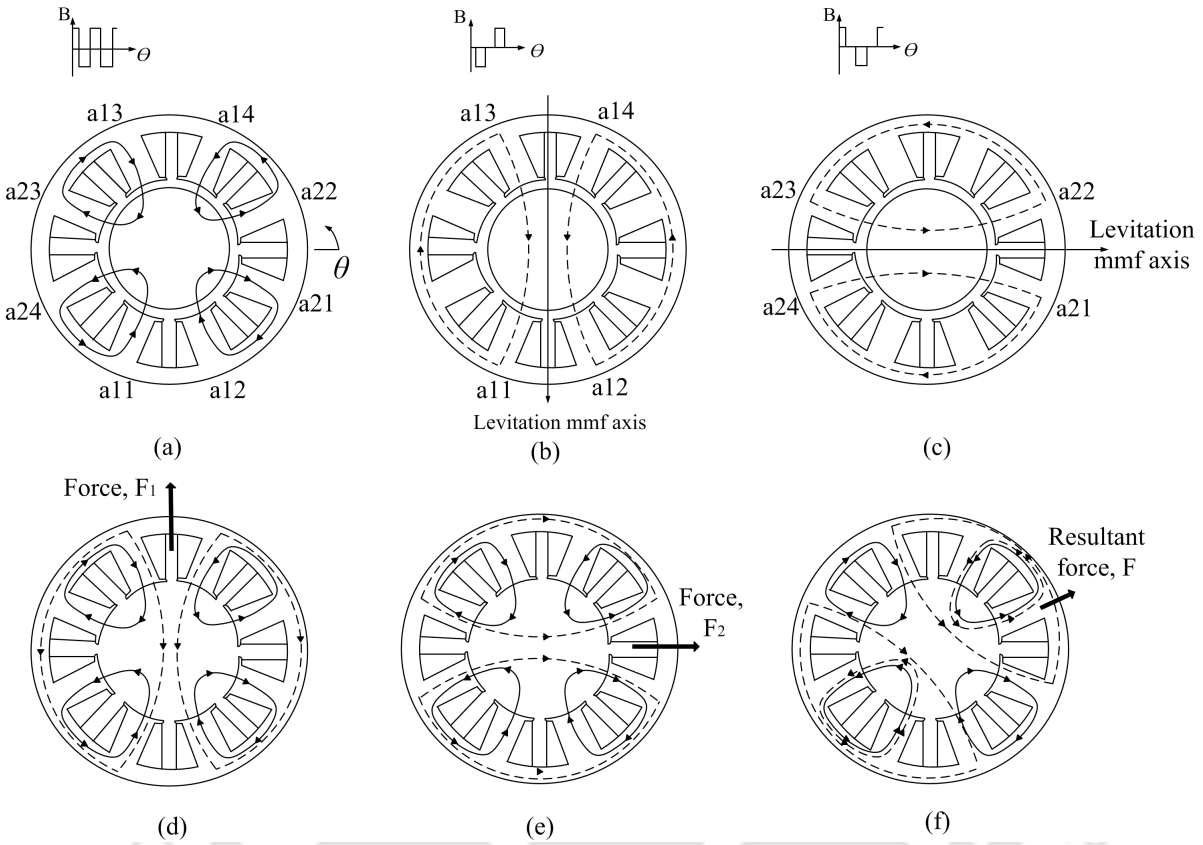

Figure 2.10: Flux distributions in a single-phase self-bearing motor with bridge configured winding due to (a) motor current (solid lines), (b) y-axis levitation current (dashed lines), (c) x-axis levitation current (broken lines), (d) motor current plus y-axis levitation current, (e) motor current plus x-axis levitation current, (f) motor current plus y-axis and x-axis levitation currents [14].

direction by changing the direction and magnitude of the levitation currents and can provide magnetic suspension to the rotor. This design is an elegant development where no additional windings are used to produce the net forces. Khoo *et al.* demonstrated the practical implementation of the BCW in a conventional four-pole permanent magnet motor for producing controllable transverse forces [16].

In 2015, the BCW design approach was proposed by Severson *et al.* [15], [85] for AC homopolar machines and the winding scheme was termed as dual-purpose no-voltage winding (DPNV) design. This winding scheme can be differentiated from the conventional windings for bearingless machines by the fact it provides separate terminals for connecting suspension currents which experiences no rotational EMF when the rotor is centred. With this theory, the authors have presented a simpler design of a drive system

which requires a low voltage rating of suspension inverter to meet the responses of the bearing control. However, the design was concentrated to only AC homopolar machines.

In 2016, the concept of BCW has been introduced in SRM for both torque and radial force production [86], [87]. In 2017, a design methodology has been proposed for proper selection of the geometrical parameters in order to achieve minimum levitation force at every rotor position and reduce the complexities associated with bearingless operation [88]. The BCW has been further applied for active suppression of unbalanced magnetic pull (UMP) in an induction motor. In this paper, the bridge currents were used to control the vibration generated in an induction motor under mixed eccentricity condition [89]. In this paper, the authors have given a generalized circuit equation coupled with the field equation for the implementation of BCW in induction motor. They have analyzed the dynamics considering three kinds of rotor eccentricity and presented simulation and experimental results.

2.4 Summary

An exhaustive literature survey has been done based on design and methodologies of controllable radial force production for bearingless operation in electrical machines viz. SRM. It has been observed that most of the works have been focused on analytical and numerical modelling of BSRM using various design approaches. The analytical modelling is very important in order to develop the control algorithm for both torque and radial force control. Many authors have used various approaches like virtual work energy method or Maxwell's Stress Tensor method in order to derive the mathematical relationships between torque, radial force and winding currents. However, most of the analytical models have not taken into account the magnetic saturation of the material. Some authors have addressed only finite element modelling and analysis to determine the radial force characteristics in SRM. However, most of the analyses are done considering only static condition.

Again, there are studies related to various control methods where authors have used different structural configuration and hybrid excitation method in order to produce controllable radial force. Some authors have given decoupling control strategy for independent control of torque and radial forces. These hybrid excitation method only solves the requirement of constant radial force and introduces a negative torque production. The hybrid pole structure on the other hand, increases the overall size and cost of the motor. Many authors have used dual winding configuration for the development of bearingless

operation in SRMs. However, single winding configuration brings additional advantages over dual winding in terms of controllable radial force production. A novel winding scheme called bridge configured winding has been introduced by Khoo which proves to be an elegant way to produce both torque and controllable radial forces using a single winding structure with a potential cost saving solution. This winding topology has been applied by researchers in polyphase motors, AC homopolar motors and in induction motor till date. However, the BCW in SRM has not been addressed in literature. This leads to a detailed study of the BCW and its behaviour when applied to SRMs.

The introduction of BCW in SRM takes into account a detailed mathematical modelling of the scheme with a step by step design procedure in order to obtain the required controllable radial forces without obstructing the normal torque production in the motor. It is also important to analyze the schemes under both static and rotating condition. Since SRMs are run by power electronic based converters and governed by a drive system, as such a comprehensive analysis of the power converters and the drive system is necessary in order to develop a drive system for bearingless operation in SRM with BCW.

Thus, it can be concluded that the BCW scheme is an elegant approach for achieving controllable radial force and torque production in SRM using the same iron and copper and it reduces the complexities associated with other winding topologies. Therefore, the thesis proposes BCW scheme in SRM and presents a detailed mathematical modelling, design procedure of the motor, development of a drive system for both torque and radial force production, fabrication of the motor and experimental validation of the radial force and torque production.

Chapter 3

Design Methodology of BSRM with Bridge Configured Stator Winding

Contents

3.1 Introduction

All rotating electrical machines are normally designed under the necessary condition that the electrical machine should serve only to convert between electrical power to mechanical power and vice-versa associated with the shaft rotation. The production of torque in electrical motors is mainly connected to the phenomenon of production of magnetic flux. It is an established fact that whenever an electrical current is passed through a coil it builds up a magnetic flux, producing a magnetic field around the conductor. This magnetic field acts as a force in the electrical motor to pull the rotor in the direction of the field resulting in production of torque. Now, electrical machines are normally designed maintaining symmetrical air gap in order to avoid unbalanced magnetic pull in the motor. It comes to light that if even a relatively small asymmetry of flux distribution exists in the air gap, a large unbalance magnetic force is produced resulting in a radial force which pulls the rotor towards the stator in the direction of the highest flux density. Unbalanced radial force acting on a rotor shaft is undesirable because it causes motor vibrations. The production of unbalanced magnetic force or radial forces are governed by various reasons. It may be due to the presence of rotor eccentricity, bearing faults, rotor vibration etc.

Conventional bearings in high-speed electrical machines shorten the overall life span of the machines due to continuous friction which limits the application of electrical machines. In order to overcome this limitation, recent research has developed the bearingless technology, which avoids the contact of bearing and shaft, thus integrating the function of magnetic bearing in the electric motor and making it suitable to operate as a conventional motor, but with the shaft levitated. Only accurately controlled force can suspend the rotor in its position, thus reducing the use of mechanical bearing and avoid the frictional losses incurred. This methodology of controllability of radial position is well established in magnetic bearing; however, it requires an additional axial space with an increase in the shaft length. As such bearingless approach becomes a favorable alternative to the traditional magnetic bearing system.

With the recent advancement in power electronics SRM are abundantly explored for high-speed applications. Due to their special doubly salient structures, SRM have an inherent feature of producing attractive magnetic force between the stator and rotor poles. The force can be divided into tangential and radial force components. The tangential component is responsible for producing torque in the rotor whereas the radial force component brings along the problem of noise and vibration in SRMs. For example, in applications in which the external load on the shaft is not balanced, or when the rotor

is not centered causing non-uniformity in the air gap, radial force exists [41] [47]. These radial forces are sometimes absorbed by the bearings and the load connected to the shaft, but the SRM, due to its special structure, offers a unique way to control the existing radial forces by producing equal and opposite forces using various methods. Several methods have been proposed and established by researchers to produce controllable radial forces for SRM.

It has already been discussed in the previous chapter that the most common winding topology of BSRM is the dual or separate winding scheme for torque and suspension which occupy the same stator slots [9]. The dual winding has been first proposed and implemented in 1998, where a mathematical model of a 12/8 BSRM and the relations between radial forces and the winding currents have been derived [5], [9]. In BSRMs having dual set winding, a control strategy was found to determine the advanced angle of square wave currents in motor winding, to obtain a stable operation [58]. In 2004, dual winding scheme for BSRM was analysed considering magnetic saturation of the motor in order to avail a stable operation of the motor under full load torque condition [11]. While these machines operate successfully, they inherently suffer from additional copper loss. In 2006, a novel 8/6 BSRM using a single winding structure was developed, where three windings were loaded with different currents in each commutating period and three torques and three radial forces were generated at the same time. The sum of three generated torques and radial forces from each winding could supply the desired torque and suspending force. The authors computed currents in the winding analytically and derived its relation with radial force and torque and further validated them experimentally [13]. Individual pole excitation using sinusoidal excitation scheme was tested in a 12/8 SRM for independent control of torque and radial force. However, as the pole currents were controlled individually, the commutation strategy applied was sophisticated [60]. These machines are very expensive because they employ high rating power supplies and the control methodology is complex. The concept of producing both torque and levitation force without using separate winding was introduced by Amrhein *et al.* [90] in 1999 in a bearingless PM motor. In 2005, a single set of winding called BCW was introduced for poly-phase self-bearing machines which could generate both torque and radial force using the same winding [14]. In 2015, the BCW design approach was proposed for ac homopolar machines and the winding scheme was termed as dual purpose no voltage winding design [15], [85]. In 2016, the concept of BCW was introduced in SRM for both torque and radial force production [86], [87]. In 2017, a design methodology was proposed for proper selection of the geometrical parameters in order

to achieve minimum levitation force at every rotor position and reduce the complexities associated with bearingless operation [88]. In 2018, BCW was introduced for active suppression of unbalanced magnetic pull (UMP) in induction motor [89]. It can be observed that, the bridge winding allows the same set of winding in a conventional motor to sustain both torque and radial forces and thus avoid reduction of stator slot area for torque production, generally obtained using dual set of winding. This methodology has thus been introduced in a 12/8 SRM.

The main objective of this chapter is the design and development of a 12/8 BSRM configurable for BCW. Initially, the bridge configured winding topology is presented with its working principle explaining in brief the behaviour of the winding scheme for radial force and torque production. The study continues further with its incorporation in SRM. In order to understand and investigate the actual behaviour of the motor with BCW scheme, a mathematical model has been derived in order to obtain the theoretical relations between the torque and radial forces with the torque producing current termed as the main current and the levitation currents termed as the bridge currents. A step by step design methodology has been provided for the proposed motor considering analytical design procedures. A 12/8 SRM of 750 W has been designed for the prototype of the design and the design has been verified using finite element method. In order to verify the bridge configured theory, a finite element model has been developed for the proposed motor neglecting the magnetic saturation of the material. Continuing with the study, the model has been analysed considering the magnetic saturation of the material and the relations have been obtained and verified. In this chapter, both virtual work principle and Maxwell stress tensor method has been used to obtain the mathematical model. However, in this chapter only static analysis has been done and the radial forces and torque production has not been analysed under transient conditions. The coupling of the model with power electronic based converter circuits has been done in the subsequent chapters.

3.2 Bridge configured concentrated winding topology for BSRM

Bridge configured winding (BCW) is a specialized combined set of stator winding containing double layer of coils in each stator teeth. One special feature of BCW is that the bridge connection requires only one power supply for normal torque production and six isolated low power supplies for radial force production. The bridge connection

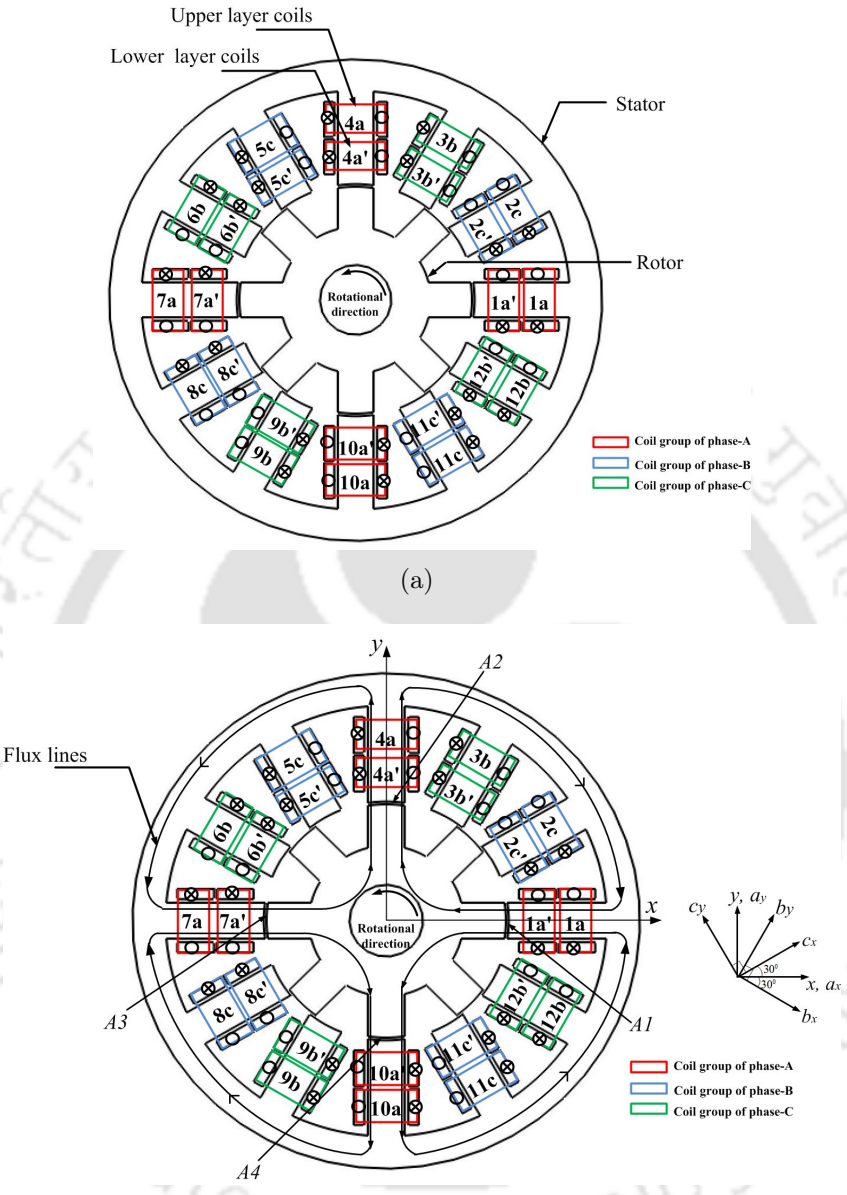

Figure 3.1: (a) Cross-section of a 12/8 BSRM with its coil distribution for BCW and (b) Four pole magnetic flux distribution in phase-A

does not require any special structure to house the windings and can be implemented in motors just as conventional windings are done. The principal advantage of the work is the impetus on designing BSRM to utilize same set of stator winding for both torque and radial force production and thus provide a cost saving solution. The only disadvantage of bridge winding is that, the main current supply and the bridge current supply has to be isolated from each other in order to avoid short circuit of windings. However, it can

be accomplished by keeping separate ground or using isolation transformers for both the main current and bridge current supplies. Figure 3.1(a) represents the coil distribution in each stator tooth for a 12/8 BSRM for BCW. Figure3.1(b) shows the four pole magnetic flux distribution produced by the main current. $A1$, $A2$, $A3$ and $A4$ represent the air gaps with the four pole magnetic field formation for phase-A winding. Phase-B winding is situated at one-third rotational position of phase-A winding, and phase-C winding is situated at two-third rotational position of phase-A winding. The axes x and y are taken as the reference axes for the direction of radial forces. In this case, for phase-A a_x and a_y are aligned with x and y axes, b_x and b_y for phase-B winding, and c_x and c_y for phase-C winding as shown in Figure 3.1(b). The direction of radial force in case of phase-B and phase-C differs from that in phase-A. A transformation of co-ordinates is required. In SRMs, all the three phase are not excited at the same moment but each phase is sequentially excited at one time.

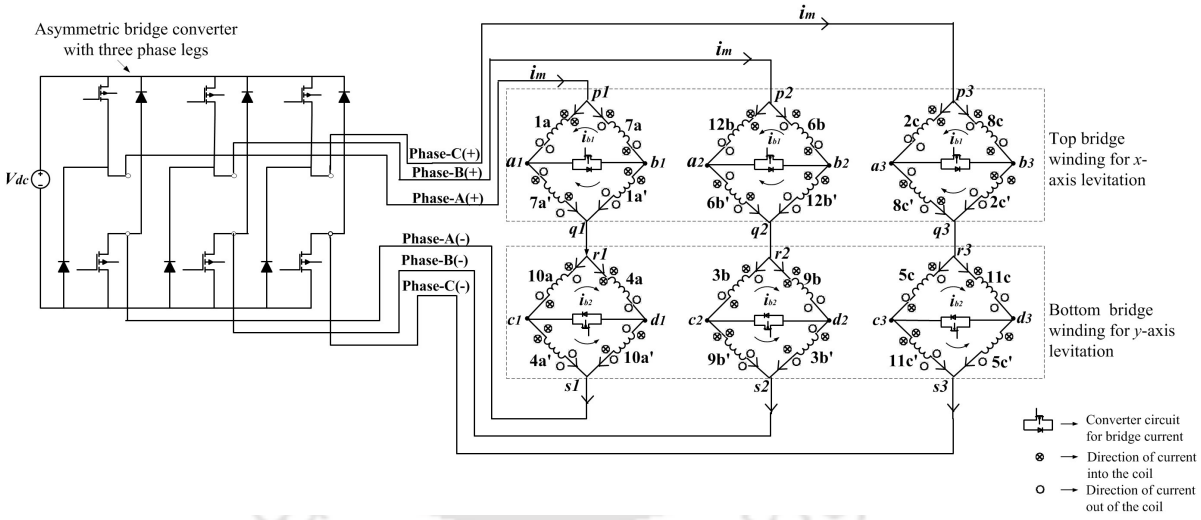

Figure 3.2: Winding configuration for BCW BSRM with an asymmetric bridge converter

The BCW looks like a Wheatstone bridge circuit which consists of one pair of terminals per phase for the main current supply and two pairs of terminals for the bridge current supply. Each phase winding is connected to a phase leg of an asymmetric bridge converter as shown in Figure 3.2. The BCW in a 12/8 BSRM is a concentrated winding scheme. Each phase winding occupies four stator teeth, where the coils along the x-axis are employed for the x-directional radial force and the coils along y-axis are used for the y-directional radial force. It can be observed from Figure 3.2 that the BCW consists of two sets of bridge windings termed as the top bridge winding and the bottom bridge

winding. The main current, i_m which produces the machine torque is divided into two parallel paths. Certain end connections are brought out to form the terminals called bridge terminals. A small isolated supply in between the bridge terminals provides the bridge currents i_{b1} and i_{b2}, responsible for production of the radial forces in x and y direction. BSRM with BCW requires three single phase winding connection for the main current and is termed as phase-A, phase-B and phase-C. In Figure 3.1(b), the points $(p1 - q1 - r1 - s1)$, $(p2 - q2 - r2 - s2)$ and $(p3 - q3 - r3 - s3)$ represent the terminals of phase-A, phase-B and phase-C for the torque producing main current i_m. The points $(a1 - b1)$ and $(c1 - d1)$, $(a2 - b2)$ and $(c2 - d2)$, $(a3 - b3)$ and $(c3 - d3)$ represents the terminal points for the bridge currents i_{b1} and i_{b2} in phase-A, phase-B and phase-C. The main current and bridge current polarities are designated at the exterior and interior of the arms of the bridges respectively. Each arm of the bridge represents a single coil, for example coil $1a$ and $7a^{'}$ are connected in series and forms a coil set occupying two stator slots. Similarly, a second coil set $7a$ and $1a^{'}$ in the parallel branch of the bridge are connected in series to form another coil set. The coils of top bridge in each phase winding are utilized for x-directional radial force and coils of bottom bridge for y-directional radial force control with reference to the axes x and y as shown in Figure 3.1(b). Figure 3.3 shows the winding layout of BCW for phase-A, phase-B and phase-C.

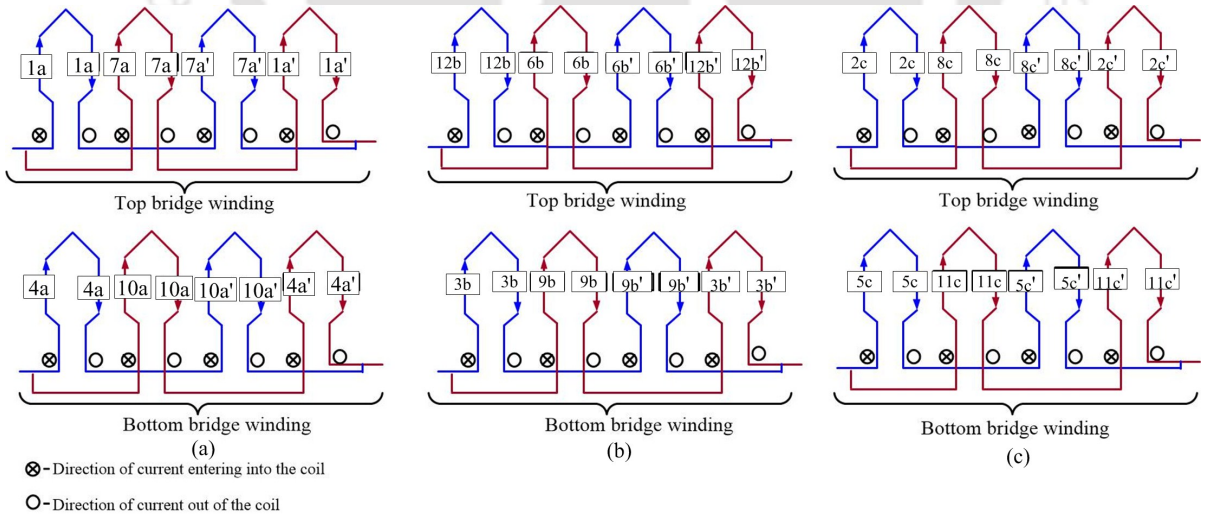

Figure 3.3: Winding layout of the bridge configured stator winding of (a) phase-A (b) phase-B and (c) phase-C. Top bridge comprises the coils for x-directional radial force and bottom bridge comprises the coils for y-directional radial force.

Figure 3.4 shows the physical connection of the BCW for phase-A winding in a 12/8

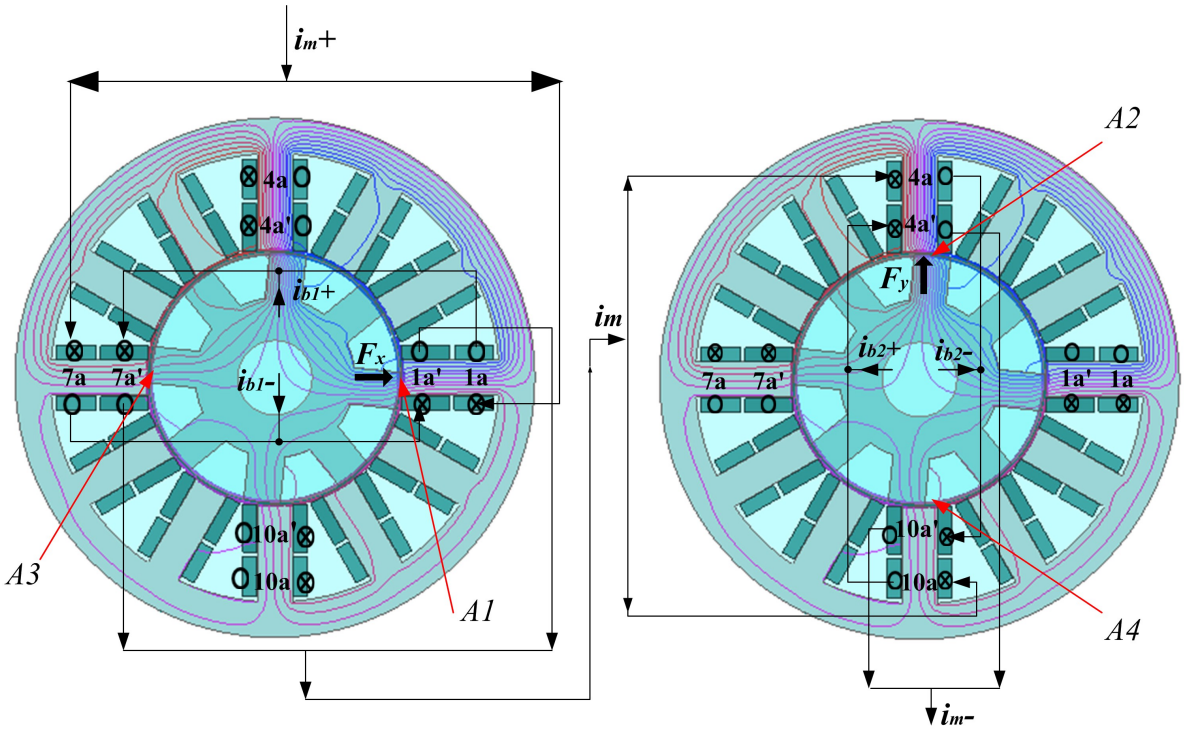

Figure 3.4: Physical connection of coils in 12/8 BCW BSRM for phase-A winding

BSRM. The main current i_m is responsible for producing the four pole magnetic flux which produces the torque in the motor. If the bridge current, i_{b1} is allowed to pass through the terminals between coil sets $(1a - 7a^{'})$ and $(7a - 1a^{'})$ in the direction as shown in Figure 3.4, the magnetic field density in the air gap $A1$ increases while that in $A3$ decreases, resulting in a radial force F_x as shown. Similarly, if bridge current i_{b2} is passed through coil sets $(4a - 10a^{'})$ and $(10a - 4a^{'})$, the magnetic field density increases in air gap $A2$ and decreases in $A4$ producing a radial force F_y in the direction as shown in Figure 3.4. The connection for phase-B and phase-C windings are done similarly.

3.2.1 Circuital analysis of winding currents in BCW

As seen in Figure 3.5 (a), the two parallel paths of phase-A in the top bridge are $(p1 - a1 - q1)$ and $(p1 - b1 - q1)$. Let the main current from the power converter be i_m. At node $p1$, the current i_m gets divided into two currents i_1 and $i_m - i_1$. Applying Kirchhoff's current law (KCL) at node $p1$, the current can be given as,

$$i_m - (i_1 + i_m - i_1) = 0. \tag{3.1}$$

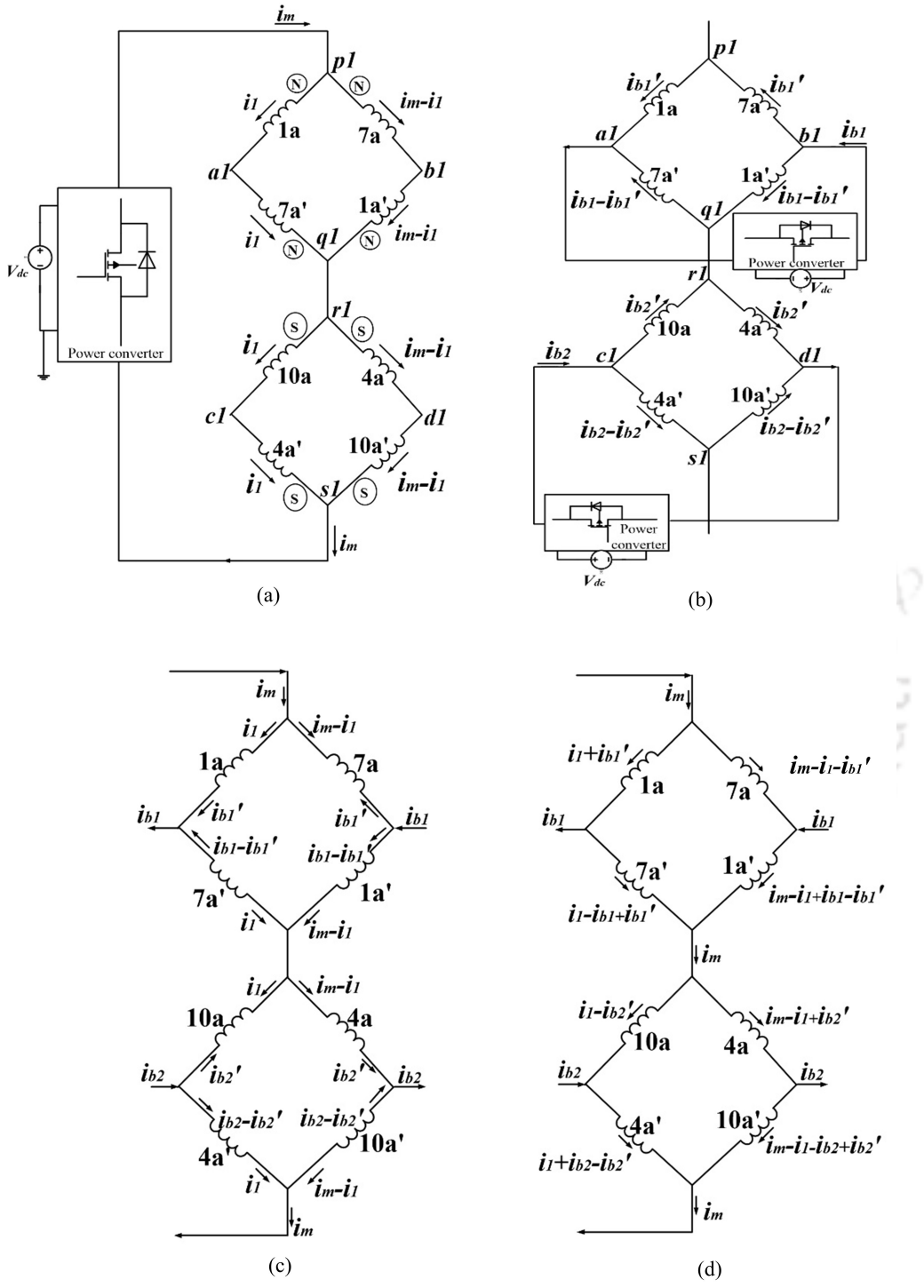

Figure 3.5: (a) Main current, i_m (b) bridge currents, i_{b1} and i_{b2} (c) distribution of main current and bridge currents (d) net distribution of currents in each coil of phase-A winding

Thus the current flowing through coils (1a- 7a') is i_1 and current through coils (7a-1a') is $(i_m - i_1)$. The two parallel paths of phase-A in the bottom bridge are $(r1 - c1 - s1)$ and $(r1 - d1 - s1)$. The current at point $r1$ is again i_m. Thus, current flowing through coil (10a-4a') is i_1 and through (4a-10a') is $(i_m - i_1)$ and current flowing out at terminal $s1$ is i_m. When a positive current flows in the direction as shown in Figure 3.5 (a), the coils in top bridge gives north polarity (N) and the coils in bottom bridge gives south polarity (S) resulting in a four pole magnetic field. Let i_{b1} be the bridge current in the top bridge circuit and i_{b2} be the bridge current in the bottom bridge winding. With the injection of bridge current i_{b1} in top bridge circuit as shown in Figure 3.5 (b), the current distribution in the respective coils changes. Let the bridge current i_{b1} get divided into two currents, i'_{b1} and $(i_{b1} - i'_{b1})$. Applying KCL at node $b1$, the bridge current flowing is given by,

$$i_{b1} - (i_{b1}{}' + i_{b1} - i_{b1}{}') = 0. \tag{3.2}$$

Thus, the bridge current in coils of top bridge,(1a-7a) is i'_{b1} and in coils (1a'-7a') is $(i_{b1} - i'_{b1})$. Similarly, the bridge current in coils of bottom bridge, (10a-4a) is i_{b2} and in coil (4a'-10a') is $(i_{b2} - i'_{b2})$. As, there is symmetry between each phases hence the distribution of currents in coil groups of phase-B and phase-C are same as in phase-A. When the coil current in the pole of air gap $A1$ is greater than the current in pole of air gap $A3$, the magnetic field density in $A1$ exceeds that in $A3$. It results in the generation of a radial force in the positive x-direction. Similarly, a radial force can be generated in the positive y-direction.

3.3 Mathematical model of BSRM with BCW

For controlled operation of bearingless motor it is necessary to derive an accurate theoretical description for the magnetic radial forces and torque with the winding current, owing to every rotational position. In order to study the behavior of the motor with the main current and the bridge current a mathematical model has been developed in this section.

3.3.1 Analytical model using virtual work method

The magnetic equivalent circuit of phase-A consists of coils in four stator teeth as shown in Figure 3.6. The voltage sources in each stator tooth represent magnetomotive forces and the resistances represent the permeances in the air gaps. For simplicity, only

phase-A magnetic equivalent circuit is considered. This is possible because SRM has little mutual inductance between phases and it has symmetry in the geometrical structure. Each phase winding comprises of four diametrically opposite stator teeth. Figure 3.7 represents a magnetic equivalent circuit of phase-A of the motor. The BCW BSRM consists of two coils per stator tooth and a single set of winding per phase. Hence, the number of turns of the winding is assumed as N. It can be observed that the currents in one stator tooth produces flux in the same direction, hence the two magnetomotive forces can be represented as one source as shown in Figure 3.7.

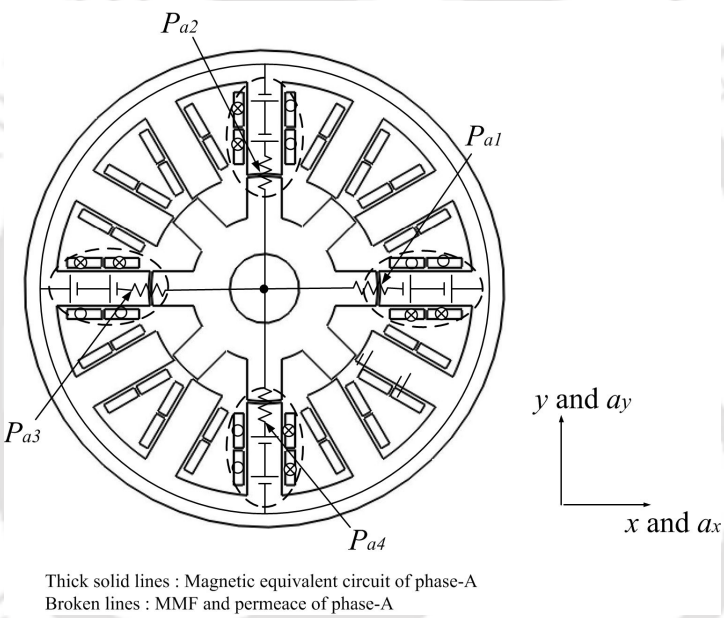

Figure 3.6: Representation of MMF and permeance in phase-A

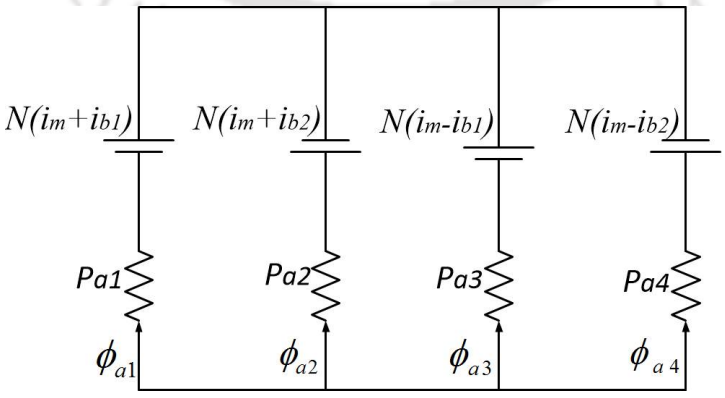

Figure 3.7: Magnetic equivalent circuit of phase-A

The magnetomotive force (MMF) equation is solved at each of the branch of circuit

of phase-A of the machine. The voltage sources $N(i_m + i_{b1})$, $N(i_m + i_{b2})$, $N(i_m - i_{b1})$ and $N_m(i_m - i_{b2})$ in Figure 3.7 represents the magnetomotive forces. ϕ_{a1}, ϕ_{a2}, ϕ_{a3} and ϕ_{a4} are the magnetic fluxes in each tooth of phase-A of the motor and P_{a1}, P_{a2}, P_{a3} and P_{a4} are the permeances of each of the four air gaps in phase-A of the motor and N is the number of turns of the stator winding.

Considering that the sum of mmf's in each branch is equal to another one, hence the magnetomotive forces in each branch can be equated in terms of one another as

$$\frac{\phi_{a2}}{P_{a2}} + N(i_m + i_{b2}) = \frac{\phi_{a1}}{P_{a1}} - N(i_m + i_{b1}) \tag{3.3}$$

$$\frac{\phi_{a3}}{P_{a3}} - N(i_m - i_{b1}) = \frac{\phi_{a1}}{P_{a1}} - N(i_m + i_{b1}) \tag{3.4}$$

$$\frac{\phi_{a3}}{P_{a3}} + N(i_m - i_{b2}) = \frac{\phi_{a1}}{P_{a1}} - N(i_m + i_{b1}) \tag{3.5}$$

From Gauss's Law of magnetism, we know that the sum of magnetic flux in a closed surface is zero, therefore,

$$\phi_{a1} + \phi_{a2} + \phi_{a3} + \phi_{a4} = 0. \tag{3.6}$$

Thus, the flux ϕ_{a1} ~ϕ_{a4} can be derived as

$$\begin{aligned}\phi_{a1} = \tfrac{P_{a1}}{P}[&-N(i_m + i_{b1})(P_{a2} + P_{a3} + P_{a4}) + N(i_m + i_{b2})P_{a2} \\ &+ N(i_m - i_{b1})P_{a3} + N(i_m - i_{b2})P_{a4}]\end{aligned} \tag{3.7}$$

$$\begin{aligned}\phi_{a2} = \tfrac{P_{a2}}{P}[&-N(i_m + i_{b1})P_{a1} + N(i_m + i_{b2})(P_{a1} + P_{a3} + P_{a4}) \\ &- N(i_m - i_{b1})P_{a3} - N(i_m - i_{b2})P_{a4}]\end{aligned} \tag{3.8}$$

$$\begin{aligned}\phi_{a3} = \tfrac{P_{a3}}{P}[&N(i_m + i_{b1})P_{a1} + N(i_m + i_{b2})P_{a2} \\ &- N(i_m - i_{b1})(P_{a1} + P_{a2} + P_{a4}) + N(i_m - i_{b2})P_{a4}]\end{aligned} \tag{3.9}$$

$$\begin{aligned}\phi_{a4} = \tfrac{P_{a4}}{P}[&-N(i_m + i_{b1})P_{a1} - N_m(i + i_{b2})P_{a2} \\ &- N(i_m - i_{b1})P_{a3} + N(i_m - i_{b2})(P_{a1} + P_{a2} + P_{a3})],\end{aligned} \tag{3.10}$$

where, P is the sum of all the permeances.

The permeances P_{a1} ~P_{a4} in each of the air gap of phase-A can be divided into three parts of permeances, P_1 as the direct permeances between the stator and the rotor tooth and P_2 ~P_3 as the fringing path permeances as shown in Figure 3.8. Fringing permeance plays an important role in determining the value of inductance hence in the present study

it has been modeled considering the fringing flux paths as elliptical lines.

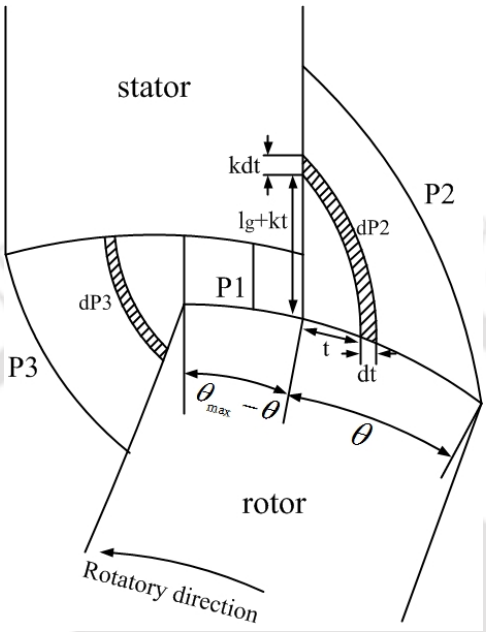

Figure 3.8: Assumed magnetic paths and permeances

The assumed magnetic paths are considered as elliptical lines using a variable k which depends on the rotational position and the length of the air gap. As seen in Figure 3.8, t is a position on the rotor circular surface, dt is the derivative of t, dP_2 and dP_3 are permeances of infinitesimal width of the assumed magnetic path. The length of flux path is given by average of lengths of semi-major and semi-minor axes of the ellipse as

$$l = \frac{\pi}{4}(t + l_g + kt), \tag{3.11}$$

where, l is the average length of the magnetic path and k is a constant to determine the shape of the elliptical flux path. k has to be calculated from each flux path obtained from FEM analysis. Regardless of length of the air gap l_g, k is dependent on t/l_g. So, it can be said that k is a function of θ and l_g. A linear relationship of l and l_g is obtained as

$$\frac{l}{l_g} = \frac{\pi}{4}(1 + \frac{t}{l_g}(1 + k)) \tag{3.12}$$

which can be simplified to a linear relationship as

$$\frac{l}{l_g} = a\frac{t}{l_g} + \frac{\pi}{4}. \tag{3.13}$$

Substituting Equation 3.13 into Equation 3.12 we get

$$k = \frac{4}{\pi}a - 1 \tag{3.14}$$

A cross-section of dP_2 can be approximated as

$$S = \frac{h(dt + kdt)}{2} \tag{3.15}$$

where, S is the area of cross-section of dP_2, h is the stack length. Hence, a relationship between dP_2, l_g and t/l_g can be given as

$$dP_2 \times l_g = \frac{\mu_0 S}{l} \times l_g \tag{3.16}$$

where μ_0 is the permeability of air. The Equation 3.16 can be written as

$$dP_2 = \frac{8\mu_0 hc}{\pi} \times \frac{1}{4ct + \pi l_g} dt \tag{3.17}$$

Thus, the permeance P_1 can be derived by integrating the paths

$$P_1 = \int_0^{\theta_{\max}-\theta} \frac{\mu_0 hr}{l_g} d\theta = \frac{\mu_0 hr(\theta_{\max} - \theta)}{l_g} \tag{3.18}$$

where, θ is the rotor rotational position, h is the stack length of the motor, r is the radius of the rotor, θ_{max} is the complete overlap position of the stator and rotor tooth, μ_0 is the permeability of air and l_g is the air gap length. Taking cross-section of dP_2 and integrating the paths we get,

$$P_2 = \int_0^{r\theta} dP_2 = \frac{2\mu_0 h}{\pi} \ln(\frac{4ar\theta}{\pi l_g} + 1) \tag{3.19}$$

Similarly,

$$P_3 = \frac{2\mu_0 h}{\pi} \ln(\frac{4ar\theta}{\pi l_g} + 1) \tag{3.20}$$

where, a is a constant which has to be obtained from finite element model. The total permeance P_a of air gap $A1$ is the sum of direct permeance P_1 and the fringing permeances

P_2 and P_3, and is obtained as

$$P_a = \frac{\mu_0 hr(\theta_{\max} - \theta)}{l_g} + \frac{4\mu_0 h}{\pi} \ln\left(\frac{4ar\theta}{\pi l_g} + 1\right) \tag{3.21}$$

Equation 3.21 is same for permeances P_{a1}, P_{a2}, P_{a3} and P_{a4} in all the four air gaps of phase-A provided the rotor is non-eccentric. However, considering displacement of the rotor and substituting $(l_g \pm x)$ and $(l_g \pm y)$ into the air gap length of Equation 3.21 and approximating with first order Taylor series, the permeances in the four air gaps can be written as

$$P_{a1} = \frac{\mu_0 hr(\theta_{\max} - \theta)(l_g + x)}{l_g^2} + \frac{4\mu_0 h}{\pi} \ln\left(\frac{4ar\theta(l_g + x)}{\pi {l_g}^2} + 1\right) \tag{3.22}$$

$$P_{a2} = \frac{\mu_0 hr(\theta_{\max} - \theta)(l_g + y)}{l_g^2} + \frac{4\mu_0 h}{\pi} \ln\left(\frac{4ar\theta(l_g + y)}{\pi {l_g}^2} + 1\right) \tag{3.23}$$

$$P_{a3} = \frac{\mu_0 hr(\theta_{\max} - \theta)(l_g - x)}{l_g^2} + \frac{4\mu_0 h}{\pi} \ln\left(\frac{4ar\theta(l_g - x)}{\pi l^2} + 1\right) \tag{3.24}$$

$$P_{a4} = \frac{\mu_0 hr(\theta_{\max} - \theta)(l_g - y)}{l_g^2} + \frac{4\mu_0 h}{\pi} \ln\left(\frac{4ar\theta(l_g - y)}{\pi {l_g}^2} + 1\right). \tag{3.25}$$

In order to calculate inductances, it is required to derive flux linkage of the main winding. From the magnetic circuit of the motor the relation of flux linkage can be written as

$$\psi = (-\phi_{a1} + \phi_{a2} - \phi_{a3} + \phi_{a4})N \tag{3.26}$$

Again we know that flux linkage is the product of inductance and current in the winding per phase, i.e.

$$\psi = Li \tag{3.27}$$

Hence comparing Equation 3.26 and Equation 3.27 and equating the coefficients of Equation 3.22 to Equation 3.25, we get the inductance matrix [L] as

$$[L] = \begin{bmatrix} L_{11} & L_{12} & L_{13} & L_{14} \\ L_{21} & L_{22} & L_{23} & L_{24} \\ L_{31} & L_{32} & L_{33} & L_{34} \\ L_{41} & L_{42} & L_{43} & L_{44} \end{bmatrix} \tag{3.28}$$

where,

$$L_{11} = \frac{P_{a1}}{P}(P_{a2} + P_{a3} + P_{a4})N^2 \tag{3.29}$$

$$L_{12} = \frac{P_{a1}P_{a2}}{P}N^2 \tag{3.30}$$

$$L_{13} = -\frac{P_{a1}P_{a3}}{P}N^2 \tag{3.31}$$

$$L_{14} = \frac{P_{a1}P_{a4}}{P}N^2 \tag{3.32}$$

$$L_{21} = \frac{P_{a1}P_{a2}}{P}N^2 \tag{3.33}$$

$$L_{22} = \frac{P_{a2}}{P}(P_{a1} + P_{a3} + P_{a4})N^2 \tag{3.34}$$

$$L_{23} = \frac{P_{a2}P_{a3}}{P}N^2 \tag{3.35}$$

$$L_{24} = -\frac{P_{a2}P_{a4}}{P}N^2 \tag{3.36}$$

$$L_{31} = -\frac{P_{a1}P_{a3}}{P}N^2 \tag{3.37}$$

$$L_{32} = \frac{P_{a2}P_{a3}}{P}N^2 \tag{3.38}$$

$$L_{33} = \frac{P_{a3}}{P}(P_{a1} + P_{a2} + P_{a4})N^2 \tag{3.39}$$

$$L_{34} = \frac{P_{a3}P_{a4}}{P}N^2 \tag{3.40}$$

$$L_{41} = \frac{P_{a4}P_{a1}}{P}N^2 \tag{3.41}$$

$$L_{42} = -\frac{P_{a4}P_{a2}}{P}N^2 \tag{3.42}$$

$$L_{43} = \frac{P_{a4}P_{a3}}{P}N^2 \tag{3.43}$$

$$L_{44} = \frac{P_{a4}}{P}(P_{a1} + P_{a2} + P_{a3})N^2 \tag{3.44}$$

Since, stored magnetic energy is half of the product of inductance and square of the current, it can be expressed as

$$W = \frac{1}{2}\,[I]\,[L]\,[I]^T \tag{3.45}$$

where,

$$I = [(i_m + i_{b1}) \quad (i_m + i_{b2}) \quad (i_m - i_{b1}) \quad (i_m - i_{b2})]$$

and

$$I^T = \begin{bmatrix} (i_m + i_{b1}) \\ (i_m + i_{b2}) \\ (i_m - i_{b1}) \\ (i_m - i_{b2}) \end{bmatrix}$$

The torque of one phase can be derived from the rate of change of the stored magnetic energy with respect to the rotational positions as

$$T = \frac{\partial W}{\partial \theta} \tag{3.46}$$

$$T = \frac{2\mu_0 hrN^2}{l_g}\left[1 - \frac{16al_g}{\pi(\pi l_g + 4ar\theta)}\right](4i_m^2 + 2i_{b1}^2 + 2i_{b2}^2) \tag{3.47}$$

The radial forces of Phase-A in the horizontal and vertical direction x and y can be represented by

$$F_x = \frac{\partial W}{\partial x} = K(\theta)i_m i_{b1} \tag{3.48}$$

$$F_y = \frac{\partial W}{\partial y} = K(\theta)i_m i_{b2} \tag{3.49}$$

where, x and y are the air gap displacements in the horizontal and vertical axes and $K(\theta)$ is the constant of proportionality and is a function of θ. When the rotor has eccentric displacements in the x-direction the bridge current i_{b1} has to be turned on in order to generate a restoring force and can be regulated until the rotor is balanced. Following the same method when there is displacement in the y-direction, bridge current i_{b2} needs to be

controlled in order to generate a radial force in y-direction. The magnitude and direction of forces can be regulated by keeping the main current, i_m as constant and controlling the bridge currents i_{b1} and i_{b2} independently. It has to be noted that the generation of radial force in x-direction depends on both i_m and i_{b1}. Similarly in y-direction it depends on both i_m and i_{b2} respectively.

3.3.2 Torque and radial forces in region of magnetic saturation using virtual work method

In the previous section, the expressions of radial forces and torque have been derived from a linear magnetic equivalent circuit method of the proposed motor without considering magnetic saturation. However, it is very difficult to realize stable operation of the motor in real time when the motor operates at full load torque as the motor undergoes non-linearity condition. Therefore, in the next part of the study magnetic saturation is included in finding the permeances in each air gap and relations of torque and radial forces have been derived. Finite element method (FEM) has been used in verifying the analytical calculations in the following sections.

As explained in section 3.4.1, the fluxes are solved using magnetic equivalent circuit of the proposed motor and are same as Equation 3.7 to Equation 3.10. From Figure 3.8, it is assumed that the fringing magnetic paths have the shape of ellipse. Thus, the permeances P_2 and P_3 have been assumed with elliptical lines using a variable k as shown in Figure 3.8. The semi-major axis is assumed as t and the semi minor axis as $l_g + kt$. The variable k can be calculated from each magnetic flux path. Hence, a FE analysis is carried out by changing the magneto-motive force in one stator pole winding in order to find the influence of magnetic saturation on k. A general expression between t/l_g and k is derived. A constant 'c' is obtained from the relationship between t/l_g and k and 'c' changes when magnetic saturation between the stator poles and rotor poles arises [11]. The value of 'c' remains constant as long as the motor is in linear region and decreases once it reaches the region of saturation i.e. in the non-linear region c becomes a function of current. The relation between k and t/l_g can be approximated as

$$k = \frac{t/\mathrm{l}_g}{c + t/\mathrm{l}_g} \tag{3.50}$$

Following Takemoto's approach the permeance $P1$, $P2$ and $P3$ are derived as

$$P_1 = \int_0^{\theta_{\max}-\theta} \frac{\mu_0 hr}{l_g} d\theta \tag{3.51}$$

$$P_2 = P_3 = \int_0^{\theta} \frac{\mu_0 hr(cl_g - 2r\theta)}{(cl_g - 2r\theta)(2l_g - \pi r\theta)} d\theta \tag{3.52}$$

where, θ is the rotor rotational position, h is the stack length of the motor, r is the radius of the rotor, θ_{max} is the complete overlap angle of the stator and rotor tooth, μ_0 is the permeability of air and l_g is the air gap length. The total permeance P_a of air gap $A1$ is the sum of direct permeance and the fringing permeances and is obtained as

$$P_{a1} = P_1 + P_2 + P_3. \tag{3.53}$$

However considering displacement of the rotor and substituting the air gap l_g with $l_g \pm x$ and $l_g \pm y$ in the radial x and y direction, the permeances in the four air gaps can be written as

$$P_{a1} = \frac{\mu_0 hr(\theta_{\max}-\theta)(l_g+x)}{l_g^2} + \frac{2\mu_0 h}{\pi(\pi c-2)}[\pi c \ln(\frac{cl_g^2+r\theta(l_g+x)}{cl_g^2}) + (\pi c-4)\ln(\frac{2l_g^2+\pi r\theta(l_g+x)}{2l_g^2})], \tag{3.54}$$

$$P_{a2} = \frac{\mu_0 hr(\theta_{\max}-\theta)(l_g+y)}{l_g^2} + \frac{2\mu_0 h}{\pi(\pi c-2)}[\pi c \ln(\frac{cl_g^2+r\theta(l_g+y)}{cl_g^2}) + (\pi c-4)\ln(\frac{2l_g^2+\pi r\theta(l_g+y)}{2l_g^2})], \tag{3.55}$$

$$P_{a3} = \frac{\mu_0 hr(\theta_{\max}-\theta)(l_g-x)}{l_g^2} + \frac{2\mu_0 h}{\pi(\pi c-2)}[\pi c \ln(\frac{cl_g^2+r\theta(l_g-x)}{cl_g^2}) + (\pi c-4)\ln(\frac{2l_g^2+\pi r\theta(l_g-x)}{2l_g^2})], \tag{3.56}$$

$$P_{a4} = \frac{\mu_0 hr(\theta_{\max}-\theta)(l_g-y)}{l^2} + \frac{2\mu_0 h}{\pi(\pi c-2)}[\pi c \ln(\frac{cl_g^2+r\theta(l_g-y)}{cl^2}) + (\pi c-4)\ln(\frac{2l_g^2+\pi r\theta(l_g-y)}{2l_g^2})]. \tag{3.57}$$

In order to calculate inductances, it is required to derive flux linkage of the main winding. From the magnetic circuit of the motor the relation of flux linkage can be written as

$$\psi = (-\phi_{a1} + \phi_{a2} - \phi_{a3} + \phi_{a4})N \tag{3.58}$$

Again we know that flux linkage is the product of inductance and the total current in the winding per phase, i.e.

$$\psi = Li \tag{3.59}$$

Hence, comparing Equation 3.58 and Equation 3.59 and equating the coefficients of Equation 3.7 to Equation 3.10, we get the inductance matrix as

$$[L] = \begin{bmatrix} L_{11} & L_{12} & L_{13} & L_{14} \\ L_{21} & L_{22} & L_{23} & L_{24} \\ L_{31} & L_{32} & L_{33} & L_{34} \\ L_{41} & L_{42} & L_{43} & L_{44} \end{bmatrix} \tag{3.60}$$

where,

$$L_{11} = \frac{P_{a1}}{P}(P_{a2} + P_{a3} + P_{a4})N^2 \tag{3.61}$$

$$L_{12} = \frac{P_{a1}P_{a2}}{P}N^2 \tag{3.62}$$

$$L_{13} = -\frac{P_{a1}P_{a3}}{P}N^2 \tag{3.63}$$

$$L_{14} = \frac{P_{a1}P_{a4}}{P}N^2 \tag{3.64}$$

$$L_{21} = \frac{P_{a1}P_{a2}}{P}N^2 \tag{3.65}$$

$$L_{22} = \frac{P_{a2}}{P}(P_{a1} + P_{a3} + P_{a4})N^2 \tag{3.66}$$

$$L_{23} = \frac{P_{a2}P_{a3}}{P}N^2 \tag{3.67}$$

$$L_{24} = -\frac{P_{a2}P_{a4}}{P}N^2 \tag{3.68}$$

$$L_{31} = -\frac{P_{a1}P_{a3}}{P}N^2 \tag{3.69}$$

$$L_{32} = \frac{P_{a2}P_{a3}}{P}N^2 \tag{3.70}$$

$$L_{33} = \frac{P_{a3}}{P}(P_{a1} + P_{a2} + P_{a4})N^2 \tag{3.71}$$

$$L_{34} = \frac{P_{a3}P_{a4}}{P}N^2 \tag{3.72}$$

$$L_{41} = \frac{P_{a4}P_{a1}}{P}N^2 \tag{3.73}$$

$$L_{42} = -\frac{P_{a4}P_{a2}}{P}N^2 \tag{3.74}$$

$$L_{43} = \frac{P_{a4}P_{a3}}{P}N^2 \tag{3.75}$$

$$L_{44} = \frac{P_{a4}}{P}(P_{a1} + P_{a2} + P_{a3})N^2 \tag{3.76}$$

The corresponding magnetic field energy can be expressed as

$$W = \frac{1}{2}\,[I]\,[L]\,[I]^T \tag{3.77}$$

The torque can be derived from the rate of change of the stored magnetic energy with respect to the rotational position as

$$T = \frac{\partial W}{\partial \theta} \approx \left(4i_m^2 + 2i_{b1}^2 + 2i_{b2}^2\right) \tag{3.78}$$

where, θ is the rotor position.
The radial forces in the horizontal and vertical directions x and y can be represented as

$$F_x = \frac{\partial W}{\partial x} = K(\theta) i_m i_{b1} \tag{3.79}$$

$$F_y = \frac{\partial W}{\partial y} = K(\theta) i_m i_{b2} \tag{3.80}$$

where, $K(\theta)$ is the proportionality constant. This expression of $K(\theta)$ obtained is difficult to express as a simple mathematical expression. Though this approach helps in developing an accurate permeance model, it leads to the requirement of a complex controller algorithm for the torque and radial force control. In order to derive a simplified

expression, the mathematical modelling is further carried on in the following subsection.

3.3.3 Analytical model using Maxwell's stress tensor method

In this section, Maxwell's stress tensor method has been used for mathematical modelling of the proposed motor. The calculation is done by neglecting the magnetic saturation of the motor. In this section, the magnetic flux paths are assumed as circular and straight flux lines. In order to derive a simpler model, the force and torque are derived by directly integrating the flux densities at the rotor and the stator surface. According to Maxwell's stress tensor method, the force per unit area along a certain dimensional mechanical angle on the rotor surface can be expressed as

$$dF_n(\theta) = \frac{B_n^2(\theta)}{2\mu_0} dA \tag{3.81}$$

where, B is the magnetic field density, A is the area of air gap and μ_0 is the permeability of air.

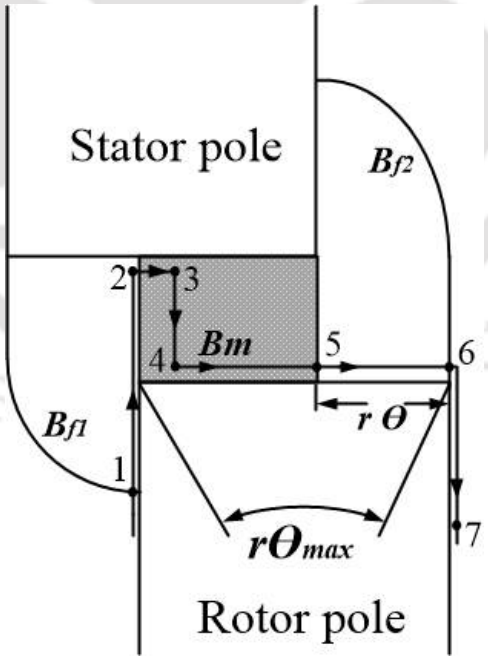

Figure 3.9: Integration of flux line paths at stator and rotor tooth

Figure 3.9 shows the relative position of the stator and rotor tooth with an enlarged view of the air gap. The flux paths are supposed to be radial across the air gap and

the flux lines are either orthogonal or parallel to the integration paths. Following these assumptions the perpendicular and parallel integration paths in the enlarged air gap are shown in Figure 3.9. Paths 1-2 and 3-4 are the integration path parallel to the flux lines and the paths 2-3, 4-5 and 5-6 are the integration paths perpendicular to the flux lines. B_m is the main flux density, and B_{f1} and B_{f2} are the fringing magnetic flux densities.

The radial and tangential force acting on the rotor as shown in Figure 3.9 can be given as,

$$F_r = \frac{1}{2\mu_0} \iint_A (B_r^2 - B_t^2) dA \tag{3.82}$$

$$F_t = \frac{1}{\mu_0} \iint_A (B_r B_t)\, dA \tag{3.83}$$

The integration of the field path perpendicular to the flux lines is,

$$F_r = \frac{1}{2\mu_0} \iint_A B_r^2 dA \tag{3.84}$$

The integration of the path parallel to the flux lines is,

$$F_t = -\frac{1}{2\mu_0} \iint_A B_t^2 dA \tag{3.85}$$

The length of the integral path can be expressed as,

$$\begin{aligned} l_{34} &= l_g \\ l_{23} + l_{45} &= r\theta_{\max} - r\theta \\ l_{56} &= r\theta \end{aligned} \tag{3.86}$$

where, θ_{max} is the rotor arc angle and r is the radius of the rotor. The forces acting on the rotor pole as shown in Figure 3.9 can be derived from the above equations as follows.

The radial force component equals,

$$F_r = \frac{h}{2\mu_0} \left(\int_2^3 {B_m}^2 dl + \int_4^5 {B_m}^2 dl + \int_5^6 {B_{f2}}^2 dl \right) \tag{3.87}$$

And the tangential force component equals,

$$F_t = \frac{h}{2\mu_0}\left(\int_1^2 {B_{f1}}^2 dl - \int_3^4 {B_m}^2 dl\right) \tag{3.88}$$

where, h is the stack length of the rotor.

The torque acting on the rotor pole can be written as,

$$T = F_t r = \frac{hr}{2\mu_0}\left[\int_1^2 B_{f1}^2 dl - B_m^2 dl\right] \tag{3.89}$$

The main flux density at $A1$ and $A3$ can be obtained from the straight flux lines as,

$$B_{mA1} = \frac{\mu_0 N I_1}{l_g} \tag{3.90}$$

$$B_{mA3} = \frac{\mu_0 N I_3}{l_g} \tag{3.91}$$

where, N is the number of turns per stator tooth and I_1 and I_3 are the net currents in the poles of air gaps $A1$ and $A3$ as given in Table.3.1. In the previous section, the

Table 3.1: Distribution of currents in coils of phase-A

Air gaps(coil numbers)	**Net current distribution**
A1(coils 1a and 1a')	$I_1 = i_m + i_{b1}$
A2(coils 4a and 4a')	$I_2 = i_m + i_{b2}$
A3(coils 7a and 7a')	$I_3 = i_m - i_{b1}$
A4(coils 10a and 10a')	$I_4 = i_m - i_{b2}$

fringing flux densities were assumed as elliptical lines. In this section they are assumed as straight and circular flux lines and can be expressed as

$$B_{fA1} = \frac{\mu_0 N I_1}{l_g + \frac{\pi}{4} r\theta} \tag{3.92}$$

$$B_{fA3} = \frac{\mu_0 N I_3}{l_g + \frac{\pi}{4} r\theta} \tag{3.93}$$

The radial force acting on air gaps $A1$ and $A3$ with the introduction of bridge currents

is given as

$$F_{A\,1} = \frac{{B_{ma1}}^2 A}{2\mu_0} + \frac{{B_{fa1}}^2 A}{2\mu_0}$$
$$= \frac{\mu_0 hrN^2}{2}\left[\frac{\theta_{\max}-\theta}{{l_g}^2} + \frac{16\theta}{(4l_g+\pi r\theta)^2}\right]{I_1}^2 \tag{3.94}$$

$$F_{A\,3} = \frac{{B_{ma3}}^2 A}{2\mu_0} + \frac{{B_{fa3}}^2 A}{2\mu_0}$$
$$= \frac{\mu_0 hrN^2}{2}\left[\frac{\theta_{\max}-\theta}{{l_g}^2} + \frac{16\theta}{(4l_g+\pi r\theta)^2}\right]{I_3}^2. \tag{3.95}$$

Thus, the net radial force produced by Phase-A on x and y axis can be expressed as

$$F_{xa} = F_{A1} - F_{A3}$$
$$= \frac{\mu_0 N^2 hr}{2}\left[\frac{\theta_{\max}-\theta}{{l_g}^2} + \frac{16\theta}{(4l_g+\pi r\theta)^2}\right][{I_1}^2 - {I_3}^2] \tag{3.96}$$

$$F_{ya} = F_{A2} - F_{A4}$$
$$= \frac{\mu_0 N^2 hr}{2}\left[\frac{\theta_{\max}-\theta}{{l_g}^2} + \frac{16\theta}{(4l_g+\pi r\theta)^2}\right][{I_2}^2 - {I_4}^2]. \tag{3.97}$$

Therefore, the radial forces can be expressed as,

$$F_x = 4K_f(\theta) i_m i_{b1} \tag{3.98}$$

$$F_y = 4K_f(\theta) i_m i_{b2} \tag{3.99}$$

where,

$$K_f(\theta) = \frac{\mu_0 N^2 hr}{2}\left[\frac{\theta_{\max}-\theta}{{l_g}^2} + \frac{16\theta}{(4l_g+\pi r\theta)^2}\right] \tag{3.100}$$

Thus, from Equation 3.89, Equation 3.90 and Equation 3.92, the net torque produced by phase-A can be expressed as

$$T_A = T_{A\,1} + T_{A\,2} + T_{A\,3} + T_{A\,4}$$
$$= K_t\ N^{\,2}({I_1}^2 + {I_2}^2 + {I_3}^2 + {I_4}^2), \tag{3.101}$$

where,

$$K_t = \frac{\mu_0 hr}{2}\left[\frac{1}{l_g} + \frac{16(l_g - r\theta)}{(4l_g - \pi r\theta)^2}.\right] \tag{3.102}$$

When the rotor rotates from an unaligned position to an aligned position, the motor generates positive torque which can be represented as

$$T_1 = \mu_0 hr\left[\frac{1}{l_g} - \frac{16(l_g - r\theta)}{(4l_g - \pi r\theta)^2}\right] N^2({I_1}^2 + {I_2}^2 + {I_3}^2 + {I_4}^2), \tag{3.103}$$

And while rotating from aligned to unaligned position it generates negative torque as

$$T_2 = \mu_0 hr\left[-\frac{1}{l_g} + \frac{16(l_g + r\theta)}{(4l_g + \pi r\theta)^2}\right] N^2({I_1}^2 + {I_2}^2 + {I_3}^2 + {I_4}^2). \tag{3.104}$$

However, because of the selection of the integration of the flux paths and the assumptions of the fringing flux lines as circular and straight lines in the analytical model, the accuracy in the model might be affected [63]. The modification relative to $K_f\ (\theta)$ is approximated as a third order polynomial and given as

$$K'\ (\theta) = K_f(\theta)\ (1 + k_{\ 1}\,|\theta\ | + k_{\ 2}|\theta\ |^2 + k_{\ 3}|\theta\ |^3) \tag{3.105}$$

where k_1=1.1, k_2= -2 and k_3=15. These values are referred from [63] and adjusted for accuracy according to the analytical model developed in the thesis.
Thus, the instantaneous radial force can be expressed as

$$\begin{bmatrix} F_x \\ F_y \end{bmatrix} = 4\, i_m \begin{bmatrix} K'(\theta) & 0 \\ 0 & K'(\theta) \end{bmatrix} \begin{bmatrix} i_{b1} \\ i_{b2} \end{bmatrix} \tag{3.106}$$

and

$$T = N^2 K_t \begin{bmatrix} 4{i_m}^2 \\ 2{i_{b1}}^2 \\ 2{i_{b2}}^2 \end{bmatrix} \tag{3.107}$$

From the above equations it is recognized that the average torque and radial force is determined by i_m, θ, i_{b1} and i_{b2} at every point. The magnitude and direction of forces can be regulated by controlling the bridge currents i_{b1} and i_{b2} independently. Hence,

Equation. 3.106 can be re-written for phase-A ($-15^0 \leq \theta \leq 0^0$) as

$$\begin{bmatrix} F_{ax} \\ F_{ay} \end{bmatrix} = 4i_m \begin{bmatrix} K'(\theta) & 0 \\ 0 & K'(\theta) \end{bmatrix} \begin{bmatrix} i_{b1a} \\ i_{b2a}. \end{bmatrix} \tag{3.108}$$

During the conduction period of phase-B ($0^0 \leq \theta \leq 15^0$) as

$$\begin{aligned} \begin{bmatrix} F_{bx} \\ F_{by} \end{bmatrix} &= \begin{bmatrix} \cos 30^0 & \sin 30^0 \\ -\sin 30^0 & \cos 30^0 \end{bmatrix} \begin{bmatrix} F_x \\ F_y \end{bmatrix} \\ &= 4i_m \begin{bmatrix} \cos 30^0 & \sin 30^0 \\ -\sin 30^0 & \cos 30^0 \end{bmatrix} \begin{bmatrix} K'(\theta) & 0 \\ 0 & K'(\theta) \end{bmatrix} \begin{bmatrix} i_{b1b} \\ i_{b2b} \end{bmatrix} \end{aligned} \tag{3.109}$$

During the conduction period of phase-C ($15^0 \leq \theta \leq 30^0$) as

$$\begin{aligned} \begin{bmatrix} F_{cx} \\ F_{cy} \end{bmatrix} &= \begin{bmatrix} \cos 30^0 & -\sin 30^0 \\ \sin 30^0 & \cos 30^0 \end{bmatrix} \begin{bmatrix} F_x \\ F_y \end{bmatrix} \\ &= 4i_m \begin{bmatrix} \cos 30^0 & -\sin 30^0 \\ \sin 30^0 & \cos 30^0 \end{bmatrix} \begin{bmatrix} K'(\theta) & 0 \\ 0 & K'(\theta) \end{bmatrix} \begin{bmatrix} i_{b1c} \\ i_{b2c} \end{bmatrix} \end{aligned} \tag{3.110}$$

Considering radial displacements of x and y into Equation 3.96 and Equation. 3.97, the expression for radial forces in phase-A can be given as

$$\begin{aligned} F_{xa} &= F_{A1} - F_{A3} \\ &= {K_{fx}}' {I_1}^2 - {K_{fx}}'' {I_3}^2 \end{aligned} \tag{3.111}$$

$$\begin{aligned} F_{ya} &= F_{A1} - F_{A3} \\ &= {K_{fy}}' {I_1}^2 - {K_{fy}}'' {I_3}^2, \end{aligned} \tag{3.112}$$

where

$${K_{fx}}' = \frac{\mu_0 N^2 hr}{2} \left[\frac{\theta_{\max} - \theta}{(l_g - x)^2} + \frac{16\theta}{(4(l_g - x) + \pi r\theta)^2} \right] \tag{3.113}$$

$${K_{fx}}'' = \frac{\mu_0 N^2 hr}{2} \left[\frac{\theta_{\max} - \theta}{(l_g + x)^2} + \frac{16\theta}{(4(l_g + x) + \pi r\theta)^2} \right] \tag{3.114}$$

$$K_{fy}{}' = \frac{\mu_0 N^2 hr}{2}\left[\frac{\theta_{\max}-\theta}{(l_g-y)^2}+\frac{16\theta}{(4(l_g-y)+\pi r\theta)^2}\right] \tag{3.115}$$

and

$$K_{fy}{}'' = \frac{\mu_0 N^2 hr}{2}\left[\frac{\theta_{\max}-\theta}{(l_g+y)^2}+\frac{16\theta}{(4(l_g+y)+\pi r\theta)^2}.\right] \tag{3.116}$$

Thus, from the above derivations it is clear that the radial forces F_x and F_y are directly proportional to the products of the main current and the bridge currents i_{b1} and i_{b2} in the windings. There, the radial forces can be controlled by this bridge current within the same winding by building a proper current control algorithm. It has to be noted that in the term $K'(\theta)$, the first term in the parenthesis is due to the main flux and the second term is due to the fringing flux and is dependent on the rotor position θ. The second term goes to zero as the rotor comes to an aligned position. At the aligned position, the torque become zero but the radial force is maximum. Hence, in case of BSRM the commutation of the bridge current and the motor main current has to be done carefully in order to avoid zero or negative torque.

3.4 Design Procedure of BSRM with BCW

The performance analysis of SRM for self-bearing or levitation purpose requires an accurate design and dimensions for the stator and rotor laminations, windings, pole numbers and pole arcs. The detailed design procedure of conventional SRMs has been described in [3, 33, 36, 91, 92]. Krishnan in 2001 has developed an output equation for SRM by following the basic output equation of induction machines and DC machines. The procedure outlined in this section has used the basic initial dimension selection of existing induction motor for the design of SRM. In this thesis, for the development of a prototype of the proposed motor, the design methodology of a conventional SRM as given by Krishnan [3] has been followed. However, the design method varies in a way that instead of focusing only on the torque production, an approach is made such that considerable radial force is also obtained as the rotor rotates.

The dimensions of the proposed motor are selected such that that substantial amount of both torque and radial force are produced at every rotational angle of the motor. The final design of the motor is achieved through an iterative process of steady state performance calculation. Once the dimensions are fixed, the inductance at every position under rated condition are calculated. This chapter contains the selection of various

machine variables such as rotor and stator pole arc angles, core length, bore diameter, back of the core thickness, number of turns in each phase winding, air gap length etc. This section describes in brief a step by step design procedure to develop a prototype of a SRM capable of both torque and levitation force production for bearingless purpose. The design of the motor at steady state and rated condition has been verified using FE analysis.

The motor is initially designed considering the rated power and rated torque of normal SRM. The design specifications for the SRM comprises of the required power output P in W, mechanical speed N in rad/s, allowable peak phase current i_p, and available DC supply voltage V_{dc} in V for the system. The torque developed by a machine is given as

$$T_{req} = \frac{P}{2\pi\left(\frac{N}{60}\right)}\text{Nm} \tag{3.117}$$

In this thesis, the rated output power of the motor is selected as 750 W and the rated speed as 1500 rpm. Thus, the average torque of the motor is calculated as 4.7 Nm.

3.4.1 Frame size selection

The design procedure of an SRM, with regards to the physical dimensions of the machine, is normally compared equivalent to an induction motor according to the standards of International Electrotechnical Commission (IEC) IEC 60072 for rotating electrical machines [93]. A comparison with an equivalent induction motor fixes the frame size of the SRM to be designed. This is advantageous as in many applications a SRM may be used to replace other machines. The IEC fixes the dimensions for all electrical machines according to the International Standards Organization (ISO) regulations and National Electrical Manufacturers Association (NEMA) regulations.

3.4.2 Stator and rotor core design

The design procedure differs from the way conventional SRMs are designed where focus is more on torque production. It is to be noted that the principle of torque and radial force production in SRM is entirely dependent on the change in inductance for every change in radial and rotational position of the rotor.

As seen in Figure 3.10, the region from θ_1 to θ_3 is the slope of rising inductance. The region, 0-θ_1 is the unaligned position and the inductance starts rising from θ_1 to θ_3. θ_1 is the position when the stator rotor overlap. From θ_3 to θ_4, the rate of inductance is zero,

and torque produced in this region is zero. Hence, the effective torque producing region is from θ_1 to θ_3. The region from θ_1 to θ_7 can produce radial force, but it is minimum at θ_1 and maximum at θ_4. Hence, care has to be taken such that both torque and force are produced with substantial amount of current. The overlap region is available from θ_1 to θ_3 and is ideally the best region for each phase of the motor to produce torque as well as radial force. As such, proper selection of rotor and stator tooth arc is one of the design criteria for BSRM in order to obtain an optimal torque and radial force without unnecessary requirement of excess current. Since it is a 12/8 motor, for one complete electrical rotation of the rotor it has to traverse 45^0 (mechanical degree). The number of phases, N_p of the driver circuit is taken as 3-phase and the conduction period of one phase (θ_d) is selected as 15^0. From the IEC 60072 standard, the rated speed is fixed as 1500 rpm, the frame size as 71 mm, the power output is chosen as 750 W, the rated average torque as 4.7 Nm, the rated current as 10 A. The dimensions of the rotor are

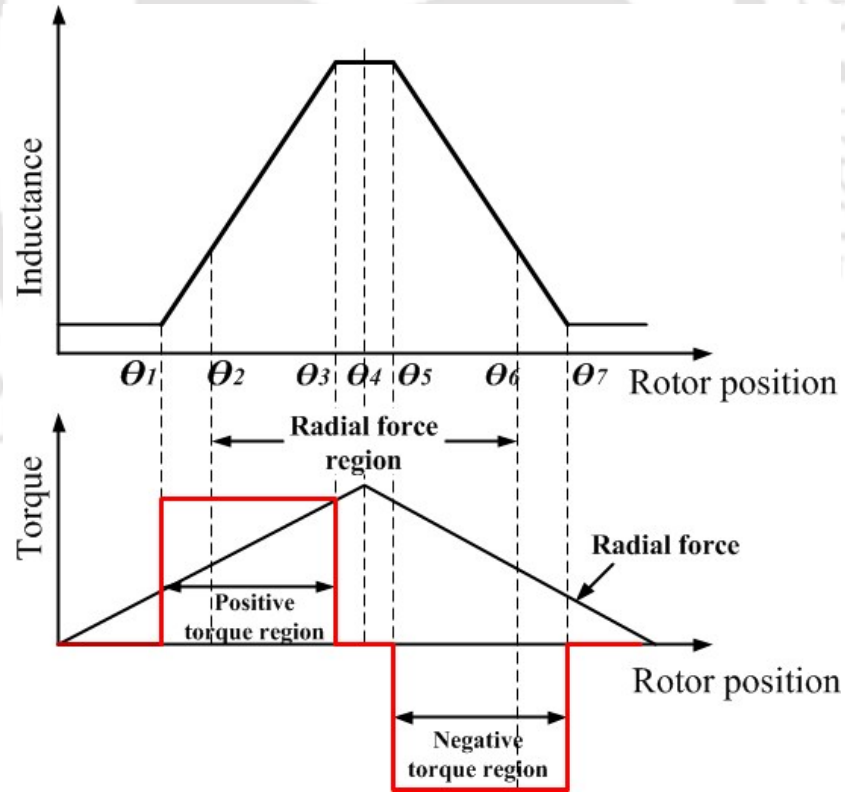

Figure 3.10: Inductance, torque and radial force region of BSRM

selected based on the availability of a SRM rotor with 8 teeth in the laboratory. Again, it is a good practice to design the motor under the condition of maximum flux density which is usually taken as the knee point value of the B-H curve of the material used in

Table 3.2: Dimensions of the rotor

Parameters	**Values**
Rotor outer diameter, D_r	65.4 mm
Height of the rotor tooth, h_r	13.44 mm
Rotor tooth arc angle, β_r	16.87^0
Stack length, h	53 mm
Back of the rotor core, C_r	11.15 mm
Shaft diameter, D_{sh}	16.7 mm
Air gap length, l_g	0.5 mm
Material of the core	M-19 steel
Weight of the rotor, m	1.18 kg

the stator and rotor. The material selected for the proposed motor is M-19 steel and assuming the maximum flux density B_{sat} as 1.5 T, the calculations are taken forward.

The outer diameter is calculated as [7],

$$\begin{aligned} D_o &= (\text{Frame} \quad \text{Size} - 3) \times 2 \\ &= (71 - 3) \times 2 = 136 \text{ mm} \end{aligned} \tag{3.118}$$

where the frame size is taken according to IEC standards [93]. The 3 mm subtraction is taken in industry to account for the foot of the machine, which is used for mounting. The frame size is referred to as the distance of the centre of the shaft to the ground where the motor is mounted. The dimensions of the rotor are already fixed as given in Table 3.2, hence by fixing the air gap length, l_g as 0.5 mm, the stator bore diameter is calculated as

$$D = 2l_g + D_r = 66.4 \text{ mm} \tag{3.119}$$

where, D is the stator bore diameter, l_g is the air gap length and D_r is the rotor diameter. The stator pole area is calculated as,

$$A_s = \frac{D}{2} h \beta_s = 0.5 \times 10^{-3} \text{ m}^2 \tag{3.120}$$

where, D is the stator bore diameter, h is the stack length and β_s is the stator tooth arc angle in radian. The area of the yoke is assumed to be equal to the stator pole area,

$$A_y = A_s \tag{3.121}$$

The stator pole arcs have to be chosen to accommodate the stator pole flux density. Thus, if w_{sp} is the pole width given in terms of pole arc as follows,

$$w_{sp} = D \sin\left(\frac{\beta_s}{2}\right) = 9.24 \text{ mm}, \tag{3.122}$$

The back of the core thickness of the stator (C_s) has to be a minimum of 0.5 w_{sp} [3]. Considering mechanical robustness and minimization of vibration it can be kept within a range of

$$w_{sp} > C_s \geq 0.5 w_{sp} \tag{3.123}$$

In practice, it is recommended to choose a little higher value for C_s than its minimum. Thus,

$$C_s = 9.28 \text{ mm} \tag{3.124}$$

The stator tooth height is given by

$$h_s = \frac{D_o}{2} - C_s - \frac{D}{2} = 25.52 \text{ mm} \tag{3.125}$$

Table 3.3: Dimensions of the stator

Parameters	**Values**
Bore diameter, D	66.4 mm
Stator outer diameter, D_o	136 mm
Back of the stator core, C_s	9.28 mm
Height of the stator tooth, h_s	25.22 mm
Stator tooth arc angle, β_s	16^0
Stack length, h	53 mm
Number of turns, N	40
Clearance between shaft and rotor	0.5 mm
Material of the core	M 19 steel

Figure 3.11 shows the schematic diagram of the rotor and the stator core designed for the proposed prototype of the motor. The various parameters are labelled in the diagram.

3.4.3 Coil design

The BCW consists of two layers of coil in each stator tooth. Figure 3.12 shows a section of the stator slot which comprises of the upper layer of coil and lower layer of

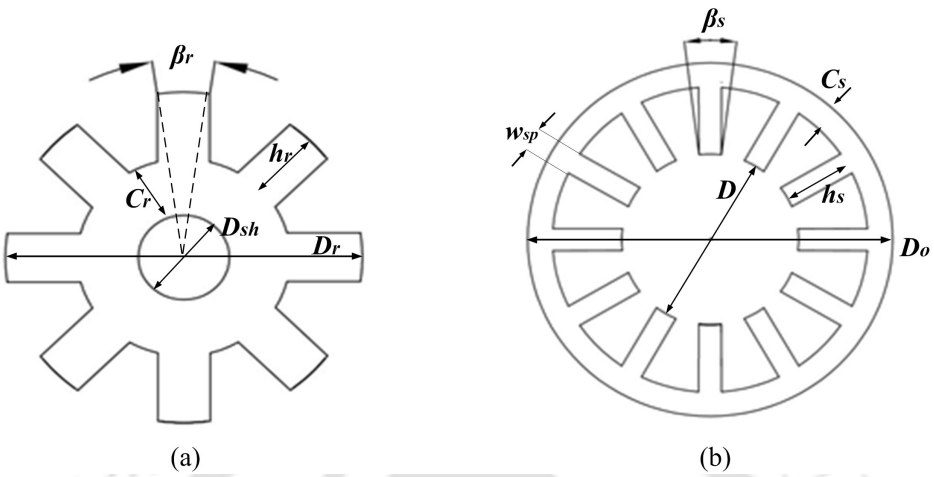

Figure 3.11: Design of (a) rotor and (b) stator

coil. The entire slot area can be calculated by assuming the geometry as a trapezoidal section, where a is the inner width of the segment, b is the outer width and h_s is the height of the slot or stator tooth. The slot comprises of two layers of coils, upper coils and lower coils. The slot is assumed as trapezoidal for a relatively simple calculation of the slot area. The area of the total slot is calculated as,

$$\begin{aligned} A_{(s)} &= \frac{(a+b)h_s}{2} \\ &= \frac{(8.14347+21.5057201)*25.52}{2} = 378.3238 \text{ mm}^2 \end{aligned} \tag{3.126}$$

Assuming a maximum allowable current density of copper as $J = 4$ A/mm^2 in the coils

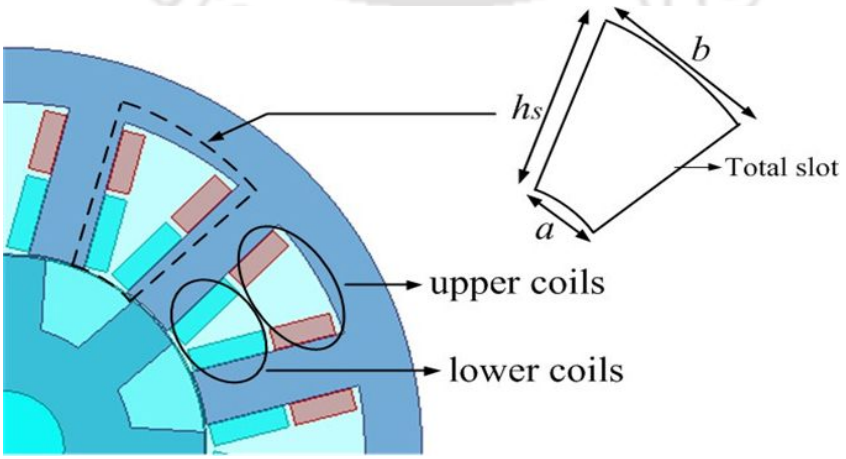

Figure 3.12: Calculation of the slot area

and peak current as 10 A, the minimum area of conductor is given by

$$\begin{aligned} a_{(c)} &= \tfrac{i}{2J} \\ &= 1.25\ \text{mm}^2 \approx 1.3\ \text{mm}^2 \end{aligned} \tag{3.127}$$

Hence, the diameter of the wire including insulation is given by

$$d_{(w)} = \sqrt{\frac{4a_c}{\pi}} + 0.1 = 1.386\ \text{mm} \tag{3.128}$$

From the standard chart of American wire gauge (AWG), for a minimum current of 10 A the diameter of wire without insulation is 1.3 mm (approx.) and area of cross section of conductor is 1.3 mm^2. Thus, from the standard table the AWG is taken as 16. Assuming a coil wedge thickness of 2 mm, the maximum height of the winding (h_w) which can be accommodated in the space inclusive of the wedge is given by

$$h_w = h_s - h_{wedge} = 25.52 - 2 = 23.52\ \text{mm} \approx 24\ \text{mm}. \tag{3.129}$$

Assuming the winding packing factor as 0.3 and wire diameter as 1.3 mm the number of turns that can be accommodated in that stator tooth can be given as,

$$N = \frac{378.323 \times 0.3}{\pi\left(\frac{1.3}{2}\right)^2} = 82.9 \approx 83 \tag{3.130}$$

Thus, for two sets of coil per tooth the number of turns in each coil is taken as 40. The selection of N as 40 in each coil in the stator is based on the maximum current carrying capacity of the conductor. Since, the production of torque and radial force depends on the mmf of the coil i.e. on both the number of turns and current, hence by selecting an appropriate number of turns, sufficient force and torque can be produced with smaller magnitude of current.

The total slot area is calculated as 378.323 mm^2 and the total area of the coil in the stator teeth is given as

$$A_c = 1.3 \times 40 \times 4 = 208\ \text{mm}^2 \approx 200\ \text{mm}^2 \tag{3.131}$$

Thus, slot area per coil is calculated as

$$A_{c(1)} = 1.3 \times 2 \times 40 = 104\ \text{mm}^2 \approx 100\ \text{mm}^2 \tag{3.132}$$

Thus, the copper slot fill factor is calculated as

$$\begin{aligned} Slot\ fill\ factor(\%) &= \frac{total\ area\ of\ conductor}{Slot\ area} \\ &= \frac{200}{378.323} \times 100\% \approx 50\% \end{aligned} \tag{3.133}$$

The number of turns per coil has a major effect in the production of radial force and torque. As the primary objective of the design procedure is to obtain sufficient torque and radial force without additional requirement of current, a finite element optimization is done based on the number of winding turns. On the basis of the initial scheme, the influence of the number of turns on radial force and torque is calculated by the finite element simulation analysis of SRM. By taking a constant current of 6 A as the main current and 1 A as the bridge current, the torque and radial force is calculated for different number of turns. From Figure 3.13 and Figure 3.14 it can be observed that, the number

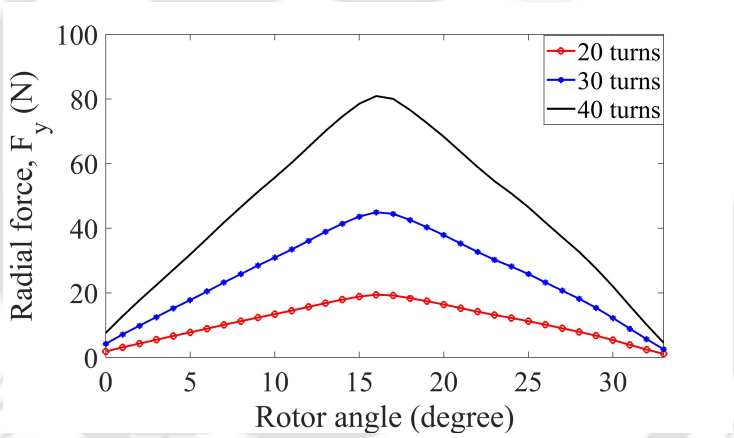

Figure 3.13: Radial force, F_y for various number of turns of coil

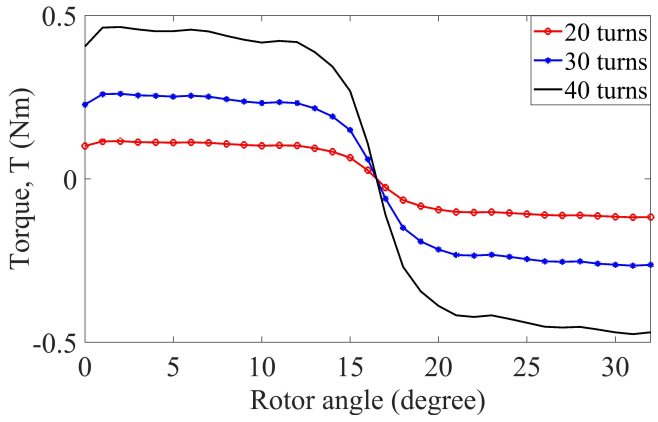

Figure 3.14: Torque for various number of turns of coil

of turns has a significant effect on the magnitude of torque and force. As the maximum number of turn which can be accommodated in the stator slot of the designed motor is approximately 83, and further increment in number of turns will require additional space. Again decrease in the number of turns requires additional current to produce the required torque and force which affects the current carrying capacity of the conductor. Thus, in order to avoid increase in current the number of turns is fixed as 40 for producing the desired torque and force in the proposed motor.

3.4.4 Selection of rotor and stator tooth arc angles

The stator and rotor tooth arc angle selection plays a crucial role in the preliminary design process [3], [35]. The torque characteristics are dependent on the inductance profile in SRMs. From the equation of torque as given in Equation 2.6, it is clear that the production of torque depends on the rate of changing inductance according to the rotor position. The inductance profiles are determined in terms of stator and rotor pole arcs angles and the number of rotor poles. The standard design of SRM normally has the rotor pole arc angle (β_r) greater than the stator pole arc angle (β_s) [3].

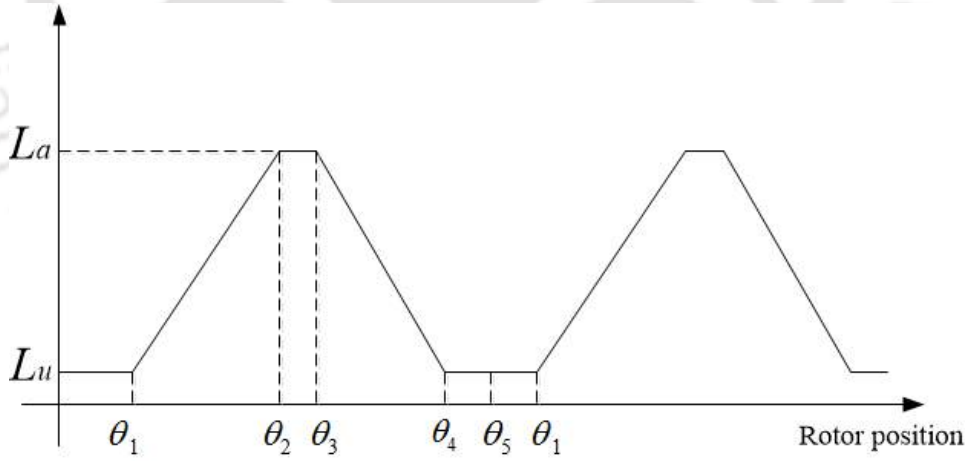

Figure 3.15: Inductance profile of an SRM

Figure 3.15 shows the four distinct inductance region of a conventional SRM. The region 0 - θ_1 and θ_4 - θ_5 shows the region where the stator and rotor poles do not overlap making minimum flux linkage and minimum inductance and almost a constant region. This region do not contribute to torque production. The inductance in this region is known as unaligned inductance, L_u. From θ_1 - θ_2, the stator-rotor poles overlap. This increases the inductances with the rotor position providing a positive slope. Current through the winding in this regions produces positive torque i.e. motoring torque. From

θ_2 - θ_3, the stator-rotor poles completely overlap keeping the inductance maximum and constant and this inductance is known as the aligned inductance, L_a. Since, there is no change in inductance the torque production in this region is zero. This is mainly due to the fact that the rotor arc angle is greater than the stator pole arc angle. Thus this fact serves a useful function by providing useful time for the stator current to come to zero when it is commutated, thus preventing the occurence of negative torque. This zone is preferably called as a dead time zone. θ_3 - θ_4 is the region when the rotor is moving away from the stator pole. This has decreasing inductance profile contributing to negative torque generation.

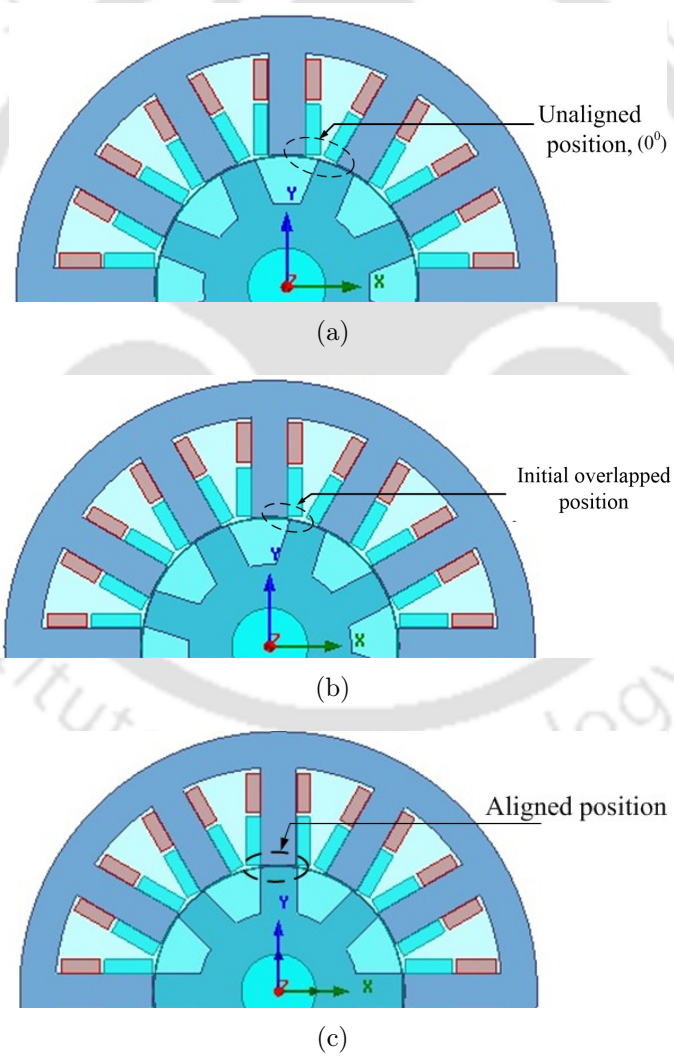

Figure 3.16: (a) Unaligned position (b) initial overlapped position and (c) aligned position

In the present study of designing BSRM, the rotor position for excitation and commu-

tation has to be fixed based on an optimal production of torque and radial force. Figure 3.16(a) shows the unaligned rotor position, Figure 3.16(b) show the initial stator-rotor overlapped position and Figure 3.16(c) shows the aligned position. In order to identify the best torque and radial force producing region, a FE model is built in Ansoft Maxwell 2D with the specification as given in Table 3.2 and Table 3.3. The iteration is started from stator arc angle of 15^0 ($< \beta_r$) and varying upto 19^0 ($> \beta_r$) and the various force and torque profiles are observed. In the simulation, the unaligned position as shown in Figure 3.16(a) is considered as the 0^0 rotor angle and the excitation is started from this position and continued for a rotational angle of 32^0. As the dimension of the rotor are fixed with reference to an available rotor of a SRM having 8 teeth, the rotor tooth arc angle is therefore selected as 16.87^0. Figure 3.17(a) and Figure 3.17(b) shows the

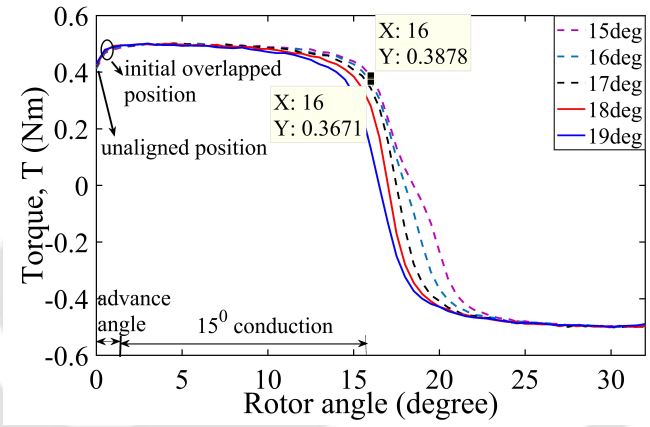

(a)

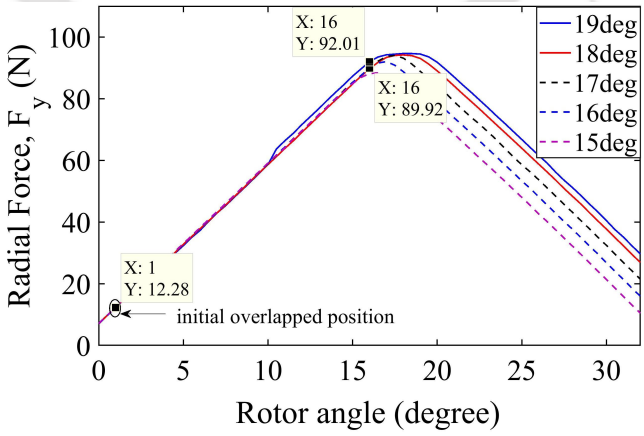

(b)

Figure 3.17: (a) Torque and (b) radial force profiles for varying stator tooth arc angles, (β_s)

variation in torque and force profile of BSRM with the change in β_s for a constant main current supply of 4 A in coils of phase-A and assuming a bridge current supply of 1 A in coils of y-axis. Taking the number of turns N as 40, the total ampere turns in stator coils of $A1$ and $A3$ is 160 AT and in $A2$ and $A4$ is 200 AT and 120 AT. In this case, the unaligned position is considered as 0^0 and continued for a full rotation. From Figure 3.17(a) it can be observed that at the initial overlapped position the torque is slightly higher than the unaligned position (0^0) and at the aligned position, the torque becomes zero. However, from the initial overlapped angle (1^0) to the nearly aligned position (16^0) the torque remains positive, which makes it clear that for a rotational angle of 15^0, an adequate amount of torque is produced. Similarly, from Figure 3.17(b) it can be observed that at the initial overlapped position, the radial force obtained is around 12 N, which is equal to the lifting force, F_l required to levitate the rotor. Thus, in the region from initial overlapped position to a nearly aligned position, sufficient torque and radial force can be produced. Owing to these observations, the initial overlapped position is selected as the turn-on angle position (0^0) and the nearly aligned position as the turn off angle position (15^0) as shown in Figure 3.18. This rotational angle is hereby fixed for the proposed motor and is followed throughout the thesis. It is again observed from Figure 3.17(b) that the radial force region increases with the increase in stator tooth arc angle. As β_r is kept fixed at 16.87^0, so by keeping an initial advance angle of 1^0 and the conducting period as 15^0, for β_s greater than 16.87^0 the torque reduces fast as shown in Figure 3.17(a). At the aligned position the values of torque for the stator arc angle as 15^0 and 16^0 are 0.3878 Nm and 0.3671 Nm and that of forces are 88.19 N and 89.92 N respectively. Thus, it is favorable to take the stator tooth arc angle as 16^0 in order to get a better value of both torque and force.

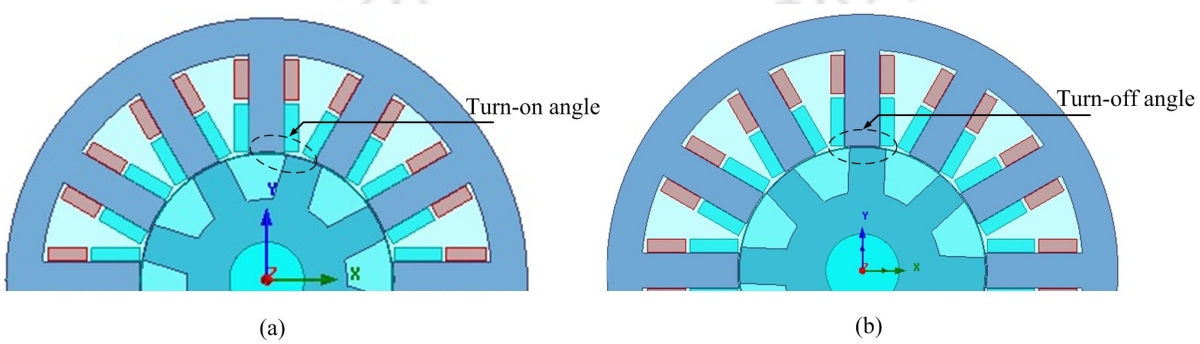

Figure 3.18: (a) turn on angle position (b) turn-off angle position

3.5 Analytical procedure for inductance calculation

The design of a SRM needs to be verified from the flux linkages versus current characteristics for both the aligned and unaligned positions. The flux linkages and the values of inductance are analytically obtained using the flux tube method [3]. The length of each flux lines is mathematically derived using magnetic equivalent reluctance circuit of each flux path at both aligned and unaligned rotor positions. Considering the geometrical parameters of the motor and using the magnetomotive force (mmf) equation, the inductance is obtained. While the evaluation of aligned flux linkages can be accurate, the same cannot be said for the unaligned values. The leakage fluxes and the path of the mutual flux complicate the accurate estimation of the unaligned flux linkages and unaligned inductance. In this section, a detailed analytical procedure is followed for calculating both aligned and unaligned inductance and has been verified using FE analysis [3], [7].

3.5.1 Analytical calculation of aligned inductance

The calculation of inductance plays a major role in designing an SRM and in determining the performance characteristic of the machine. The procedure outlined in this section is to determine the inductance of the machine at various rotor positions and obtain the machine's characteristics at rated condition. The following section gives an analytical approach of calculating the aligned and unaligned inductance of the motor considering the pattern of flux lines under both conditions. The process is based on an analytical expression involving the motor dimensions and certain assumptions as input variables. The design of an SRM for rated current can be verified from the flux linkages vs. current characteristics for both unaligned and aligned positions. The values of inductance are analytically calculated and FE analysis is used to accurately estimate the flux linkages and the inductance. The analytical technique to calculate the unaligned inductance may have a 10-15% error compared to its actual value. The mean lengths of the flux paths are analytically derived using the following assumptions.
The rotor pole area A_r is given by

$$A_r = \left(\frac{D}{2} - l_g\right) h\beta_r = 5.4618e^{-04}\ \mathrm{m}^2 \tag{3.134}$$

The rotor pole flux density B_r is given by

$$B_r = \frac{B_s A_s}{A_r} = 1.4430\ \mathrm{T} \tag{3.135}$$

where, B_s is the magnetic field density at saturation level and is taken as 1.5 T.
The area of the rotor core A_{rc} is given by

$$A_{rc} = \frac{A_s}{B_r} = 3.648\, e^{-04}\ \mathrm{m}^2 \tag{3.136}$$

Neglecting leakage and fringing, the mean air gap area can be approximately written as

$$A_g = \left(\frac{D}{2} - \frac{l_g}{2}\right)\left(\frac{\beta_r + \beta_s}{2}\right) h = 5.377\, e^{-04}\ \mathrm{m}^2 \tag{3.137}$$

The flux density in the air gap B_g, is given by

$$B_g = \frac{A_s B_s}{A_g} = 1.466\ \mathrm{T}. \tag{3.138}$$

The magnetic field intensity of the air gap, H_g is calculated as

$$H_g = \frac{B_g}{4\pi \times 10^{-7}} = 1167000\ \mathrm{AT/m} \tag{3.139}$$

The flux density in the stator yoke, B_y is given by

$$B_y = \frac{A_s B_s}{A_y} = 1.5\ \mathrm{T} \tag{3.140}$$

where, A_y is equal to A_s as given in Equation 3.121.
The flux density in the rotor pole B_r is given by

$$B_r = \frac{A_s B_s}{A_r} = 1.443\ \ \mathrm{T} \tag{3.141}$$

Since, the flux density of the rotor core is about 80 % of the maximum flux density B_{sat}, hence the flux density in the rotor core B_{rc} is given by

$$B_{rc} = \frac{0.8 B_s A_s}{A_{rc}} = 1.2\ \ \mathrm{T} \tag{3.142}$$

The magnetic field intensities in the stator pole, stator yoke, rotor pole and rotor core are designated as H_s, H_y, H_r and H_{rc}, respectively. They are obtained from the $B - H$ characteristics shown in Figure 3.19 as follows. The mean length of the flux path, l_y for

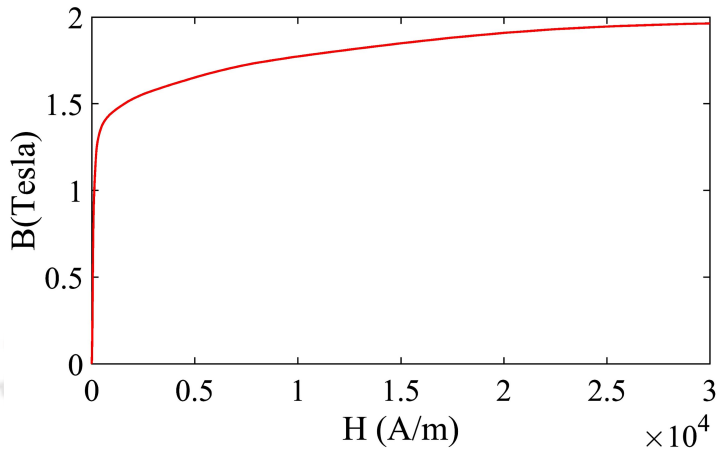

Figure 3.19: B-H characteristic curve of M-19 steel

a circular yoke SRM is calculated as

$$l_y = \pi\left(\frac{D_o}{2} - \frac{C_s}{2}\right) = 198 \text{ mm} \tag{3.143}$$

The mean lengths of the paths in various sections are given as follows

$$l_s = h_s + \frac{C_s}{2} = 30 \text{ mm}, \tag{3.144}$$

$$l_g = g = 0.5 \text{ mm}, \tag{3.145}$$

$$l_r = \frac{D}{4} - \frac{g}{2} + \frac{h_r}{2} - \frac{D_{sh}}{2} = 15.9 \text{ mm}, \tag{3.146}$$

$$l_{rc} = \pi\left(\frac{D}{4} - \frac{g}{2} - \frac{h_r}{2} + \frac{D_{sh}}{2}\right) = 60.1 \text{ mm}. \tag{3.147}$$

Now, the total ampere-turns F i.e. the magnetomotive force required for the machine to operate at rated current can be calculated. The magnetic circuit equation is written as

$$F = 2\left(H_s l_s + H_g l_g + H_r l_r\right) + \left(\frac{H_{rc} l_{rc}}{2}\right) + \left(\frac{H_y l_y}{2}\right) \approx 1280 \text{ AT}, \tag{3.148}$$

The aligned inductance at rated peak current i_p of 10 A, neglecting leakage is calculated as

$$L_a = \frac{F B_s A_s}{i_p^2} = 9.64 \text{ mH}. \tag{3.149}$$

3.5.2 Analytical calculation of unaligned inductance

For analytical study and FE simulation, two rotor angle positions are considered, i.e. unaligned and aligned. In the analytical modelling of unaligned inductance, seven flux paths are illustrated as shown in Figure 3.20. In Figure 3.20, the flux path 1 is assumed to have a flux of ϕ_1 in the stator pole. It crosses the air gap, splits evenly in the rotor back core and then re-crosses the air gap to the other pole and splits evenly to flow in the stator yoke. Figure 3.21 represents the magnetic equivalent reluctance circuit of flux tube 1. The reluctances of the stator pole, air gap, rotor core, stator yoke are denoted as $\mathcal{R}_s$,$\mathcal{R}_g$,$\mathcal{R}_{rc}$ and $\mathcal{R}_y$. Let the area of cross section of flux path 1 in the stator pole, air gap, rotor core and stator yoke be denoted as A_s, A_g, A_{rc} and A_y respectively. If the stator flux density is B_s, then the flux in path 1 in the stator can be found if the area of cross section of the flux path is known.

Flux path 1: In order to calculate the length and area of the flux path 1, let us consider the Figure 3.22. The area of cross section of the stator pole can be given as

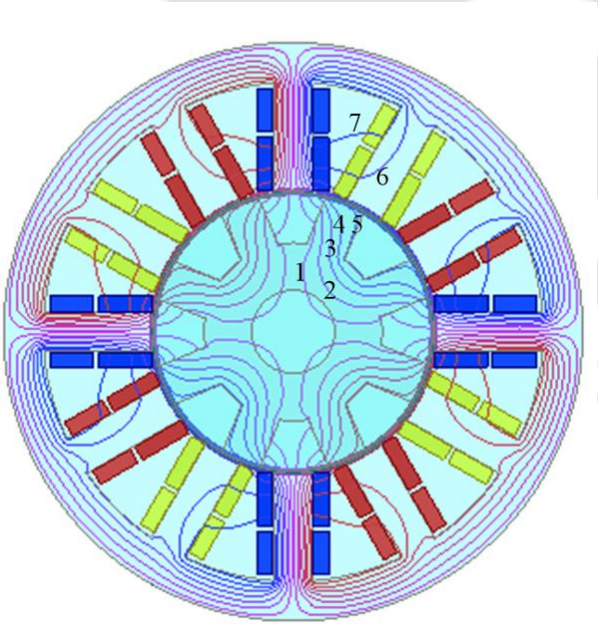

Figure 3.20: Distribution of seven flux paths for analytical calculation of unaligned inductance

$$A_{sp1} = \frac{1}{4}\left(\frac{D}{2}\beta_s h\right) = 131.28\ \text{mm}^2 \tag{3.150}$$

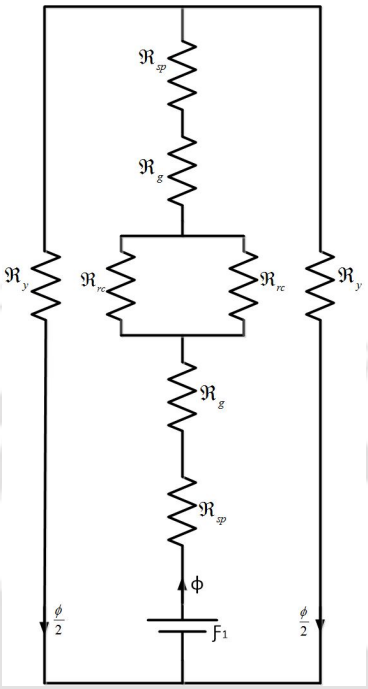

Figure 3.21: Magnetic equivalent reluctance circuit of flux tube 1

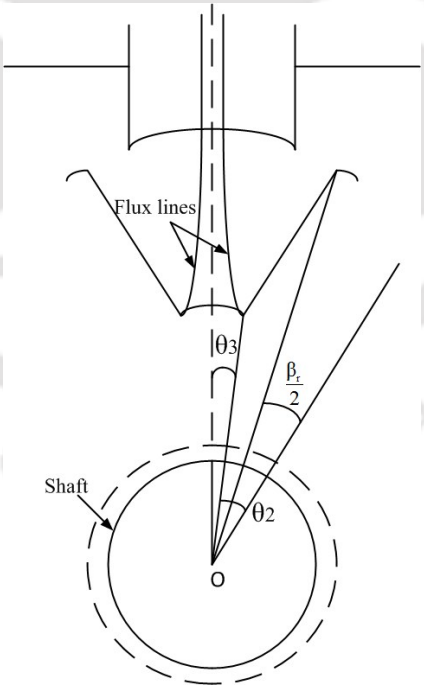

Figure 3.22: Flux path 1 in fully unaligned position

The length of the flux path in the air gap is

$$l_{g1} = \frac{D}{2} - l_g - h_r = 21.56\,\text{mm}^2 \tag{3.151}$$

where, l_g is the length of the air gap during alignment and h_r is the height of the rotor tooth. The cross section of the flux path at the rotor is obtained as follows. The arc subtended by half of the rotor pole is given by

$$\frac{\beta_{\mathrm{r}}}{2}\left(\frac{D}{2}-g\right) \tag{3.152}$$

The angle θ_2 is given as

$$\theta_2 = \frac{\frac{\beta_r\left(\frac{D}{2}-l_g\right)}{2}}{\left(\frac{D}{2}-l_g-h_r\right)} = 0.227 \text{ rad} \tag{3.153}$$

The rotor pole pitch is given by

$$\theta_{rp} = \frac{2\pi}{N_r} = 0.785\text{rad} \tag{3.154}$$

The angle θ_3 is derived as

$$\theta_3 = \frac{1}{2}\left(\frac{2\pi}{N_r}\right) - \theta_2 = \frac{\theta_{rp}}{2} - \theta_2 = 0.148 \text{ rad} \tag{3.155}$$

where, θ_{rp} is the rotor pole pitch and N_r is the number of rotor poles. The area of cross section on the rotor periphery is

$$A_{r1} = 2\theta_3\left(\frac{D}{2}-l_g-h_r\right)h = 338.521 \text{ mm}^2. \tag{3.156}$$

And the average area of cross section of flux path 1 is

$$A_{g1} = \frac{A_{sp1}+A_{r1}}{2} = 103.584 \text{ mm}^2. \tag{3.157}$$

The length of the flux path on each side of the rotor back yoke is

$$l_{ry1} = \pi\left(\frac{D_{sh}}{4}+\frac{D}{4}-\frac{l_g}{2}-\frac{h_r}{2}\right) = 46.983 \text{ mm}. \tag{3.158}$$

where, D_{sh} is the rotor shaft diameter.
The area of cross section of the rotor back yoke for the flux path 1 is

$$A_{ry1} = \left(\frac{D}{2}-l_g-h_r-\frac{D_{sh}}{2}\right)L = 700.13 \text{ mm}^2. \tag{3.159}$$

The length of the flux path in the stator is

$$l_{sp1} = h_s = 25.520 \text{ mm} \tag{3.160}$$

The length of the flux path in the stator back yoke is

$$l_{sy1} = \frac{\pi(D_o - C_s)}{2} = \frac{\pi(D + 2h_s + C_s)}{2} = 206.276 \text{ mm}, \tag{3.161}$$

where C_s is the stator back iron thickness. Its area is given by

$$A_{sy1} = C_s L = 491.84 \text{ mm}^2. \tag{3.162}$$

Thus, the mmf of flux path 1 is given by

$$F_1 = \left(2\Re_{sp1} + 2\Re_{g1} + \frac{\Re_{sy1}}{2} + \frac{\Re_{ry1}}{2}\right)\phi_1 \tag{3.163}$$

and the stator pole flux in path 1 is

$$\phi_1 = B_s.A_{sp1} \tag{3.164}$$

The reluctance of the stator pole is

$$\Re_{sp1} = \frac{l_{sp1}}{\mu_0 A_{sp1}} = 1.49 \times 10^5 \tag{3.165}$$

Similarly, the reluctances of the air gap, rotor yoke and the stator yoke are given as

$$\Re_{g1} = \frac{l_{g1}}{\mu_0 A_{g1}} = 1.657 \times 10^5 \tag{3.166}$$

$$\Re_{ry1} = \frac{l_{ry1}}{\mu_0 A_{ry1}} = 5.35 \times 10^4 \tag{3.167}$$

$$\Re_{sy1} = \frac{l_{sy1}}{\mu_0 A_{sy1}} = 3.339 \times 10^5 \tag{3.168}$$

The inductance contributed by the flux path 1 at unaligned position is thus calculated as,

$$L_{u1} = \frac{F_1 B_s A_{sp1}}{i_p^2} = 0.242 \text{ mH}. \tag{3.169}$$

Flux path 2: For calculating the length and area of flux path 2, let us consider

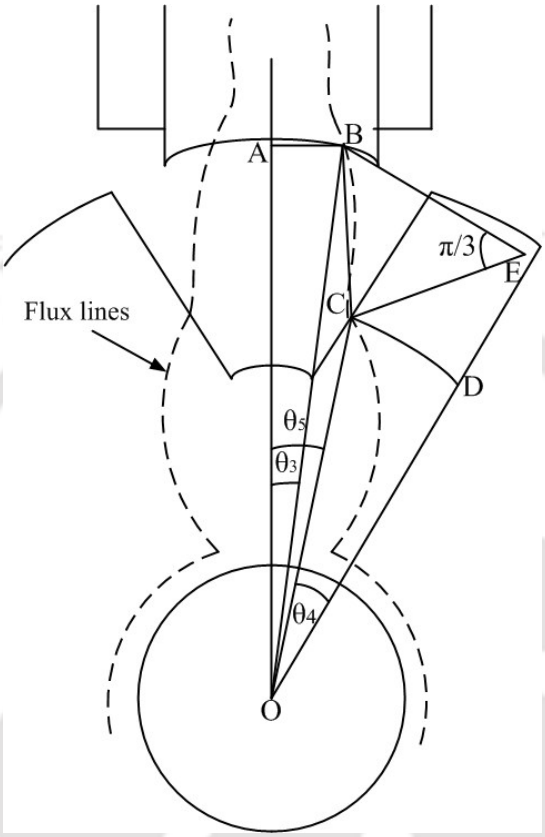

Figure 3.23: Flux path 2 in fully unaligned position

the diagram as shown in Figure 3.23, where the broken lines represent the flux lines. Considering the length of the flux path 2 through the air gap as the arc BC, it can be calculated by finding the chord length BC and using this as a radius by constructing an equilateral triangle BCE. D is a point on the rotor to compute the angle subtended by the arc at the centre. Point D is used to determine the co-ordinates of point C and thus determine the length of the arc BC.

The area of the flux path at stator pole is given as

$$A_{sp2} = \frac{\beta_s}{4}\frac{D}{2}h = 65.676 \text{ mm}^2 \tag{3.170}$$

and the area of the path at rotor pole is

$$A_{rp2} = \frac{h_r}{4}h = 178.08 \text{ mm}^2. \tag{3.171}$$

The area of cross section of the flux path is thus calculated as

$$A_{g2} = \frac{A_{sp2} + A_{rp2}}{2} = 121.878 \text{ mm}^2. \tag{3.172}$$

The length of flux path in stator pole is given as

$$l_{sp2} = h_s = 25.52 \text{ mm}. \tag{3.173}$$

The length of the flux path in rotor pole is given as

$$l_{rp2} = \frac{h_r}{4} = 3.36 \text{ mm}. \tag{3.174}$$

The length and area of the cross section of the flux path in rotor back are

$$l_{ry2} = l_{ry1} = 46.982 \text{ mm} \tag{3.175}$$

$$A_{sy2} = A_{sy1} = 491.84 \text{ mm}^2. \tag{3.176}$$

From Figure 3.23, let us consider the length of flux path 2 to be the arc BC. By assuming that the center of the shaft is origin (0,0), the length of BC is computed as

$$OB = \frac{D}{2} = 35.5 \text{ mm}, \tag{3.177}$$

$$\theta_3 = \frac{\beta_s}{4} = 0.0698 \text{ rad}. \tag{3.178}$$

The coordinates of B (x_1,y_1) are

$$(x_1, y_1) = \left[\frac{D}{2}\sin(\theta_3), \frac{D}{2}\cos(\theta_3)\right] = (2.476, 35.413), \tag{3.179}$$

The coordinates of C (x_2, y_2) are

$$OD = \left(\frac{D}{2} - l_g - \frac{3}{4}h_r\right) = 24.92 \text{ mm}, \tag{3.180}$$

$$CD = \left(\frac{D}{2} - l_g\right)\frac{\beta_r}{2} = 5.152 \text{ mm}, \tag{3.181}$$

$$\theta_4 = \frac{CD}{OD} = 0.207\,\text{rad}, \tag{3.182}$$

$$\theta_5 = \frac{\theta_{rp}}{2} - \theta_4 = 0.128\,\text{rad}, \tag{3.183}$$

$$(x_2, y_2) = [OD\sin(\theta_5), OD\cos(\theta_5)] = (3.187, 24.715). \tag{3.184}$$

The chord BC is then given as

$$BC = \sqrt{(x_2 - x_1)^2 + (y_2 - y_1)^2} = 12.104\,\text{mm}. \tag{3.185}$$

Then, the length of the flux in path 2 may be considered as an arc BC. Thus,

$$l_{g2} = ArcBC = [BC]\left(\frac{\pi}{3}\right) = 12.675\,\text{mm} \tag{3.186}$$

The magnetic circuit equation for the flux path 2 is given by

$$F_2 = [2(\Re_{sp2} + \Re_{g2} + \Re_{rp2}) + \Re_{ry2} + \Re_{sy2}]\phi_2. \tag{3.187}$$

The corresponding reluctances are given as

$$\Re_{g2} = \frac{l_{g2}}{\mu_o A_{g2}} = 8.2766\text{e} \times 10^4 \tag{3.188}$$

$$\Re_{sp2} = \frac{l_{sp2}}{\mu_o A_{sp2}} = 3.0922\text{e} \times 10^4 \tag{3.189}$$

$$\Re_{rp2} = \frac{l_{rp2}}{\mu_o A_{rp2}} = 1.5015\text{e} \times 10^4 \tag{3.190}$$

$$\Re_{ry2} = \frac{l_{ry2}}{\mu_o A_{ry2}} = 5.3402\text{e} \times 10^4 \tag{3.191}$$

$$\Re_{sy2} = \frac{l_{sy2}}{\mu_o A_{sy2}} = 3.3375\text{e} \times 10^5 \tag{3.192}$$

Thus, the inductance offered by flux path 2 is given by

$$L_{u2} = F_2 \frac{B_s A_{sp2}}{i_p^2} = 0.252\,\text{mH}, \tag{3.193}$$

Flux path 3: An enlarged view of the flux path 3 is shown in Figure 3.24. It is

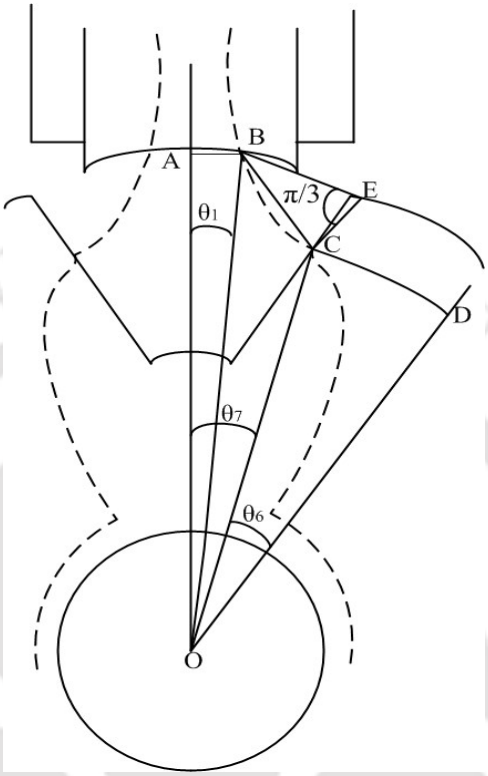

Figure 3.24: Flux path 3 at fully unaligned position

assumed that the width of the flux path is over an arc of 3/32 (β_s) in the stator. The step by step calculations of the flux path in the stator and rotor are not derived further in this section. Thus, the unaligned inductance is calculated as

$$L_{u3} = F_3 \frac{B_s A_{sp3}}{i_p^2} = 0.1206\text{mH}, \tag{3.194}$$

Flux path 4: Figure 3.25 shows the flux path 4 which leaves the stator at the tips and assumed to enter at 7/8(h_r) from the rotor pole. The inductance of this flux path 4 is given by

$$L_{u4} = F_4 \frac{B_s A_{sp4}}{i_p^2} = 0.173\text{mH}, \tag{3.195}$$

Flux path 5: Figure 3.26 shows the flux path 5 and is assumed to have a width of 3/16(h_s) on the exit at the stator pole and is confined to one eighth of the rotor pole arc. The unaligned inductance is thus given as

$$L_{u5} = F_5 \frac{B_s A_{sp5}}{i_p^2} = 0.1477\text{mH}, \tag{3.196}$$

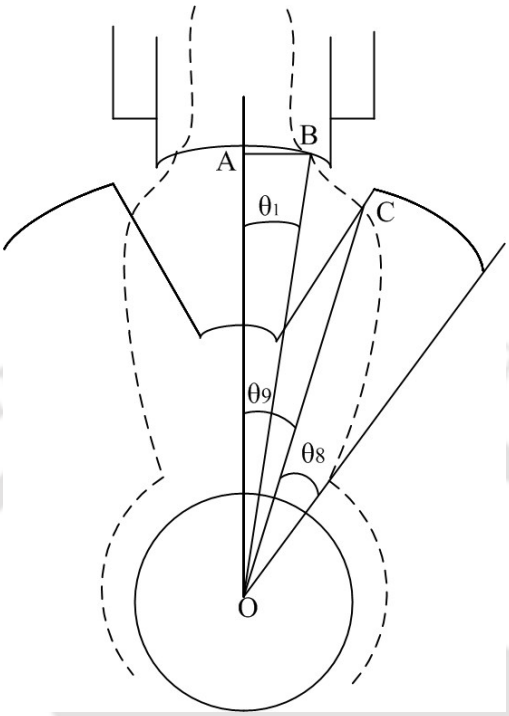

Figure 3.25: Flux path 4 at fully unaligned position

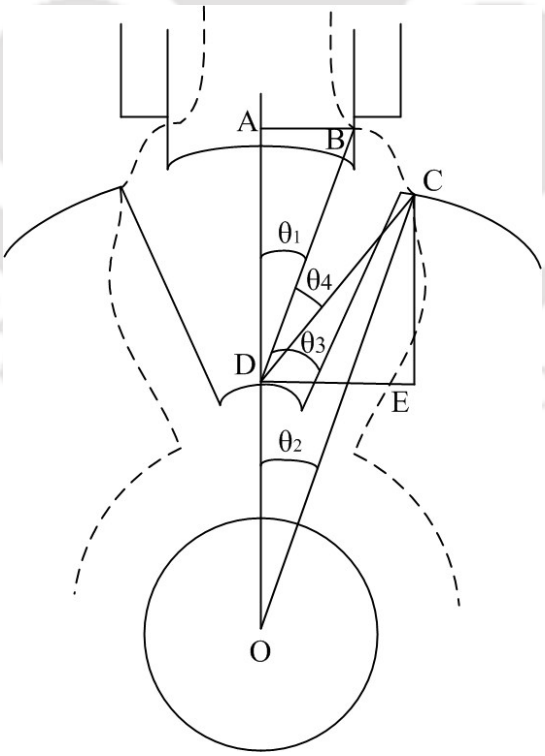

Figure 3.26: Flux path 5 at fully unaligned position

Flux path 6: The flux path as shown in Figure 3.27 can be assumed to be an arc

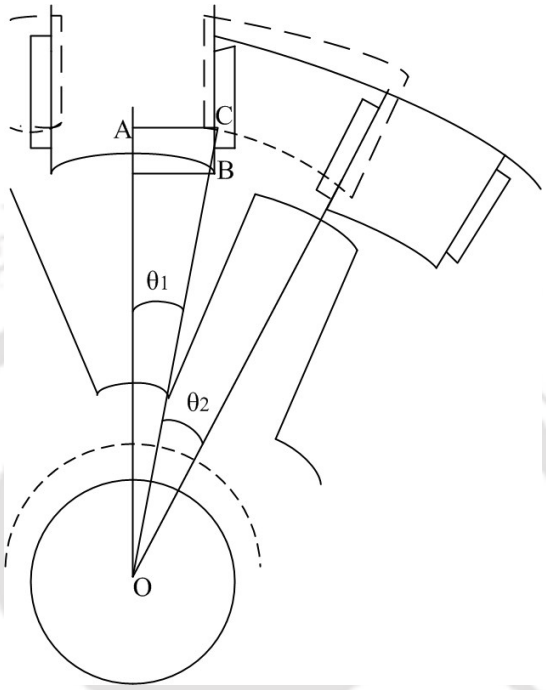

Figure 3.27: Flux path 6 at fully unaligned position

centered at the center of the shaft. The inductance is calculated as

$$L_{u6} = F_6 \frac{B_s A_{sp6}}{i_p^2} = 0.2112\text{mH}, \tag{3.197}$$

Flux path 7: For the calculation of flux path 7, the flux path is centered at B with a

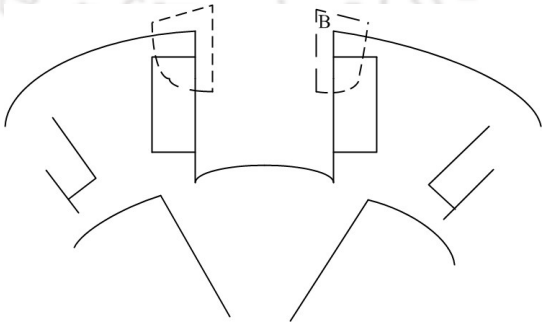

Figure 3.28: Flux path 7 at fully unaligned position

radius of $(h_s/4)$ and an angle of $(\pi/2)$.

The unaligned inductance of flux path 7 is calculated as

$$L_{u7} = F_7 \frac{B_s A_{sp7}}{i_p^2} = 0.229\text{mH}, \tag{3.198}$$

The unaligned inductance is finally obtained by the twice of the sum of all the inductances of flux paths 1 to 7 and it is given by

$$L_u = L_{u1} + 2(L_{u2} + L_{u3} + L_{u4} + L_{u5} + L_{u6} + L_{u7}) = 2.51\text{mH}. \tag{3.199}$$

3.6 Design verification of the BCW SRM under rated condition

A FE model is developed in the commercial software package, Ansoft Maxwell 2D for the prototype designed in Section 3.5. The parameters of the motor are specified in Table 3.2 and Table 3.3. The finite element mesh is constructed with 5574 elements and 11148 nodes as shown in Figure 3.29. The model is constructed with a moving air gap which allows a parametric simulation for a given current for different rotor position.

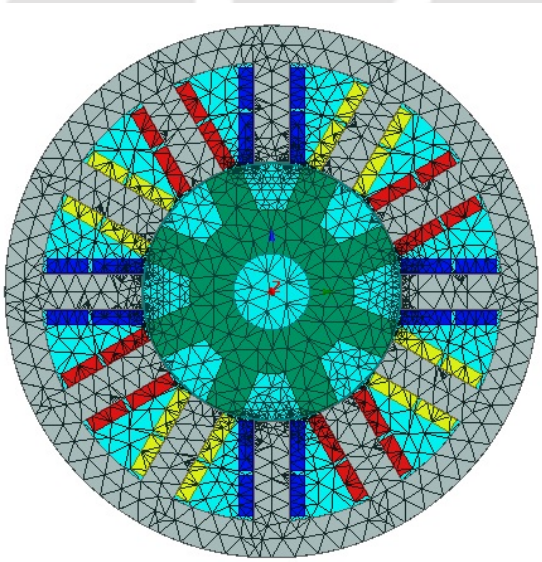

Figure 3.29: Finite element mesh of 12/8 BCW BSRM

A simulation is conducted for varying rotor currents for different rotor positions for obtaining the flux linkage (λ) characteristics and inductance (L) from the FE model. The plot of flux linkage vs. current and inductance vs. current for different rotor positions is shown in Figure 3.30 and Figure 3.31. The simulation is conducted by exciting the stator

coils from an unaligned rotor position to an aligned position. It can be observed that the FEM value of aligned inductance at rated current of 10 A is closer to the analytical value obtained. However, the analytical value of the unaligned inductance slightly varies with the FEM result. This is basically due to the assumptions made in the mathematical modelling of the flux paths at the unaligned position. Figure 3.32 shows the complete rotational torque profile of the motor for different currents from FE analysis. It can be observed that at 10 A of current, the maximum torque obtained at an overlapped rotor position is around 4.65 Nm which is close to the required torque at rated current.

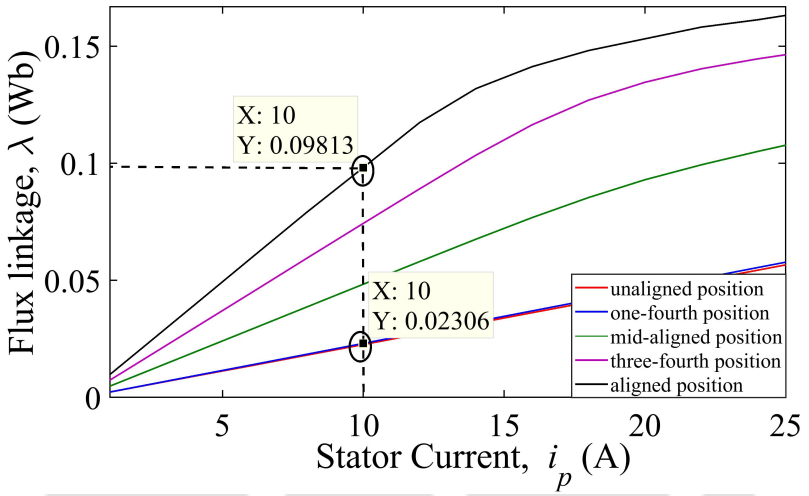

Figure 3.30: Flux linkage characteristics for varying stator current and rotor angle

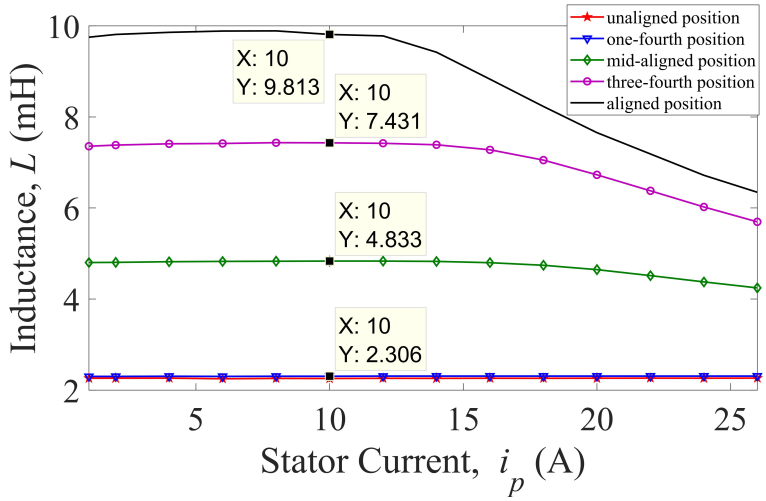

Figure 3.31: Inductance plot for various stator current at varying rotor position

In order to verify the motor design, it is necessary to analyze the performance of the motor and determine the operational limit of the motor. The maximum flux density is

Table 3.4: Comparison of inductance by various methods

Rated Phase current, i_p (A)	Aligned inductance, L_a		Unaligned inductance, L_u	
	Analytical result	FEM result	Analytical result	FEM result
10A	9.64 mH	9.813 mH	2.51 mH	2.306 mH

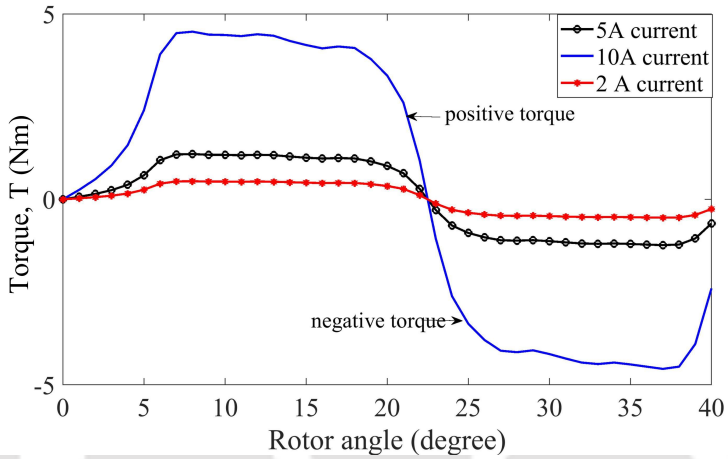

Figure 3.32: Torque profiles of a 12/8 BCW BSRM for varying current

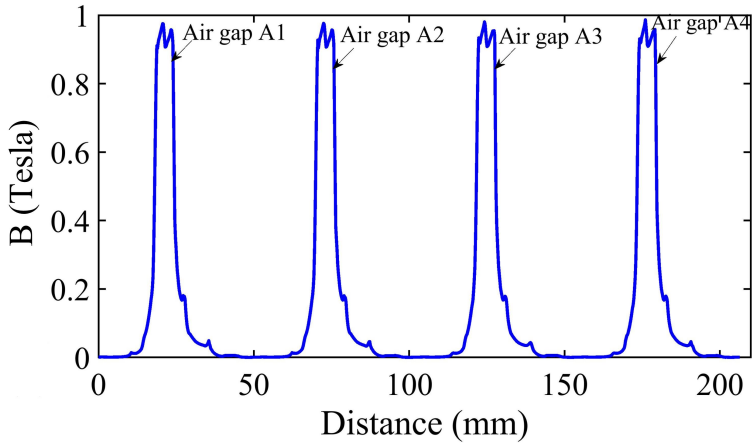

Figure 3.33: Magnetic field density at rated current of 10 A

taken as the knee point of the B-H curve of the material M-19 which is 1.5 T and since the maximum rated current is kept as 10 A, an effort is made to analyze the magnetic field density (B) of the motor for every rotational position such that magnetic saturation

does not occur. The coils of one phase comprise of the four air gaps, $A1$, $A2$, $A3$ and $A4$. The magnetic field density is plotted over the circumference of the air-gap in Figure 3.33. It is observed that the peak magnetic field density is less than the maximum flux density and the motor can operate at a rated current of 10 A.

3.7 Distribution of slot area for torque and radial force in BCW BSRM

The conventional BSRM design consists of two sets of winding embedded in the stator slots. Using separate winding in each stator tooth consumes an additional space for levitation winding. In separate winding scheme, each tooth comprises of two coils where one set of coil is utilized for torque and the other for levitation. The current for torque production flows through one coil and the current for levitation flows through the other coil per slot. It results in the reduction of effective torque as the entire slot area cannot be used for torque production. The distribution of slot area in dual winding scheme is fixed from the perspective of required radial force, hence a compromise is made in the generation of torque while producing levitation forces. However, in BCW scheme the entire slot area can be utilized either for torque or radial force as each of the coils carry the main current and the levitation current.

Assuming that the main current and the bridge current get divided into two equal

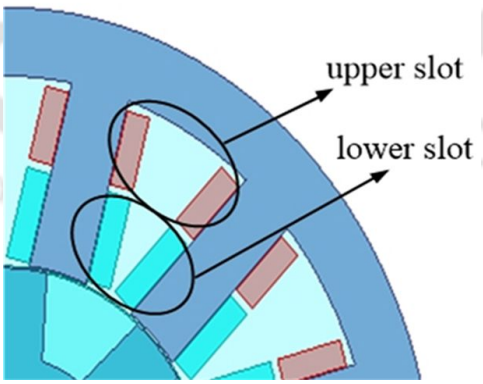

Figure 3.34: Slot areas for two layer of coils for BCW BSRM

halves in each coil, the slot area of BSRM with bridge winding can be approximated as

$$\begin{aligned} A_{s(total)} &= A_{s1} + A_{s2} \\ &= \frac{N}{J}\left(\frac{i_m}{2} + \frac{i_b}{2}\right) + \frac{N}{J}\left(\frac{i_m}{2} + \frac{i_b}{2}\right) \\ &= \frac{N}{J}\left(i_m + i_b\right) \end{aligned} \tag{3.200}$$

where, J is the current density, $A_{s(total)}$ is total slot area, A_{s1} is the slot area for the upper layer of coils and A_{s2} is the slot area for lower layer of coils.

From Equation 3.200 it can be observed that in bridge winding configuration, the entire portion of slot area is responsible in carrying the torque producing main current and radial force producing bridge current, thus utilizing the total slot area for radial force production without any loss in torque production for same number of turns. It has to be kept in mind that for radial force production using BCW, both the main current and bridge current are required and for only torque production the main current is required. In order to verify the concept, a comparative FE analysis is done between separate set winding and BCW in section 3.9.

3.8 Verification of the analytical model of BSRM with BCW using finite element modelling

With the parameters listed as in Table 3.2 and Table 3.3, a FE model is designed for BCW BSRM and verified with the mathematical model of torque and radial force as obtained in Section 3.3. The FE model is designed in Ansoft Maxwell 2D and is analyzed considering zero displacement of the rotor and shaft. Initially, the analytical model which is developed using virtual work method in Section 3.3.1 and section 3.3.2 is verified using FE model. Subsequently the analytical model using Maxwell's stress tensor method as given in Section 3.3.3 is verified with the FE model. The coils of phase-A are excited with a constant main current, i_m of 6 A. A bridge current, i_{b1} of 1 A is applied in coils of $A1$ and $A3$ and bridge current, i_{b2} of 2 A in coils of $A2$ and $A4$. The number of turns in each coil is taken as 40. Thus, the total ampere turns in the stator pole of air gap $A1$ is taken as 280 AT, $A3$ is 200 AT, $A2$ is 320 AT and in $A4$ is 160 AT.

With the difference in magnitude of current in air gaps A1, A2, A3 and A4,the magnetic field density changes and is shown in Figure 3.35. Figure 3.36 (a) and (b) shows the contour of magnetic field density in overlapped position and aligned rotor positions when main current i_m, bridge currents i_{b1} and i_{b2} are supplied in the coils of phase-A. In this analysis, the overlapped position is the turn-on angle position and considered as -15^0 and the aligned position is the turn off angle which is considered as 0^0. The conduction angle is fixed as 15^0 per phase. The magnetic field density is higher in the region of air gaps, $A1$ and $A2$, resulting in radial forces F_x and F_y. A comparative analysis is done to verify the methods used in mathematical modelling of the motor.

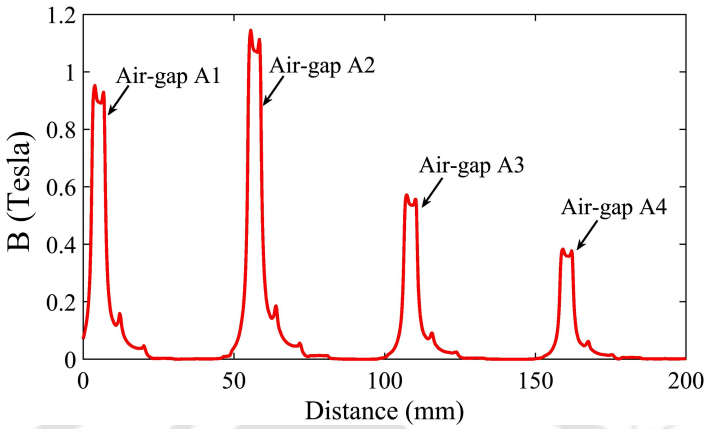

Figure 3.35: FE results of magnetic field density in air gaps of phase-A

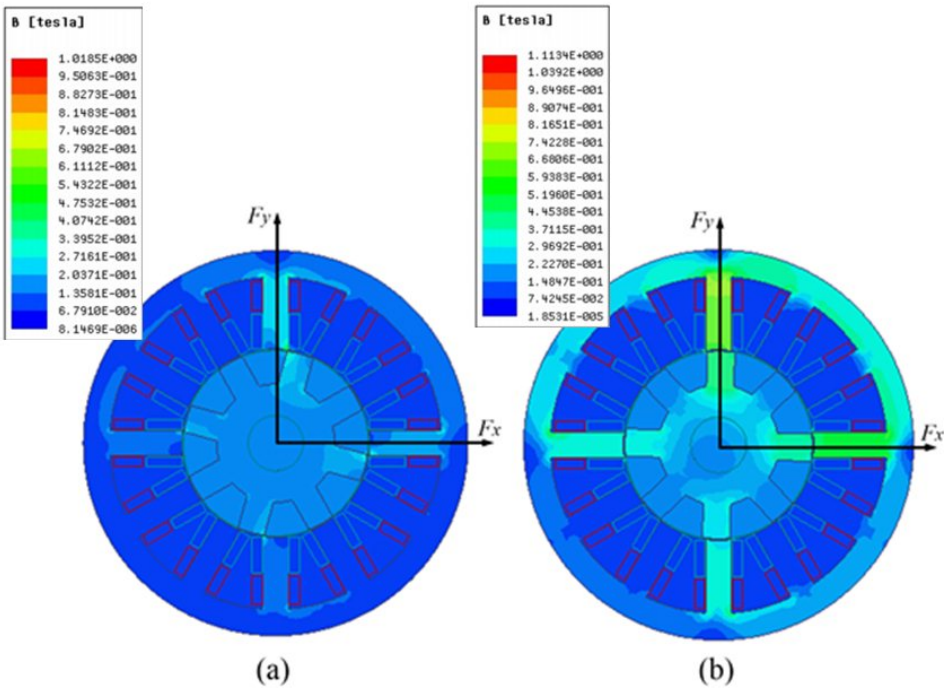

Figure 3.36: Magnetic field density plot at (a) overlapped position, $\theta = -15^0$ (b) aligned position, θ=0^0

In the virtual work method, as derived in Section 3.3.1, it is important to evaluate the value of k to determine the shape of the elliptical flux path. A relationship between k and t is obtained from the FE simulation by varying the rotor position. k is again a function of t/l_g and is obtained as shown in Figure 3.38. This relation between k and t/l_g gives a constant a which is used to obtain the fringing permeance model. The value of a is incorporated in the Equation 3.21 to calculate the radial force and torque. The

value of a is the slope of the Equation 3.13 and is obtained from the relation of l/l_g and t/l_g as shown in Figure 3.39. The value of a is obtained as 1.25.

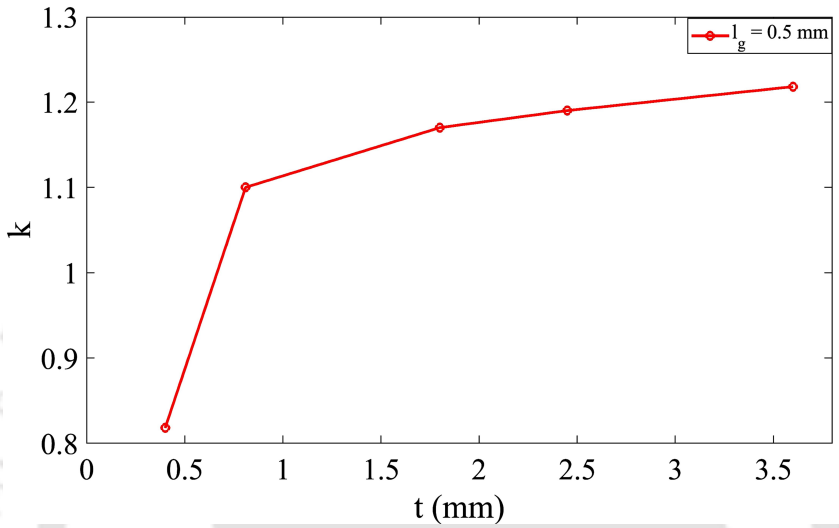

Figure 3.37: Relationship between k and t

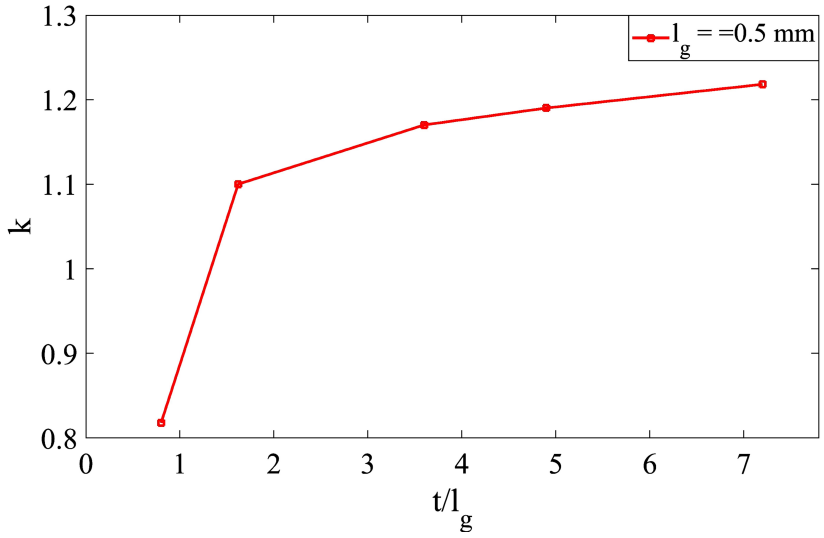

Figure 3.38: Relationship between k and t/l_g

Figure 3.40 (a) and (b) show the plots of radial force F_x versus rotor angle obtained from virtual work method and Maxwell stress tensor method using analytical solution and FE simulation. Similar plots have been obtained for radial force F_y and torque in Figures 3.41 and Figure 3.42, respectively. It can be observed that the analytical and the FE results are consistent. Because of more accurate modelling of air gap permeance using virtual work method, the analytical and FE results of radial force are much closer

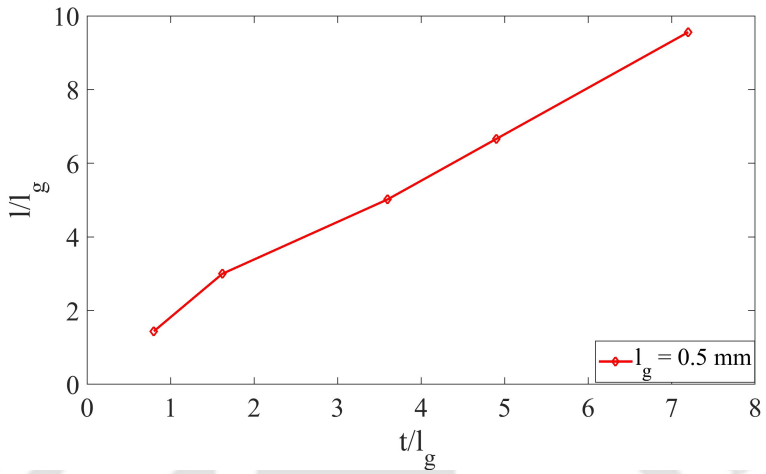

Figure 3.39: Relationship between l/l_g and t/l_g

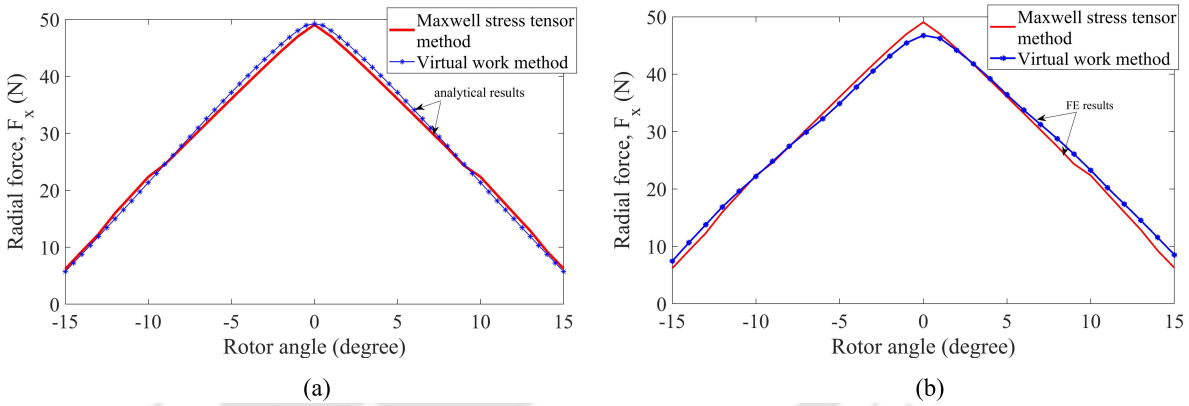

Figure 3.40: Comparison of radial force F_x obtained by virtual work method and Maxwell stress tensor method using (a) analytical solution and (b) FE simulation.

in virtual work method. Due to requirement of a FE model for predicting the shape constant value of flux path, the Maxwell stress tensor model is found to be more suitable in developing the analytical model.

The analytical model considering magnetic saturation in section 3.3.2 is verified with the FE model.The permeances in the four gaps comprises of a term 'c' which is responsible in determining the shape of the flux in the linear region and the saturated region. In order to know the value of c in linear and nonlinear regions, FE simulation is done for mmf values ranging from 600 AT to 1800 AT. Figure 3.43 shows the relationship between mmf and c at an overlapped position of the rotor and the stator.

From Figure 3.43 it can be observed that c has a constant value of 1.18 for mmf

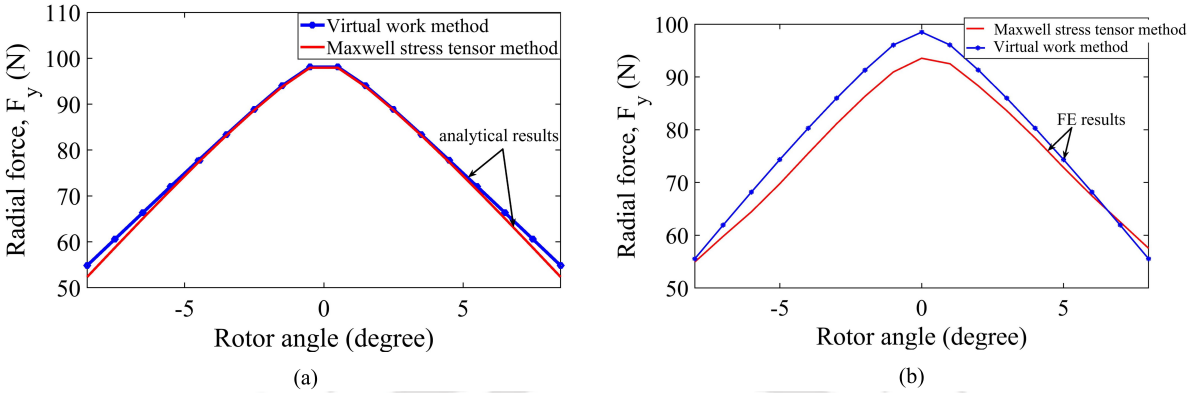

Figure 3.41: Comparison of radial force F_y obtained by virtual work method and Maxwell stress tensor method using (a) analytical solution and (b) FE simulation.

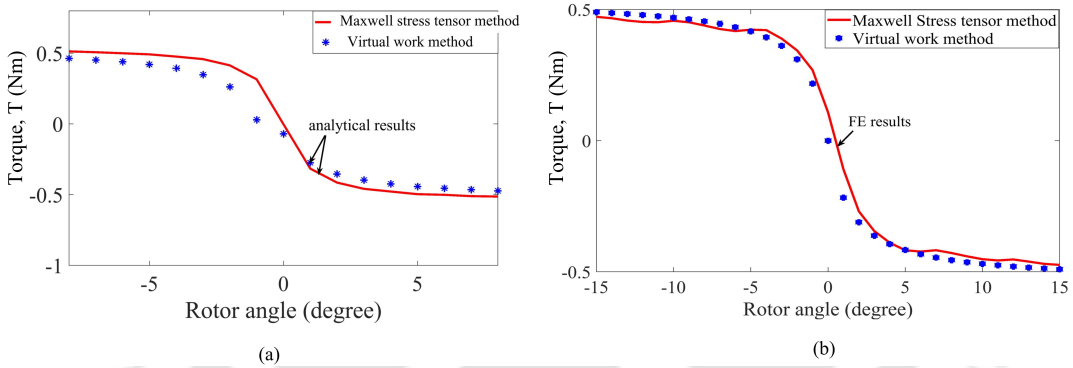

Figure 3.42: Comparison of torque obtained by virtual work method and Maxwell stress tensor method using (a) analytical solution and (b) FE simulation.

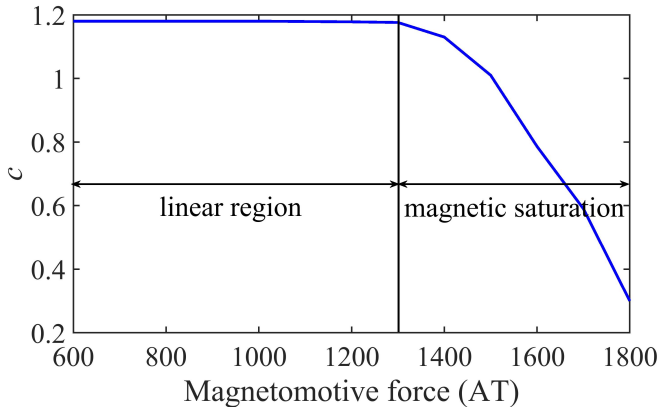

Figure 3.43: Relationship of magnetomotive force (mmf) and 'c'

between 600 AT to 1300 AT showing the region of linearity. However, with further increment of mmf the value of c decreases sharply, thus indicating the region of magnetic

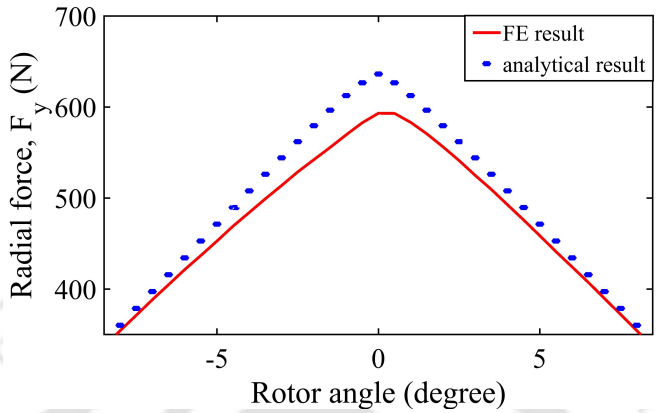

(a)

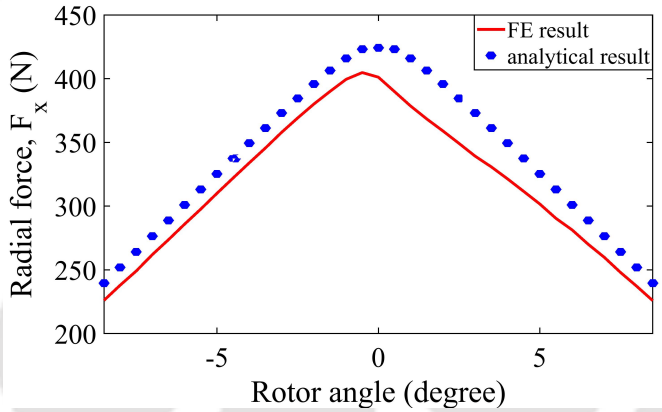

(b)

Figure 3.44: Analytical and FEA results of radial forces, (a) F_x and, (b) F_y under magnetic saturated condition

saturation. Thus, it can be stated that, the model developed shows linearity upto 1300 AT of mmf and becomes non-linear after 1300 AT. The value of c lower than 600 AT also shows linear profile, hence is not plotted in Figure 3.43. In the present study the value of c is taken as 0.95, predicted from the nonlinear region of the model. The value of c is selected as 0.95 such that it satisfies the mathematical relations of force and torque as given in Equation 3.78, Equation 3.79 and Equation 3.80.

For the production of radial forces, a magnetomotive force of 1500 AT in x-direction and 1600 AT in y-directional coils of phase-A are supplied. With this supply of mmf, the motor goes into saturation region as obtained from the FE model. The radial forces' profile obtained from FE analysis are in close match with the one obtained from the analytical model as shown in Figure 3.44(a) and Figure 3.44(b). It can be observed form Figure 3.45 that, the torque profile obtained from the analytical method considering

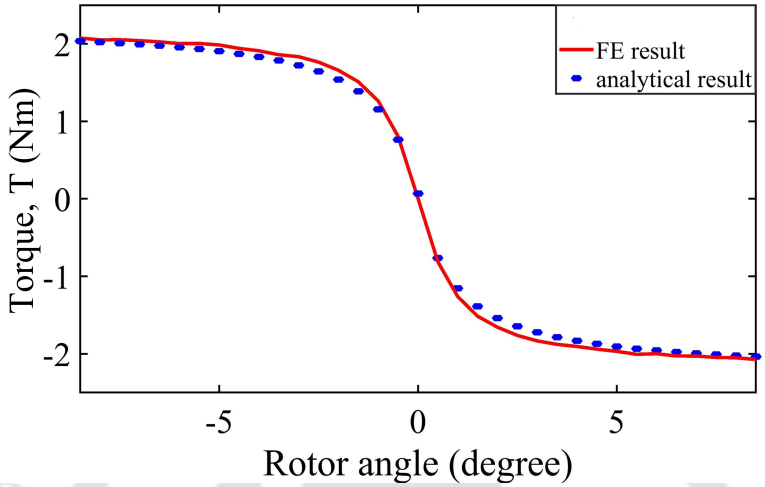

Figure 3.45: Torque profile under magnetic saturation condition

magnetic saturation, are in good agreement with the FE results obtained.

3.9 Comparative analysis of BCW and separate set of winding

From the theory of BCW, the same winding can produce torque and radial forces without requiring additional winding for radial force production. This is advantageous over the existing separate winding scheme as established by Takemoto *et al*. The BCW is capable of producing radial force using low value of bridge current as both the motor main current, i_m and the bridge currents, i_{b1} and i_{b2} flow thorough all the coils in each phase winding. In BCW scheme, without the supply of bridge currents, the motor can operate as a normal torque producing motor. However, in case of separate winding in BSRM, the motor main current flows through the main winding for torque and the suspension currents flow through another set of suspension windings as shown in Figure 3.46. As a result, all the coils per slot per phase are not utilized for torque and it compromises in the torque production. This requires increment in the main current to produce the required torque. In order to establish the concept, a comparative analysis is done between the separate set of winding and the BCW. A FE simulation is done to compare the analysis.

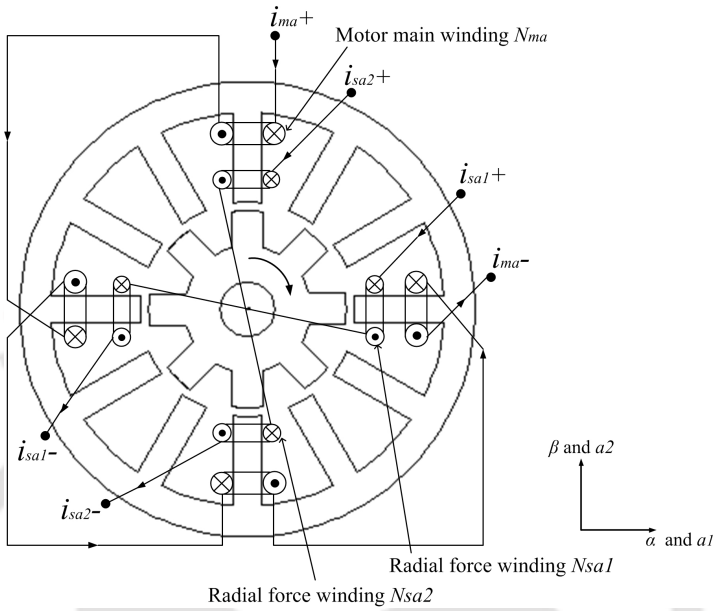

Figure 3.46: Phase-A winding configuration for separate set of windings [9].

3.9.1 Comparison of torque and radial forces

In order to validate the concept of utilization of the slot area for effective torque and force production using bridge winding scheme, a FE analysis is done between separate set winding and BCW. For separate set winding, the number of turns per coil for is assumed as $N_m = 40$ and for radial force $N_s = 40$. The main current and levitation currents are considered as, $i_m = 6$ A, $i_{s1} = 1$ A and $i_{s2} = 2$ A. For the bridge winding, the number of turns per coil is also assumed as N = 40 and the main current and bridge currents as $i_m = 6$ A, $i_{b1} = 1$ A and $i_{b2} = 2$ A.

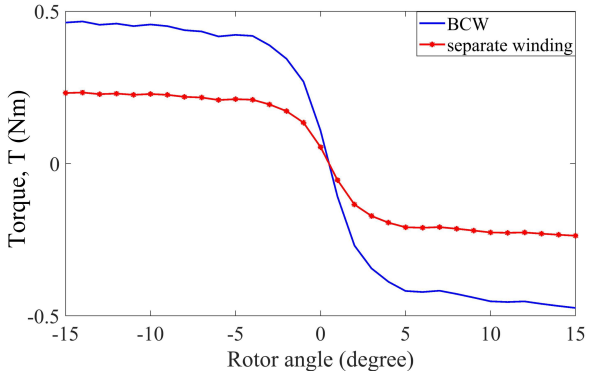

Figure 3.47: Comparison of torque for BCW and separate set of winding

From the results obtained as shown in Figure 3.48(a) and Figure 3.48(b) it can be

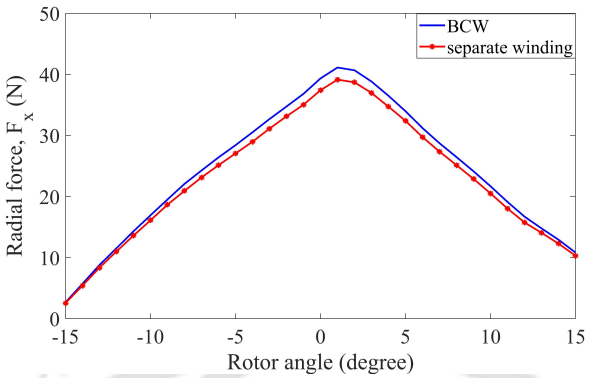

(a)

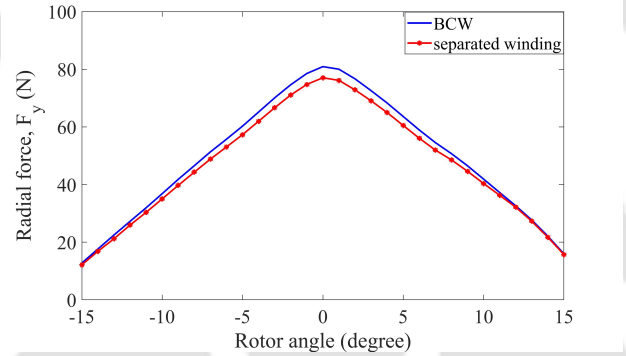

(b)

Figure 3.48: Comparison of radial forces, (a) F_x and (b) F_y for BCW and separate set of winding

observed that there is very less significant change in the radial forces by separate winding and BCW. A small increment is observed in the peak value of F_x and F_y. However, it can be observed from Figure 3.47 that with the same amount of current in phase-A, the torque obtained from BCW shows a 50 % increment than that produced using separate set winding. Thus, the concept of utilization of the total slot area for substantial amount of torque and radial force production using BCW is justified. This topology proves to be an effective design for applications where BSRMs with high torque production are in demand.

3.9.2 Comparison of copper losses

The copper losses can be analytically obtained and compared between the separate set winding and BCW. For bridge configured winding, assuming that each coil carries

both i_m and i_{b1} for levitation, the copper loss is calculated as,

$$P_{cu(ph)} = {I_{(ph)}}^2 R_{s(ph)} \tag{3.201}$$

where, $I_{(ph)}$ is the total current flowing in the phase winding and $R_{s(ph)}$ is the equivalent phase resistance.

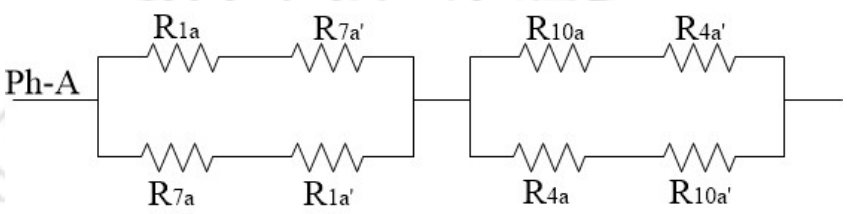

Figure 3.49: Equivalent resistive circuit of phase-A for BCW

For number of turns as 40 the effective DC resistance of each coil is calculated as

$$R_s = \frac{N\rho l_c}{A_{(c)}} = \frac{40 \times 1.68 \times 10^{-8} \times 1}{1.3 \times 10^{-6}} = 0.5\,\Omega. \tag{3.202}$$

where, ρ is the resistivity of copper, l_c is the length of the conductor and A_c is the area of the conductor. The equivalent resistance in phase-A is given as

$$\begin{aligned} R_{s(ph)} &= [(R_{1a} + R_{7a'}) \| (R_{7a} + R_{1a'})] + \\ &\quad [(R_{10a} + R_{4a'}) \| (R_{4a} + R_{10a'})] \\ &= 1\,\Omega. \end{aligned} \tag{3.203}$$

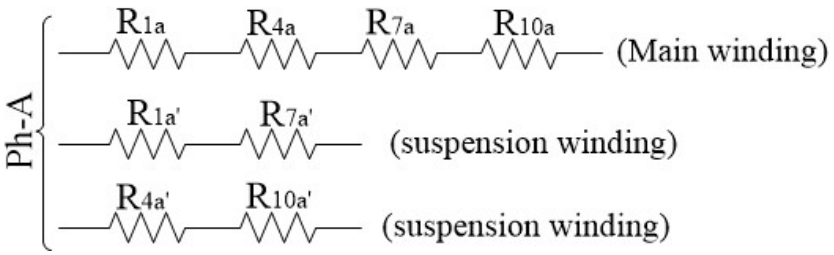

Figure 3.50: Equivalent resistive circuit of Phase-A for dual set of winding

For separate set of winding, the upper layer of coil is considered for motor winding and the lower layer of coils for the levitation winding. The number of turns N_1, in upper coil is taken as 40 and the lower coil N_2 as 40. The effective resistance of each upper

and lower coil is given as

$$R_{s1} = \frac{N_1 \rho l_c}{A_{(c)}} = \frac{40 \times 1.68 \times 10^{-8} \times 1}{1.3 \times 10^{-6}} = 0.5\,\Omega \tag{3.204}$$

$$R_{s2} = \frac{N_2 \rho l_c}{A_{(c)}} = \frac{40 \times 1.68 \times 10^{-8} \times 1}{1.3 \times 10^{-6}} = 0.5\,\Omega \tag{3.205}$$

In separate set winding, the upper coils are connected in series to form the motor winding and the lower coils are connected in series separately, hence, the equivalent resistance of the motor winding and levitation winding per phase is given as

$$\begin{aligned} R_{s1(eq)} &= R_{1a} + R_{4a} + R_{7a} + R_{10a} \\ &= 2\,\Omega. \end{aligned} \tag{3.206}$$

$$R_{s2(eq)} = R_{1a'} + R_{7a'} = 1\,\Omega. \tag{3.207}$$

Thus, the copper loss can be given as

$$P_{cu(ph)} = ({I_m}^2 R_{s1(eq)} + {I_s}^2 R_{s2(eq)}) \tag{3.208}$$

For the BCW, the values of main current, i_m is taken within the range of 0-6 A and

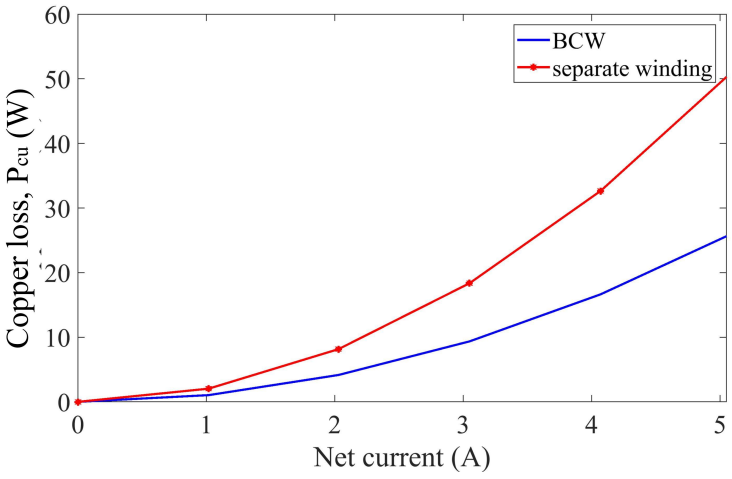

Figure 3.51: Comparison of copper losses between BCW and separate set of winding

bridge current i_{b1} taken as 0-1 A and the sum of i_m and i_{b1} is taken as i current as given in Equation 3.201. For the separate winding, the corresponding values of main current

I_m and suspension current I_s are taken as 0-6 A and 0-1 A respectively. The copper loss is calculated for varying currents in the coil and the result is plotted as shown in Figure 3.51. It is evident from Figure 3.51 that for a given performance of the motor, the copper loss in separate set of winding is found to be more pronounced than the proposed BCW scheme. This analysis makes the BCW a noteworthy approach for the design of BSRM.

3.10 Summary

In this chapter, a special stator winding called bridge configured winding has been introduced for SRM which has the ability to produce both torque and radial forces within the same stator winding, unlike the additional use of separate winding scheme for bearingless motors or active magnetic bearing for levitation purpose. Initially, the chapter develops a procedure for analytically developing a mathematical model in order to predict the behavior of the motor with the main torque producing current and the bridge currents supplied. The relationships of the electromagnetic torque and radial forces with the main current and bridge currents have been derived in order to develop a closed loop stable operation of the motor system. In order to implement the winding configuration for both torque and radial force production, the dimensions of the rotor are obtained from an existing 8 pole rotor of an SRM in the laboratory. With reference to the dimensions of the rotor, a stator having 12 pole is designed and a step-by-step design procedure is considered for the development of a prototype for the motor. A 12/8 SRM of rated power of 750 W and rated speed of 1500 rpm is designed and modelled following the IEC 60032 [93] standard techniques of designing a motor. The design verification using analytical and FE analysis has been discussed in detail. A detailed analytical technique has been described for calculation of aligned and unaligned inductance of the designed prototype. Finite element analysis has been used to verify the design for rated operation. The analytical techniques to calculate inductance gives a 8-10% error in unaligned inductance value when compared with FE results. FE analysis is further done for verification of the mathematical model of the BCW BSRM. The results obtained are close to the analytical results. Further down, a comparative analysis is done between BCW and separate set winding, which shows the effective utilization of the entire slot area for torque and force production in case of BCW BSRM. A comparison of copper loss between BCW and separate set winding is also presented in this chapter.

भारतीय प्रौद्योगिकी संस्थान गुवाहाटी
Indian Institute of Technology Guwahati

Chapter 4

Modelling and Simulation of a Drive System for BSRM with BCW

Contents

4.1 Introduction

In the previous chapter, the characteristics of radial force and torque production in SRM with BCW have been studied and analyzed under static conditions. However, SRM in practical is operated by a power electronic converter circuit. The drive system of SRM consists of mainly four basic components viz. power converter, control logic circuit, position sensor and motor. The torque producing main current consist of a current controller which controls the torque of the motor. Along with the torque control the speed is also controlled from the derivative of the rotor angular position. However, for the levitation control, two control loops are necessary to control the rotor's radial position in both horizontal and vertical direction using current controllers. Figure 4.1 shows a general block diagram of a BSRM drive.

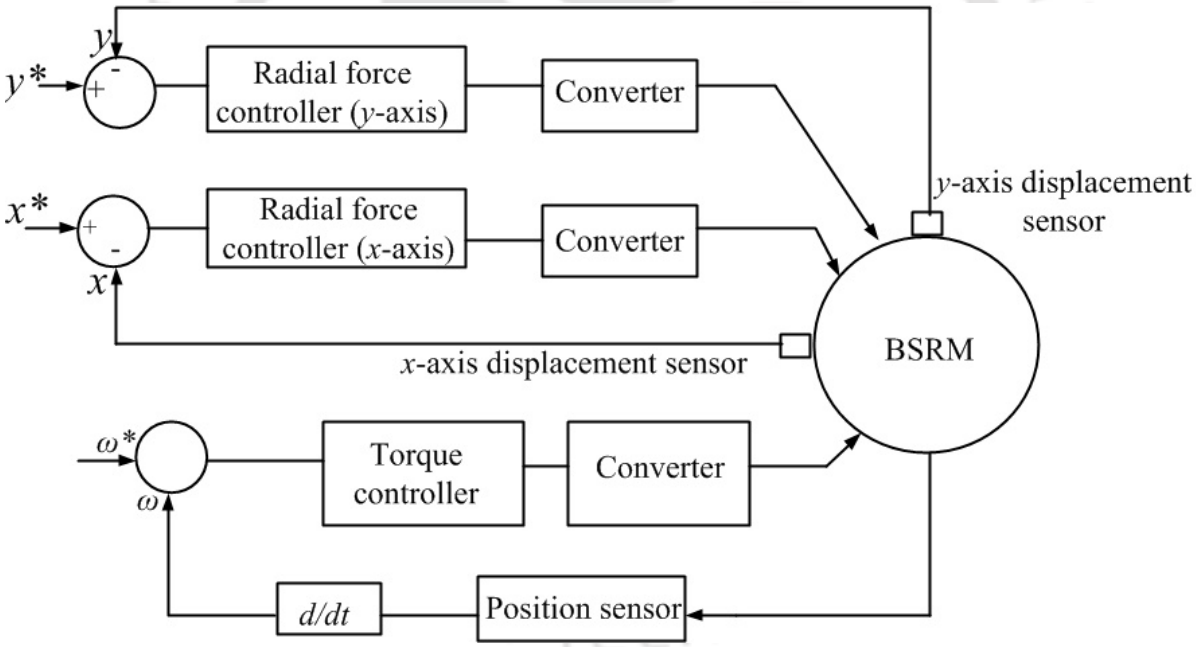

Figure 4.1: Basic control scheme of a BSRM drive system

Literature shows that BSRM consists of a drive system for the control of average torque and instantaneous suspension force to produce stable operation [57]. Such drive system mainly comprises of the dual set winding in the stator [35]. In addition, there are references which propose hybrid pole structure and feature a separate torque and force control algorithm implemented in the drive scheme [79]. BCW as implemented by Khoo, has been incorporated in a brushless permanent magnet motor and the torque and force control algorithm in the drive system is different from BSRMs. However, there

are no studies which demonstrate the implementation of bridge winding in BSRM with a speed-current control drive for torque and radial force control.

The aim of this chapter is to study and develop a simulation model which can be used to analyse the BCW for both torque and radial force production with a controlled drive system for bearingless/self-bearing operation in SRM. The BCW has radial force or levitation currents called bridge currents i_{b1} and i_{b2} in each of the phases. The prototype selected in this thesis is a 12/8 SRM which requires a 3-phase converter circuit for motoring operation and six single phase converters for x and y directional forces i.e. two single phase converters per motor phase for radial forces. In this chapter, the FE model as developed in Chapter 3 is simulated with a power converter circuit. Under dynamic condition the SRM requires a speed or torque control along with a current nested controller for stable operation. The present analysis in this chapter is based on two test cases, i) with speed-current control for the bridge winding drive system, ii) under constant speed operation considering static rotor eccentricity. The simulation is further carried forward considering the rotor radial displacement and the effect of the bridge currents to bring back the rotor to its central position using a closed loop displacement control.

4.2 Drive system model for BSRM with BCW

SRMs are electronically controlled motors and operate with power converters. The power converter circuit used in this paper for producing torque in the bridge configured BSRM is the conventional voltage source asymmetric bridge converter. Since it is a 12/8 motor hence, for one complete electrical rotation, the rotor has to traverse a mechanical angle of 45^0. Thus, in the driver circuit the conduction period (θ_s) has to be fixed as mechanical 15^0. The circuit designed is a voltage source asymmetric bridge converter having three phase-legs for the main motor current i_m and six separate 1-phase voltage source asymmetric bridge converters for the bridge currents, i_{b1} and i_{b2}. Figure 4.2 shows a schematic of an asymmetric converter circuit with three phase legs for the main current i_m, which consists of six power switches (basically MOSFETs) and six freewheeling diodes connected with the motor windings. The power converters for the bridge currents are represented as x-axis bridge current circuit and y-axis bridge current circuit and are connected in between the phase windings. The switching topology of the main current i_m and bridge currents i_{b1} and i_{b2} in each phase is explained in Table 4.1. Each individual current through the phase windings, for both the main current and the bridge currents

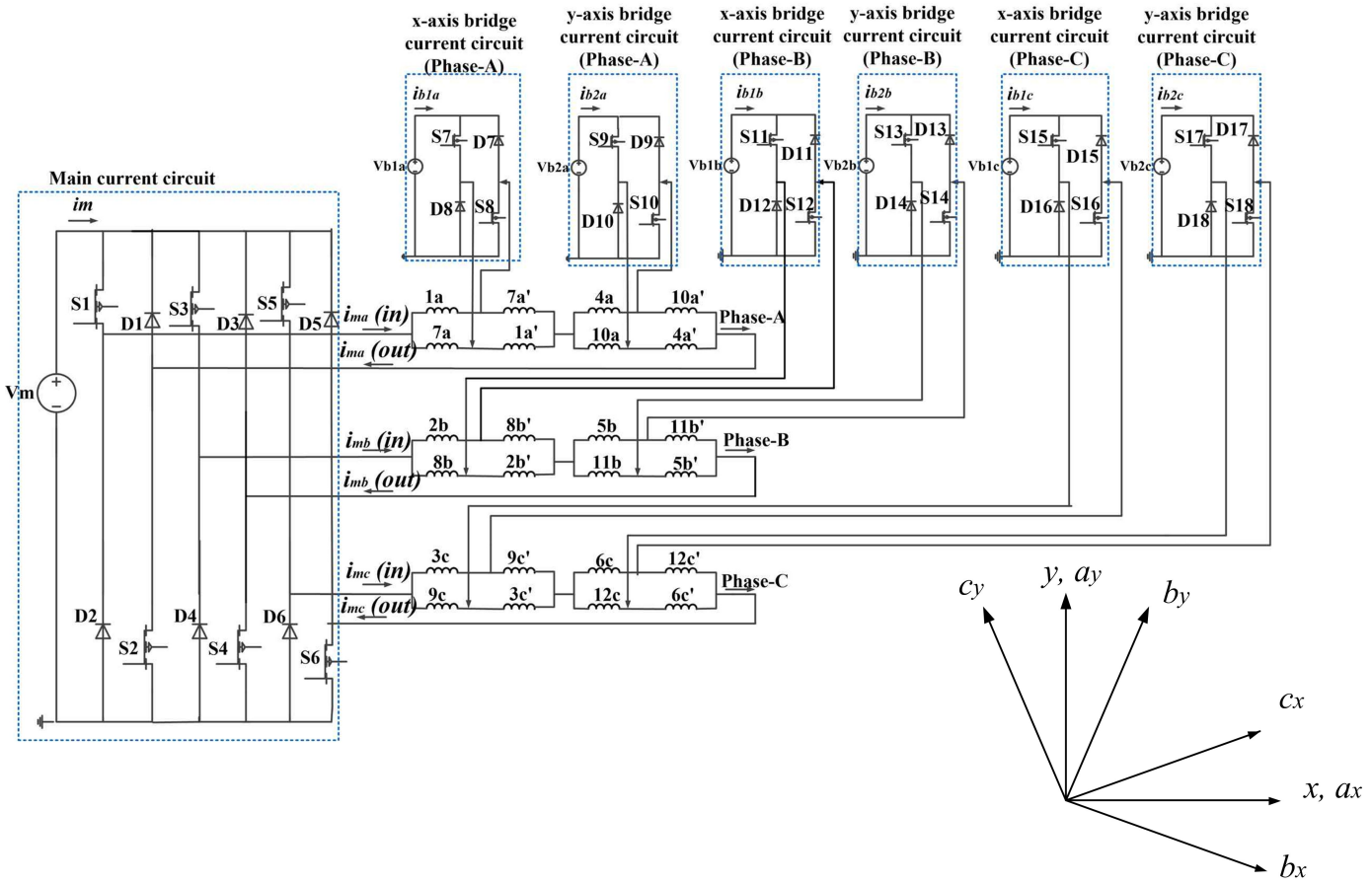

Figure 4.2: Schematic of power converters for the main current and bridge currents for BSRM with BCW [94].

are summarized in Table 4.2. The conduction angle is defined as θ_d i.e. the number of degrees during which the power switches are turned on for the current conduction. In this case, the conduction angle of the main current and the bridge currents in each phase is kept same in order to avoid negative torque production. A DC voltage source is used as the main power supply and the gates of the MOSFETs are turned on using PWM control signal. This PWM signal produces pulsating DC current and by varying the amount of 'on' time of each pulse, the peak current can be controlled. When switches S1 and S2 are turned on, the main current, i_{ma} flows through the phase-A winding and when the switches are turned off, the current freewheels through diodes D1 and D2. As soon as phase-A current is commutated, phase-B conducts and similar sequence follows in phase-C. Thus, with sequential switching the torque is produced. For the bridge current in phase-A, switches S7 and S8 conduct and current i_{b1a} flows through the winding to produce radial force in the direction of a_x of the reference axes $x-y$ and when switches

S9 and S10 conduct, bridge current i_{b2a} flows to produce radial force in the direction of a_y as shown in Figure 4.2. Similarly, force can be produced along b_x and b_y using bridge currents i_{b1b} and i_{b2b}, and along c_x and c_y using bridge currents i_{b1c} and i_{b2c} as given in Table 4.1 and Table 4.2.

Table 4.1: Switching topology of the proposed drive system

Phase windings	**Conduction period for i_m,i_{b1},i_{b2}**	**Switches for i_m**	**Switches for i_{b1}**	**Switches for i_{b2}**
Phase-A	$0^0 - 15^0(\theta_a)$	S1, S2	S7, S8	S9, S10
Phase-B	$15^0 - 30^0(\theta_b)$	S3, S4	S11, S12	S13, S14
Phase-C	$30^0 - 45^0(\theta_c)$	S5, S6	S15, S16	S17, S18

Table 4.2: Currents in each phases of the drive system

Phase windings	**Main current**	**Bridge currents**
Phase-A	i_{ma}	i_{b1a}, i_{b2a}
Phase-B	i_{mb}	i_{b1b}, i_{b2b}
Phase-C	i_{mc}	i_{b1c}, i_{b2c}

4.3 Control principles for driving and levitation in BSRM with BCW

The concept of controlling speed under bearingless operation is introduced in this section. The control principle of motor operation depends on the excitation of the phase winding at increasing inductance. The torque production for motoring and regeneration is shown in Figure 4.3. The waveforms shown are for only one phase. The torque is positive for increasing inductance region and negative for decreasing inductance region. The total torque is the combination of the torque pulses produced by sequential phase switching. It can be observed that the average torque is controlled by adjusting the conduction angle θ_d and the magnitude of winding peak current I_p. In order to adjust the winding current a current controller is necessary.

For radial force production in BCW BSRM, the drive requires two feedback loops of the rotor displacement in the x and y directions. This radial displacement is controlled by a current controller for the bridge currents. The bridge currents are governed by a switching logic based on the rotor position and the current controller controls the

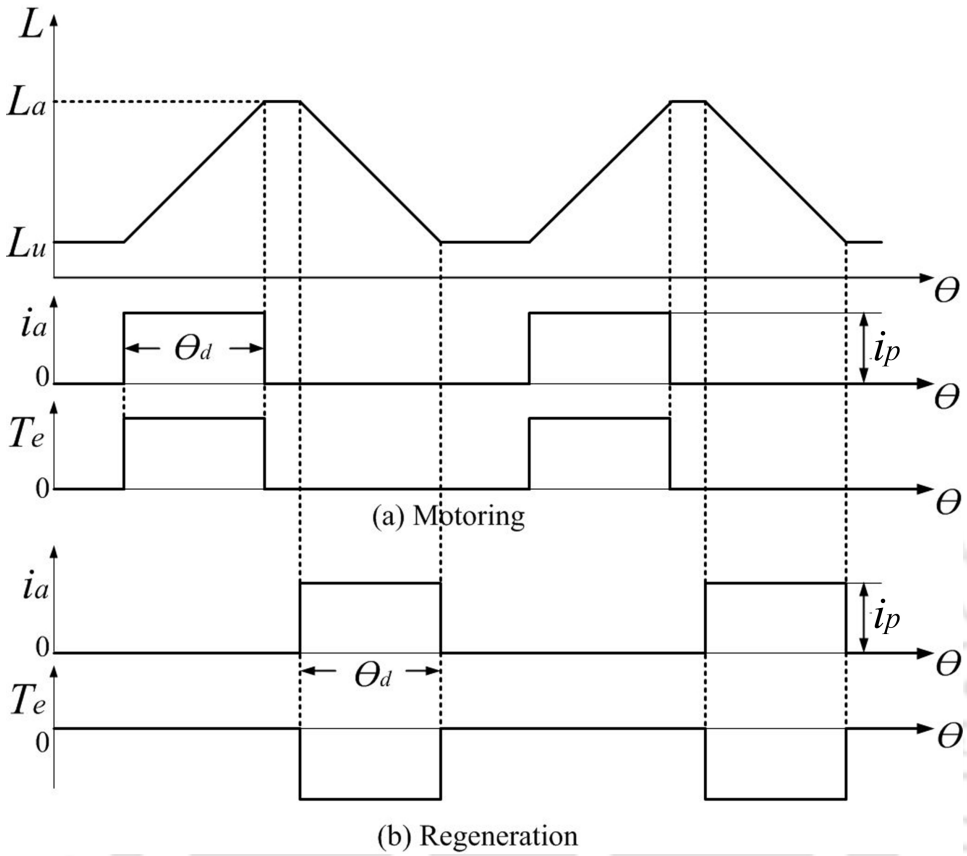

Figure 4.3: Motoring and regeneration sequence in SRM

magnitude of the peak current. In the following section, a simulation model of a speed controller is developed for motor operation and current controllers are developed for each individual bridge currents for radial force production. Further, the radial forces produced, are controlled using a radial displacement control technique.

4.3.1 Modelling of a speed and current control drive system for BSRM with BCW

The speed control of an SRM generally requires an inner phase current control loop and an outer speed control loop, as commonly used in DC machine drives. Figure 4.4 shows the schematic of the speed-current controlled drive system of BSRM with BCW. For the main current i_m, a 3-phase asymmetric bridge converter circuit is used and three separate single phase asymmetric bridge converter circuits are connected in each phase's bridge terminals for the radial force production in x-direction. Three more single phase converters are connected for the y directional radial force. Each phase for torque and

force production conducts for a period of θ_d =15^0. The speed is measured and provided as a negative feedback with a reference speed, ω_{ref}. The speed error is processed through a PI controller and a limiter to yield the main current (i_m^*) command and another current limiter to yield the bridge current command (i_{b1}^*). The current command for the main current and bridge currents are compared with the hysteresis window, $\Delta\ i_m$ and $\Delta\ i_{b1}$ to obtain the i_{max} and i_{min} which keeps the current within the reference value. The hysteresis window is selected by choosing a deviation band between the actual current and the reference current. The reference current $i_{m_a}^*$ is compared with the peak motor winding current i_p for phase-A. Similarly, the reference bridge current $i_{b1_a}^*$ of phase-A is compared with the bridge current i_{b1} in the motor winding. The required control signals are then generated which are steered to the corresponding gate of the MOSFETs in each phase-leg. The switching logic of the hysteresis controller for the main current in phase-A is given as

$$\begin{aligned} &If\ (i_{ma}^* - i_{ma}) \geq \Delta i_m,\ \text{then}\ V_a = V_{dc} \\ &(i_{ma}^* - i_{ma}) \leq -\Delta i_m \text{ and } i_{ma}^* \geq 0,\ \text{then}\ V_{dc} = 0 \\ &(i_{ma}^* - i_{ma}) \leq -\Delta i_m \text{ and } i_{ma}^* \leq 0, \text{then}\ V_{dc} = -V_{dc} \end{aligned} \tag{4.1}$$

where $\Delta\ i_m$ is the hysteresis window and V_{dc} is the DC supply voltage. To turn on phase-A, a positive voltage is applied and the switches S1 and S2 are switched on. When the current error is less than or equal to $-\Delta\ i_m$, either of S1 and S2 in phase-A leg gets turned off and the current freewheels through diode D1 or D2. This means the voltage v_{dc} across the phase winding is zero. If both the switches are turned off, the current gets commutated and the voltage is equal to $-V_{dc}$ as long as the remaining current flows through the winding. Phase-A gets commutated based on the rotor position and sequentially phase-B and phase-C conduct. The same logic is followed by the bridge current i_{b1}. In this section, the bridge currents i_{b1a}, i_{b1b} and i_{b1c} are injected in phase-A, phase-B and phase-C in order to obtain forces along the axes, a_x, b_x and c_x. The supply for bridge current i_{b2} is not connected.

The proposed drive system is designed and developed in Ansoft SIMPLORER©. The 2D finite element model of the 12/8 BCW BSRM designed in Ansoft Maxwell 2D is simulated with the drive system and analyzed. The motor is a voltage input model. In Ansoft Maxwell, a 12/8 SRM is designed and the coils are defined. The coil terminals are left open so that an external circuit can be connected in the Simplorer platform. The coils are connected in the form of bridge winding in Simplorer and a voltage source 3-phase converter is connected for the main current supply. Three separate 1-phase

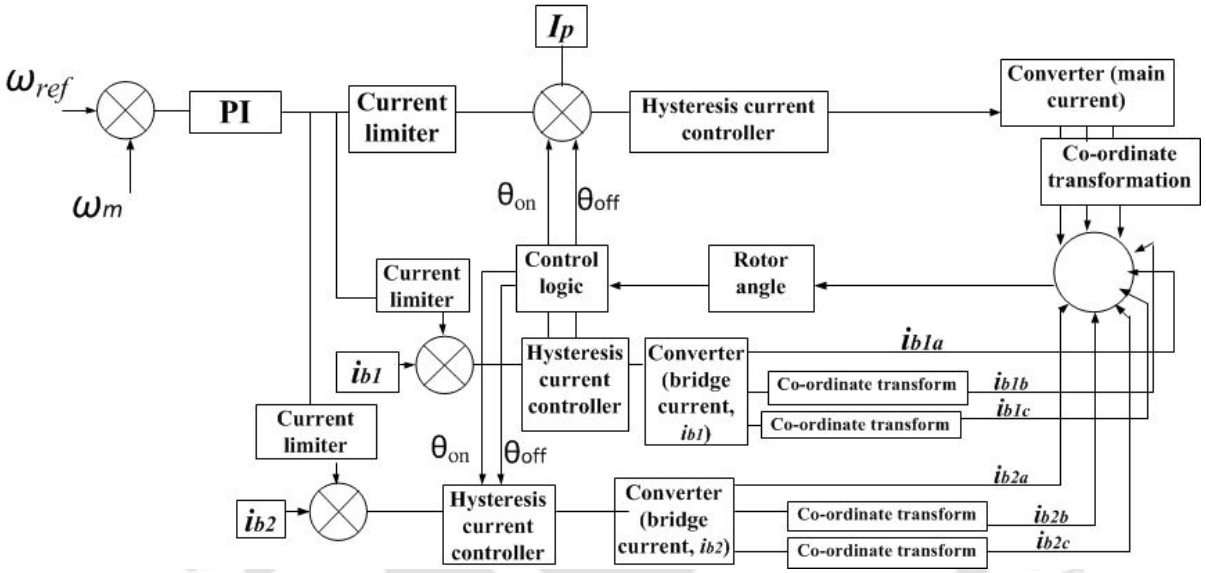

Figure 4.4: Block diagram for speed and current control drive of BSRM with BCW

converters are connected at the bridge points of phase-A, B and C. The Figure 4.5 shows the drive system of a 12/8 BCW BSRM developed in SIMPLORER.

Table 4.3: Parameters of the drive system

Parameters	Values
Current limiter gain (main current)	10 A
Current limiter gain (bridge current)	2 A
DC link voltage (for main current i_m)	50 V
DC link voltage(for bridge current i_{b1})	30 V
Integral gain constant, K_{in}	50
Proportional gain constant, K_p	10

4.4 Simulation results of the drive system

The drive system of the BSRM with BCW is implemented in SIMPLORER© as shown in Figure 4.5. The model of the motor in Ansoft Maxwell is simulated in parallel with the drive system in Simplorer. The model is simulated and analysed till it reaches a steady state value and comprehends the control methodology applied for the proposed motor. In this section, only the bridge current i_{b1} is injected in between the winding in order to produce x-direction radial force. The parameters of the drive system are listed

in Table 4.3. The reference speed ω_{ref}, is taken as 1500 rpm and compared with the simulated speed. The waveforms of the main current i_m and the bridge current i_{b1} in each phase are shown in Figure 4.6 and Figure 4.7. It can be observed that the main current reaches a peak value of around 9 A when the motor reaches a steady state. The bridge current i_{b1} reaches a peak value of around 1.7 A as the motor reaches the steady state speed.

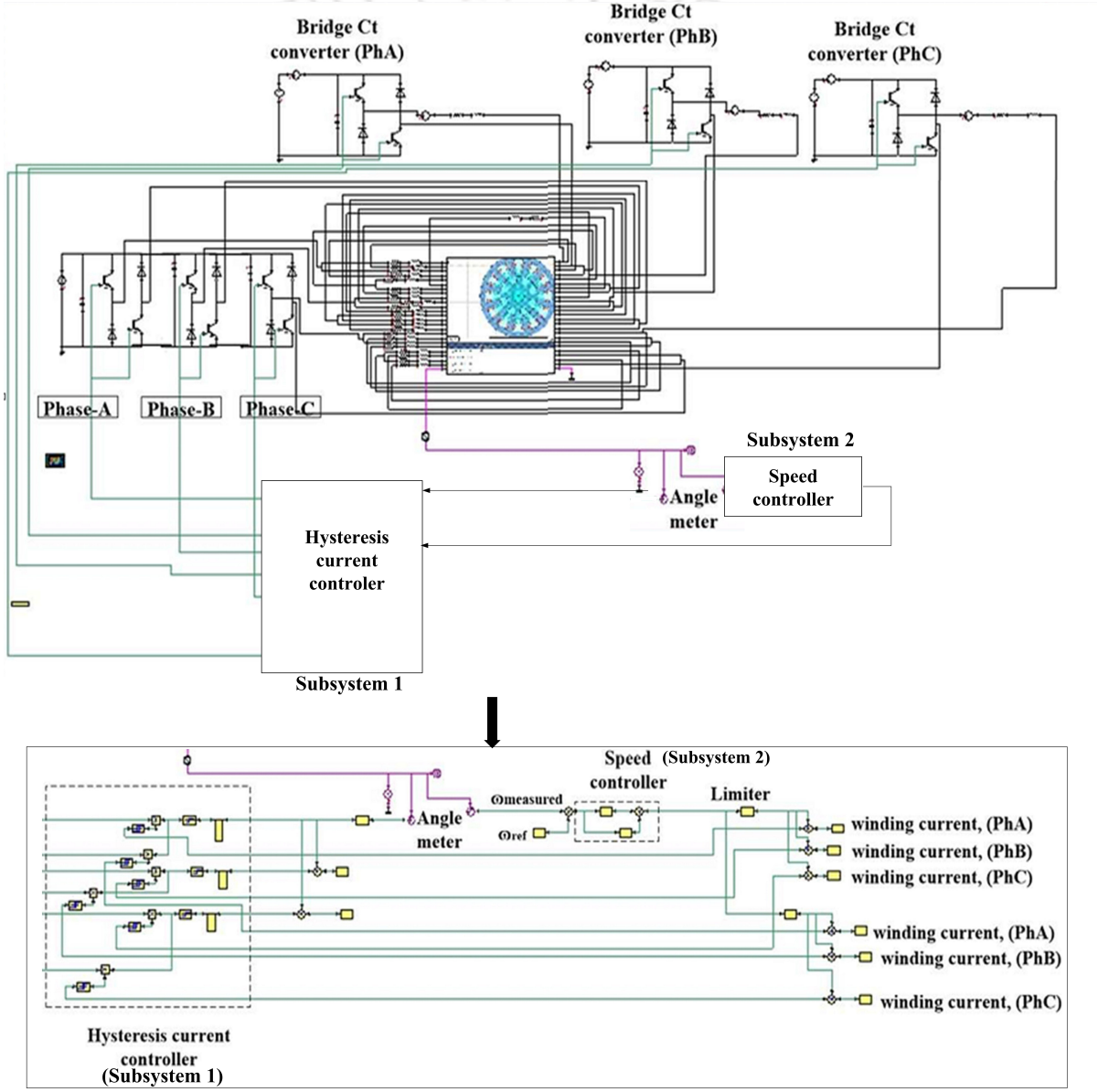

Figure 4.5: Speed-current controlled drive system of BSRM with BCW in SIMPLORER©

The phase voltage across each bridge i.e the top bridge and the bottom bridge are

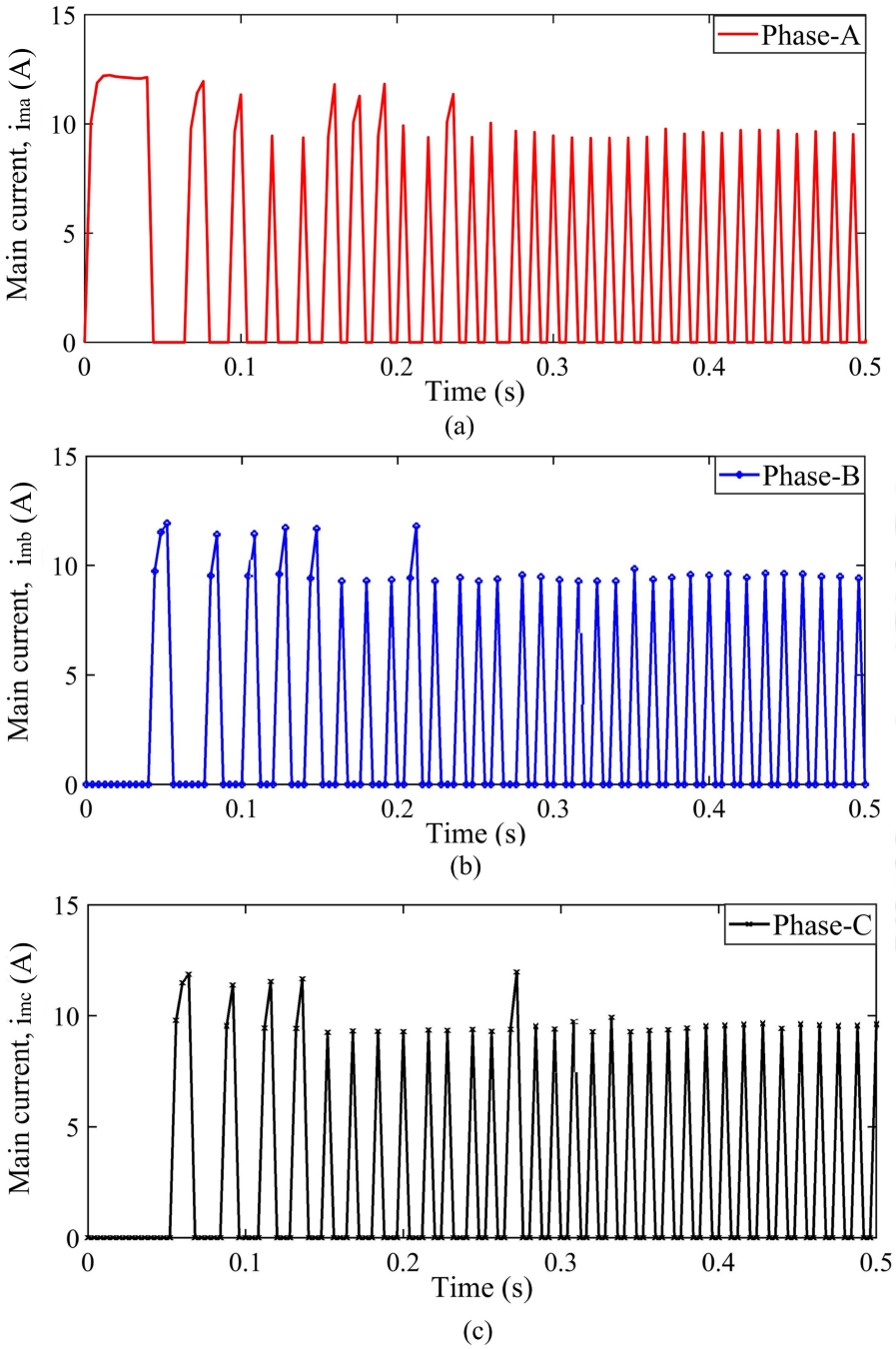

Figure 4.6: Waveforms of the main current, i_m in (a) phase-A (b) phase-B and (c) phase-C

obtained as shown in Figure 4.8 and Figure 4.9. λ_a, λ_b and λ_c represents the flux linkages for phase-A, phase-B and phase-C windings. With the injection of bridge currents in coils of top bridge winding, the respective flux linkages changes as shown in Figure 4.10(a). However, it can be observed from Figure 4.10(b) that the flux linkages in coils of bottom

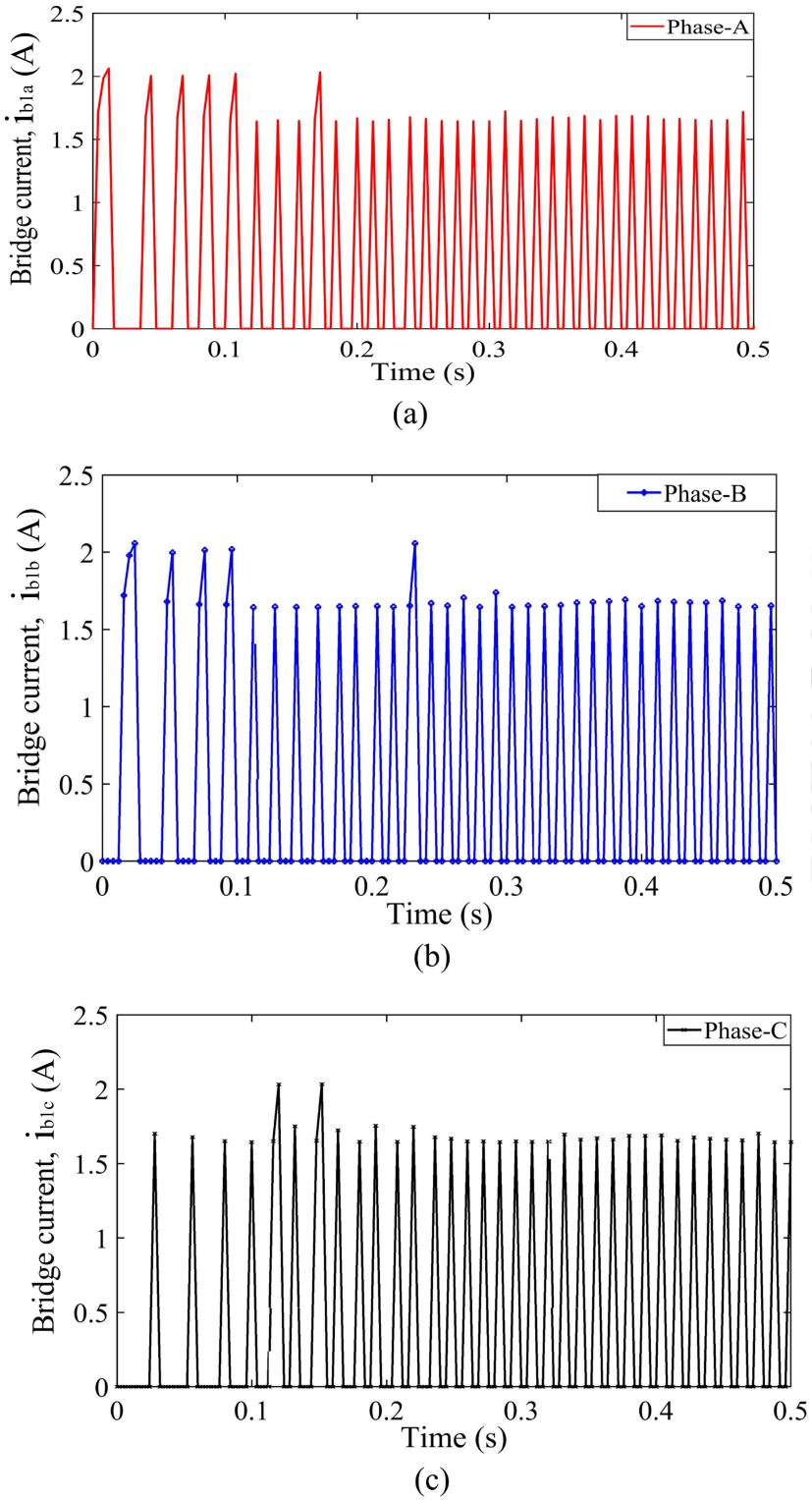

Figure 4.7: Waveforms of the bridge current, i_{b1} in (a) phase-A (b) phase-B and (c) phase-C

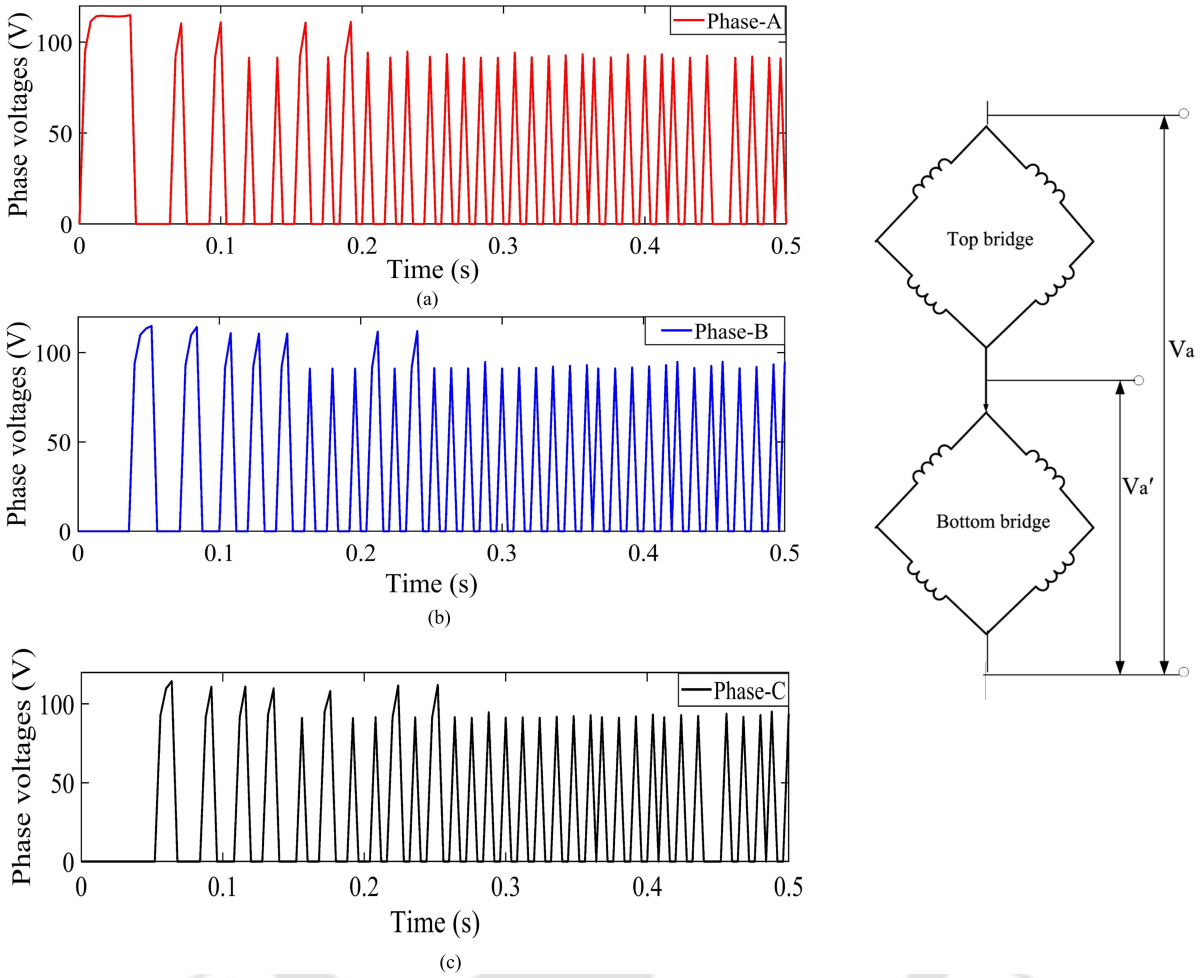

Figure 4.8: Voltages across top bridge winding (a) V_a (b) V_b and (c) V_c

bridge winding remains unaffected since the current in the winding is not perturbed by injecting bridge current i_{b2}.

The rotor speed ω obtained from the simulation is compared with ω_{ref}. The speed error is amplified and regulated using a PI controller. The output of the speed controller is a current command signal. This current command is compared with the current feedback signals of the windings. The generated current is then allowed to pass through a hysteresis current window to control the main current and the bridge current. Each phase winding current is commutated based on the rotor angle and the hysteresis controller. It can be observed from Figure 4.11 that the motor rotates at the desired speed with the control scheme, considering torque and radial force production simultaneously. The control of speed by PI controller gives a satisfactory response with less overshoot as shown in Figure 4.11 and it can be observed that the BSRM can reach a steady state

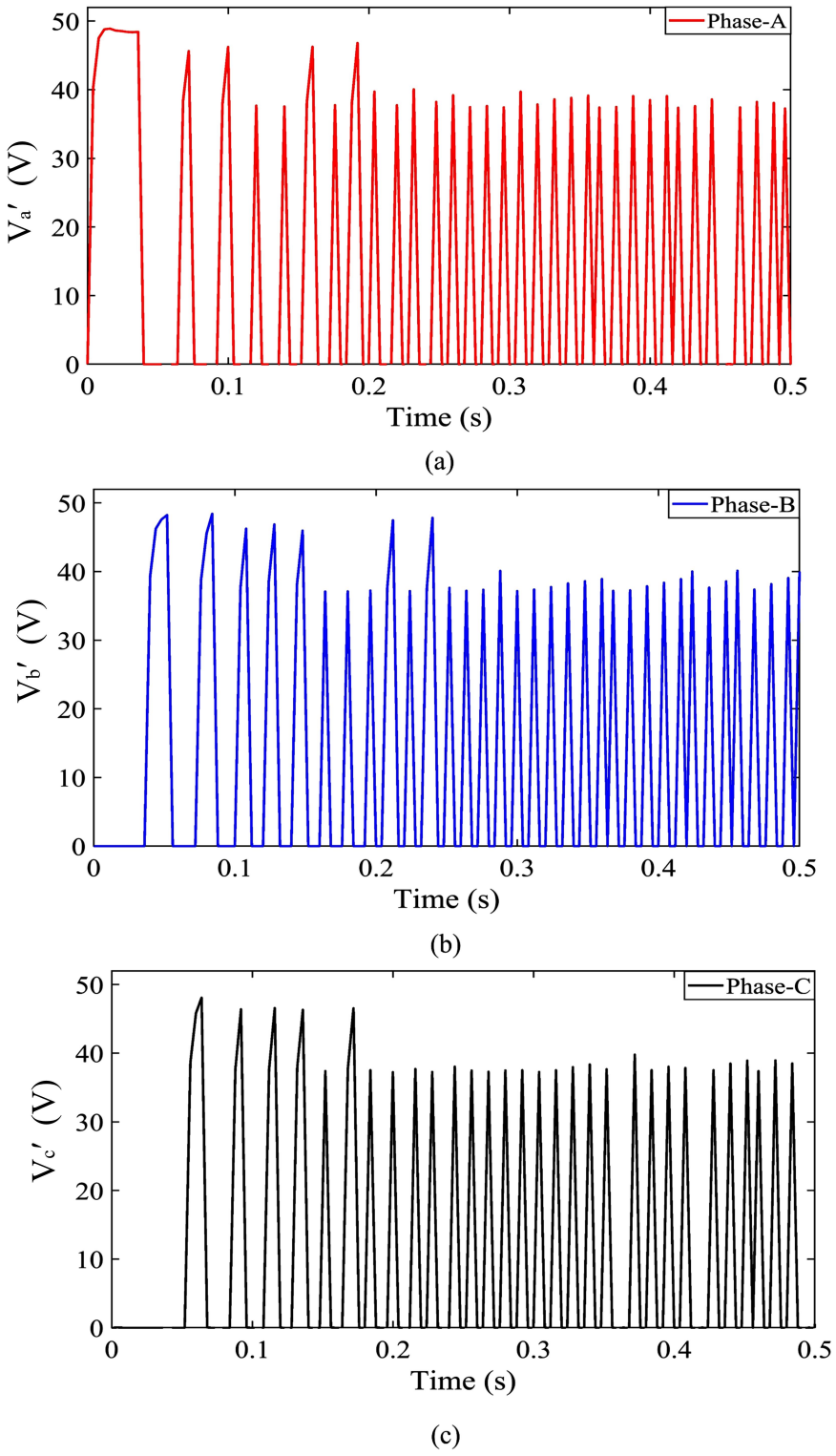

Figure 4.9: Phase voltages across bottom bridge winding (a) V_a' (b) V_b' and (c) V_c'

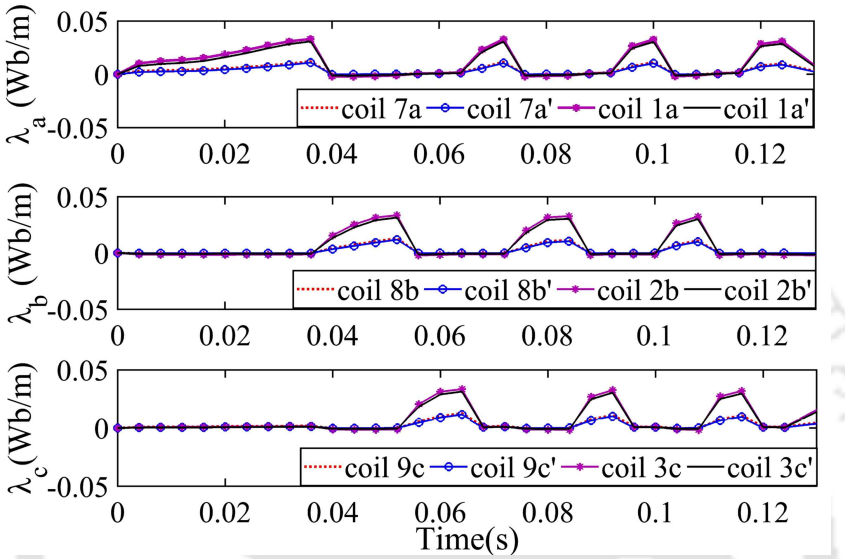

(a)

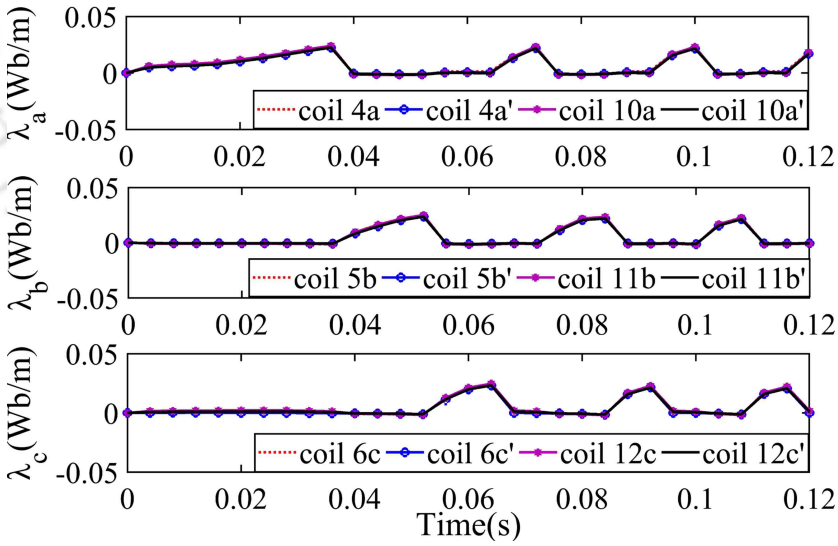

(b)

Figure 4.10: Flux linkages in coils of (a) top bridge winding with both main current i_m and bridge current i_{b1} (b) bottom bridge winding with only main current i_m and bridge current $i_{b2} = 0$

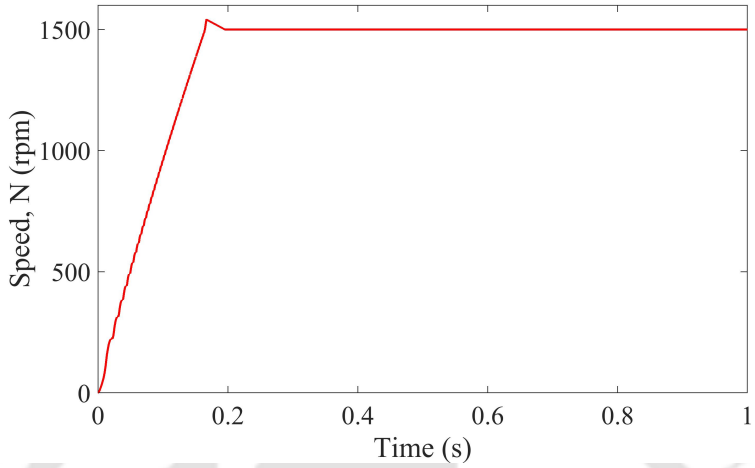

Figure 4.11: Speed response using PI controller

while both motoring and generating forces.

Figure 4.12 (a) and (b) show the FE simulation results of radial force in the horizontal and vertical directions. The radial force is produced along the axes, a_x, b_x and c_x as each phase is injected with bridge current i_{b1}. However, due to the geometrical shift of the motor for phase-B and phase-C, injecting the same amount of bridge current does not produce equal radial force in each phases. The current required in phase-B and phase-C is more than that of phase-A. From Figure 4.12 (b) it is observed that very less radial force is produced in the vertical direction as the bridge current i_{b2} is not injected in the coils of y-axis. This FE results are obtained from the simulation of the model in Ansoft Maxwell. Figure 4.13 shows the results of the net radial displacement produced due to forces produced along the horizontal and vertical axes. The results of the displacement are computed from the radial force values using the equation of radial forces from the mathematical model. Figure 4.12 and Figure 4.14 exemplifies that both radial force and torque are achieved using the bridge winding scheme in BSRM. It can also be observed from Figure 4.15(a) and Figure 4.15(b), that the actual phase current for both main current and bridge current in phase-A, is able to track the reference current with the hysteresis current control method and chopped at regular intervals. The currents for phase-B and phase-C are obtained similarly. Figure 4.16 shows the pulsating power output at a steady state speed of 1500 rpm and it can be observed that the peak output power is around 700 W.

The commutation logic for the turn on and turn off angle is steadily maintained with varying speed condition producing positive torque at every phase reversal. Figure 4.17(a) shows the waveforms of the rotational position of the rotor for each phase's conduction.

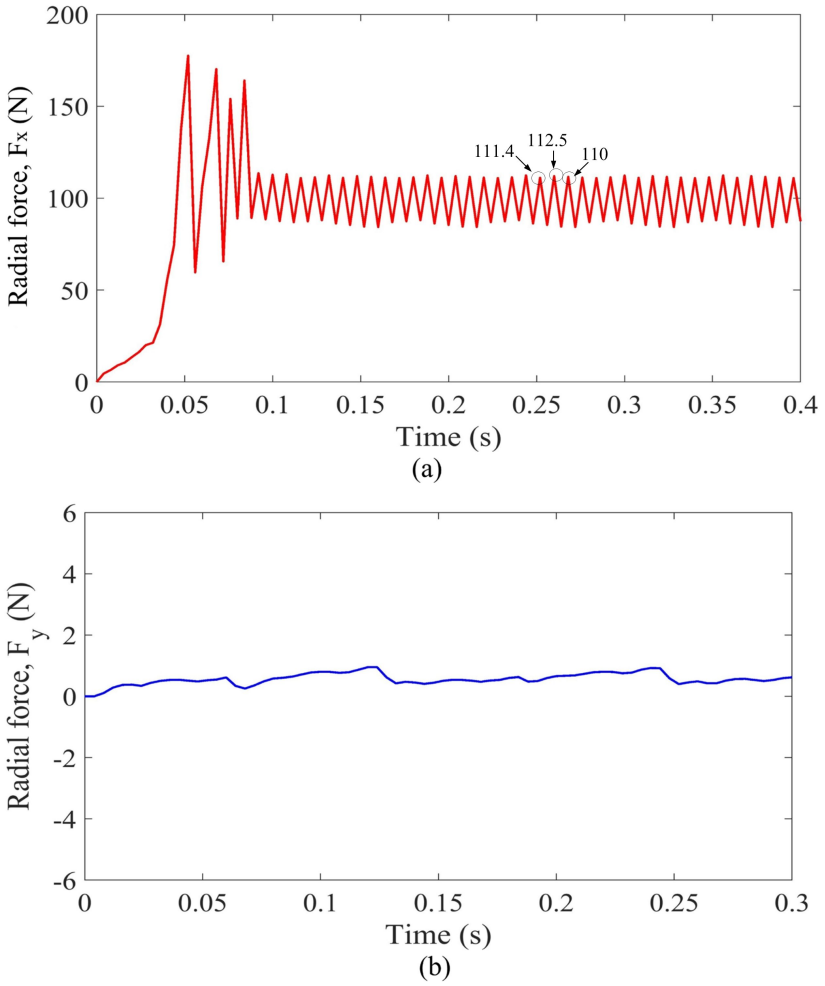

Figure 4.12: FE simulation results of radial forces (a) F_x and (b) F_y

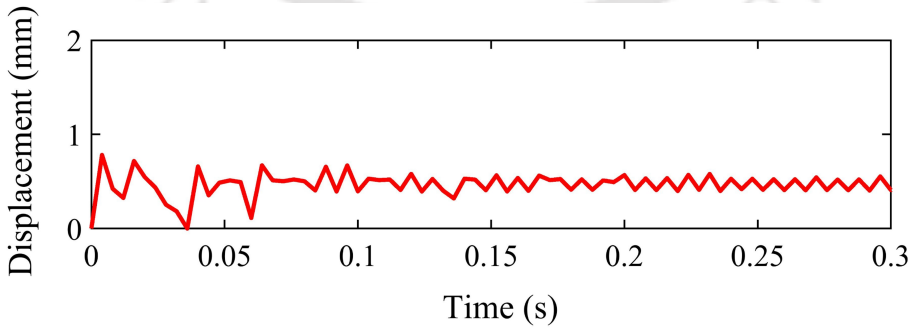

Figure 4.13: Simulation result of radial displacement

In the figure θ_a, θ_b and θ_c represents the rotational angle for phase-A, phase-B and phase-C conduction period. The waveforms of the PWM gate signals as shown in Figure 4.17(b) shows that a stability in the switching frequency of the gate signals are attained

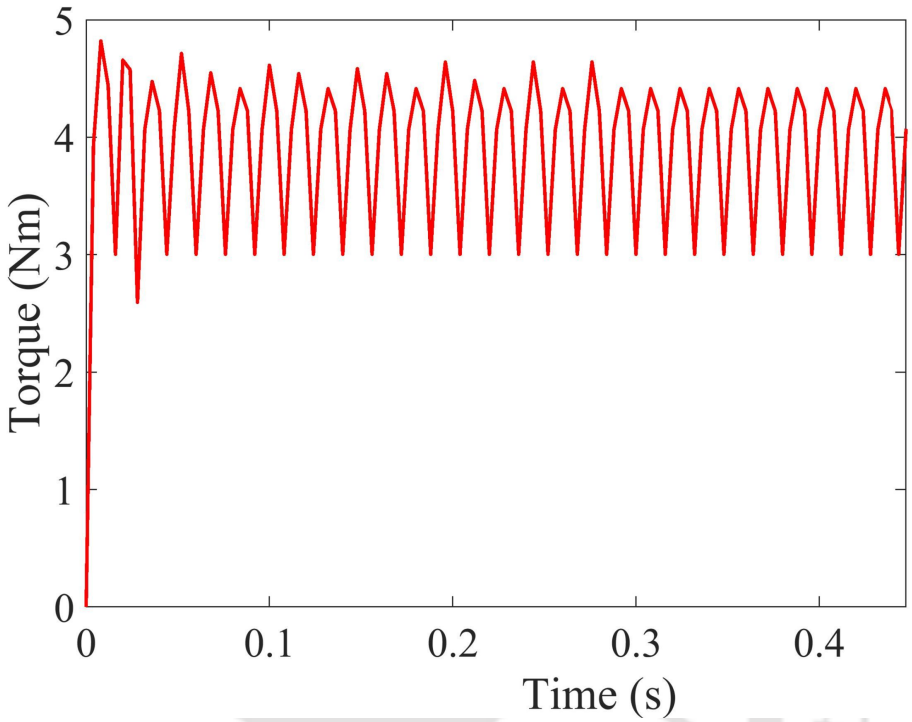

Figure 4.14: Simulation result of torque

as the motor reaches the steady state speed. The results plotted in Figure 4.6, Figure 4.7, Figure 4.12, Figure 4.17(b) etc. show variation in phase currents, forces, rotor position etc. during start up and then becomes stable once the motor reaches a stable position and the desired speed. The analysis conducted in this section is done for the motor under no load condition. Thus, from this analysis in this section it can be concluded that with the bridge current excitation, the profile of the torque is not effected and positive torque is produced with each switching of phase. It is also observed that there is very less effect in the magnitude of torque with the injection of bridge current. Thus the BCW design provides the flexibility to provide both levitation force as well as motoring torque.

4.5 Control of radial displacement using PID control

The capability of the bridge current is again explored in this section. It can produce an equal and opposite radial force by decreasing current in the coils which are placed in the positive x-axis direction i.e. towards which the shaft gets displaced by x mm and by increasing the current in the opposite coil [95]. As such a closed loop control of the system is necessary. Assuming a main current i_m and bridge current i_{b1}, the required

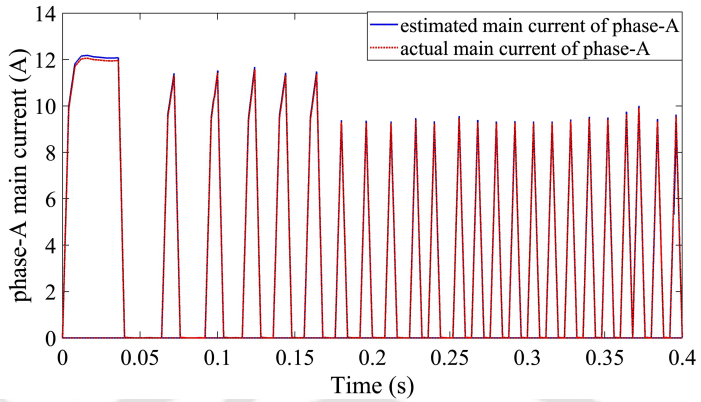

(a)

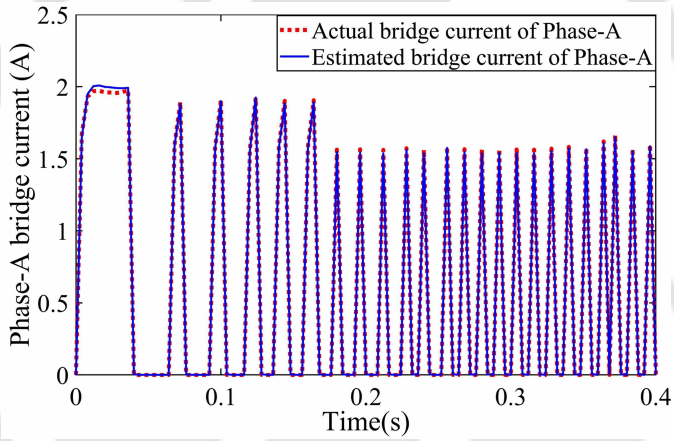

(b)

Figure 4.15: Profiles of actual current and estimated current in phase-A for (a) main current i_m and (b) bridge current i_{b1}.

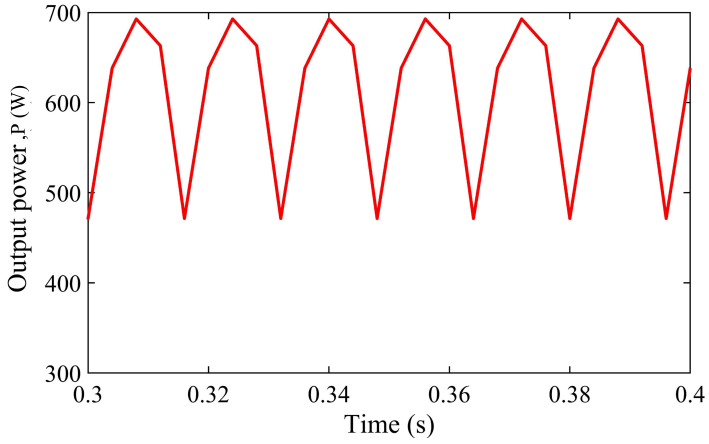

Figure 4.16: Output power of the motor at steady state.

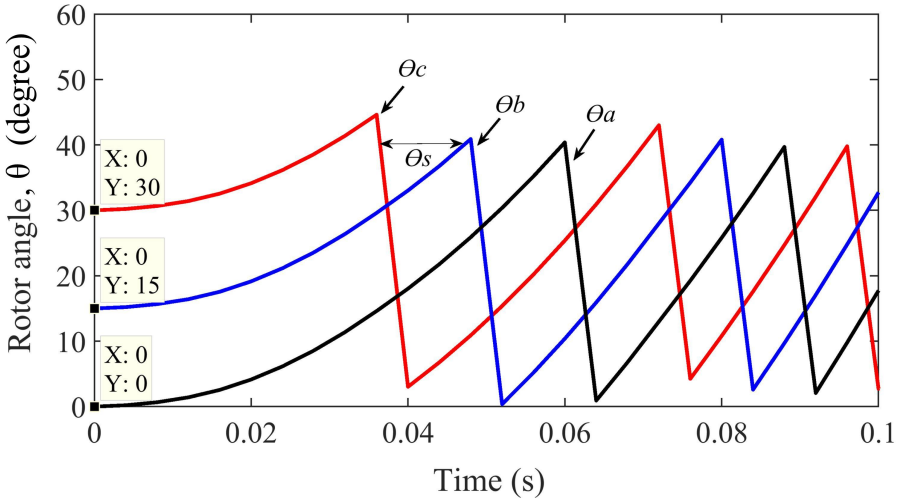

(a)

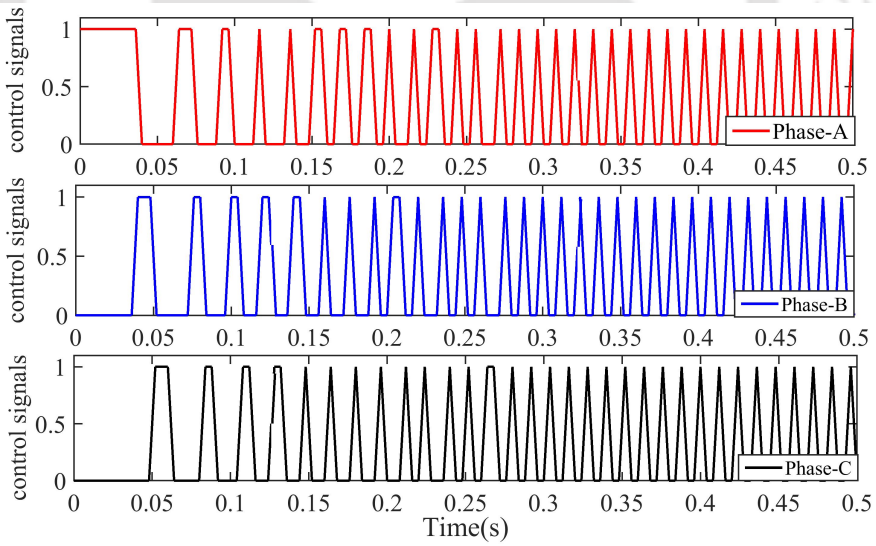

(b)

Figure 4.17: (a) Rotor angle (b) PWM control signals.

radial force can be represented with reference to Equation 3.111 as

$$F_x{}' = \frac{\mu_0 N^2 A_g}{2(l_o + x)^2}(i_m + i_{b1})^2 - \frac{\mu_0 N^2 A_g}{2(l_o - x)^2}(i_m - i_{b1})^2. \tag{4.2}$$

After partial differentiation of F_x with respect to x and i_{b1}, it can be written as

$$\begin{aligned} F' = &\left[\frac{\mu_0 hrN^2}{2}\left(\frac{-2(\theta_m-\theta)}{(l_0+x)^3} - \frac{128\theta}{(4l_0+4x+\pi r\theta)^3}\right)(i_m+i_{b1})^2\right]\Delta x - \\ &\left[\frac{\mu_0 hrN^2}{2}\left(\frac{2(\theta_m-\theta}{(l_0-x)^3} + \frac{128\theta}{(4l_0-4x+\pi r\theta)^3}\right)(i_m-i_{b1})^2\right]\Delta x + \\ &\left[\mu_0 hrN^2\left(\frac{(\theta_m-\theta)}{(l_0+x)^2} + \frac{16\theta}{(4l_0+4x+\pi r\theta)^2}\right)(i_m+i_{b1})\right]\Delta i_{b1} - \\ &\left[\mu_0 hrN^2\left(\frac{(\theta_m-\theta)}{(l_0-x)^2} + \frac{16\theta}{(4l_0-4x+\pi r\theta)^2}\right)(i_m-i_{b1})\right]\Delta i_{b1} \end{aligned} \tag{4.3}$$

Linearizing Equation 4.3 using Taylor series expansion it can be written in the form as

$$\Delta f = -K_x\Delta x + K_i\Delta i_{b1}, \tag{4.4}$$

where, K_x is the open loop translational stiffness and K_i is the force current factor. The above equation represents the equation of radial magnetic force as a function of both current and rotor radial displacement. The current i_{b1} is the force regulating current in the x-axis and the excitement of the displacement is the force F_x.

Considering the dynamics of the rotor system, Equation 4.4 can be written as

$$m\frac{d^2\Delta x}{dt^2} + K_x\Delta x = K_i\Delta i_{b1}. \tag{4.5}$$

Thus, the control equation or the transfer function of the system can be written as

$$\frac{\Delta x(s)}{\Delta i_{b1}(s)} = \frac{K_i}{K_x + ms^2}. \tag{4.6}$$

The values of K_x and K_i are calculated for every value of main current (i_m) and bridge current (i_{b1}) at different rotor angle (θ), as obtained from the FE results and used in the simulation. An ideal sensor gain is modelled to amplify the displacement and compare with a reference value which then goes through a PID controller to generate the desired radial force commands. Figure 4.18 shows the block diagram of a PID controller where x^* is taken as the reference of the displacement. The position error e_x is added to the PID controller so that the force command F_x^* is generated. The force tries to move the rotor to its opposite direction, thus gradually reducing the displacement x. The output of the controller decreases until the position is on the reference and gives zero position error. The values of the controller gains viz. K_p, K_{in} and K_d are varied and simulated in

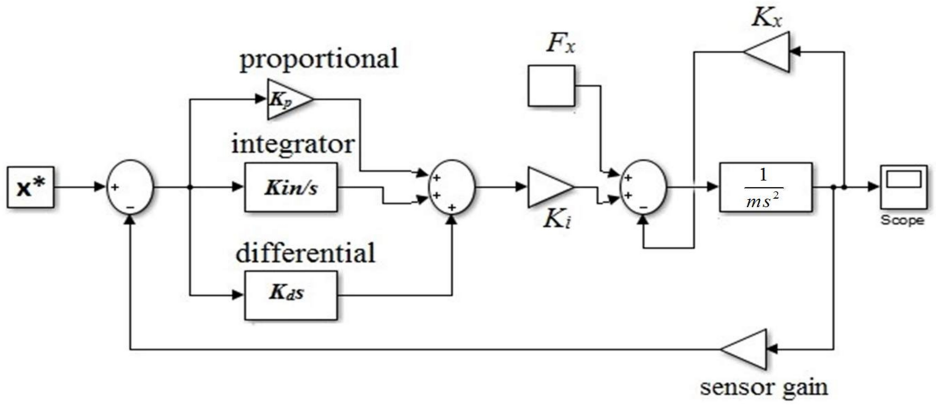

Figure 4.18: Simulink model of a PID controller for displacement control

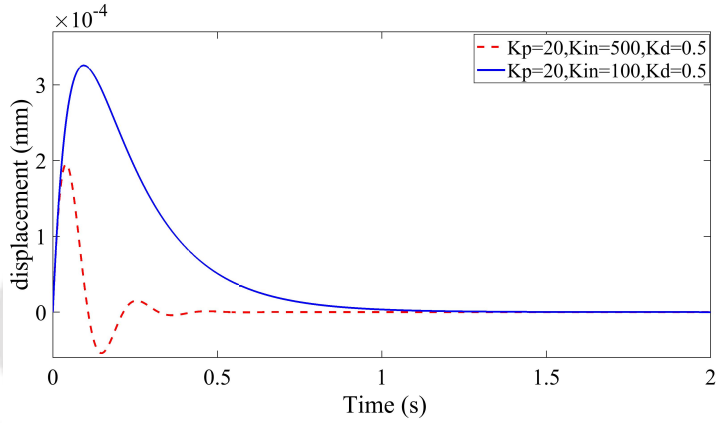

(a)

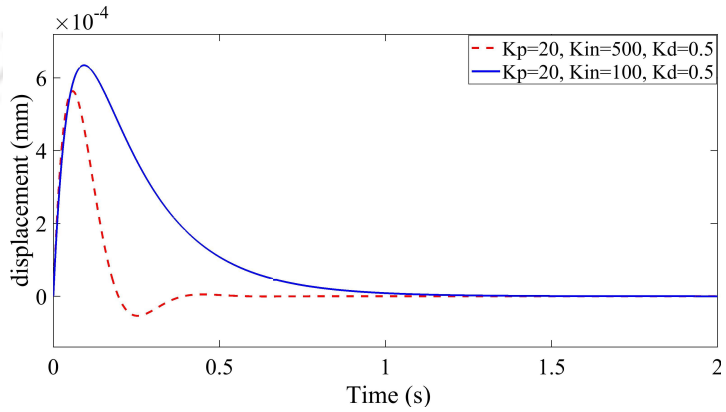

(b)

Figure 4.19: Response of radial displacement using PID controller at (a) $\theta = 0^0$ and (b) $\theta = -15^0$.

order to obtain the best response of the system. The response of the system is checked at different rotor angle (θ). The controller gains are taken as, K_p=20, K_d=0.5 and varying the value of K_{in} at 100 and then 500. It can be observed that when K_{in}=100 the response of displacement is slow. Therefore the best response is obtained at K_{in}=500. The value of the sensor gain is taken as 1000. Figure 4.19(a) and 4.19(b) show the response of the radial displacement using a PID controller. It can be observed from the response that the radial displacement is significantly mitigated by the PID controller and the rotor settles smoothly to its centre position.

4.6 Principle of current control algorithm for BSRM with BCW

An effective control scheme as suggested by Takemoto *et al.* used square wave currents as the main current and the calculated levitation currents are tracked by a hysteresis current controller in each phase. The method is analysed mathematically and verified using FE analysis. In the present work, a control scheme is proposed where both the main current and the bridge current are calculated and injected in the respective coils to obtain the required levitation force. In this case, the conduction width of the main current and the bridge current are kept same. With the parameters listed as in Table 3.2, the weight of the rotor system is calculated as 1.22 kg. Hence, the minimum force required to lift the rotor and shaft is calculated as 12 N. In this case, Takemoto's approach of square wave i_m is applied and the levitation current is predicted analytically. In this case, the main current is responsible in producing both torque and radial force. The net radial force and the average torque are coupled by three variables i.e. i_m, i_b and the rotor position θ. The net radial force F is the vector sum of F_x and F_y as referred to Equation 3.106 and is given as

$$\begin{aligned} F &= \sqrt{F_x^2 + F_y^2} \\ &= 4K'(\theta) i_m \sqrt{i_{b1}^2 + i_{b2}^2} \end{aligned} \tag{4.7}$$

And the torque is referred to Equation 3.107 and is given as

$$T = N^2 K_t(\theta)(4i_m^2 + i_{b1}^2 + i_{b2}^2) \tag{4.8}$$

The relationship between torque and radial force in each phase can be obtained as

$$T = 2\left(\frac{F^2}{K'(\theta)i_m^2}K_t(\theta) + 2N^2K_t(\theta)\right) \tag{4.9}$$

It can be observed from Equation 4.9 that there are two variables i_m and θ in the equation. The main current is required for both torque and radial force production, hence in BCW scheme radial force cannot be produced without the main torque producing current, i_m. In this section, an attempt is made to identify the amount of current required to lift the rotor system in each phase from an unaligned to an aligned position. The bridge current is calculated under two conditions, (a) constant value of i_m and (b) varying value of i_m. The bridge current is calculated for each rotor position required to obtain the minimum lifting force in a particular direction. Figure 4.20 (a) shows the waveform of square-wave main current i_m and the bridge current i_{b1} and i_{b2} in phase-A, phase-B and phase-C. It can be seen in Figure 4.20 (a) that, the torque becomes zero at 0^0 rotor angle and goes to negative beyond that. In order to avoid this negative torque, the rotor is rotated for a mechanical angle of 15^0 and each phase is excited for a 15^0 angle of rotation. Another approach as shown in 4.20 (b) is the scheme where the main current and the bridge currents are calculated analytically as described in the next section.

4.6.1 Analytical calculation of winding currents

In bearingless motors it is important to supply current in the windings in accordance with the radial force required for suspension of the rotor and shaft. It can be observed from the analytical model given in Equation 4.7 that the net radial force depends on the rotor position θ and the total phase current in the coils. The current responsible for the radial forces in x and y direction are composed of the main current i_m and bridge currents i_{b1} and i_{b2}. From the equation of torque obtained in Equation 4.8, it can be seen that the torque becomes zero as the rotor angle (θ) goes to zero i.e. as the rotor pole gets completely aligned with the stator pole the torque becomes zero. In this case, before reaching zero position, the subsequent phase has to be excited i.e. in each phase the switching of currents should take place before the rotor gets completely aligned with the stator pole. Thus, at the zero degree rotor angle the main current can be calculated by equating the torque Equation 4.8 to zero [63].

In the levitation operation the torque shall be minimum if the derivative of torque with respect to θ is zero. From Equation 4.8 the main current i_{ma} in phase-A can be

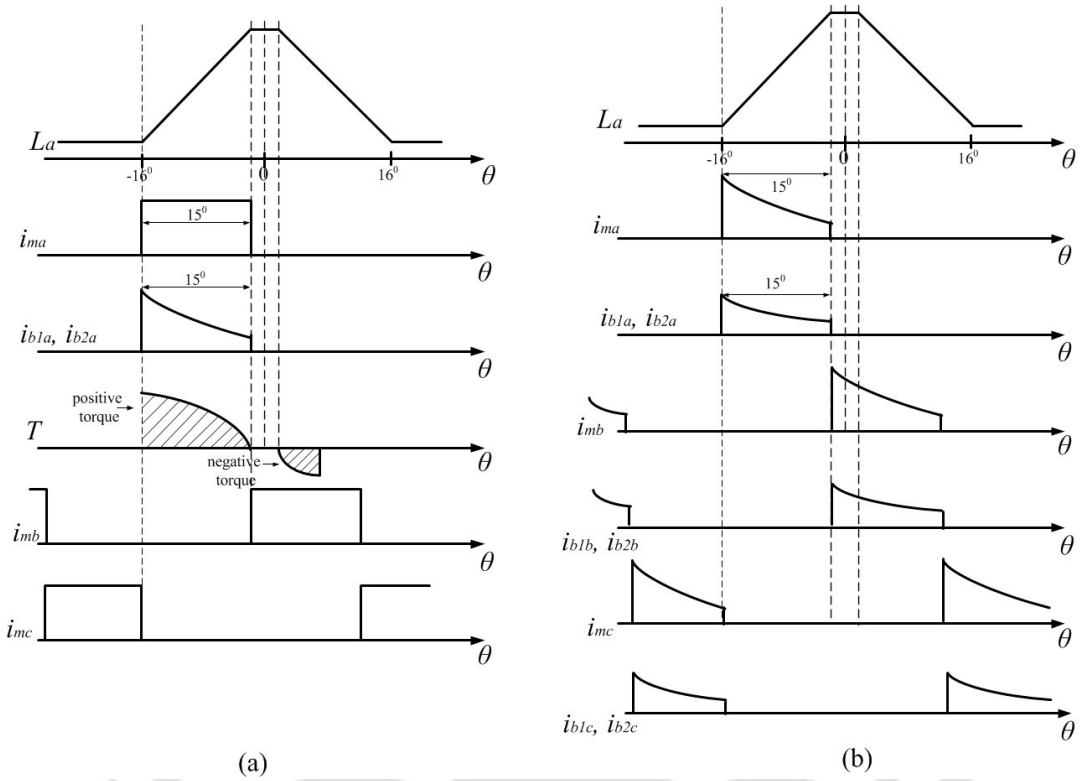

Figure 4.20: Waveforms of current and torque with (a) square wave main current (b) proposed variation in main current bridge currents

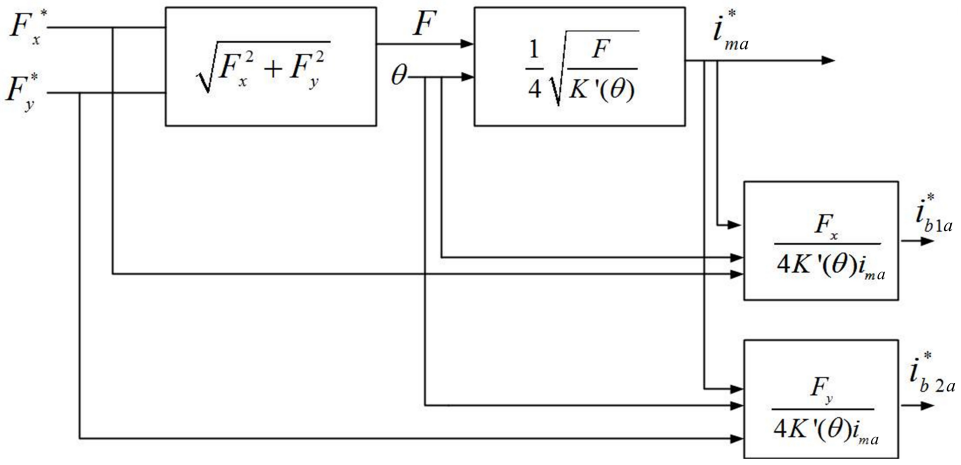

Figure 4.21: Current calculating algorithm for radial force in phase-A.

obtained as

$$\begin{aligned} 4N^2 i_{ma}^2 &= 2N^2(i_{b1a}^2 + i_{b2a}^2) \\ \Rightarrow i_{ma} &= \sqrt{\tfrac{1}{2}(i_{b1a}^2 + i_{b2a}^2)} \end{aligned} \tag{4.10}$$

Thus, putting Equation 4.10 in Equation 4.7 the current i_{ma} per phase can be derived

as

$$i_{ma} = \frac{1}{4}\sqrt{\frac{F}{K'(\theta)}} \tag{4.11}$$

Since the value of the main current is dependent on the rotor position, the current commutation is required before the rotor reaches the zero degree rotor angle. The next phase must start conducting before the rotor reaches zero degree and in this way the continuity has to be maintained. Figure 4.21 shows the method of calculation of the current commands per phase for the desired radial forces. Hence, if i_{ma} is known, the bridge currents can be calculated in the levitation region from Equation 3.109. Since there is geometrical shift of the rotor in each phase, the current commands for phase-B and phase-C require a co-ordinate transformation. Similarly, the bridge currents in phase-B and phase-C can be calculated.

4.6.2 Verification with FE model

In order to verify the analytical method of current calculation, an FE analysis is done. Two different current calculation schemes are applied, firstly using a square wave i_m and secondly by varying i_m. Initially, the main current i_m is fixed at 6 A in each phase and the required bridge current i_{b2a} is calculated for phase-A by taking a constant radial force of 12 N in each rotor position. The bridge currents i_{b2b} and i_{b2c} are calculated analytically using Equation 109 and Equation 110. The values of K'(θ) are calculated analytically for a rotor angle of -15^0 to 0^0 for one phase using Equation 3.100. Figure 4.23 shows the plot of the analytically calculated values of the bridge currents. Figure 4.24 shows the constant radial force, F_y of 12 N obtained from the FE model. These values are obtained by putting the calculated bridge current values in the FE model. Figure 4.25 shows the torque obtained from the FE model using the calculated bridge currents for a 12 N force. It can be observed that, by using square wave main current, the required bridge current, i_{b2} can be computed properly and a constant radial force of 12 N can be generated at every rotational position. The FEM and analytical results suggests that, less bridge current is required in the region where the stator and rotor poles are overlapped and aligned. It can also be seen that while maintaining a constant radial force, the torque decreases. In order to avoid zero torque production, the current in the next phase has to start rising. It can be observed from Figure 4.23 that at zero degree rotor angle the torque approaches a minimum value, as such the current in phase-B is increased in order to obtain the value of 12 N. The zero degree rotor angle is the overlapped position of rotor i.e. the turn-on angle of phase-B. Similarly, the phase-C is

excited with the currents required to obtain a 12 N of force. Thus, by proper switching of currents in each phase the zero torque production can be avoided and by controlling the current with the required bridge current values, each phase can produce 12 N of force at each rotor position.

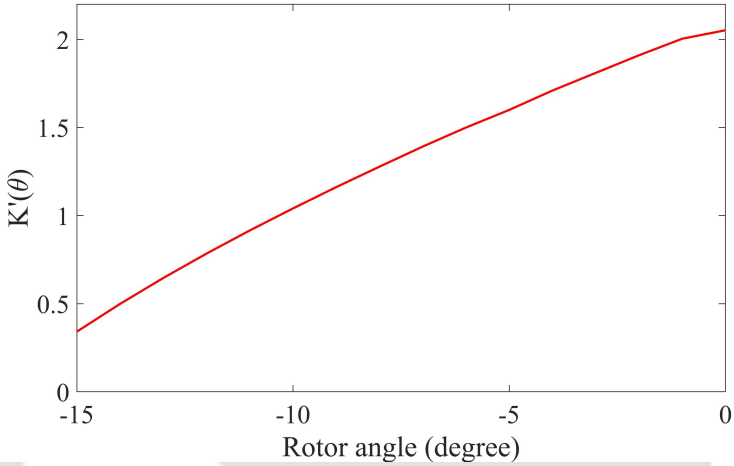

Figure 4.22: Analytical value of $K'(\theta)$ per phase.

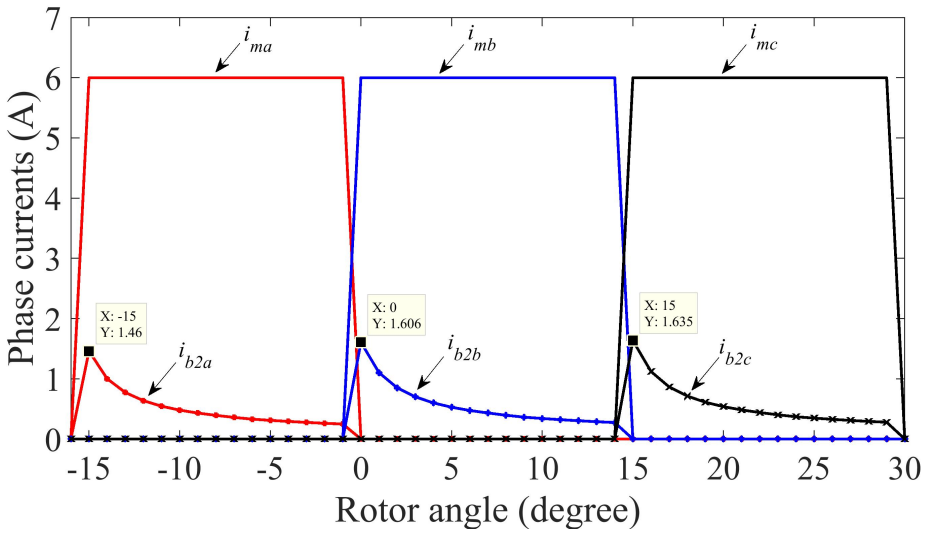

Figure 4.23: Analytical results of main current i_m and bridge current i_{b2} in phase-A, phase-B and phase-C

In the second scheme the main current i_m is obtained using Equation 4.11 and using Equation 4.10 the bridge current i_{b2} is predicted for every rotational position in phase-A. The bridge currents in phase-B and phase-C are calculated similarly using the co-ordinate

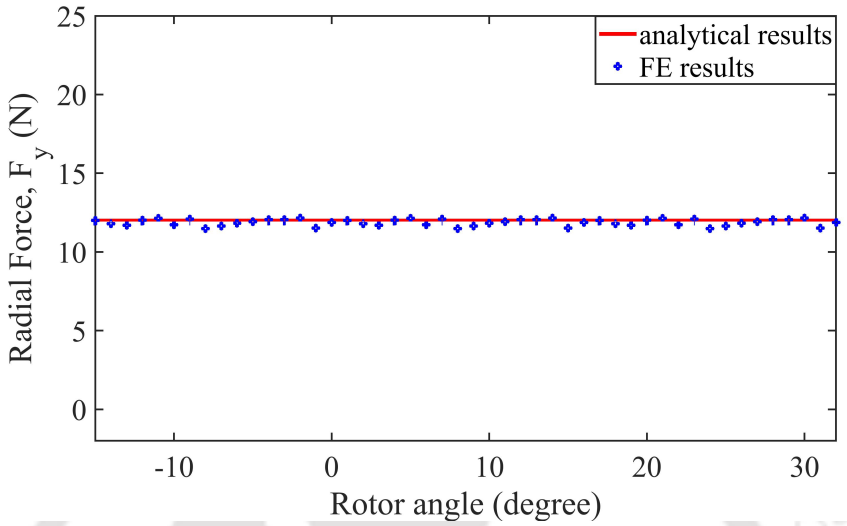

Figure 4.24: Analytical and FE results of radial force F_y

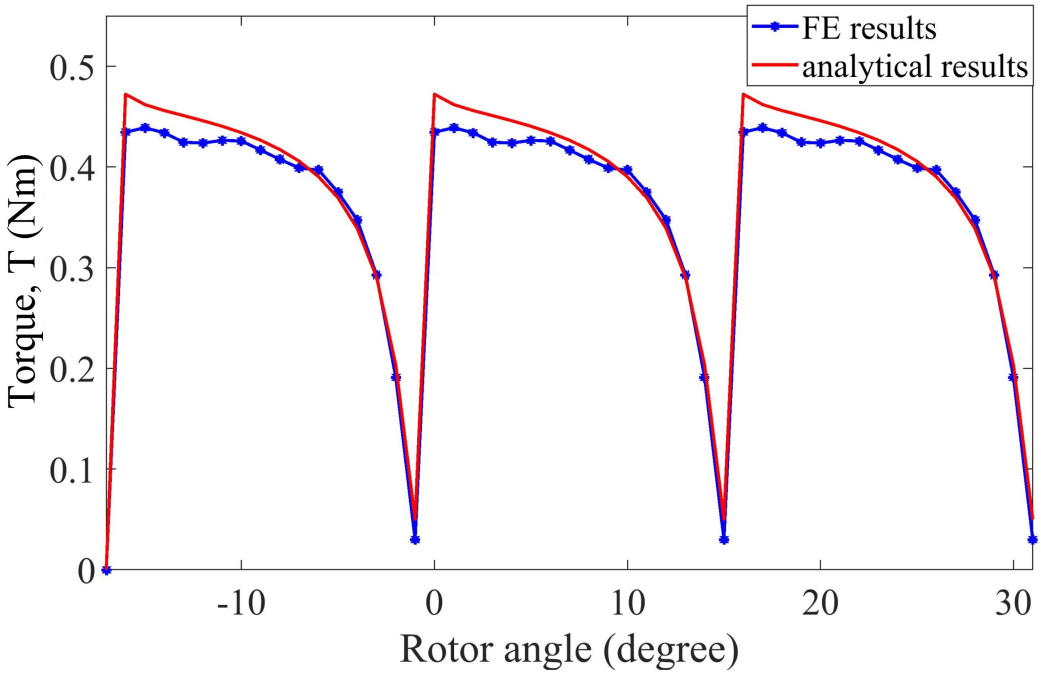

Figure 4.25: Torque with square wave i_m and varying i_{b2}

transformation. For a radial force of 12 N in the y-direction the analytical results of main current and bridge currents are obtained as shown in Figure 4.26. Figure 4.27 shows the torque obtained from analytical and FE model by using the calculated main currents and bridge currents for 12 N force.

It can be observed that with the current calculating scheme of varying main current

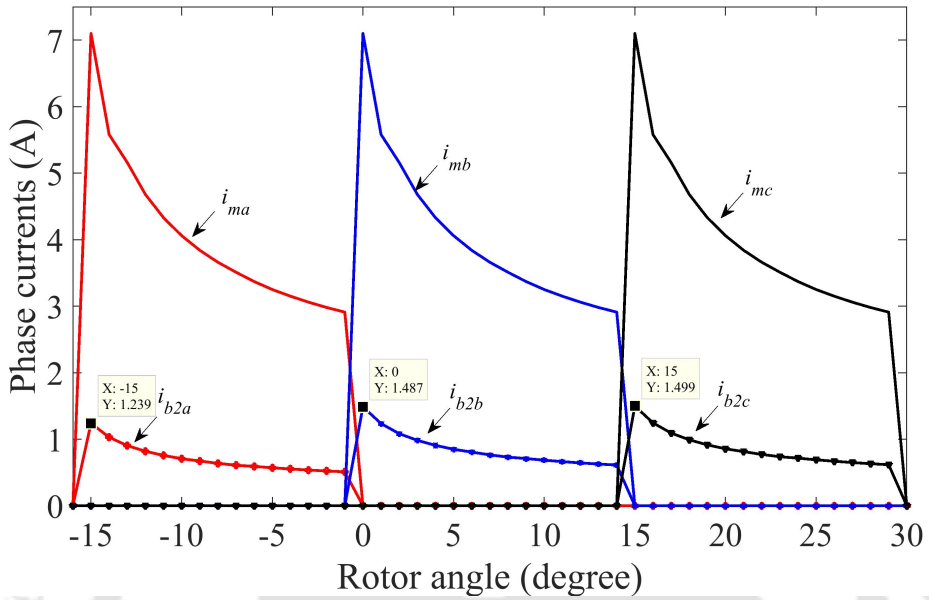

Figure 4.26: Analytical results of main current i_m and bridge current i_{b2}

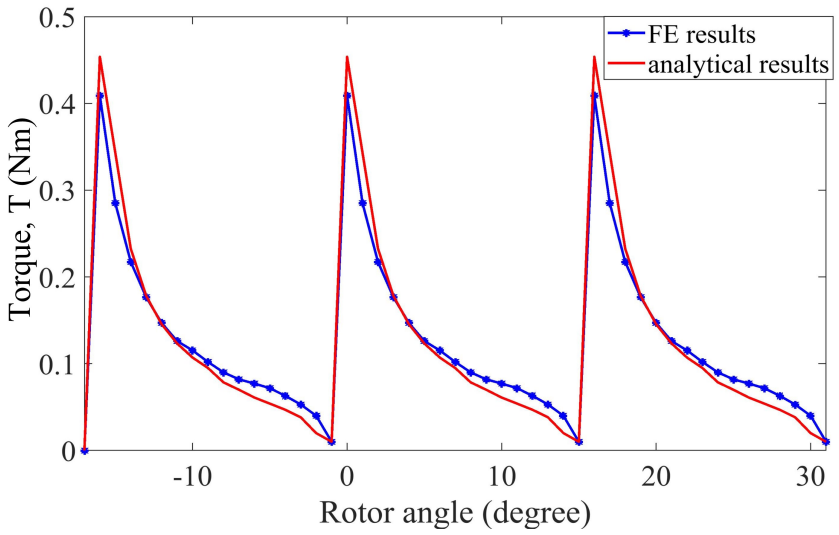

Figure 4.27: Analytical and FE results of torque for varying i_m and i_{b2}

and bridge current, the currents are high at the region of unaligned position and gradually decreases as it reaches the aligned position as seen in Figure 4.26. Moreover, the values of bridge current is higher in phase-B and phase-C. However, the torque decreases significantly as the rotor moves from the overlapped to an aligned position. Thus, this scheme makes a compromise in order to produce average torque while maintaining a constant radial force of 12 N. In this process, as the 12 N radial force is obtained in

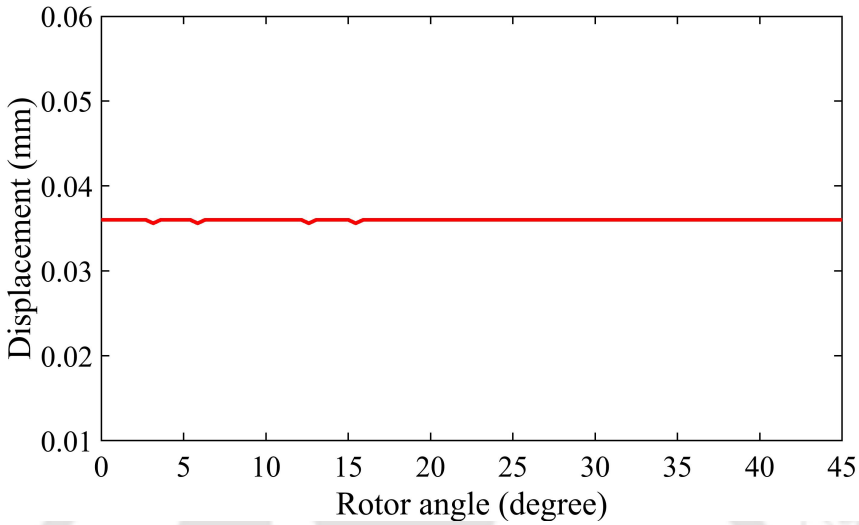

Figure 4.28: FE results of displacement in y-direction for constant radial force of 12 N

the y-axis direction a radial displacement also occurs in that direction. The radial force produced due to the injection of bridge currents creates a radial displacement of the rotor. The radial displacement is calculated analytically using Equation 3.112. This radial displacement is further analysed in the next section. Figure 4.28 shows the displacement obtained with the proposed scheme for a constant radial force of 12 N in y-direction. It can be observed from Figure 4.25 and Figure 4.27 that the magnitudes of peak average torque with both the current control scheme is same however with varying winding currents the mean torque decreases especially in regions from [-14^0, -1^0]. It can also be noted that the currents near the aligned position are smaller than those in the unaligned position for the same radial force. The obtained results illustrate how both levitation and rotation can be achieved simultaneously by maintaining the required values of current in each phase. This analysis can help in developing a closed loop controller for the levitation by controlling the bridge currents. BCW can create force by injecting bridge currents which interact with the main current and perturb the magnetic field. It has to be noted that, with only the bridge currents the motor will behave as a normal motor with no force production. This is because, with the absence of main current there will be no perturbation of current in the coils, and the bridge current will be equal in each coils. As there will be a balance in the coil currents no force will be created.

4.7 Finite element analysis of the bridge currents considering static rotor eccentricity

The current calculating algorithm as suggested in section 4.6 helps in evaluating the independent current required to be injected in the windings in obtaining the desired radial forces. The above analysis is done under direct current excitation in the coils, however practically SRMs work with a power electronic converter. In this section, a simulation is done to investigate the bridge currents in controlling the rotor displacement when the rotor is eccentric. The bridge currents and the main currents are generated using power converters.

As suggested in the principle of BCW scheme, a power converter is required for the main current and in the same winding separate isolated power converters are connected in between the bridge terminals to produce bridge currents for radial force in x and y direction. Due to the action of radial force a displacement occurs in the rotor. This occurs mainly due to the unbalance in the magnetic field which produces a lifting force in the direction of maximum magnetic field density. The radial displacement is proportional to the radial force and current in the windings. It is observed from the analysis in section 4.6 that with a radial force of 12 N, an average displacement of 0.036 mm is obtained. In this section, an FE model of the motor is designed in Ansoft Maxwell 2D considering a rotor displacement of 0.036 mm in y-direction. An asymmetric bridge converter of 50 V, 8 A current rating is designed for the main current converter. It is initially connected with the FE model and analysed under rotating condition at a constant speed of 1500 rpm.

Figure 4.29 shows the FE model of the proposed motor in Simplorer© equipped with a voltage source converter circuit for the main current i_m. Each phase's windings are connected according to the bridge configured winding and no power is supplied in the bridge terminals for force production. This simulation is done to predict the radial forces due to the presence of static rotor eccentricity. In order to obtain a non-zero torque profile, the turn-on angle is chosen as -15^0 from an overlapped position as shown in Figure 4.30(a) and the turn-off angle is chosen as 0^0 at the aligned position as shown in Figure 4.30(b).

Figure 4.31 shows the profile of the main current i_m in each phase's winding for varying rotor position. A radial force in each phase axes direction due to the radial displacement in y-direction and is shown in Figure 4.32. It can be observed that at the aligned position with main current i_m = 6.3 A, the radial force obtained is 12 N. Since,

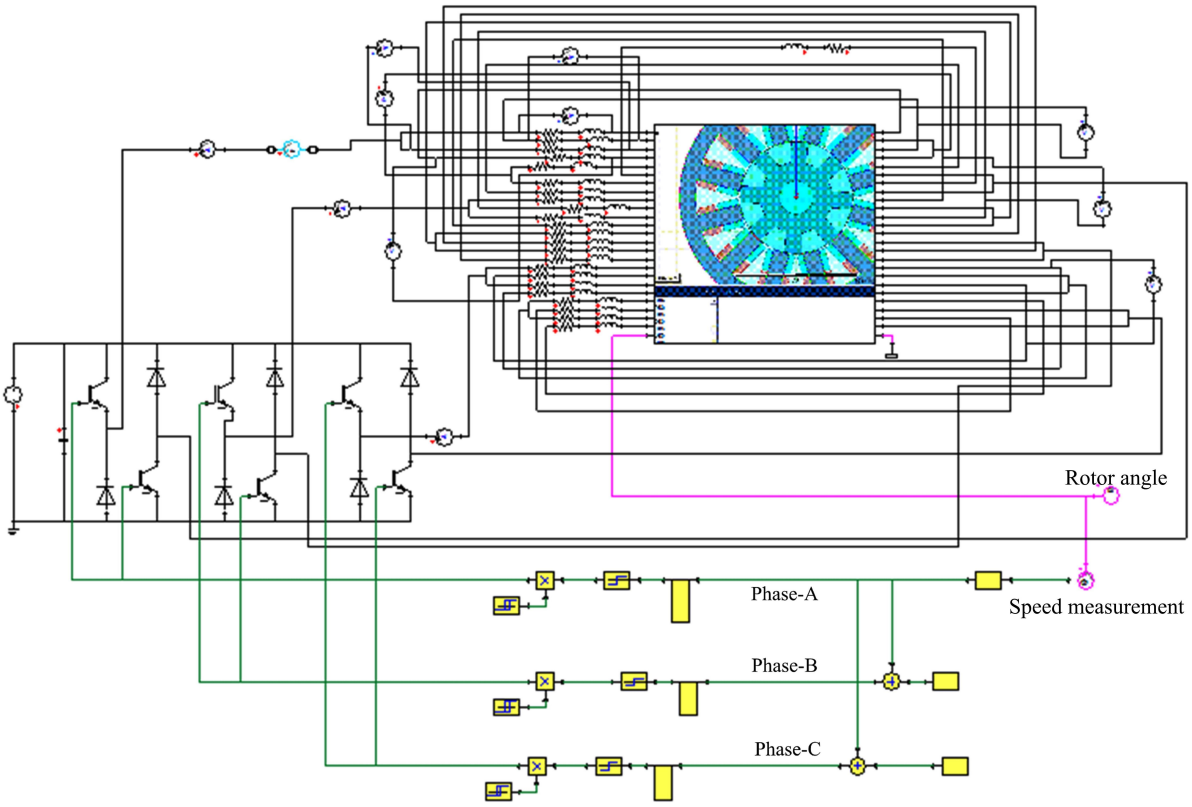

Figure 4.29: FEM simulation of the motor with the main converter drive system in Simplorer

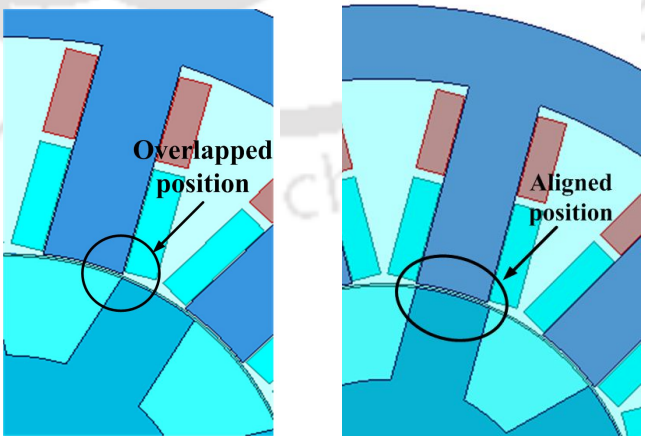

(a) (b)

Figure 4.30: Rotor position at (a) overlapped position (turn-on angle) (b) aligned position (turn-off angle)

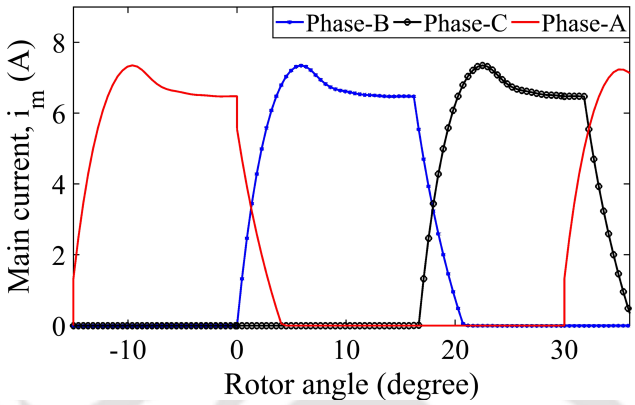

Figure 4.31: FEM results of main current i_m

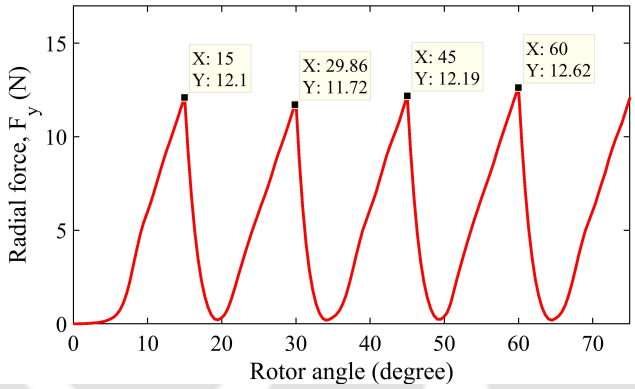

Figure 4.32: FEM results of radial forces, F_y in each phase direction.

it is a voltage source converter, the current is not constant but starts increasing and commutates after a certain period. As such, in this analysis the peak radial force at the aligned position is obtained as 12 N with the respective main current. The magnitude of the peak current for the concerned radial force is approximately same as the current calculated from the analytical method shown in Figure 4.23. Again, it has to be noted that with the change in the air gap length due to eccentricity, the flux linkage changes in each coil of the bottom bridge winding. Figure 4.33(a), (b) and (c) shows the change in flux linkages of the coils due to the presence of radial displacement in the airgap. The flux linkages in SRM are dependent on current and rotor position, so change in any of these leads to variation in the flux linkage profile.

The radial force obtained due to displacement in the rotor system can be balanced by injecting bridge current i_{b2} in between the bridge terminals (c1-d1), (c2-d2) and (c3-d3). Separate asymmetric bridge converter circuits are modelled and connected in the bridge terminals as shown in Figure 4.34. A low power rating converter of 20 V and

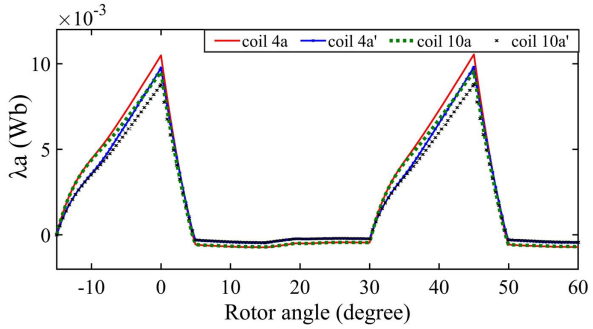

(a)

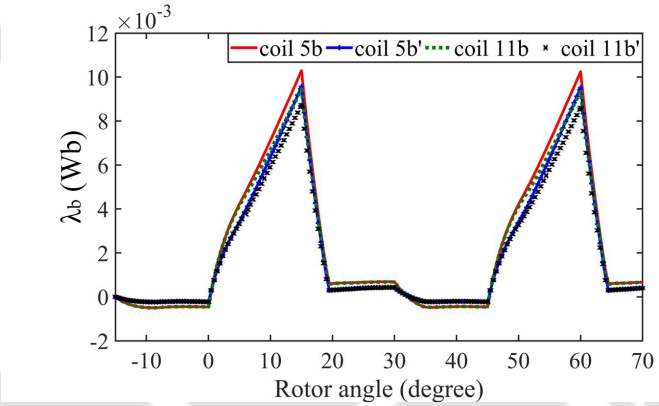

(b)

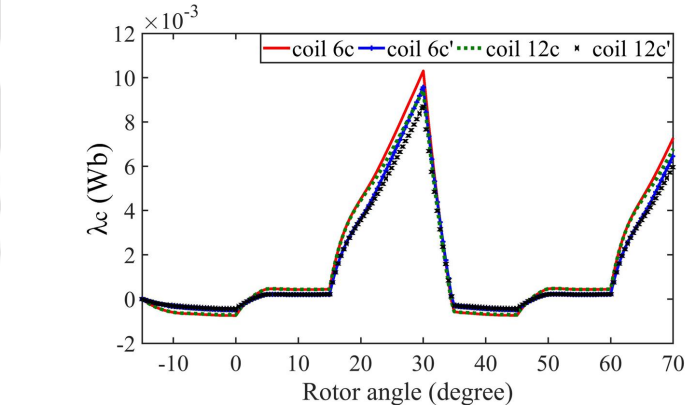

(c)

Figure 4.33: Flux linkage in (a) phase-A (b) phase-B and (c) phase-C with rotor displacement of $x = 0.036$ mm

maximum current of 1 A as reference are taken for the bridge current converters and the model is simulated. Figure 4.35 shows the reference bridge currents and the actual bridge currents to produce an equal and opposite radial force in the motor model. It can be observed from Figure 4.36 that with the injection of required bridge currents in phase-A,

phase-B and phase-C a radial force in the opposite direction can be obtained. It can

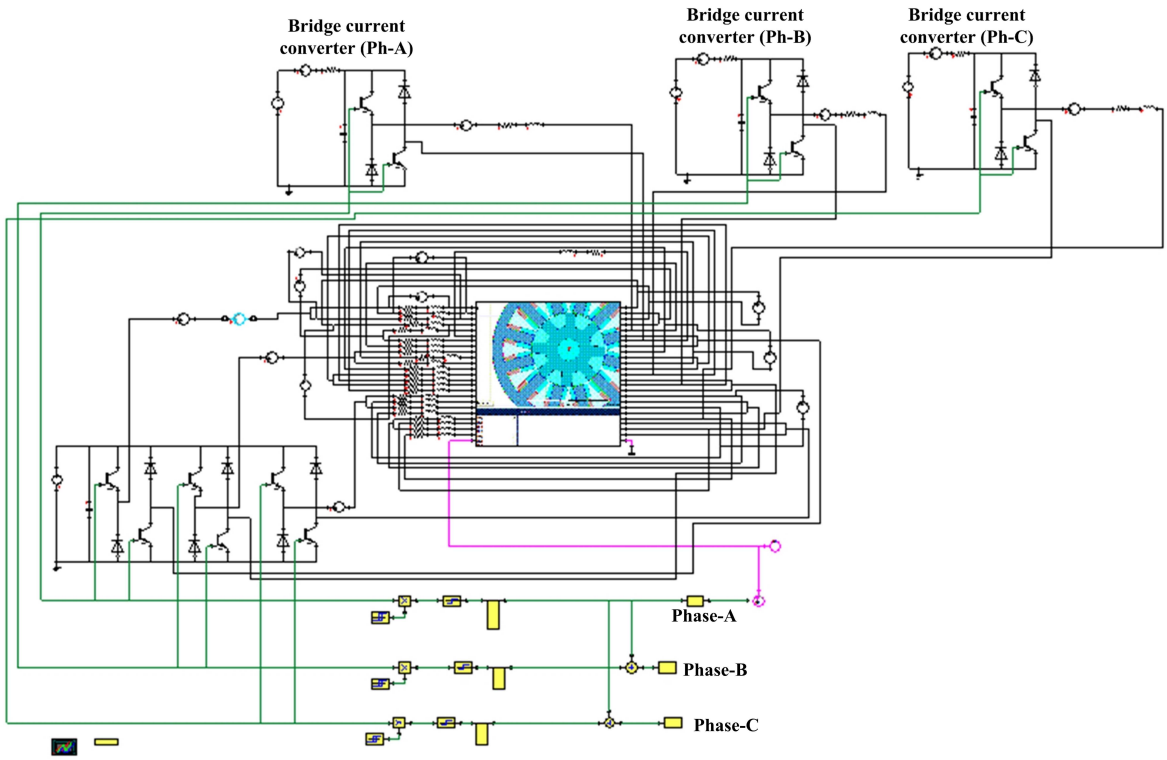

Figure 4.34: FEM of the motor with drive system for main current (i_m) and bridge current (i_{b2})

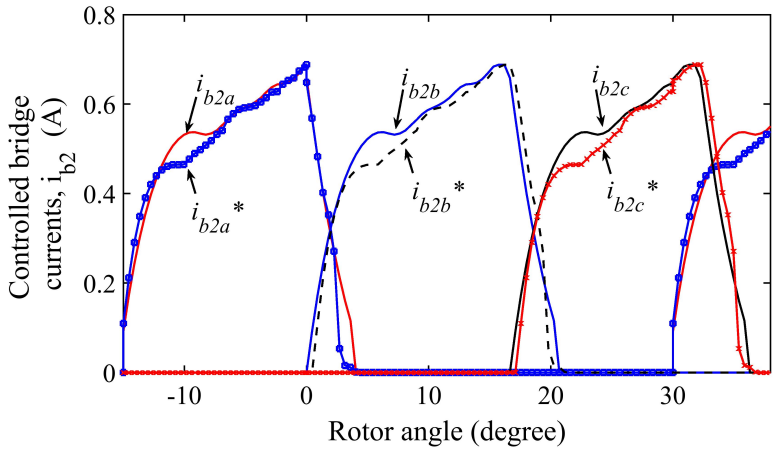

Figure 4.35: Actual bridge current, i_{b2} and reference bridge current, i_{b2}* in windings of phase-A, phase-B and phase-C

be observed from Figure 4.36 that the generation of radial force, F_y due to the rotor

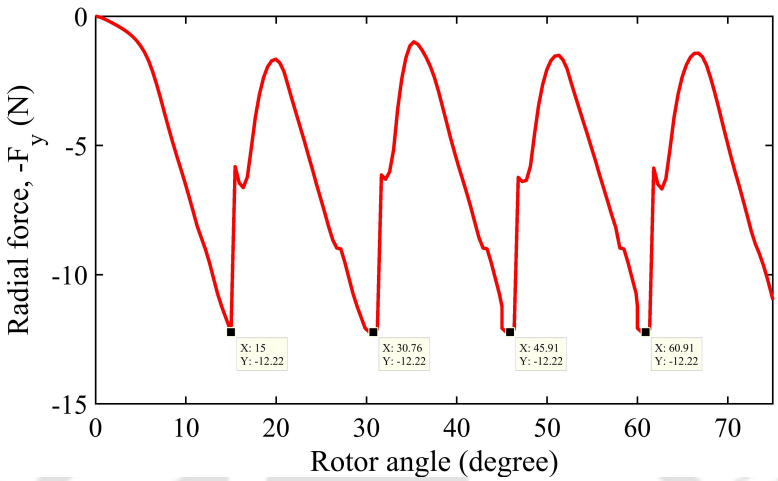

Figure 4.36: Radial force F_y in the opposite direction with bridge current i_{b2}

radial displacement can be effectively controlled by injecting controlled bridge current in the opposite stator pole. It can be observed that with the injection of required bridge currents in between the bridge terminals, a radial force is generated in the opposite y-direction resulting in a pull of the rotor towards the central position.

For the control of radial displacement, the force and current relationship as derived in Chapter 3, is used to obtain the desired bridge current to bring the rotor to its central position. The BSRM model is modelled in MATLAB/Simulink and two power converters are modelled, one for the main current i_m and another for the bridge current i_{b2}. The output from the algorithm is used as the reference current for the bridge current converter and fed into the BSRM model. The displacement is used as feedback and compared with a reference signal and the error is fed into a PID controller as shown in Figure 4.38.

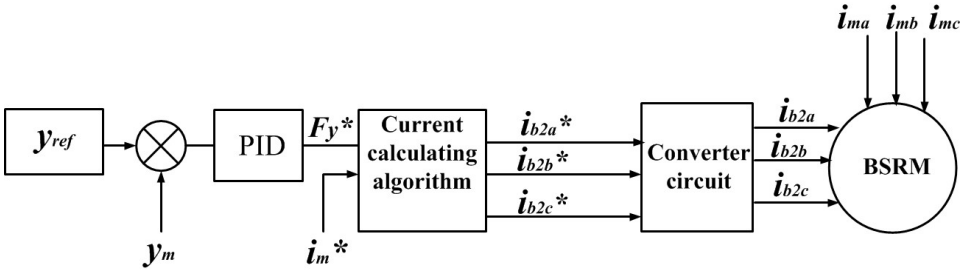

Figure 4.37: Block diagram for control algorithm of radial displacement in y-direction using bridge current

Figure 4.39 shows the response of the y-axis radial displacement from the controller output. It can be concluded that the PID controller is able to track the displacement

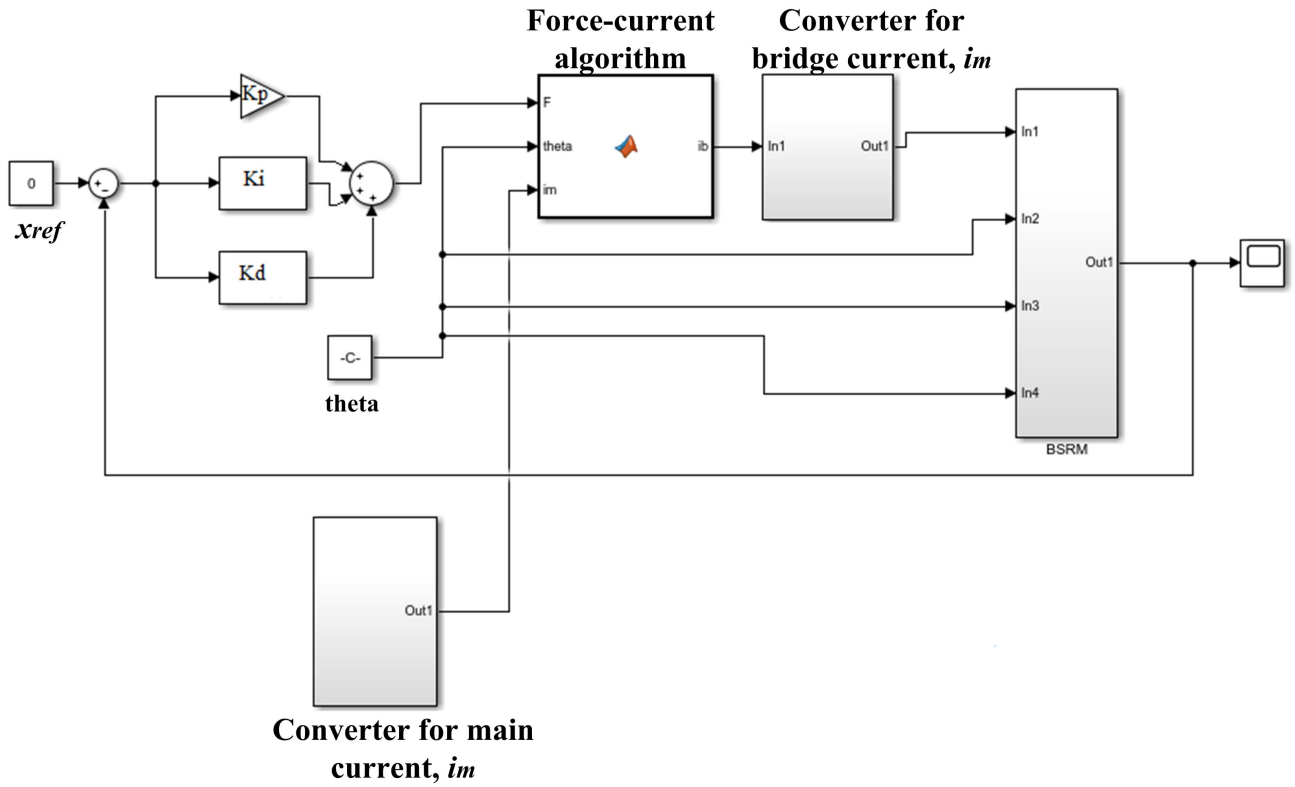

Figure 4.38: Simulink diagram of radial displacement control using PID controller

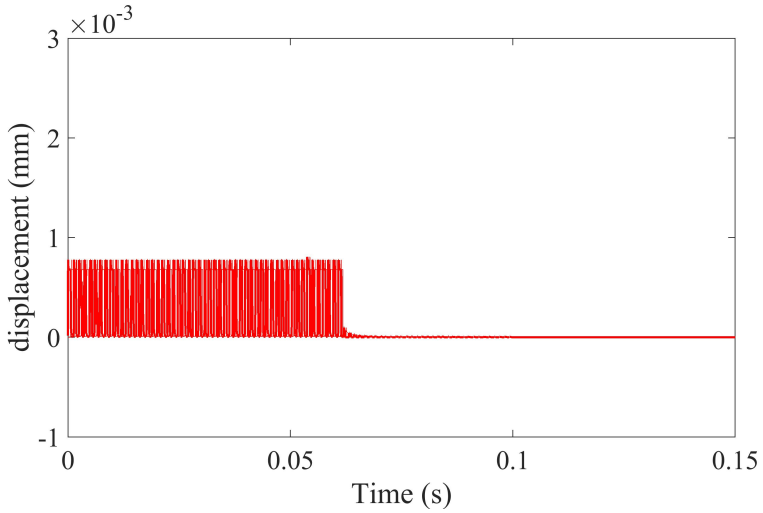

Figure 4.39: Control of radial displacement along y-axis direction

error and generate a force command required to get a stable zero position error.

Under design considerations of bearingless motors, it has to be noted that the average torque production of the motor is not hindered. An FE analysis of the BCW BSRM has

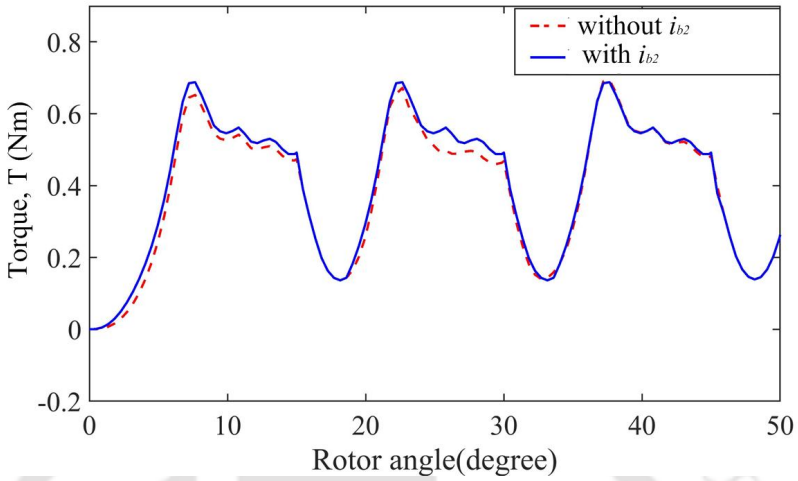

Figure 4.40: Comparison of torque with and without bridge current i_{b2}

been done with the bridge current under on and off condition and the torque production is analysed. The FEA results as shown in Figure 4.40 show the torque profile under two conditions; (i) with only main current, i_m and (ii) with both main current, i_m and bridge current i_{b2}. It can be observed that with the additional bridge current there is a little effect in the magnitude of torque but the profile of torque is not hindered and thus the performance of the machine is hardly affected. This analysis provides a significant advantage of using BCW for normal torque production by keeping the bridge terminals disconnected from the power supplies.

4.8 Conclusion

In this chapter a novel design of a speed-current controlled drive system for producing controllable radial force and torque production has been presented for BCW in BSRM. The power converters have been designed and simulated for the main current and the bridge currents, which can effectively generate the current commands for the required torque and radial forces. The results of analytical and numerical model for the drive have been significantly verified. In addition to this, the proposed drive system has been further simulated with a closed loop radial displacement control using a PID controller which can effectively control the rotor displacement. Further, based on the simulation study, a current calculating algorithm has been presented for controlling the currents in the winding for both motoring and force production. The control scheme presented in this chapter for radial force compensation using bridge currents can further help in developing a high performance control strategy with a real time controller in the future.

Chapter 5

Experimental Investigation

Contents

5.1 Introduction

The previous chapters discusses the analytical and numerical analysis of the various aspects of the BCW in switched reluctance motor. Chapter 3 presents a design methodology of a prototype for the proposed motor and discusses the numerical analysis for verification of the design. Chapter 4 provides a numerical based simulation and analysis of a speed-current control drive system for the proposed motor and also discusses the effects of the bridge current in controlling rotor radial displacement with a current control operation. This chapter presents the practical implementation of the proposed motor design and also the development of a power converter drive for the experimental purpose. The switched reluctance motor, the test rig and the converter drive has been developed from scratch for experimental analysis. The details of the development process and the experimental results have been summarized in the following sections.

5.2 Description of the test motors

For the experimental verification, two test motors have been designed and developed. The dimensions and ratings of both the motors are kept same. The SRM with the conventional winding is termed as test motor I and the SRM with BCW is termed as test motor II. The coils of both the motors are left open such that there is flexibility in the type of connections. The starting terminal of each coil is defined as 'S' and the finish terminal as 'F'. In test motor I, each phase winding comprises of four coils connected in series with the coil direction as shown in Table 5.1. Figure 5.1 represents the schematic of the test motor 1 and the coils in each stator tooth are numbered sequentially.

Table 5.1: Connection of the phase windings of test motor I

Phases	**Coil numbers**	**Terminal connections**
Phase-A	1, 4, 7, 10	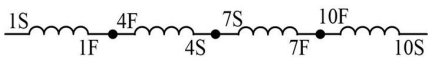
Phase-B	2, 5, 8, 11	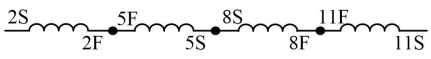
Phase-C	3, 6, 9, 12	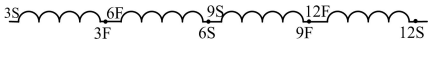

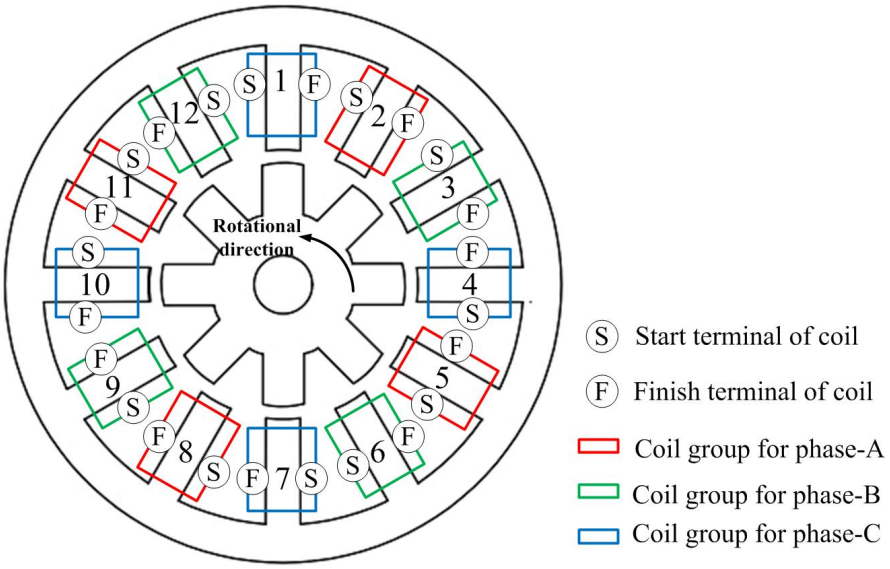

Figure 5.1: Schematic of coil groups in test motor I.

Table 5.2: Specifications of conventional SRM for test rig I

Parameters	**Values**
Rated power	750 W
Rated voltage	100 V
Number of slots	12
Number of field poles	4
Number of converter phases	3
Slots/pole/phases	4
Winding type	concentrated
Number of layers	1
Throw	1
Winding wire	SWG 22
Number of strands	2
Number of turns	80 turns/coil
Phase resistance	1.5 ohm
Class of insulation	F

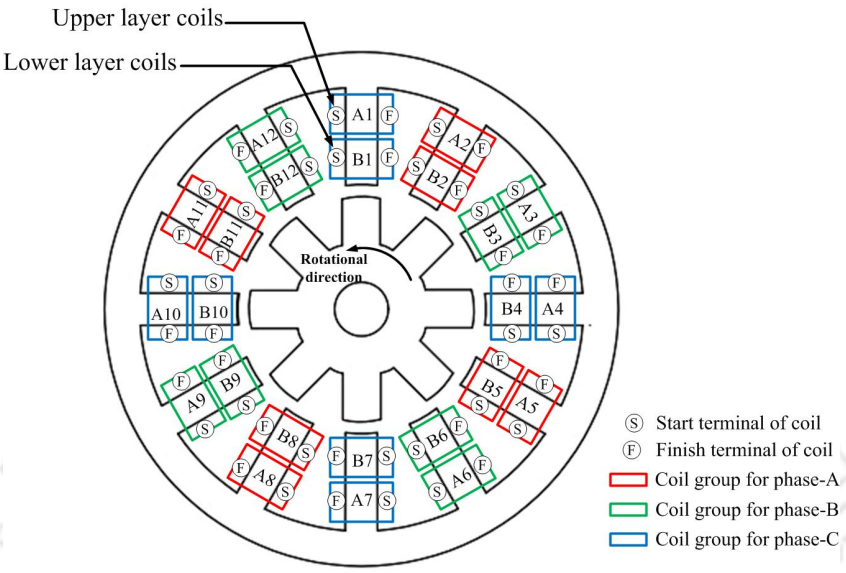

Figure 5.2: Schematic of coil groups of test motor II.

Table 5.3: Connection of the phase windings of test motor II

Phases	Top bridge	Bottom bridge
Phase-A	A10S A10F B4S B4F / A4S A4F B10S B10F	A1S A1F B7S B7F / A7S A7F B1S B1F
Phase-B	A11S A11F B5S B5F / A5S A5F B11S B11F	A2S A2F B8S B8F / A8S A8F B2S B2F
Phase-C	A9S A9F B3S B3F / A3S A3F B9S B9F	A12S A12F B6S B6F / A6S A6F B12S B12F

Table 5.2 gives the specification of the test motor I of test rig I. In test motor I, each stator tooth consists of one coil and the number of turns of coil is taken as 80 turns/coil. Figure 5.2 shows the schematic of coil groups of test motor II. The direction of coil winding and the coil numbers are defined sequentially in Figure 5.2. Table 5.3 gives the coil connections of each bridge of BCW in test motor II. In test motor II, each phase comprises of two bridges termed as top bridge and bottom bridge. Each of the bridge is connected in such a way that there is a terminal in between the coil connection. These terminals are used for connecting the bridge current power supply. Table 5.4 gives the specifications of the test motor II of test rig II. In test motor II, 'S' denotes the start terminal of the coil and 'F' denotes the finish terminal of the coil.

Table 5.4: Specifications of the SRM for test rig II

Parameters	**Values**
Rated power	750 W
Rated voltage	100 V
Number of slots	12
Number of field poles	4
Number of converter phases	3
Slots/pole/phases	4
Winding type	concentrated
Number of layers	2
Throw	1
Winding wire	SWG 22
Number of strands	3
Number of turns	40 turns/coil
Phase resistance	0.5 ohm
Class of insulation	F

5.3 Development of the experimental test set ups

The main component of the experimental set up is a 12/8 SRM configured with bridge winding. The main purpose of the development of the motor is to establish the radial force capability in a SRM which is configurable for bridge winding. The motor is designed similar to the design of electrical motor following the industrial standards. The geometrical parameters and specifications of the motor as obtained from the analytical calculations in Chapter 3, has been implemented in the practical motor. Two test set ups have been developed where test rig I contains the conventional 12/8 SRM and test rig II comprises of a 12/8 SRM with BCW. In test rig II, the test motor II has a fixed bearing on one side of the shaft and the other side has a clearance in between the rotor and shaft. A back-up bearing is provided on the shaft side which has clearance. A back up-bearing is typically required in case of power failure or control system failure. In test rig I, the motor is termed as test motor I and is wound with single layer coils. The phase winding of the motor is connected in a conventional manner i.e., four stator coils

perpendicular and in diametrically opposite slots are connected to form a phase. In test rig II, the motor is termed as test motor II and is wound with double layers of coil and the windings of the motor are connected in the form of bridge configured winding. The following section demonstrates the development of the two test rigs. The dimensions of the stator and rotor core of both the test motors are kept same.

5.3.1 Fabrication of the experimental test rigs

For fabrication of the motor, M-19 non-oriented electrical steel is used which is a soft magnetic material. Initially these sheets are laminated and cut into the shape of the stator-rotor of the motor. The cut sheets are then stacked together by pinning them down. Figure 5.3 and Figure 5.4 shows the 2D model of the stator and rotor core with dimensions developed in AUTOCAD software package. Figure 5.5(a) and Figure 5.5(b) demonstrates the practical procedure of stacking of the stator and rotor cores. Figure 5.6 shows the complete stator of the two motors after stacking. Each figure in this section below depicts the step by step development of the two test rigs.

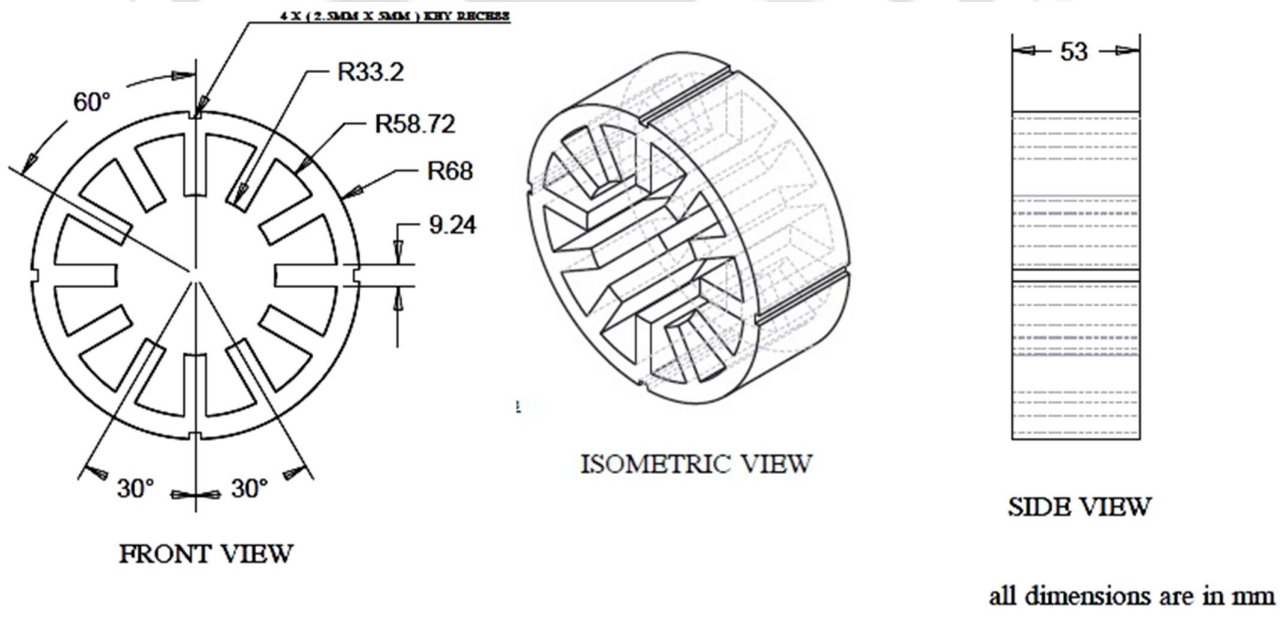

Figure 5.3: CAD model of stator with dimensions.

Figure 5.7(a) shows the stator core of test motor I, wound with single layer coil for the conventional SRM. Figure 5.7(b) shows the stator core of test motor II wound with two layer coils for BCW. Two shafts have been designed individually. The shaft for test rig I is designed such that it is supported with mechanical bearings at both ends. In

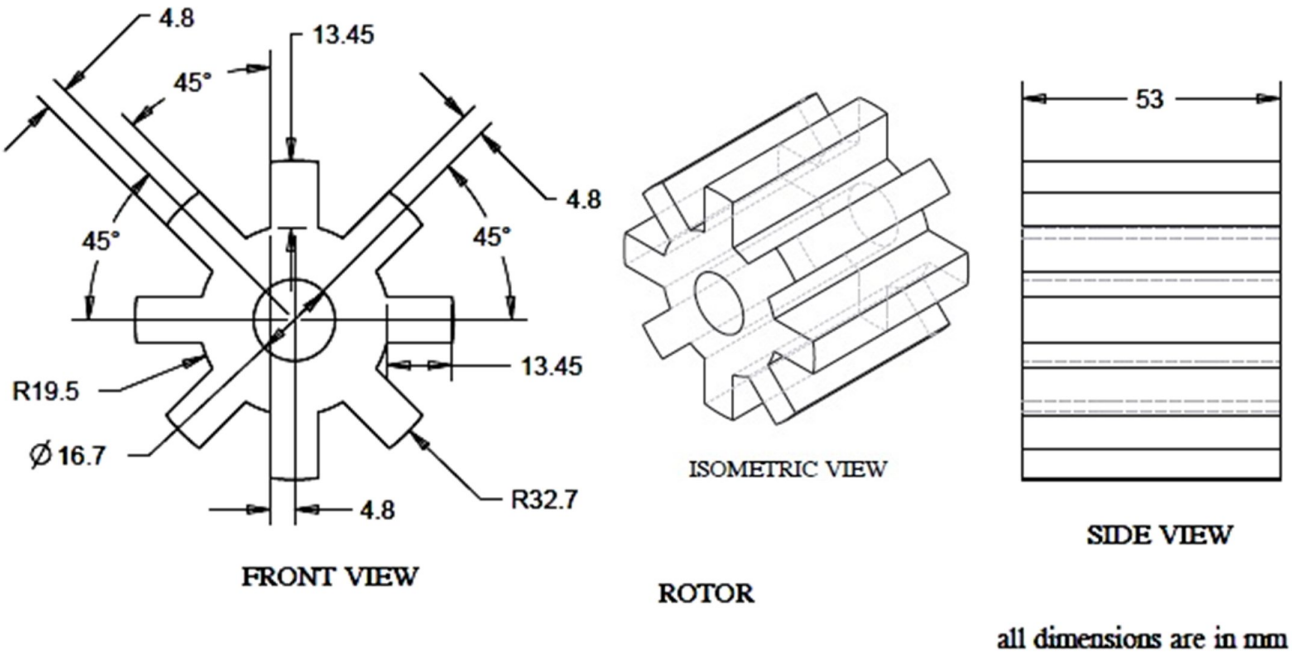

Figure 5.4: CAD model of rotor with dimensions.

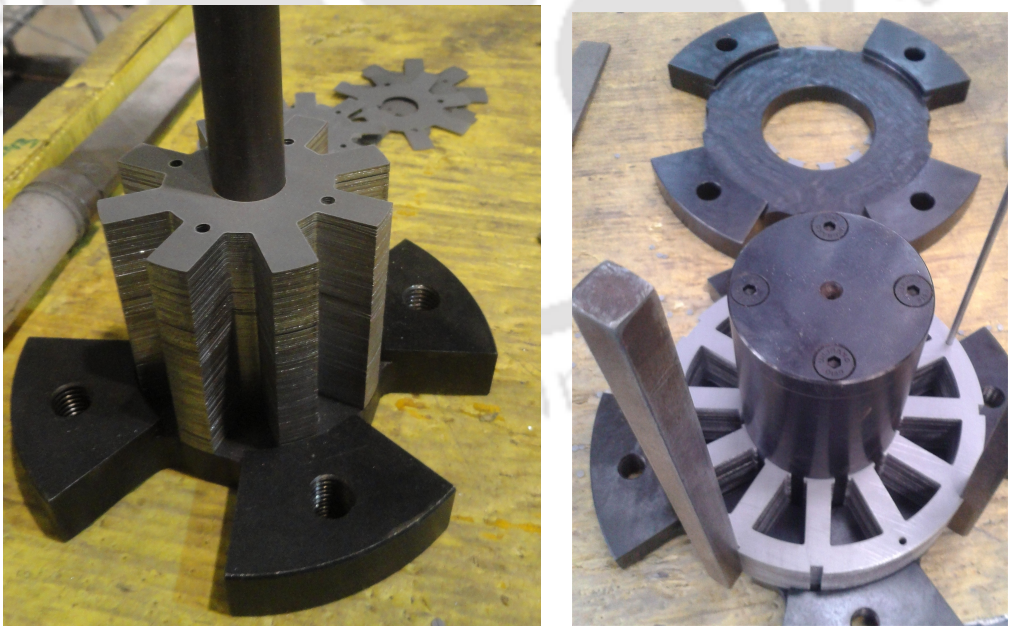

(a) (b)

Figure 5.5: Stacking of laminated steel sheets for (a) rotor and (b) stator

this case, the bearings are fixed with the end cover plate of the motor and the shaft is supported by these bearings. Figure 5.8 shows the design of the shaft with dimensions

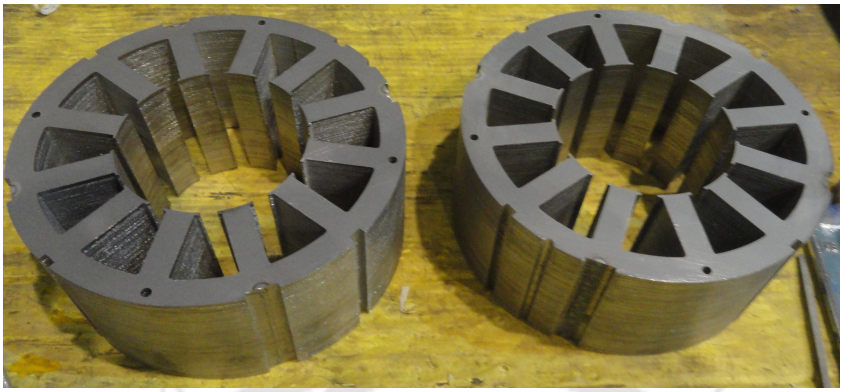

Figure 5.6: Stator cores after stacking.

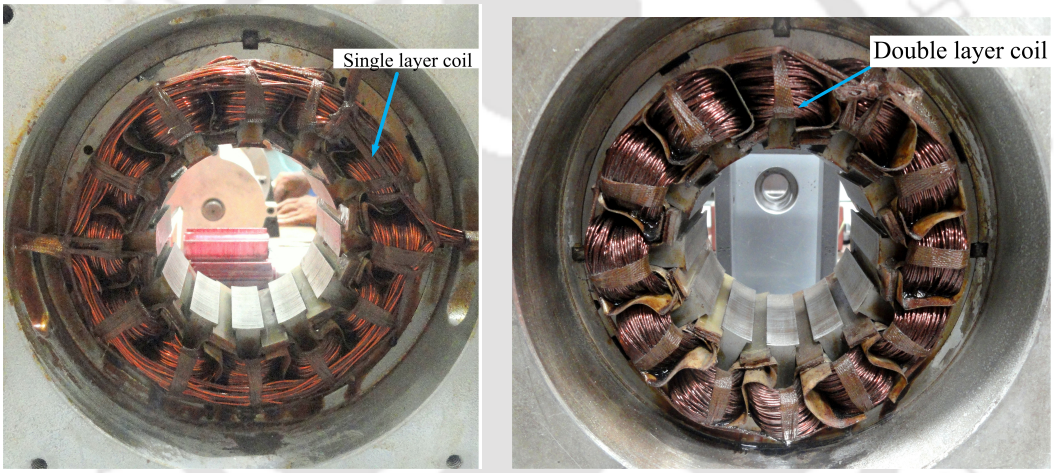

(a) (b)

Figure 5.7: Stator cores with (a) single layer coil for conventional SRM (b) double layer coil for BCW BSRM.

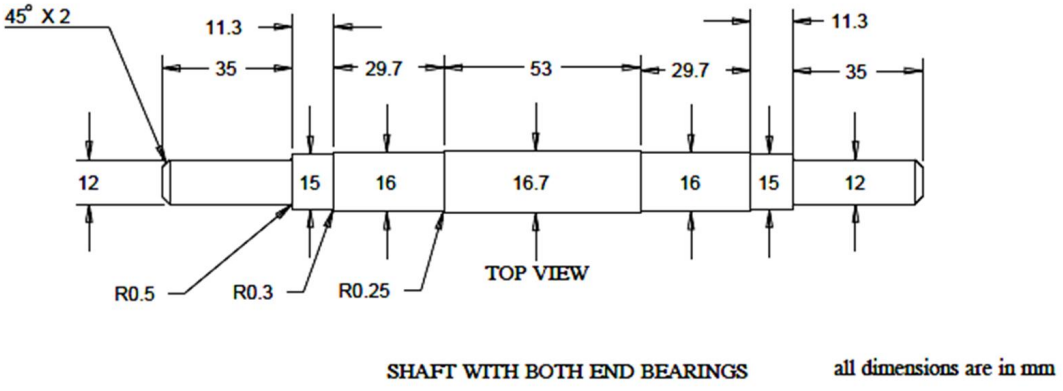

Figure 5.8: Shaft with dimensions for test rig I.

for test rig I and Figure 5.9 shows the assembled rotor and shaft for test rig I.

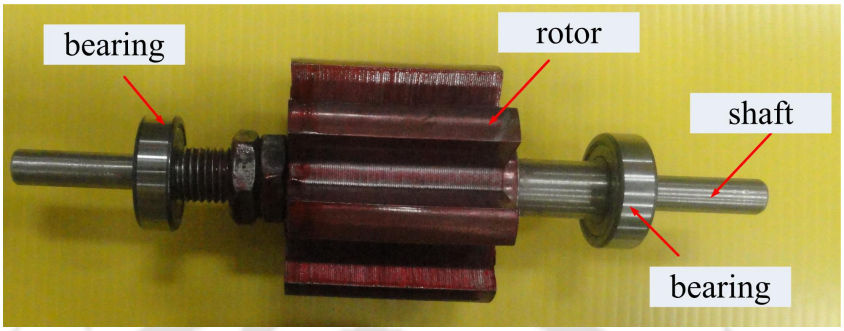

Figure 5.9: Rotor and shaft supported with bearings on both sides for test rig I.

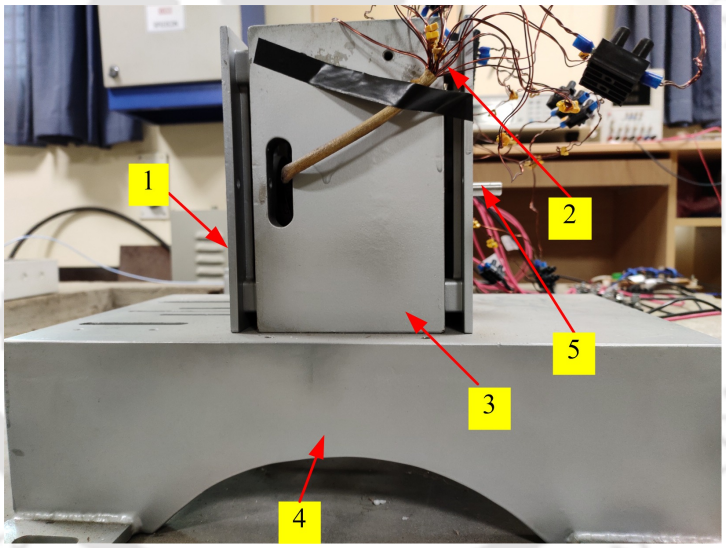

Figure 5.10: Experimental set up of the test rig I, (1) end cover plate (2) coil terminals (3) test motor with the stator housing (4) base plate (5) shaft.

Figure 5.10 shows the experimental set up of test rig I. It can be observed that the test motor I is inside a stator housing and placed over a base plate. Both the sides of the motor are covered with cover plates and the shaft is supported by the bearings placed inside the cover plates. The coils of the test motor I are connected as given in Table 5.2. The shaft for test rig II is designed in such a way that one end is supported with a fixed mechanical radial bearing and the other end features a clearance between the shaft and the rotor. The end of the shaft which has a clearance is placed inside a bearing house and a back-up bearing is placed in the bearing house. In this case the back up bearing is placed for a normal start operation of the motor. Figure 5.11 shows the design of shaft with dimensions and Figure 5.12 shows the assembled rotor and shaft for test rig

II. It can be observed in Figure 5.12 that one side of the shaft has a mechanical bearing attached to it and the other end has no bearing. There is a small threaded portion made at one side with nuts tightened on it. This is done to fix the rotor with the shaft and avoid any slip.

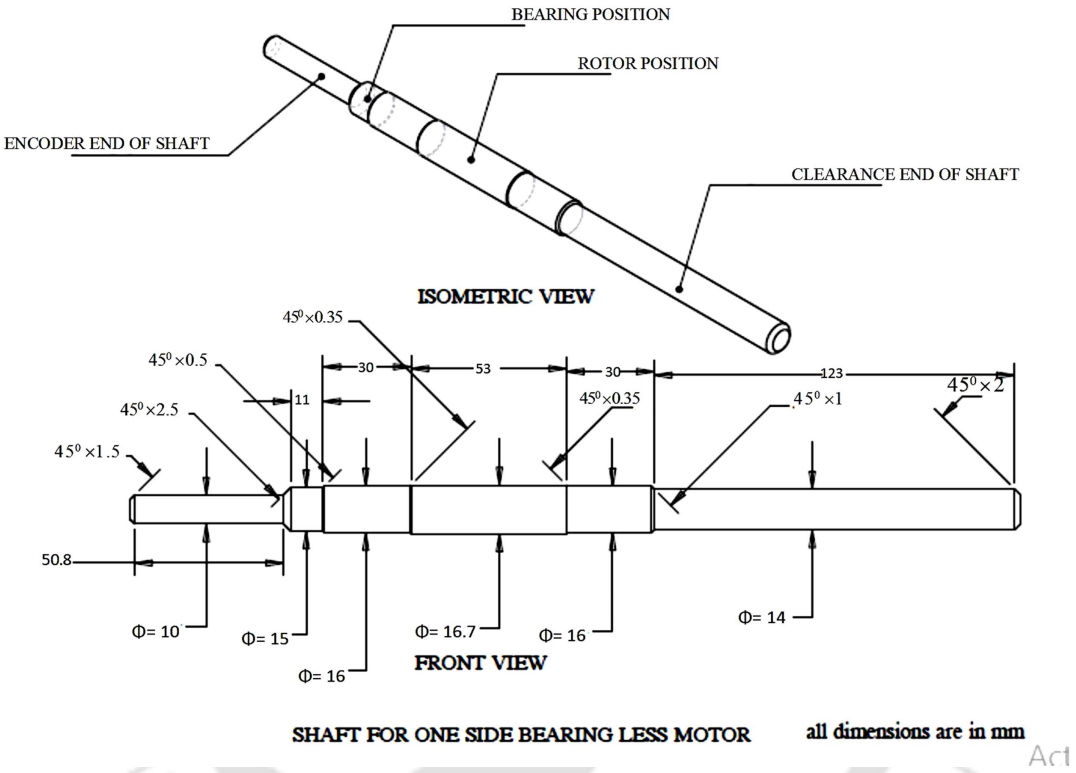

Figure 5.11: CAD model of shaft with dimensions for test rig II

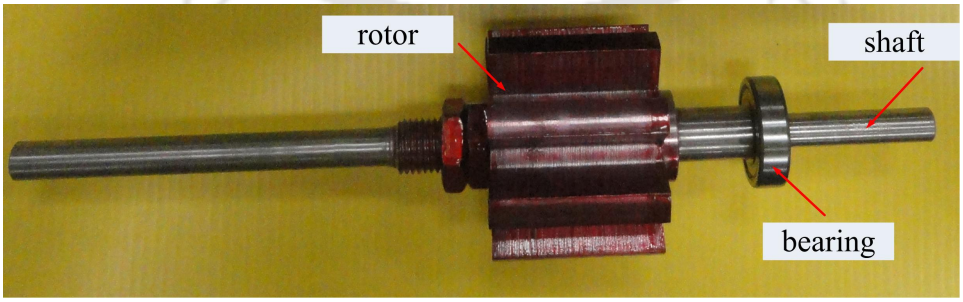

Figure 5.12: Rotor and shaft with one side bearing for test rig II

Figure 5.14 shows the set up of test rig II. Test rig II consists of the test motor II with the coil terminals left open for connection. The coils of test motor II are connected to form a bridge winding using molex screw terminal connectors. Figure 5.13 shows a CAD model of the test rig II. A mechanical bearing is fixed inside the cover plate of the motor

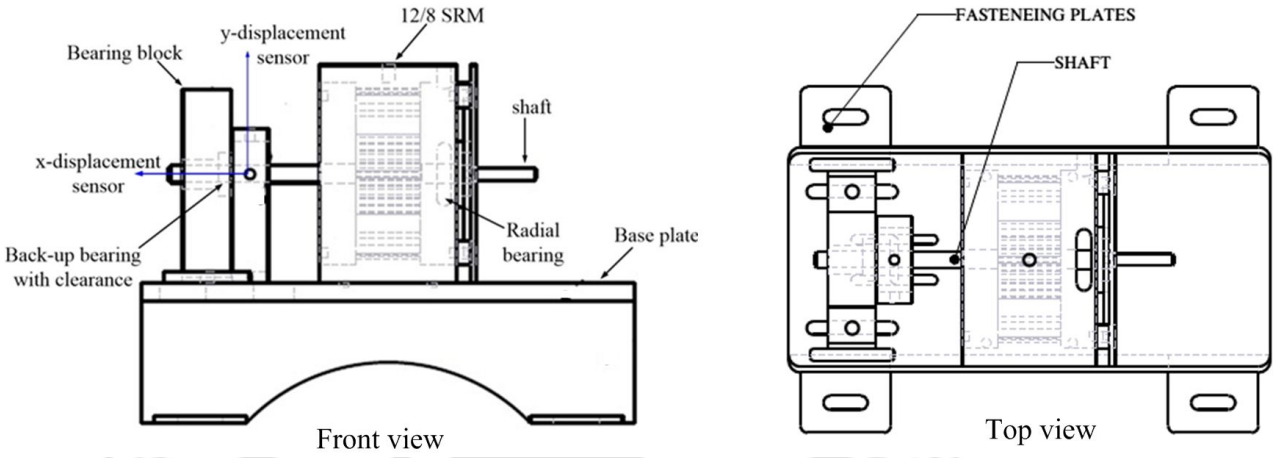

Figure 5.13: CAD model of test rig II

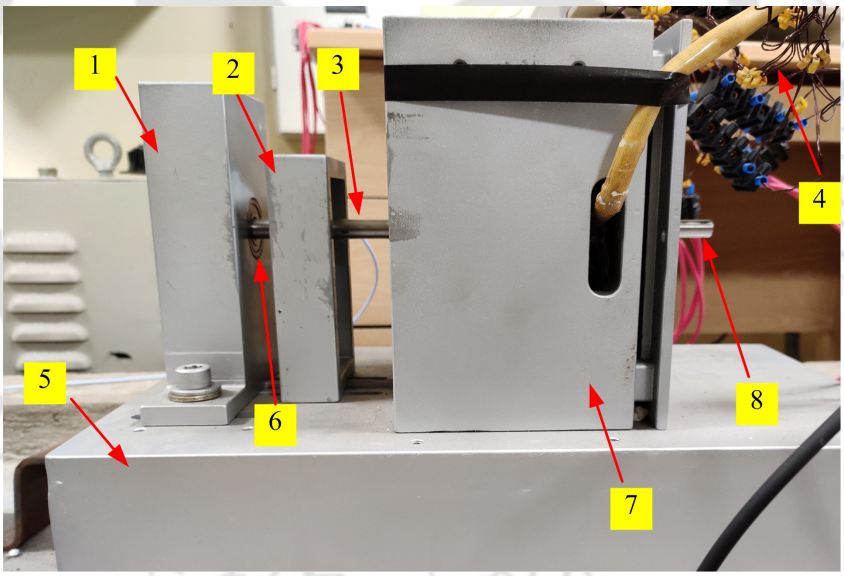

Figure 5.14: Experimental set up of the test rig II, (1) bearing block (2) displacement sensor's stand (3) shaft (4) coil terminals (5) base plate (6) back-up bearing (7) test motor with housing (8) shaft

and placed at the right side of the shaft. The left side of the shaft is supported on a back-up bearing which is placed inside the bearing house, and there is a clearance between the bearing and the shaft. The mechanical bearings are angular contact type bearings. In this set up, the test motor II is supported with mechanical bearings on one side and displacement is produced on the other side having clearance, as such axial bearing is not connected. For measurement of the displacement data a sensor stand is placed in between the motor and the bearing housing, where two proximity sensor probes in x and

y direction can be connected. Bently Nevada, 3300 XL 8 mm eddy current sensors and probes are used to measure the radial displacement of the rotor-shaft of test motor II.

5.4 Components and measuring devices used in the experimental test rigs

Test rig I and test rig II consist of the following components,

1. SRM with conventional winding for test rig I and SRM with BCW for test rig II.
2. Three phase converter for the main current in test rig I.
3. Three phase converter for the main current and single phase converter for the bridge current in test rig II.
4. A programmable DC voltage source for the main converter and separate DC voltage source for the bridge converters in test rig II.
5. Current sensors, LEM 15-NP to measure phase winding currents as shown in Figure 5.15.
6. A Bently Nevada, 3300 XL 8mm eddy current proximity transducer system for measurement of rotor-shaft displacement in test rig II as shown in Figure 5.16.
7. A NI PXIe-6363, data acquisition (DAQ) system for storing and processing of measured data as shown in Figure 5.17.
8. Connectors and 12 V battery sources for the sensors.

5.5 Hardware implementation of the asymmetric bridge power converters

In SRMs the power converter circuit is responsible for supplying power to the motor. It consists of two parts, a rectifier which supplies DC voltage and a converter which allows the flow of energy to and from the load. The working principle of this power converter has been already explained in Chapter 2. An asymmetric bridge power converter circuit is proposed for the operation of the 12/8 normal SRM with conventional winding and

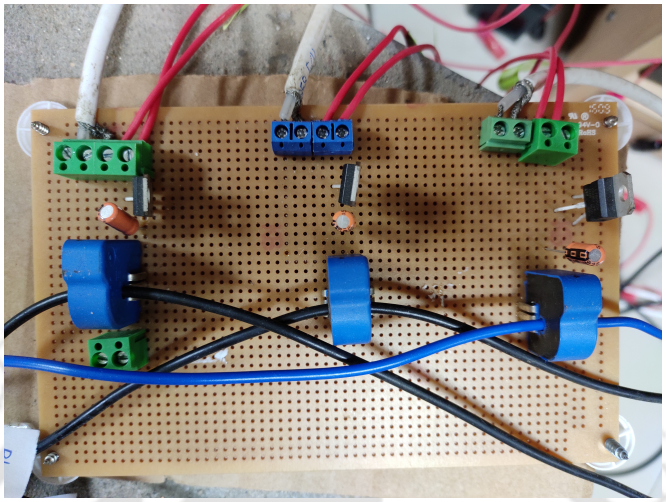

Figure 5.15: LEM 15-NP current transducers

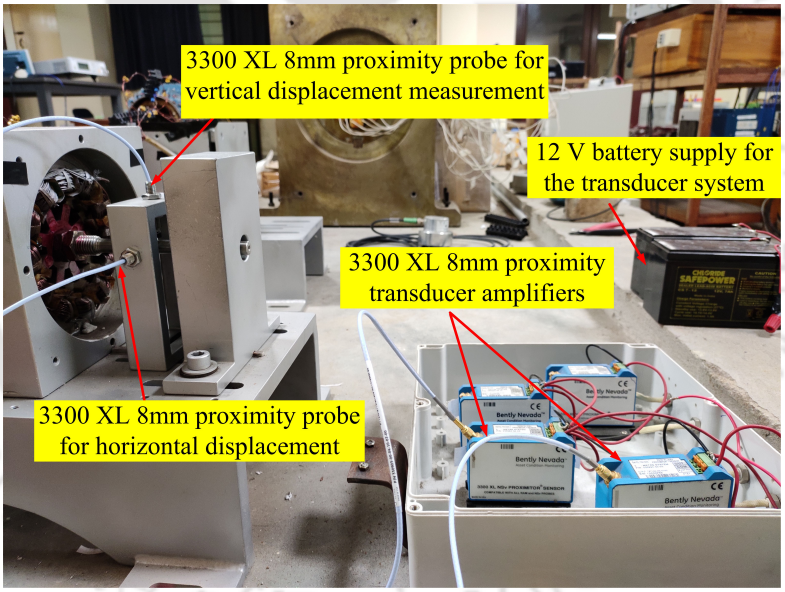

Figure 5.16: Proximity sensors for measurement of shaft displacement in test rig II

the BSRM with bridge winding. Initially, the circuit is designed in LTSpice software and then practically implemented.

The design of the converter starts with the selection of components and device ratings. The following factors have to be specified when designing the circuitry:

- power capability
- switching speed
- power rating of the driver

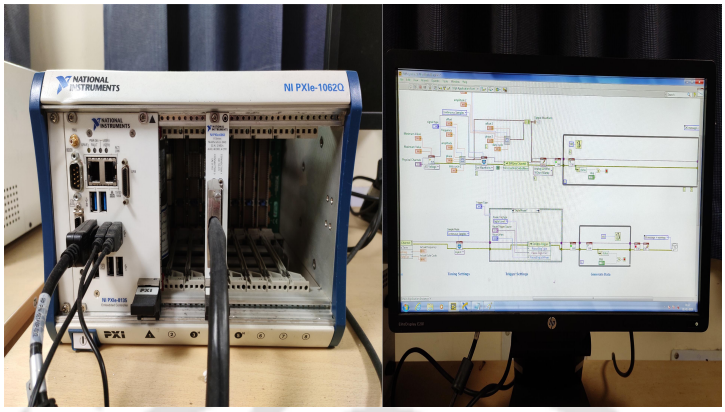

Figure 5.17: PXIE-6363 embedded controller with DAQ module for measuring and storing data

- supply voltage
- diode ratings

Since the rated voltage of the motor is taken as 100 V, the switching devices and the components have to be selected to withstand a minimum of 100 V, conduct current up to 10 A and operate at a minimum switching frequency of 1 kHz. In this case, an N-channel power MOSFET IRF540N is selected, capable to drive the motor. For controlling the MOSFETs, drivers are required to switch the two MOSFETs in each leg. In this case, the MOSFET driver IR2110 driver is chosen for driving the high side and low side MOSFETs in each phase leg. The IR2110 is a high voltage, high speed power MOSFET and IGBT driver with independent high and low side referenced output channels. For freewheeling the stored energy, diode UF5408 is used in this circuit across the load. Figure 5.18 shows the schematic of one phase leg connection with the MOSFET driver IRS2110. When the signal HIN is at logic high, the MOSFETs are turned on and current flows through the winding, and when the signals at HIN are at logic low the MOSFETs are turned off and the current freewheels through the diodes.

The IRS2110 driver is a 14 pin IC chip which needs a 5V logic supply V_{dd} since 5 V pulse signals are used. The V_{ss} is the logic supply ground and COM is the low side ground. IRS2110 is a non-isolated driver, hence both V_{ss} and COM must be connected to ground. HIN and LIN are the logic inputs and are given the same pulse i.e. both are turned on and off together. A high signal to HIN and LIN will give high output in HO and LO pins and low signal will give low outputs. The output to HO (high or low) is not with respect to ground, but with respect to V_s. A bootstrap circuit is used for driving the high side of the driver. For the bootstrap circuitry, diodes and capacitors are used

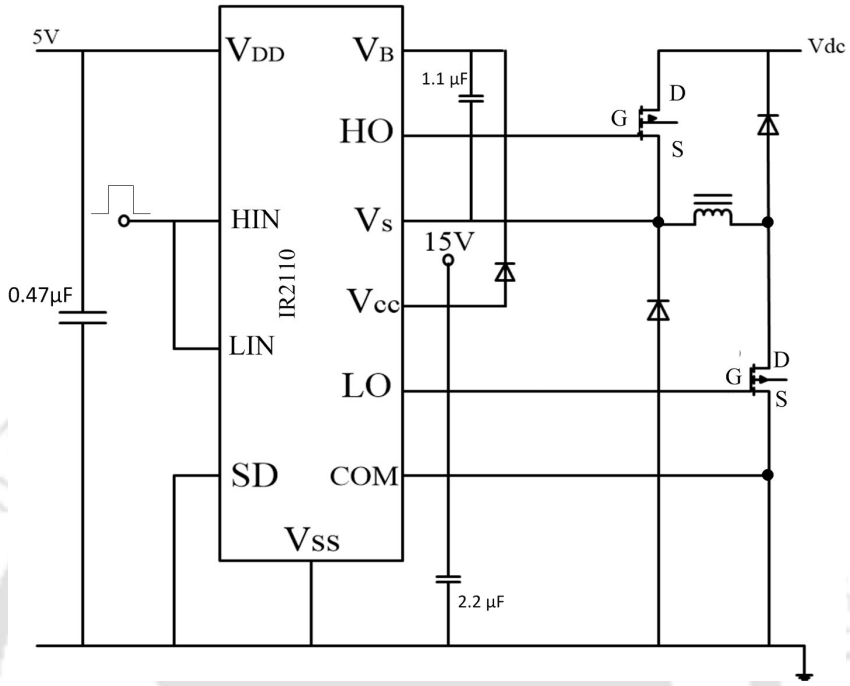

Figure 5.18: One phase leg of converter with IRS2110 mosfet driver

utilizing V_{cc}, V_B and V_s to provide the floating supply to drive the MOSFETs. V_s is the high side floating supply return. When high, the level on HO is equal to the level on V_B, with respect to V_s. When low, the level on HO is equal to V_s, with respect to V_s effectively zero. For bootstrapping circuitry a capacitor of 1.1μF is used and a Schottky diode is used as the bootstrapping diode. A capacitor of 2.2μF is used with the V_{cc} input and 0.47μF is used with the logic supply V_{DD}. The HO and LO pins are connected to the gate of the MOSFET IRF540N. The high voltage DC link source is connected to the drain of the upper MOSFET and the ground is connected to the source of the lower MOSFET. The phase winding is connected with the source of the upper MOSFET and drain of the lower MOSFET. The logic signal supplied for the gate pulses are maintained at 33.33 % duty cycle.

Figure 5.19 shows the simulation diagram of a three single phase asymmetric converter powered by individual MOSFET drivers in LTSpice software. In this simulation the gate signal in the MOSFET driver is supplied from a pulse voltage source. In practical application these logic signals or control signals are generally Pulse Width Modulation (PWM) signals applied from microcontroller boards. These signal needs isolation of grounds from the primary source before being fed into the MOSFET driver. In this work an optocoupler circuit is used for isolating the control signals. Essentially an optocoupler is a semiconductor device that uses a short optical path or link to couple a

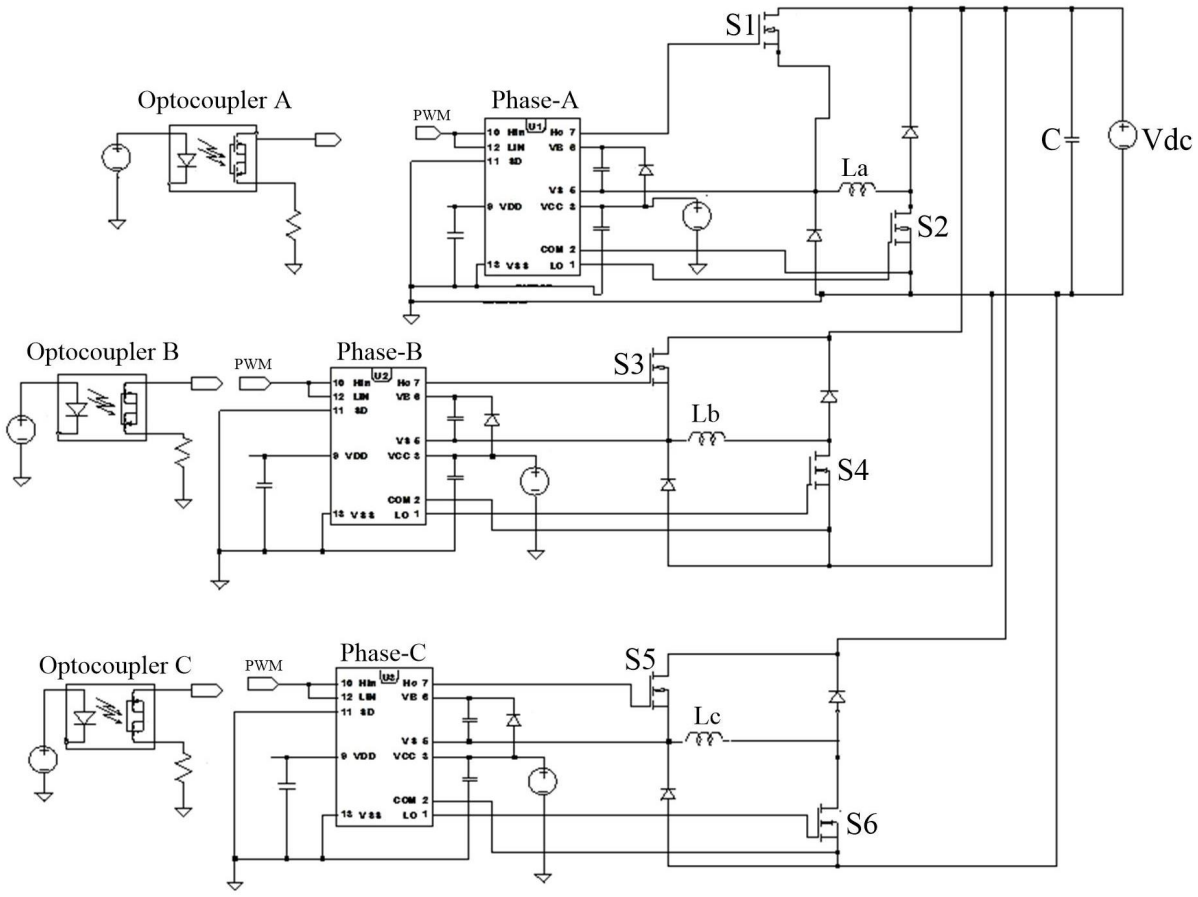

Figure 5.19: Simulation circuit of the asymmetric bridge converter in LTSpice

signal from one electrical circuit to another whilst providing electrical isolation. The optocoupler used in this work is MCT2E. In order to get a non-inverting output from the optocoupler a pull down resistor of 10 kΩ is connected in the output as shown in Figure 5.20. In this simulation, the load is referred to as the phase winding of the motor which has an impedance of 1.5 Ω and the DC link voltage supply, V_{dc} is 50 V.

The circuit developed in LTSpice is simulated to test the working function of the circuit. In this simulation, the duty cycle is taken as 33.3 % and the frequency of the gate signal is taken as 200 Hz. This simulation is done in order to observe the characteristics of the driver and its commutation strategy. As such, the model is simulated with a low frequency gate signal. Figure 5.21(a) shows the pulse voltage signals from the optocouplers, which are then fed to the logic input of the driver. These signals drive the two MOSFETs in each phase leg of the converter. The MOSFETs are turned on when the gate signal is at logic level 1 and they are turned off when the gate signal is at logic

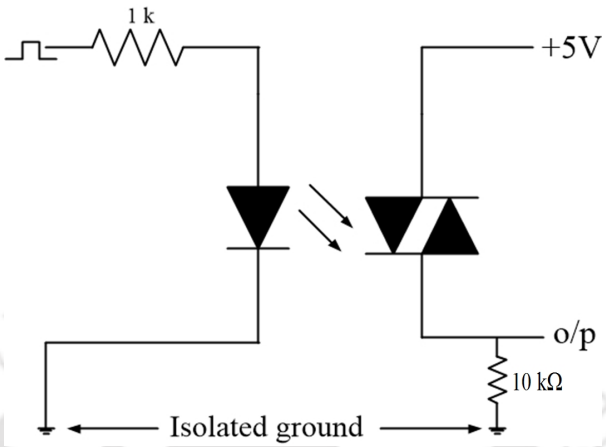

Figure 5.20: Physical connection of MCT2E optocoupler

level 0. The currents through the phase windings commutates at regular intervals in accordance with the gate pulse signal. The current flows through the winding when the gates are turned on and commutates when the gates are turned off. Figure 5.21(a) shows the simulated waveform of the PWM signals and Figure 5.21(b) shows the simulation results of the currents through the phase windings. It can be observed that the currents in each of the phases sequentially commutates at regular intervals.

In order to perform experiments with the motor system, the hardware of the converter is practically implemented. The asymmetric bridge converter as designed and simulated in LTSpice is further fabricated on circuit boards. The isolation circuit board consists of three optocoupler circuits for supplying three independent PWM signals to the MOSFETs. The PWM signals are generated using an embedded controller of National Instruments having chasis PXIe-1062Q. The controller is PXIe-8135 and the DAQ module is PXIe-6363. The output signals through the coaxial cables are connected to SCB-68B connector boxes which are connected to PXIe DAQ modules using SHC68-68-EPM cables. NI LabView software has been used for generating and storing of the measured data. Each of the circuits are individually fabricated. The following are the components used in the circuit boards.

Table 5.5: Components of the isolation circuit board

Components	**Part No.**	**Rating**
Voltage regulator	LM 7805	5 V
Optocoupler	MCT2E	-
Resistors	-	1 kΩ and 10 kΩ, 10 W

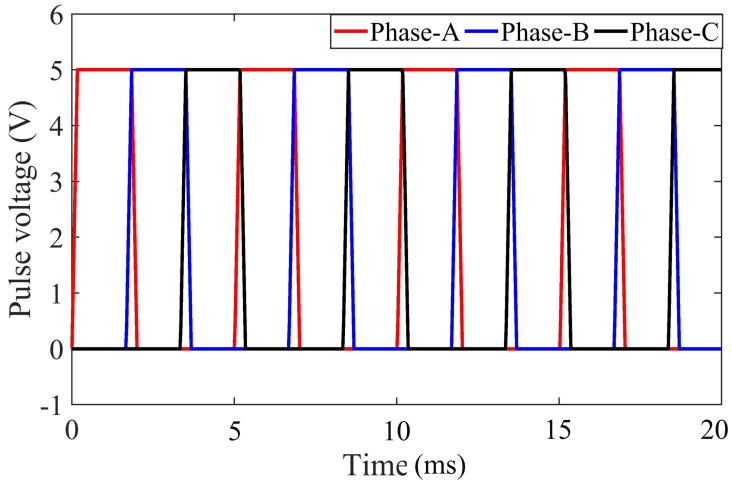

(a)

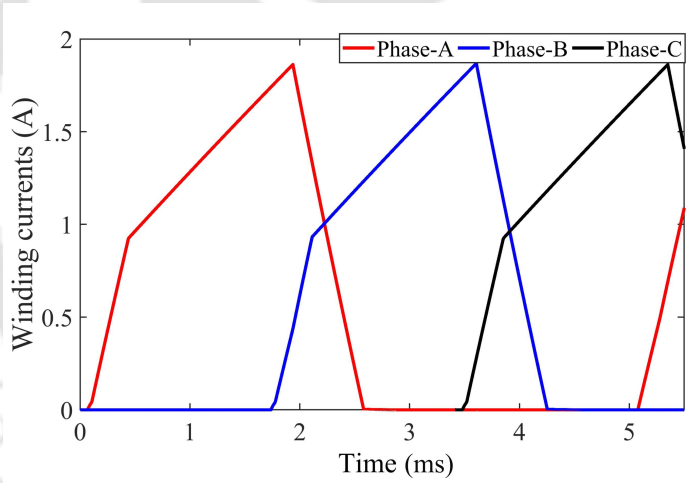

(b)

Figure 5.21: Simulated waveforms of (a) pulse voltages (b) phase winding currents

Table 5.6: Components of the asymmetric bridge converter circuit board

Components	**Part No.**	**Rating**
MOSFET driver	IRS2110	upto 500 V
Voltage regulator	LM 7805	5 V
Voltage regulator	LM 7815	15 V
Bootstrap capacitor	1.1 μ F	63 V
Diodes	UF5408	3 A, 1000 V
MOSFET	IRF540N	33 A, 100 V
DC link capacitors	Electrolytic	470 μ F, 100 V

Figure 5.22 shows the set up of the complete converter circuit for the main current. The converter circuit consists of an isolation circuit, a DC voltage link supply for the main power source and the three-leg asymmetric bridge converter. The voltage supply to the optocoupler circuits are given by 12 V batteries, regulated by voltage regulators of 5 V. The MOSFETs are triggered using PWM signals generated using a LabView program from the PXIe system as shown in Figure 5.23. This experiment is conducted in order to test the designed motor and the converter for motoring operation.

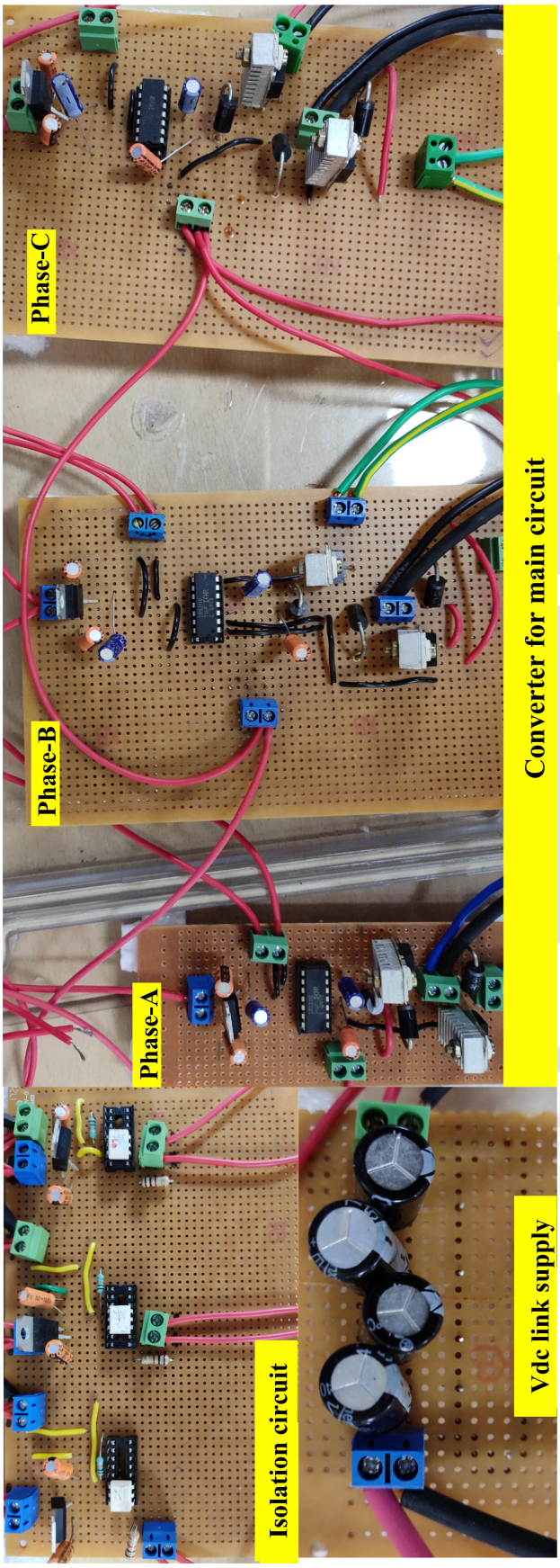

Figure 5.22: Hardware set up of asymmetric bridge power converter

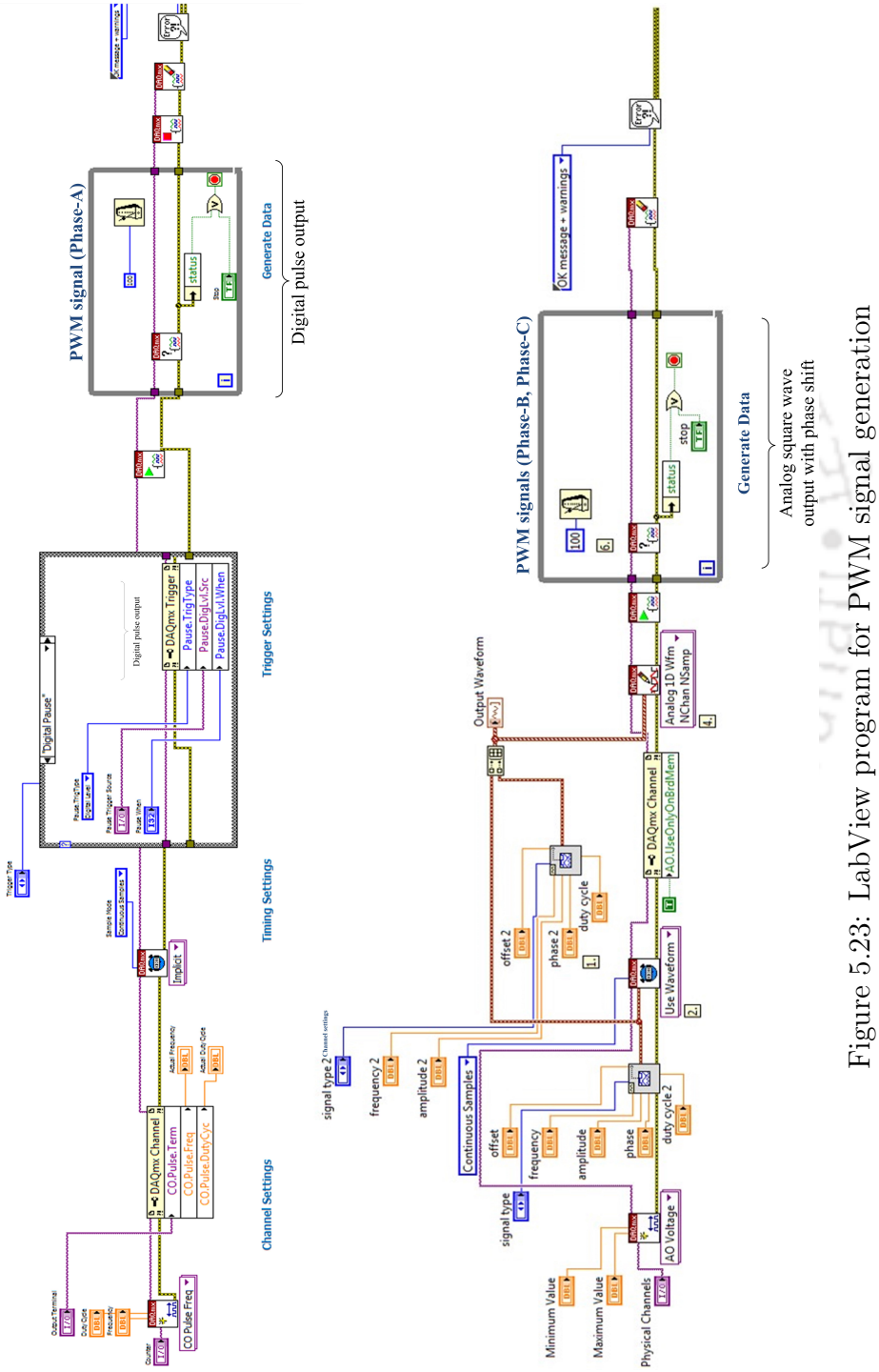

Figure 5.23: LabView program for PWM signal generation

A digital output program is assigned for generating the pulse for phase-A. The pulse for phase-B and phase-C is programmed to generate an analog voltage output having a phase shift of 120^o and 240^o. The analog output when passed through the optocoupler gives only the positive square wave pulse. These PWM signals are then fed into the logic signal input port of the MOSFET drivers of the circuit. The frequency of the signals are kept adjustable in order to run the motor at different speed. Since, the motor has three phase which is excited individually, the duty cycle of the PWM of the control signal is assigned as 33.33 %. In Figure 5.24, it can be seen that the turn on time is taken as t=0.03333 s and the total time period is taken as T= 0.1 s. For the main current converter a sequence of gate pulses is supplied in each phase as shown in Figure 5.25. Table 5.7 refers to the sequence of conducting switches in each phase legs for the main current and bridge current and the gate signals for each switches.

Table 5.7: Gate signals for each phase leg

Phase	**switches (main current)**	**switches (bridge current)**	**gate signals**
Phase-A	S1, S2	S7, S8	g1, g2, g7, g8
Phase-B	S3, S4	S9, S10	g3, g4, g9, g10
Phase-C	S5, S6	S11, S12	g5, g6, g11, g12

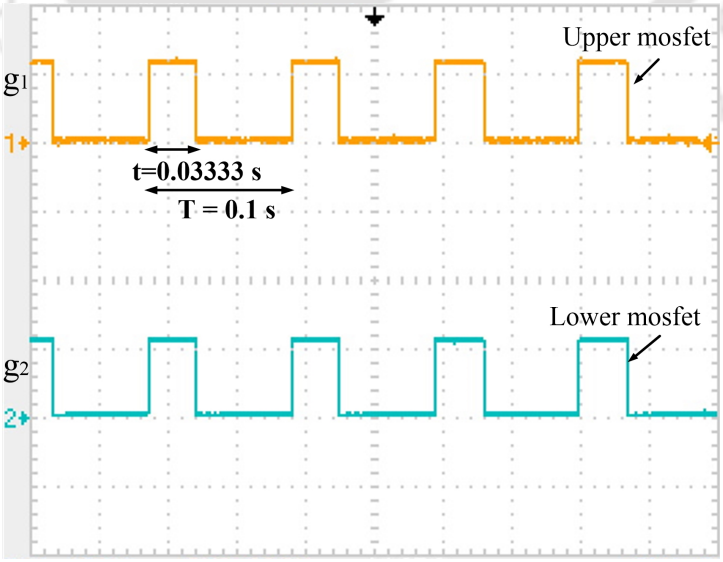

Figure 5.24: Gate signals of upper and lower mosfet of one phase.

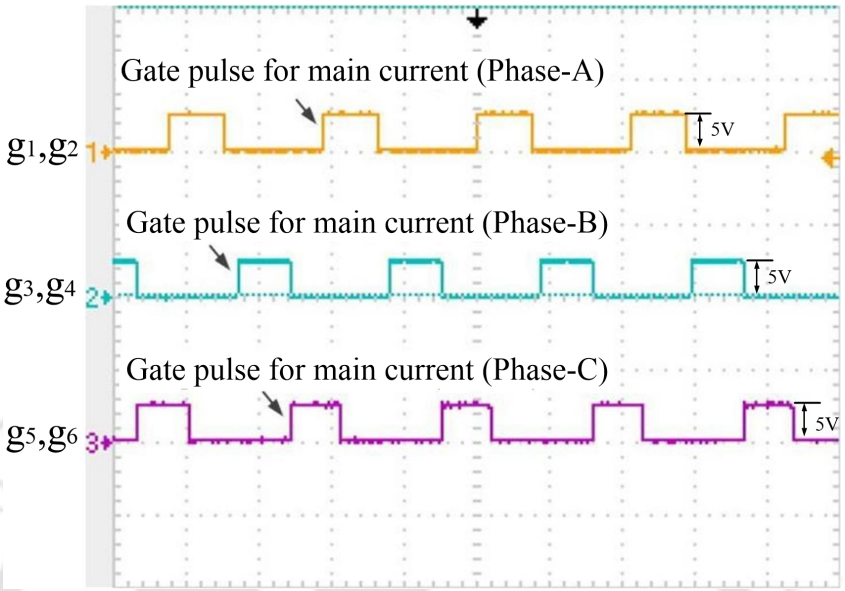

Figure 5.25: Output of the gate signals for the main converter.

5.6 Experimental analysis of test-rig I

Figure 5.26 shows the complete experimental set up of test rig I. A programmable DC power source is chosen for the DC voltage supply of the converter circuit. The phase windings of the motor are connected to each phase legs of the converter circuit. An embedded controller of NI PXIe-8135 integrated with a Data Acquisition (DAQ) module PXIe 6363 is employed for the PWM signal generation and measurement of the data. LTS 15-NP and LV 20-P are selected for measurement of phase currents and the output voltages. A 12 V battery source is connected to power the current sensors and as per requirement, the voltage is regulated to 5 V with LM7805 voltage regulators. The battery sources are connected to the sensors using 0.25 mm^2 multi strand wires. For measurement of the output signals in the DAQ system, RG 58 coaxial cables are connected with the sensor outputs. The measured data obtained from the sensors are acquired and stored in an NI DAQ system. A Techtronix oscilloscope is used for measuring the phase output voltage of the motor.

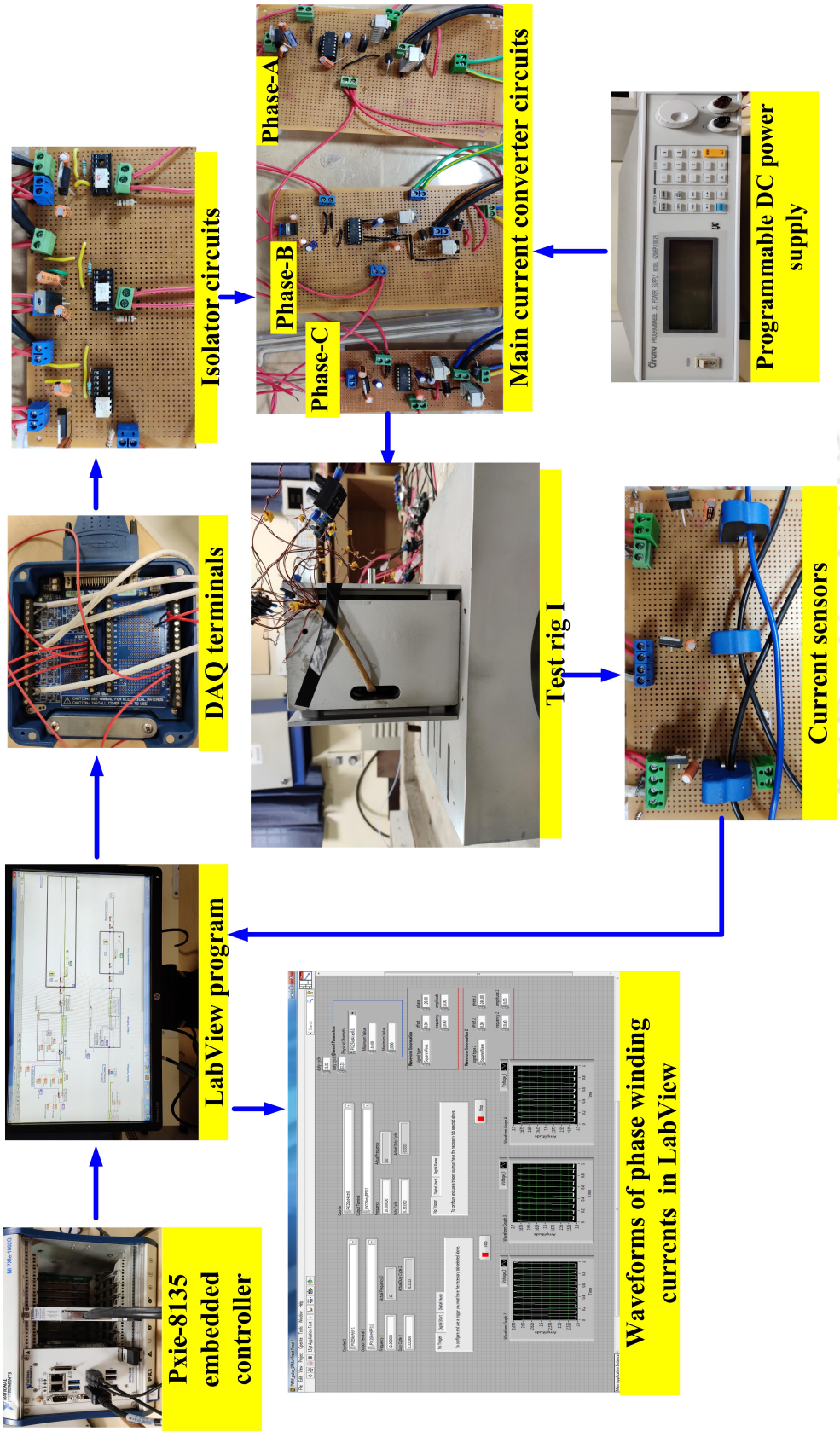

Figure 5.26: Experimental set up of test rig I.

5.6.1 Results and discussions

In this case, the DC link voltage supply is 3 V and the phase winding resistance is 1.5 Ω. The motor is allowed to run at a constant speed by keeping the frequency of the control pulse signal as 10 Hz. The angular speed of the motor is measured as 75 rpm. In this experiment the rotor angle feedback is not applied and the motor is tested by controlling the frequency of the control signals. Each phase excitation and commutation is controlled by the gate control signals of the converter circuit.

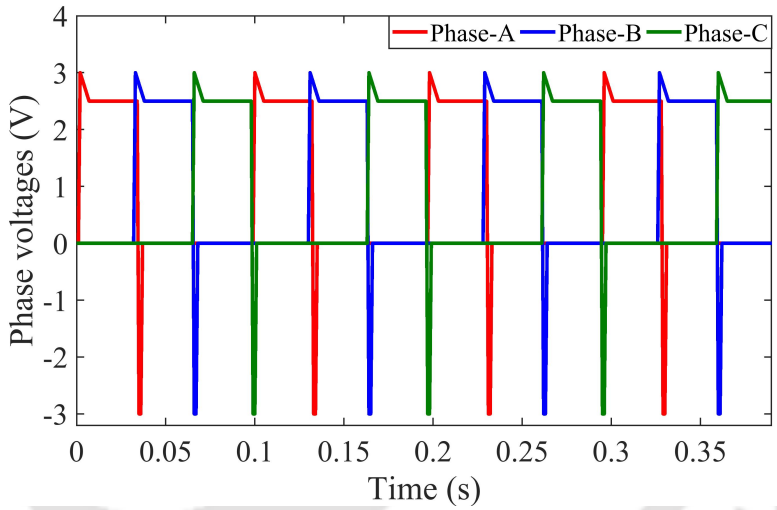

Figure 5.27: Experimental results of output voltages of test motor I.

Figure 5.27 shows the measured output voltages across each of the phase windings and Figure 5.28 shows the measured currents through the phase windings. It can be observed that the peak current in each phase is constant due to the constant speed of the motor and the winding currents are sequentially commutated at regular intervals according to the control signals. Figure 5.29 shows the experimental results of torque. The torque here obtained is not measured directly but computed from the output power divided by the rotational speed. The output power is calculated as the copper loss subtracted from the input power. The input power is calculated from the measured data of voltage and phase currents and the speed is measured as 75 rpm. It can be observed from the experimental results of test rig I, that the developed motor with the conventional winding can be operated with the asymmetric converter circuit at a constant frequency by controlling the gate control signals.

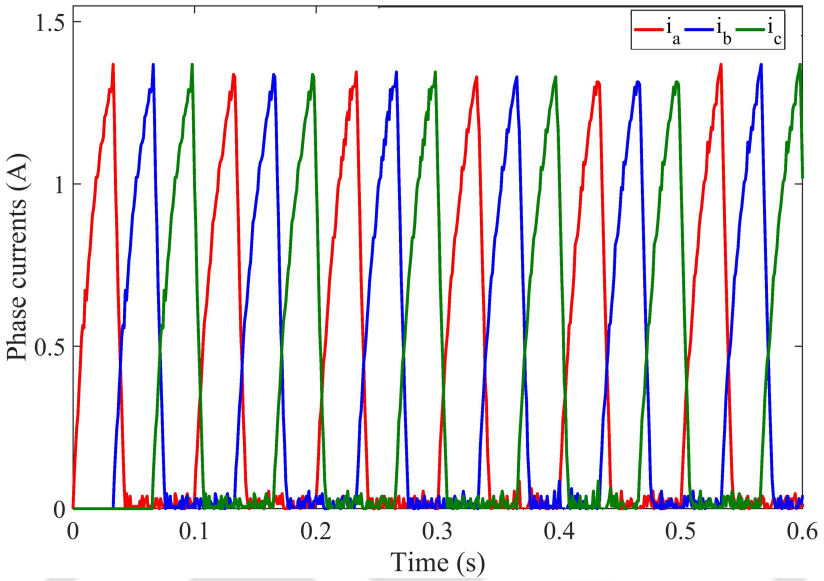

Figure 5.28: Experimental results of phase winding currents of test motor I.

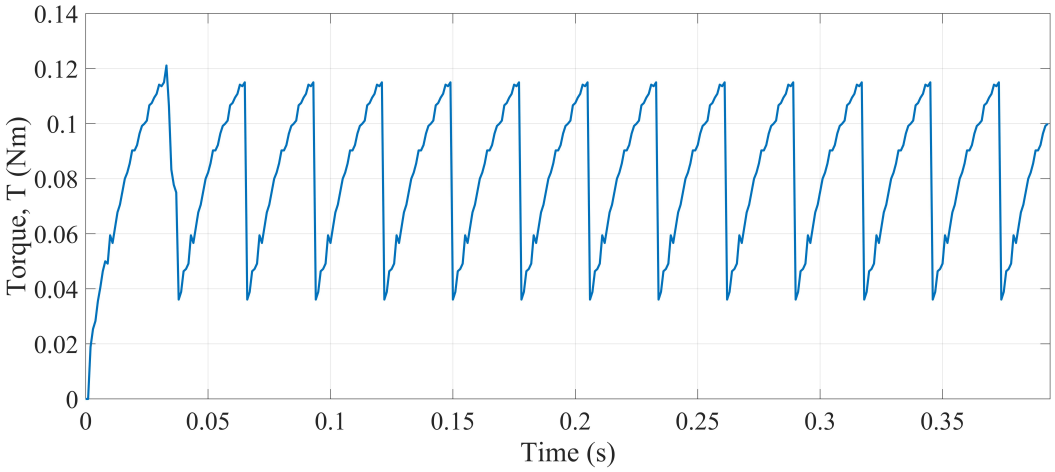

Figure 5.29: Calculated results of torque of test motor I.

5.7 Experimental analysis of test rig II

The test rig II consists of the test motor II with BCW. In this case, the motor coils are connected in the form of a bridge as shown in Table 5.4. The bridge terminals allow current injection in between the coils. The converter circuit for the main current is connected with the phase windings of the motor. A separate converter circuit powered with a separate DC power source is applied for the bridge current supply. The power supply for the bridge current features an isolated ground in order to avoid short circuit of the two power sources. It is mandatory for the main current supply and the bridge

current supply to have different grounds and operate independently of each other to provide currents to the same load. The analysis of the test motor II has been conducted in two section. In the first section, the BCW SRM is tested for motoring operation with only main current supply. With the main current, test motor II operates for torque production like a conventional SRM. In the following section, the motor is tested with both main current and the bridge current supply for torque and radial force production.

Figure 5.30 shows the experimental set up of test rig II. For measurement of the rotor-shaft displacement two Bently Nevada, 3300 XL 8 mm eddy current based displacement sensor probes have been connected and the output is measured through the LabView based DAQ measurement system. It has to be noted that only one bridge current is supplied in the top bridge winding of phase-A to check the effect of bridge current in the motor. A separate converter has been used for the bridge current supply. In this section, the experiment is conducted by supplying the bridge current in phase-A only.

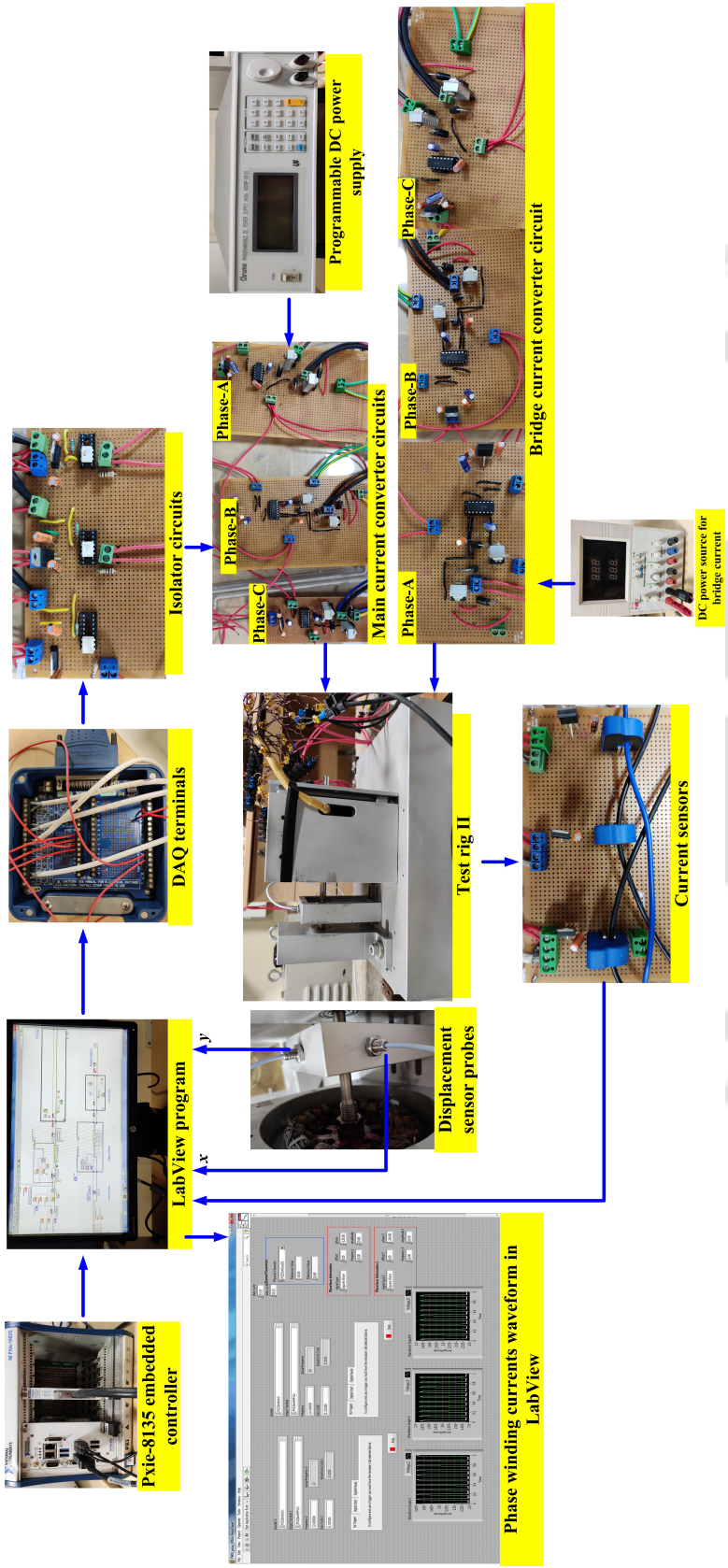

Figure 5.30: Experimental set up of test rig II.

5.7.1 Experimental analysis of test motor II with main current

For motoring operation, a 100 V DC voltage source is used. In the experiment, the motor is tested by providing a low voltage of 3 V to the main converter circuit. The phase winding resistance of the test motor II is 0.98 Ω. The LabVIEW program is commanded to generate three PWM gate signals for the main converter as shown in Figure 5.31. These PWM signals are the control signals for the MOSFET gates of the main converter circuits. The generated PWMs feature 10 Hz frequency and 33.33 % duty cycle. Figure 5.31 also shows the phase currents with reference to the gate signals and it can be observed that the currents are commutated sequentially according to the gate control signals. It has already been discussed in the previous section that in this

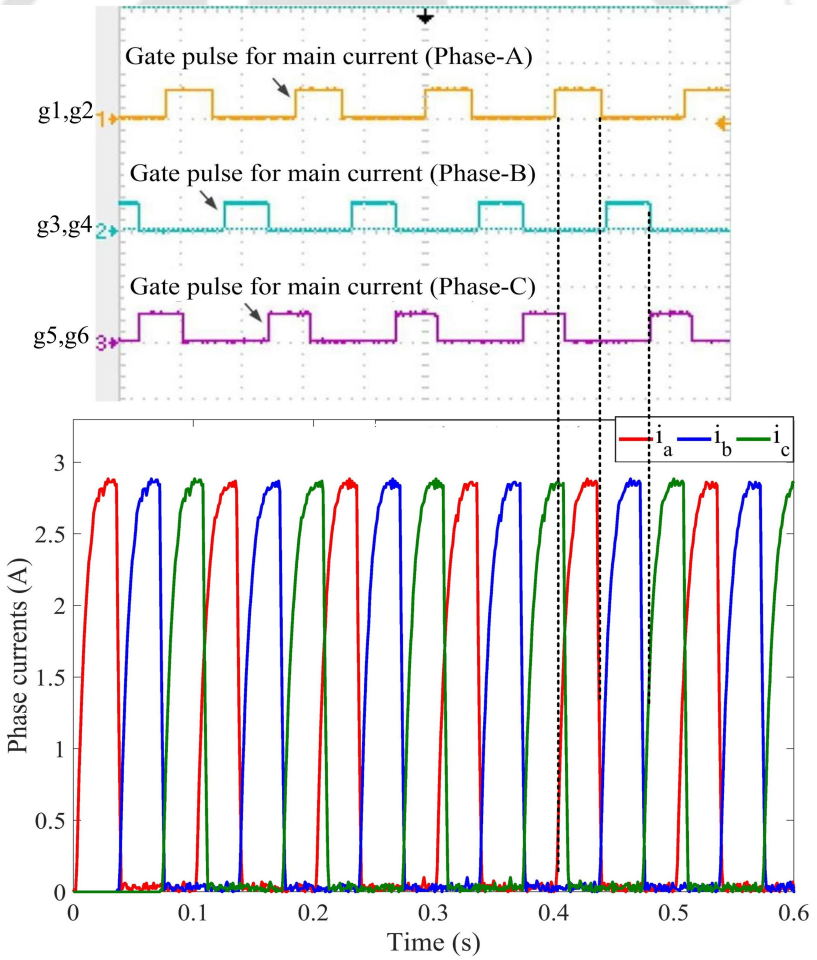

Figure 5.31: Measured phase currents with reference to control gate signals

experiment the motor is not controlled by the rotor angle feedback but by controlling the frequency of the control gate signals.In this test, only the main converter circuit

is powered. With the main converter circuit on, the current flowing through the phase windings forms a four pole magnetic field. During this test, the flow of the phase winding current is not perturbed and the currents in each stator coils are equal.

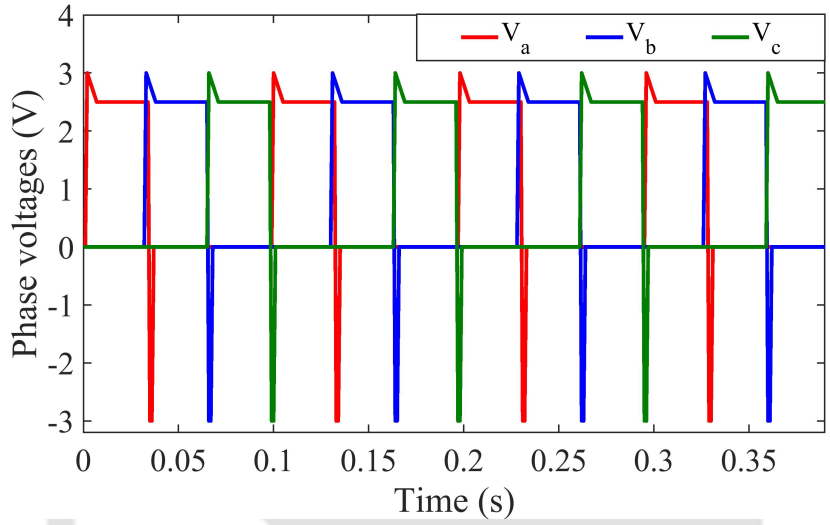

Figure 5.32: Output voltages of test motor II featuring only main current

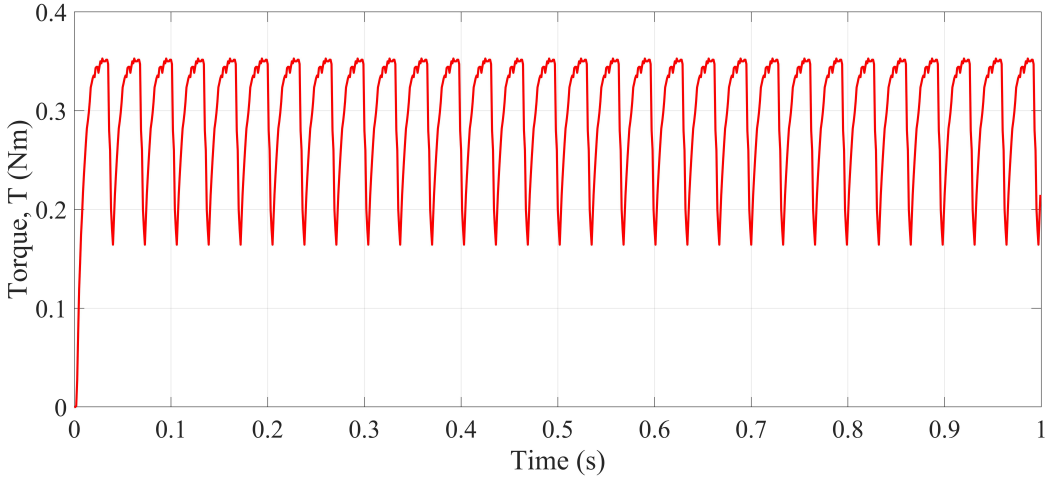

Figure 5.33: Calculated results of torque of test motor II with only main currents.

Figure 5.32 shows the voltage across the phase windings of the test motor II. It can be observed that the voltage drops from initial 3 V in all the three phases. This occurs as the DC link capacitor is suddenly charged by the DC voltage supply and then tries to reach a constant voltage as the current flows through the windings. The spike is found in all the three phases as each phase is switched and the capacitor charges and discharges with every switching. Figure 5.33 demonstrates that with only the main current supply,

the motor can operate as a normal motor with no negative torque production. The result of torque is not obtained from measurement but computed using the relation of torque with power and rotational speed. The power is calculated from the product of voltage and current and the speed is measured. This experimental analysis could prove the capability and flexibility of the bridge configured SRM to operate as a normal SRM.

From the above experimental results a comparison can be drawn between the test motor I and test motor II. Both test motor I and test motor II have the same specification but vary in the stator winding connections. The patterns of winding in test motor I and test motor II have been illustrated in Figure 5.34 and Figure 5.35.

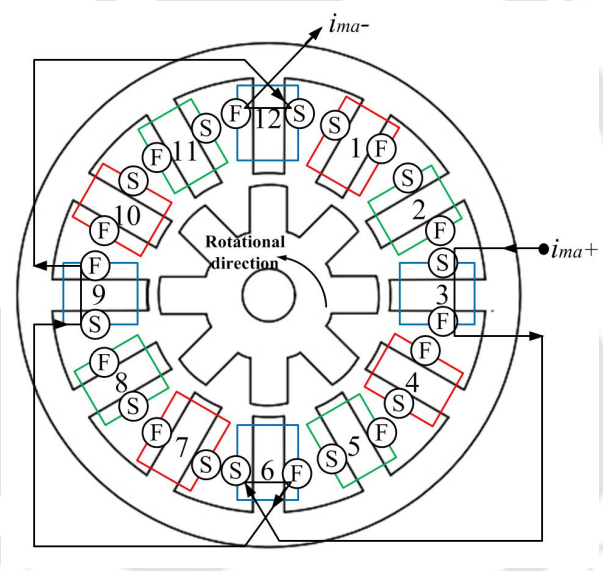

Figure 5.34: Schematic of coil connection in phase-A of test motor I

Test motor I has 80 turns/coil and test motor II has 40 turns/coil. In test motor I, each phase comprises of four coils placed in diametrically opposite stator poles and connected in series. In test motor II each stator tooth contains two coils and each phase has eight coils placed in diametrically opposite stator poles. These eight coils are connected in parallel to each other. From Figure 5.28 and Figure 5.31 it can be observed that the magnitude of phase current is higher in test motor II than in test motor I for the same voltage supply. In case of test motor I, since each phase coils are connected in series the number of turns per phase increases and as a result the impedence of the winding increases. This reduces the current through the winding and produces low torque as seen in Figure 5.29. However, in test motor II, as the coils are connected in parallel the impedence per phase winding is less and more torque is produced as seen in Figure 5.33. Thus, from this comparison it can be observed that the BCW can be a suitable

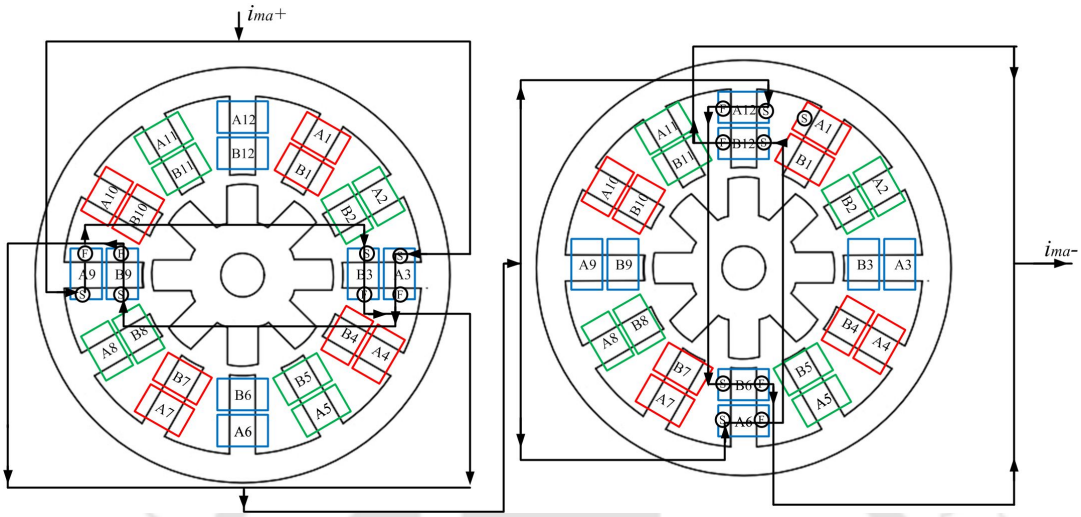

Figure 5.35: Schematic of coil connection in phase-A of test motor II

alternative where more torque production is required.

5.7.2 Experimental analysis of test motor II with bridge current

In the second analysis, the BCW BSRM in test rig II is analysed for both torque and radial force production. In this case, the converter circuit for the bridge current is connected in the bridge terminals as shown in Figure 5.36. An isolated DC voltage of 2 V is supplied to the bridge converter and the DC voltage of the main converter is kept as 3 V.

Figure 5.37 shows the testing of the converter circuits for the main current and the bridge current. The gate signals are generated from the PXIe DAQ system and fed to the MOSFETs through the optocoupler circuits. Both the main converter and the bridge converter are tested by checking the output signals from the MOSFET gates. Figure 5.38 shows the PWM gate signals for the main converter and the bridge converter. It has to be noted that the PWM signals for the main converter are kept same as in the previous analysis. A separate PWM signal for the bridge current converter is generated for phase-A which is of the same sequence as the PWM signal for phase-A in the main converter. The excitation period of bridge and the main current in phase-A are kept same such that no negative torque is obtained when radial force is generated. Figure 5.39 shows the torque profile when the main current is supplied to all the windings and the bridge current is supplied only to phase-A winding of the test motor II. It can be observed that with the additional bridge current, the profile of torque is not perturbed and there much less deviation in the magnitude of peak torque. Figure 5.40(a) and

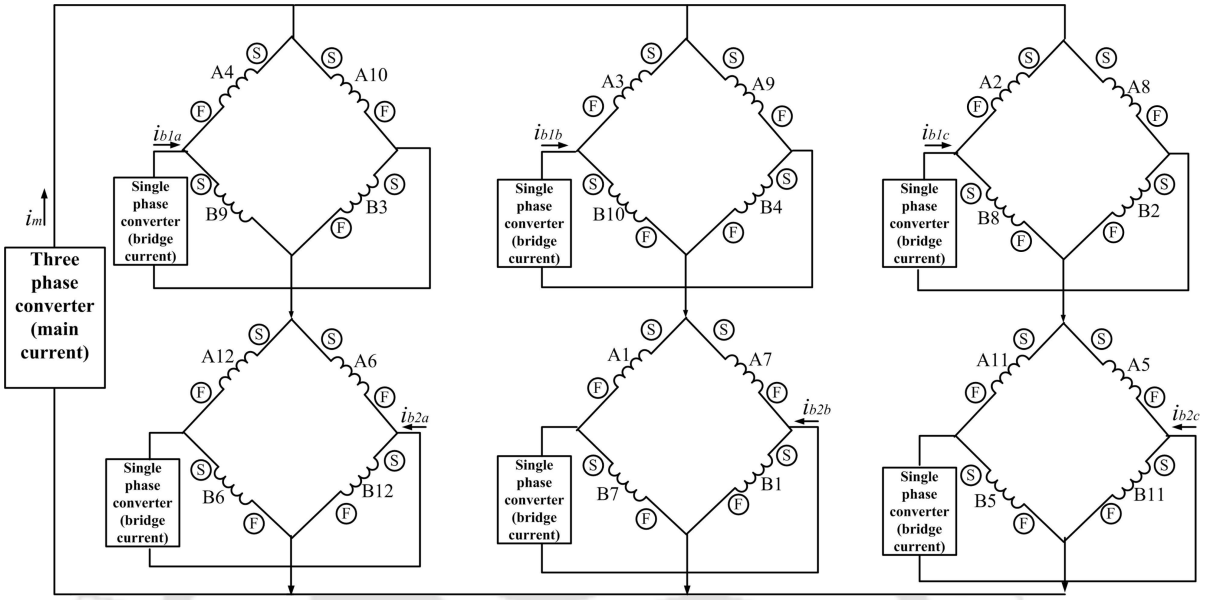

Figure 5.36: Schematic of the bridge current converter connection

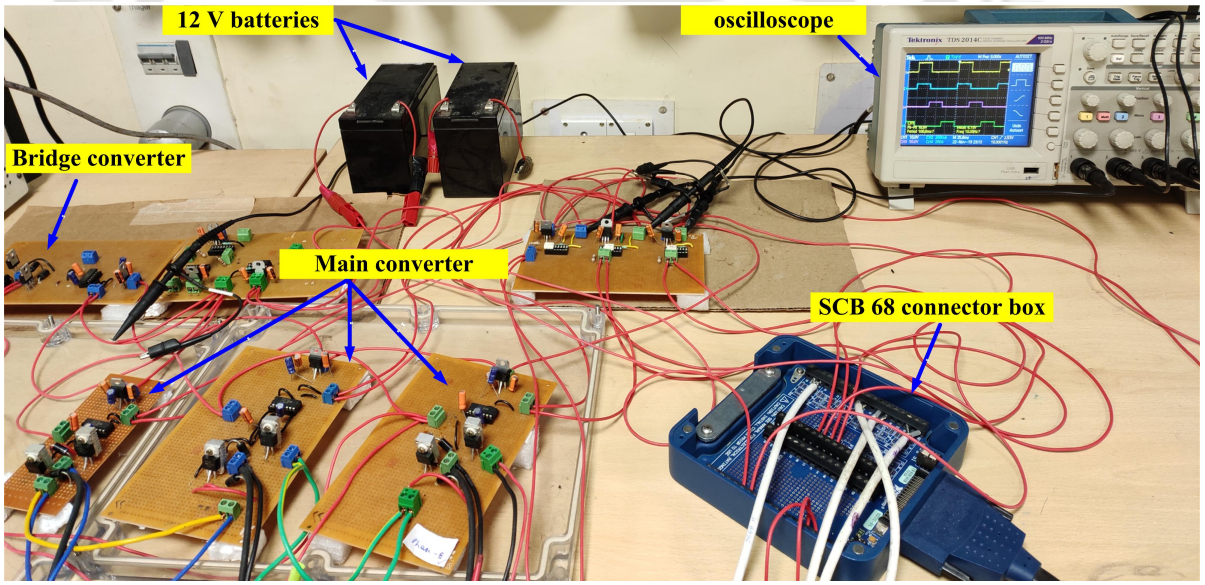

Figure 5.37: Testing of the converter circuits for test rig II

Figure 5.40(b) show the displacement produced due to the supply of the bridge current in phase-A. Figure 5.41(a) and Figure 5.41(b) are values of net displacement, and net radial forces calculated from the measured values of the displacements obtained. For computing the radial force, the mathematical expression of radial force developed in Chapter 3 is used. The values of the main current, bridge current and the displacement

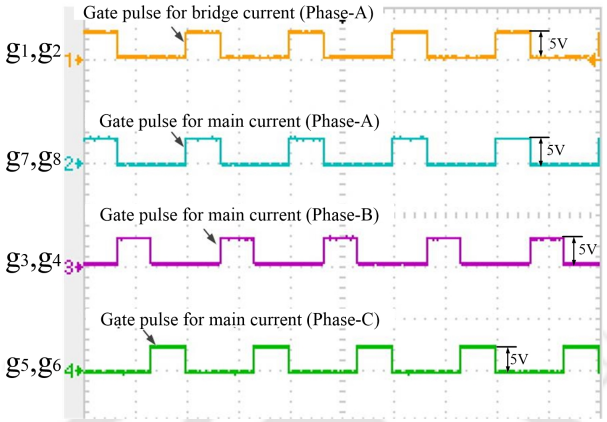

Figure 5.38: PWM gate signals for the main converter and the bridge converter

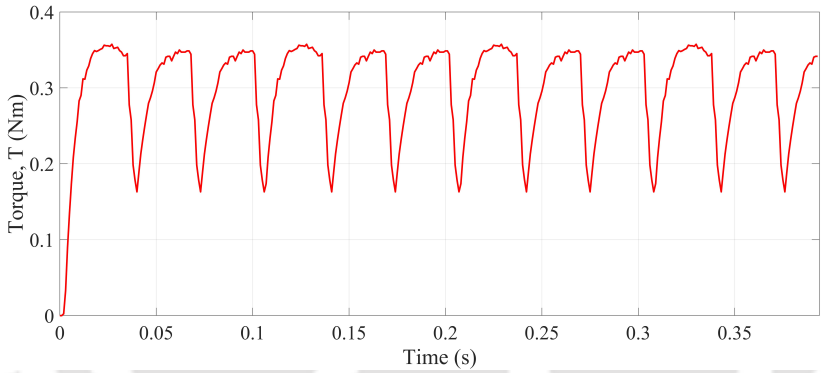

Figure 5.39: Calculated results of torque with additional bridge current in phase-A

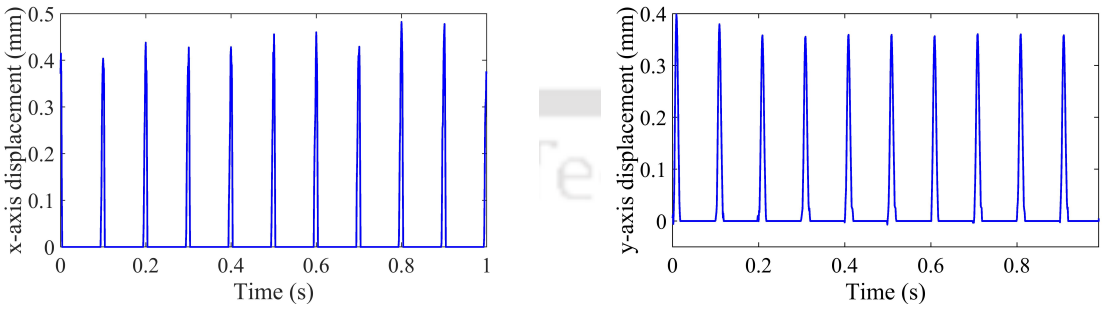

(a) (b)

Figure 5.40: Experimental results of displacement of shaft in (a) x- axis direction and (b) y- axis direction with additional bridge current in phase-A

are used in Equation 3.112 and the resultant of radial force with phase-A bridge current is calculated analytically. Though this method of calculating force is very limited, it is done to obtain the trend of the radial force produced due to the additional bridge current

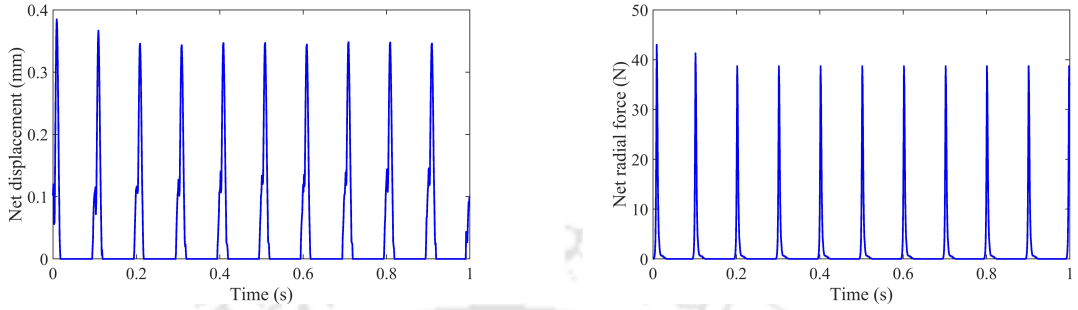

(a) (b)

Figure 5.41: Experimental results of (a) net displacement (b) net radial force with additional bridge current in phase-A

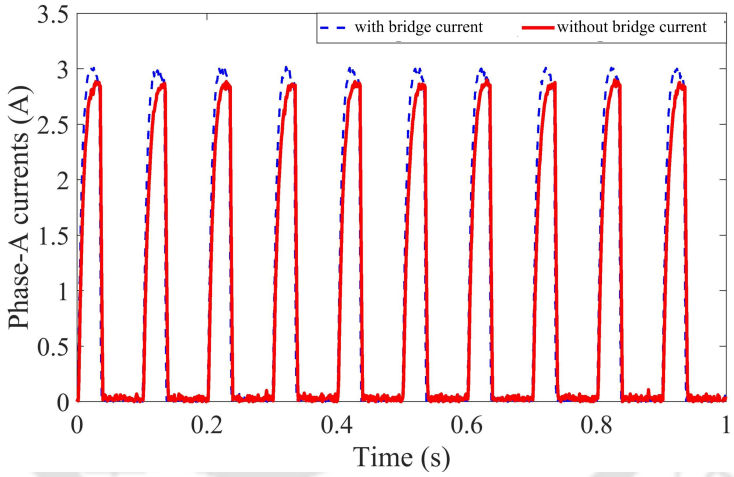

Figure 5.42: Comparison of phase-A currents with additional bridge current in phase-A.

5.7.3 Control of radial displacements using bridge currents

With the demonstration of radial displacement with bridge current in phase-A, the test rig II is further tested for control of the radial displacement present in the motor. The eddy current probes for measurement of displacement along x and y directions are adjusted to obtain the minimum displacement present in the motor under normal operating condition. As the shaft of the test rig II is supported with mechanical bearing on one side and a back up bearing on the other side, there is displacement on the side having clearance. In this section, an approach is made to mitigate the existing displacement in the motor by utilizing the bridge currents. Firstly, a passive method of

control is applied by connecting the bridge terminals in each phase as shown in Figure 5.43. No external bridge current source is used in this method. The motor is rotated by giving supply from the asymmetric bridge converter with a V_{dc} of 3 V and supply frequency of 10 Hz. Due to existing eccentricity or displacement in the motor, there lies a potential difference across the bridge terminals in each phase. When the bridge terminals are short circuited, a current flows through each bridge which tries to reduce the potential difference across the bridge terminals. A comparison is made between the shaft displacements in both x and y directions when the bridge terminals are short circuited and when they are left open. Figure 5.44 shows the radial displacement of the

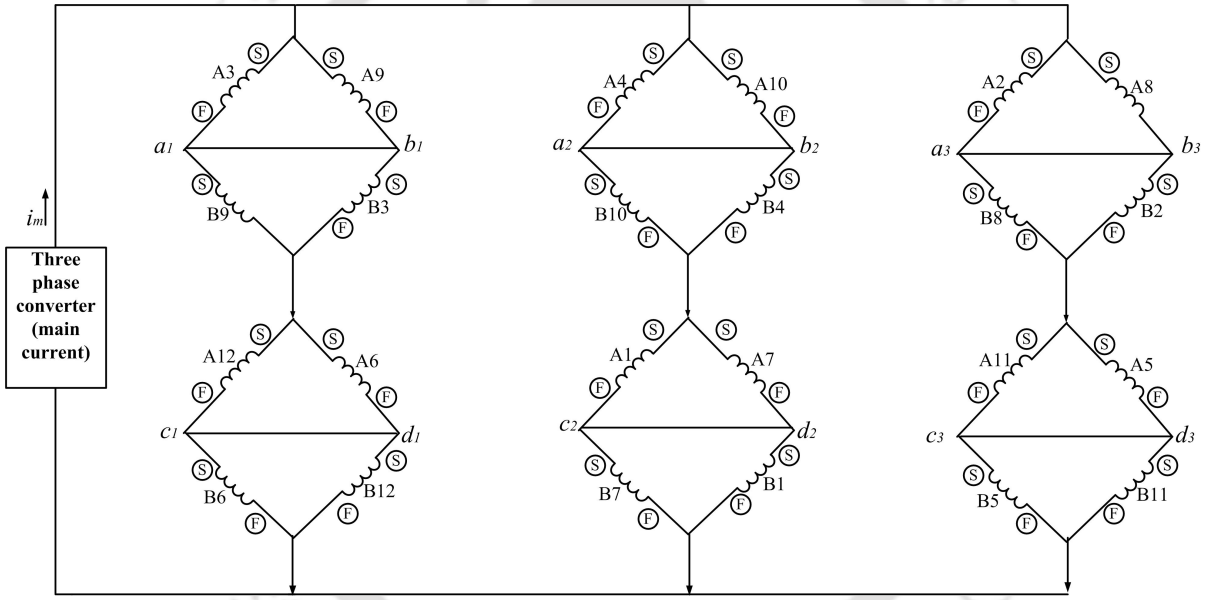

Figure 5.43: Schematic of BCW with bridge terminals short circuited

shaft in both x and y directions when the bridge terminals are short circuited and when they are left open. It can be observed that there is a significant amount of displacement in the shaft as it rotates. By short circuiting the bridge terminals it can be observed that there is a small shift in the existing displacement. This implies that, as a current flows through the bridge it tries to reduce the potential difference present across the bridge terminals. The reduction in the potential difference leads to reduction in the magnitude of the radial displacement. Figure 5.45 shows the orbit traced by the rotor along x and y direction under normal operation and when the bridge terminals are short circuited. It can be observed from Figure 5.45 that there is small effect in the rotor orbit as the bridge terminals are short circuited. This implies that if a current is allowed to flow through the bridge terminals, then a change in the rotor-shaft position can be obtained. This

concept is referred to the theoretical analysis in Section 3.3 which gives the relation of radial force with main current, bridge current and the rotor radial displacement. This, leads to the concept of injecting controlled currents in between the bridge terminals to reduce the radial displacement.

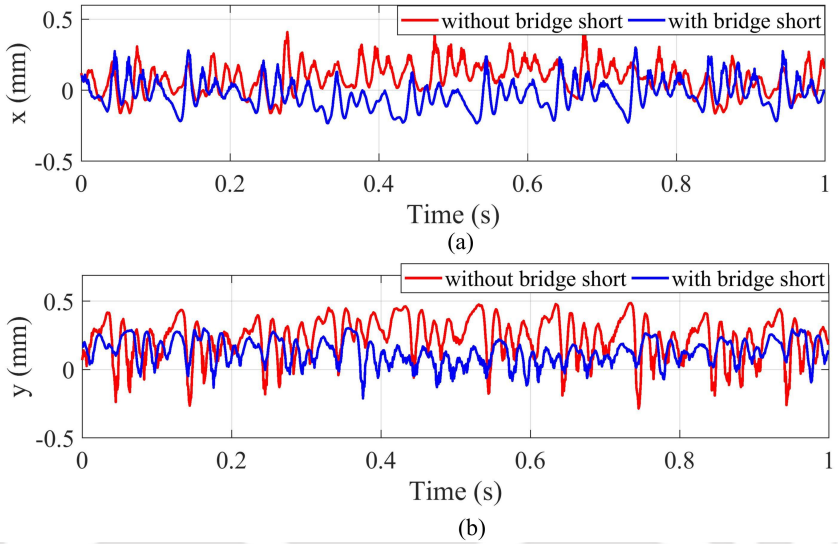

Figure 5.44: Experimental results of displacements with and without short circuiting the bridges along (a) x direction and (b) y direction.

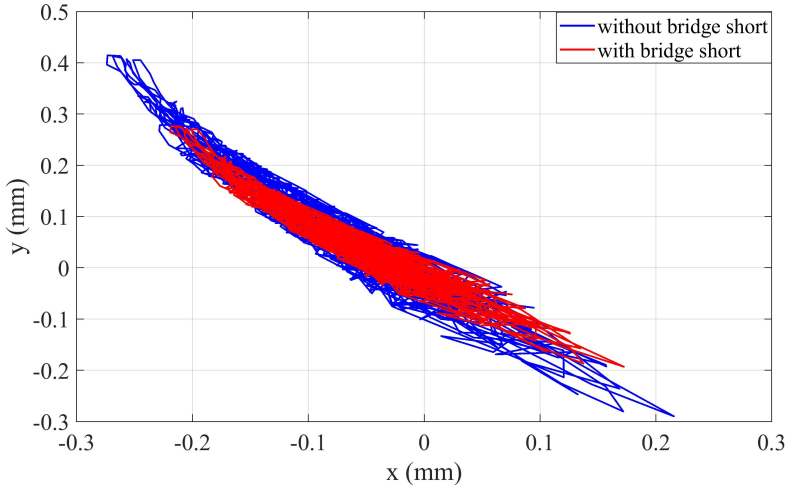

Figure 5.45: Experimental result of orbital responses with the bridge terminals short circuited and without short circuited.

The experiment is further conducted by developing a closed loop control of the system under no-load condition. The displacements measured along x and y directions using

the eddy current sensors are taken as feedback signals as shown in the block diagram in Figure 5.46. A real-time program is developed in LabVIEW using NI PXIe-8135 controller and the data acquisition modules NI PXIe-6363 and NI PXIe-6221 as shown in Figure 5.47. Each signal obtained from the displacement sensors and the current sensors is acquired using the DAQ (data acquisition) system. The sampling rate of the controller is taken as 1 KHz. The closed loop program consists of a PID controller where the process variable is the displacement data and the set point is the reference value of the shaft position. The gains of the PID are set manually as $K_p = 100$, $K_{in} = 10$ and $K_d = 1$. The displacement error is the input to the PID controller and the force current relationship is used to produce the required bridge currents in each of the three phases. The force current relationship is dependent on the main phase currents and the geometrical air gap variation at each rotor angle. The data obtained from the displacement sensors and the current sensors are measured in volts. In this case, the output of the force-current relationship is a voltage reference signal which goes as an analog voltage control signal to the power amplifiers. The amplifiers thus output the required bridge currents that go to the bridge terminals in each phase. The amplifiers for the x-directional control are connected to the bridge terminals $a_1 - b_1$, $a_2 - b_2$ and $a_3 - b_3$, and the amplifiers for y-directional control are connected to the bridge terminals $c_1 - d_1$, $c_2 - d_2$ and $c_3 - d_3$ respectively. The power amplifiers used are voltage source current controlled power amplifiers from the makers of 422 CE Copley Controls.

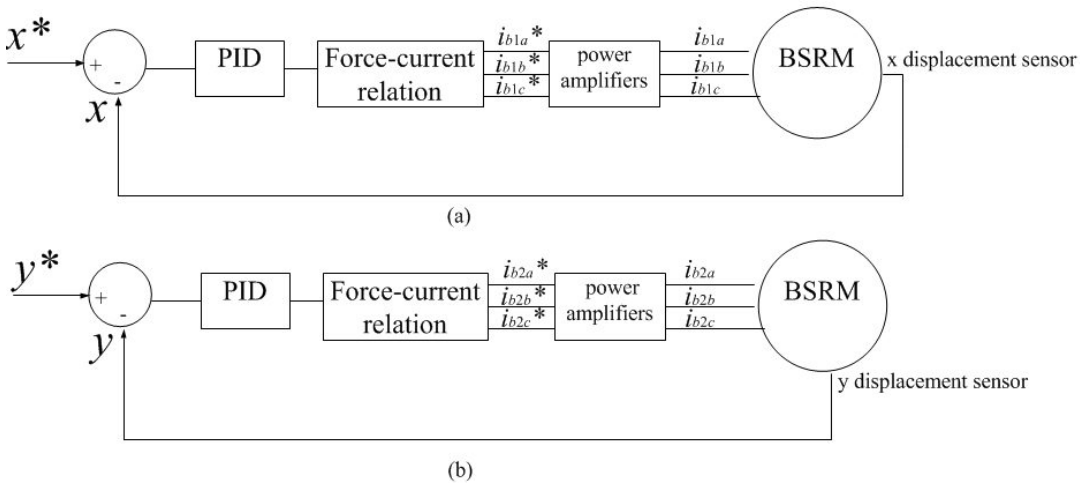

Figure 5.46: Block diagram of the closed loop control of (a) x-displacement and (b) y-displacement.

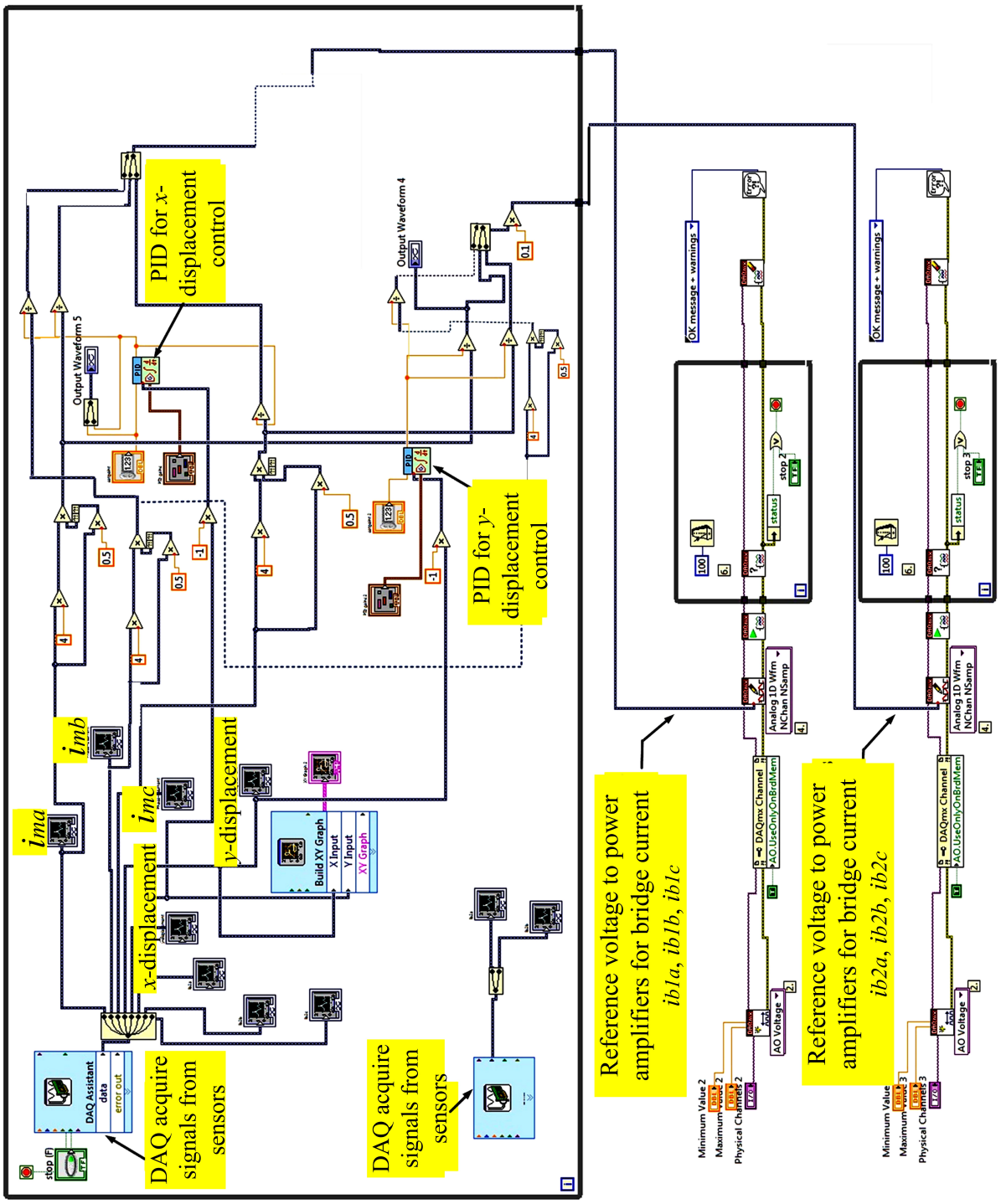

Figure 5.47: LabVIEW program for closed loop control of radial displacement

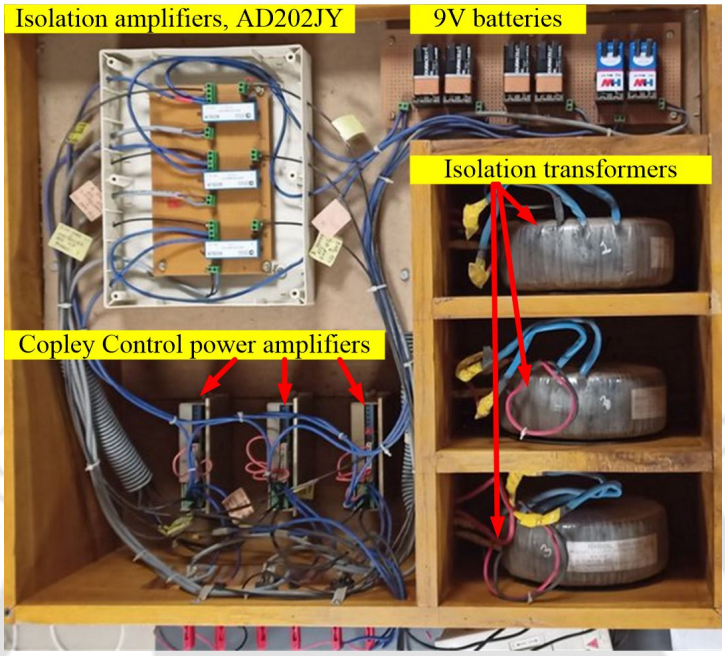

Figure 5.48: Hardware of the controllers for x - directional control.

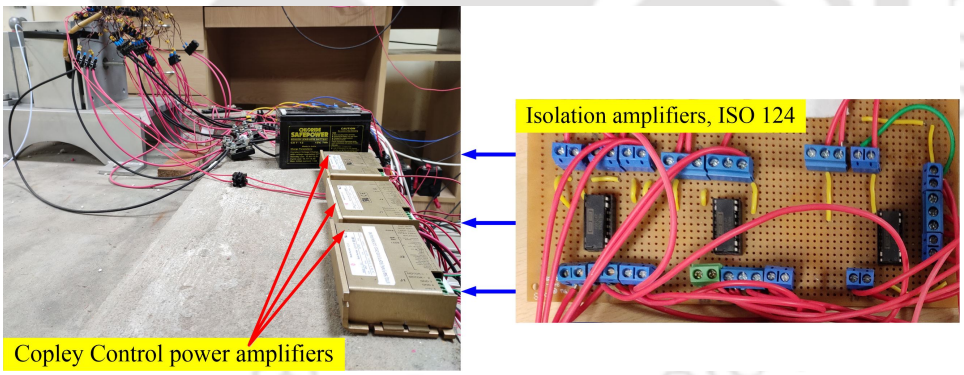

Figure 5.49: Physical connection of the controllers for y - directional control.

Figure 5.48 and Figure 5.49 show the hardware of the bridge current controllers. The controller consists of three power amplifiers for supplying bridge current in each of the three phases independently. The power amplifiers require a DC voltage input of minimum 24 V. This 24 V DC supply is obtained by using a 110 V/24 V step down transformer and a rectifier circuit. It is mandatory to isolate the bridge current supply from the mains in order to avoid short circuit of the sources. An isolation transformer is provided for the power input side of the power amplifiers whereas the input reference from the DAQ system is isolated via the isolation amplifiers (AD202JY).

Figure 5.50 shows the comparison of displacements along x and y directions with

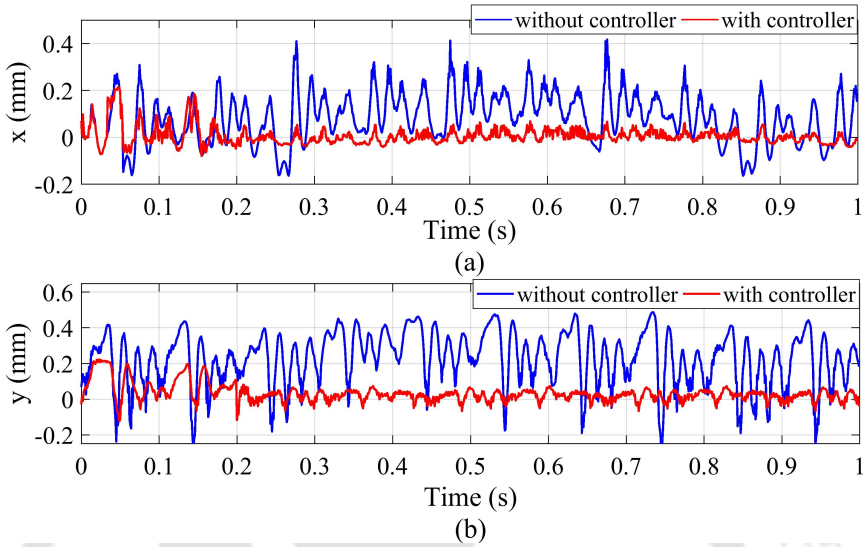

Figure 5.50: Experimental results of displacement along (a) x-direction and (b) y-direction with controller

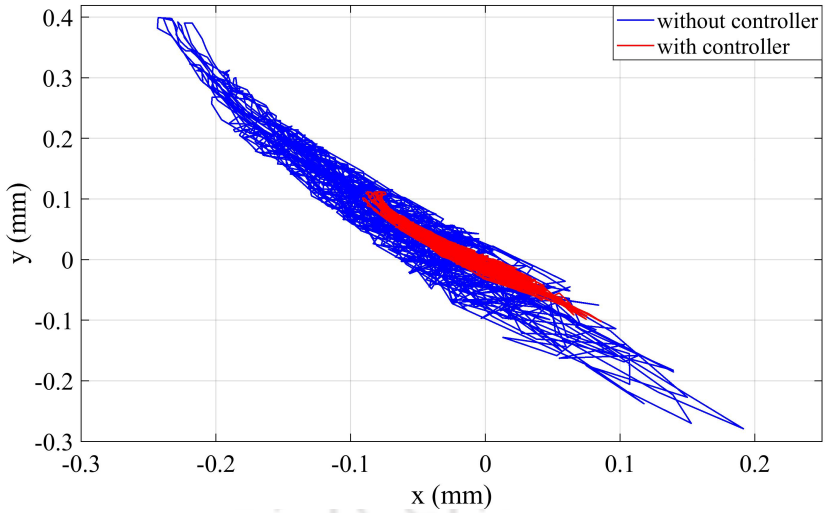

Figure 5.51: Experimental result of orbital responses with the controller and without the controller.

and without the controller. It can be observed that the radial displacement reduces substantially and the rotor rotates around a displacement of about $\pm$ 0.08 mm along x-direction and $\pm$ 0.1 mm along y-direction. From Figure 5.51 it can be observed that the rotor orbit decreases considerably with the closed loop control method. Figure 5.52 shows the measured main phase currents and Figure 5.53 and Figure 5.54 shows the measured bridge currents for the x and y-directional displacement control. A reduction of around 50-60 % could be achieved using the closed loop control as shown in Figure

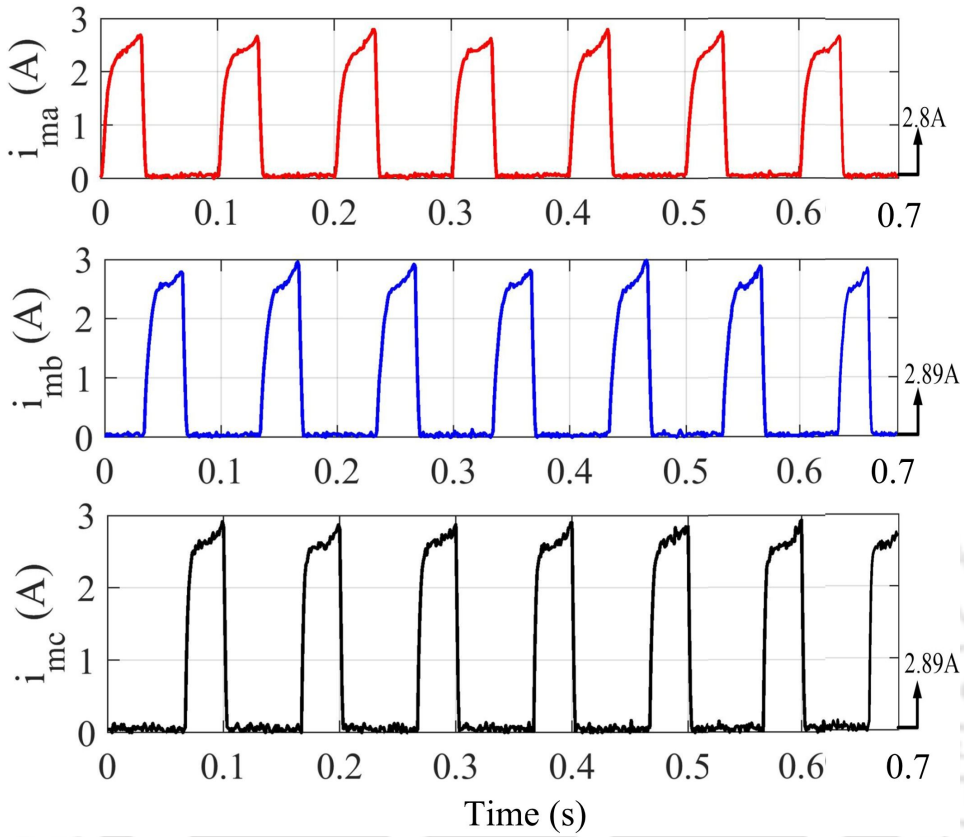

Figure 5.52: Experimental results of the main phase currents, i_{ma}, i_{mb} and i_{mc} with controller

5.55. Figure 5.56,5.57 and 5.58 shows the profile of radial forces computed from the measured displacements, measured main currents and the bridge currents. Equation 3.111 and Equation 3.112 have been used to compute the force values. The weight of the rotor as measured is 1.18 kg which implies that a minimum force of around 11.5 N is required for lifting the rotor. It can be observed from Figure 5.57 that with the current supplied in the windings, an average force of around 11.8 N is produced in the y direction and 15.15 N as the net force, F. This signifies that the currents required to produce a minimum lifting force is obtained. The force obtained is pulsating due to the switching of currents in each phase. The phase currents are commutated at the unaligned rotor position and the radial force decreases at unaligned positions. A constant force can be obtained practically with the help of a more accurate current control at the unaligned position. However, the capability of the bridge currents to produce an average levitation force has been verified.

Based on this experimental analysis, it can be concluded that the bridge currents in the BCW SRM paves its way for its effective utilization in controlling radial displacement

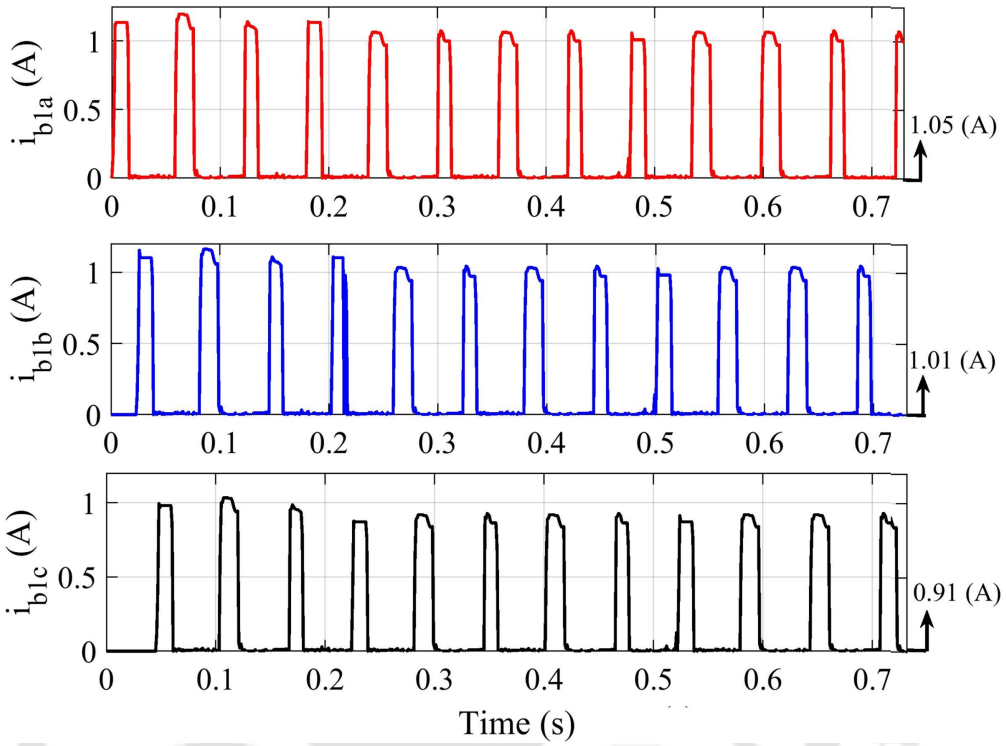

Figure 5.53: Experimental results of the bridge currents, i_{b1a}, i_{b1b} and i_{b1c}

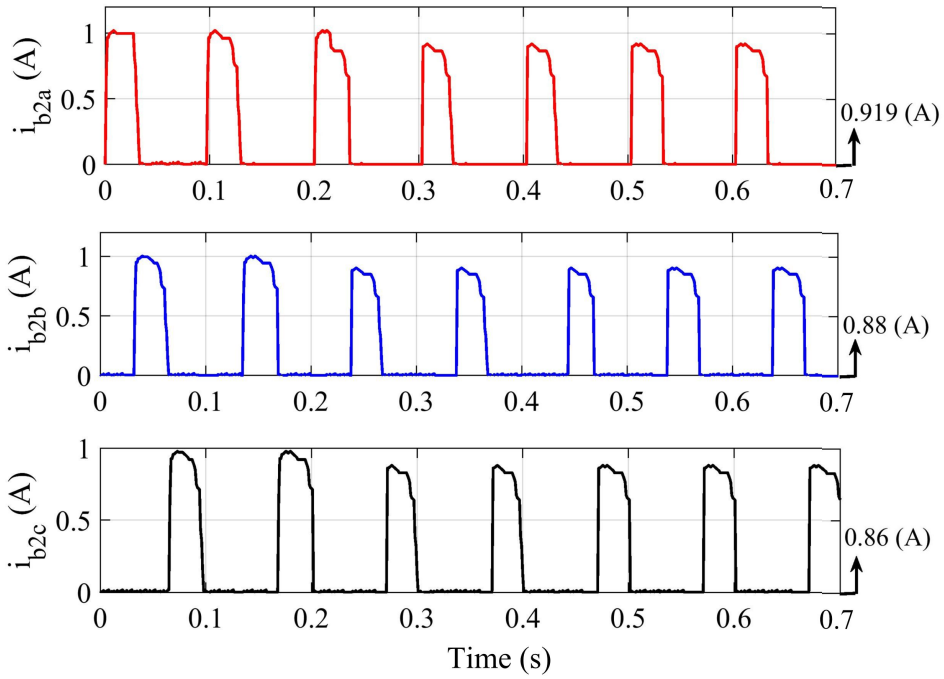

Figure 5.54: Experimental results of the bridge currents, i_{b2a}, i_{b2b} and i_{b2c}

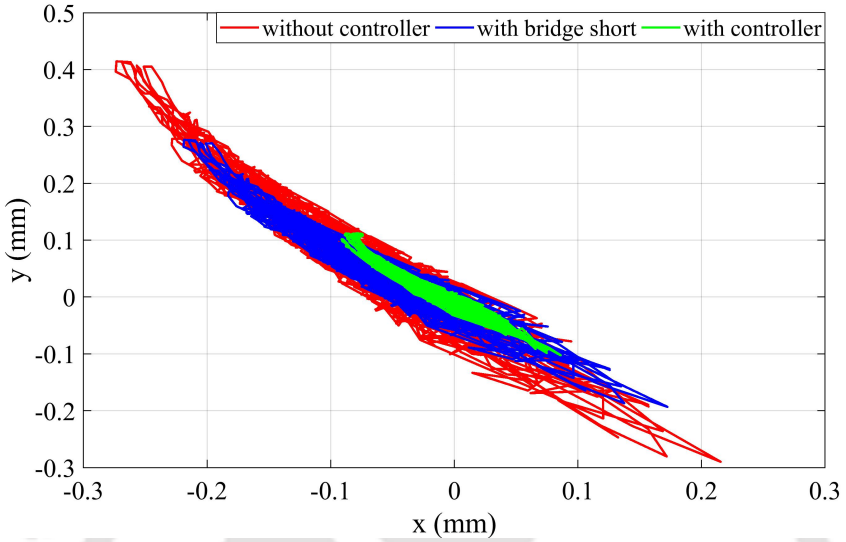

Figure 5.55: Comparison of rotor orbits without controller, with bridge short and with controller.

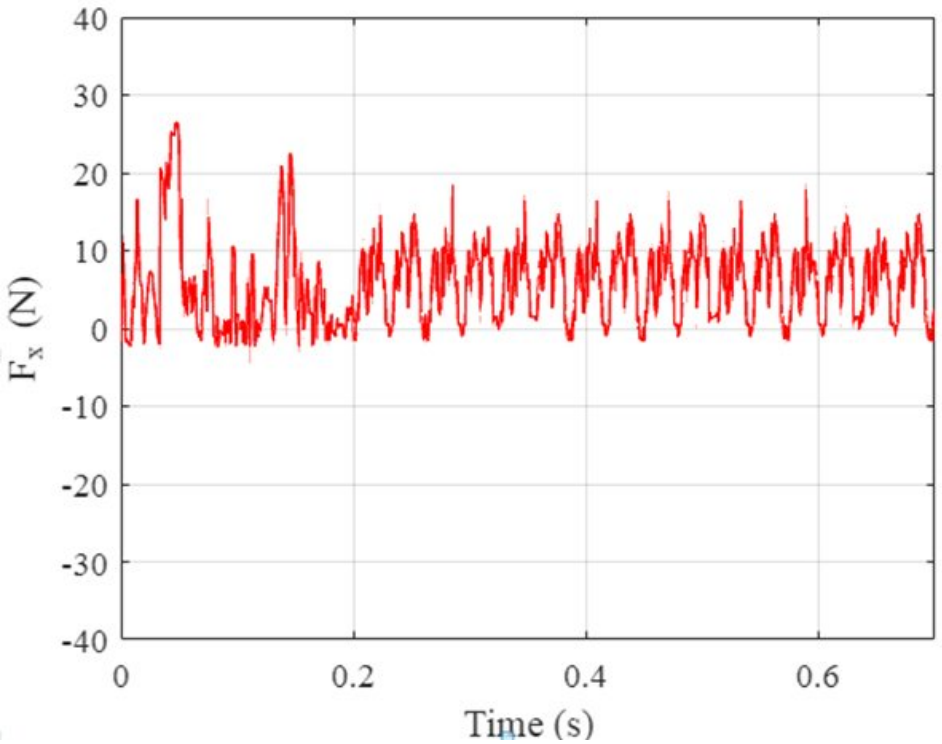

Figure 5.56: Computed radial force, F_x from measured currents.

as well as vibration in the motor. The experimental results conclude that the bridge currents are effective in controlling unbalance in the rotor-shaft. The reduction in radial displacement justifies the capability of the BCW in radial displacement control using

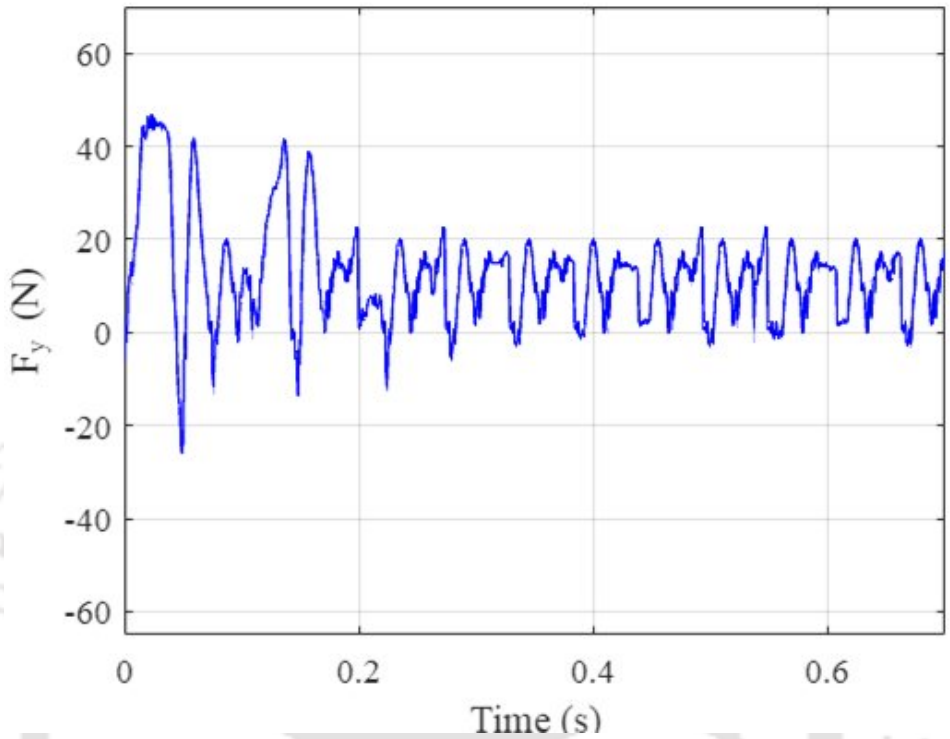

Figure 5.57: Computed radial force, F_y from measured currents.

the same set of combined stator winding in the motor.The supplied currents are also sufficient to produce an average levitation force.

5.8 Summary

The development of two experimental test rigs have been presented and a comparison between the conventional winding in SRM and the BCW BSRM has been shown. Two SRMs of 750 W have been designed fabricated as test motor I and test motor II. Test motor I has been equipped with the conventional stator winding and connected for the formation of a 4-pole magnetic field. The manufacturing of test rig 1 for test motor I has been explained in detail. Test motor II of same dimensions has been equipped with the proposed bridge configured winding. Unlike the conventional winding, the BCW comprises of concentrated double layer coils in the same stator slot and connected to form a 4-pole magnetic field as well as form additional suspension magnetic field using the same winding. The manufacturing of the test rig II for the BCW SRM has been elaborately discussed. The chapter also discusses in details the in-house fabrication and implementation of a DC power converter i.e. asymmetric bridge power converter for the

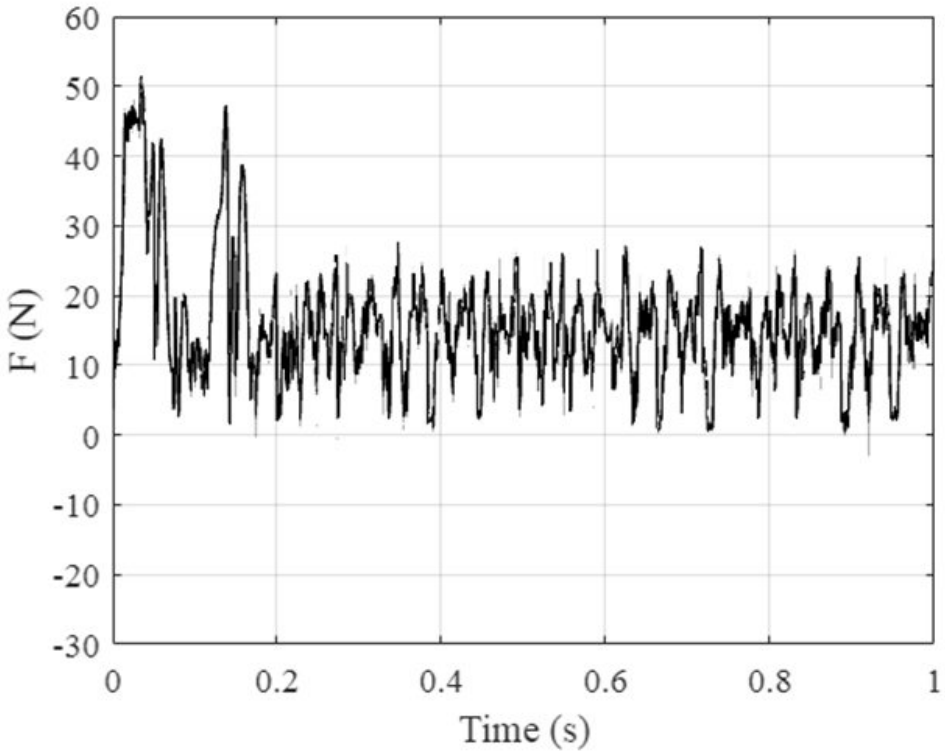

Figure 5.58: Computed net radial force, F from measured currents.

main current supply and separate power converters for the bridge current supply. Each of the test motors have been individually tested with the power converters at a constant supply frequency of 10 Hz with no-load applied to the motor. The devices used for the measurements of the currents and the voltages in each phase winding of the test motors have been explained. The main current and voltages in each phase winding of test motor I have been measured. The results obtained from experiment confirmed that the test motor I could operate at a constant speed. The power converter drive topology applied for sequential phase switching could produce a positive torque in the test motor I.

The test motor II with BCW has been initially tested for rotating operation by supplying only the main current and no bridge current is injected. The results could demonstrate the capability of the test motor II to operate as a normal motor for only torque production. The test motor II has been operated at a constant speed by supplying a control signal of constant frequency of 10 Hz under no load condition. The main current through the winding and the phase voltages have been obtained. A comparative analysis of test motor I and test motor II has been also presented.

The test motor II has been further tested for radial displacement by supplying the bridge currents in between the bridge terminals. In this thesis, the radial force production

has been tested by supplying bridge current in phase-A initially. The results obtained could demonstrate that with the injection of small amount of bridge current in phase-A winding, a net displacement of the shaft is measured which relates to a significant production of radial force in the motor. From the measured displacement values, the net radial force has been computed by using Equation 3.111 and 3.112 as given in Chapter 3. From this experimental analysis it has been demonstrated that the test motor II could produce a positive torque with an additional bridge current. It can be concluded that with the bridge current injection, the normal torque production in the motor is hardly affected. The experiment is further conducted to explore the effect of bridge currents in reducing radial displacement present in the motor. Firstly, the bridge terminals are directly connected with each other or short circuited with each other. A current flows in between the terminals to the coils which tries to reduce the unbalance or displacement present in the rotor. The results of displacements along x and y directions has been monitored and a small shift in the shaft's radial position could be observed. Secondly, the displacement is controlled actively using a closed loop PID control system. The displacement error is minimized by injecting controlled bridge currents in the bridge terminals. The experimental results demonstrate that the radial displacement could be controlled effectively with the closed loop control method. An average lifting force has also been observed with the current supplied in the windings.

Chapter 6

Conclusions and Future Works

Contents

6.1 Conclusions

Controllable radial force generation is an important aspect for self-bearing operation of SRMs. A detailed investigation of the design of SRM with a special stator winding structure called BCW has been carried out in this thesis. The possible ways of utilizing the BCW in SRM in order to achieve the objectives of the thesis has been laid out.

6.2 Summary of contribution

The thesis focuses mainly on the analysis of controllable radial force and torque production using a single winding set called BCW in SRM for introducing self-bearing capability. The analytical part of the work involves the nodal analysis of the BCW circuit, development of a mathematical model for deriving radial force and torque expressions, a design methodology of SRM for incorporating BCW and its verification by FE modelling. A simulink model of the drive system using Ansoft Simplorer is designed and the production of both torque and controllable radial force is simulated with an FE model using Ansoft Maxwell 2D. The FE simulation is extended to demonstrate the capability of the bridge currents to counteract static rotor eccentricity. The thesis further includes experimental work that involves fabrication of two SRMs— one equipped with conventional winding and the other with BCW, fabrication of asymmetric bridge converter drives, and development of two test rigs for experimental demonstration of torque and radial displacement control.

The major contribution of this thesis has been enumerated below.

(i) The aspects of BCW have been studied in context of self-bearing operation in SRM.

   a) The principle of radial force and torque using a single set of stator winding has been explained. The BCW requires a concentrated winding structure for implementation in SRMs, where one stator tooth can occupy two layers of coils. The study is carried forward by fixing the winding topology in a 12/8 SRM for introducing self-bearing operation. The distribution of coils in each stator slot, the terminals for the main current in each phase and the terminals for bridge currents have been defined. The polarity of the coils has been fixed in such a way that when the main current flows a four pole magnetic field is formed in each phase.

b) Each phase winding represents a circuit having two bridges. The distribution of currents has been identified by performing a nodal analysis of the circuit. By solving the KCL equation, the main and the bridge current flowing in each parallel path have been obtained.

(ii) For controlled operation of self-bearing or BSRM, it is necessary to derive an accurate theoretical expression for the magnetic radial forces and torque with respect to the winding currents at every rotational position. To study the behavior of the motor with both the main current and the bridge current a mathematical model has been derived by following two methods, i.e.virtual work method and Maxwell stress tensor method.

a) With the virtual work method, the magneto-motive force equation is solved at each branch of the magnetic equivalent circuit of phase-A by neglecting magnetic saturation. In this method, the shape of the flux path has to be determined. By calculating the length of the flux paths a constant value is determined from an FE model of the motor. This constant value gives the shape of the flux lines and is incorporated in the analytical model for verification of the mathematical model of torque and radial force. The virtual work method is further used to obtain the mathematical model considering magnetic saturation. However, the expression obtained from the model is large and dependent on the motor geometry.

b) With the Maxwell stress tensor method, a simplified mathematical expression of tangential force component and radial force component has been obtained by integrating the magnetic field density over the rotor surface area. In this case, the flux line paths are divided into main flux and fringing flux, where the main fluxes are assumed as straight lines and the fringing fluxes as elliptical lines. These assumptions do not require any prediction of shape constant of flux and help in obtaining a simpler relationship which is suitable for further implementation of real time control.

c) The analytical models of torque and radial force developed using the two methods have been verified with an FE model developed in Ansoft Maxwell 2D. A significant match has been obtained from the results of the analytical models and the FE model.

(iii) A step by step design methodology of SRM for controllable radial force production using BCW is presented in this thesis. A 750 W SRM has been designed from

scratch following the IEC standard of machine design. Each parameter of the motor has been analytically calculated by doing a parametric analysis. In case of salient pole SRMs, the arc angles of stator and rotor teeth play an important role in radial force and torque production. An iterative method has been followed to obtain an optimum arc angle and get required values of torque and radial force. Further the design methodology is applied in designing an SRM with a rated current of 10 A and rated torque of 4.7 Nm. The designed specifications are verified using an FE model developed in Ansoft Maxwell 2D.

(iv) A comparative study between BCW and the conventional two sets of winding in BSRM in terms of torque and radial force production has been carried out using FEM. The torque in BCW are found to be higher by 2 times. However, there is not much difference in the magnitude of radial forces. Further, the BCW and the dual set winding has been compared to determine the copper loss considering same amount of current in both the cases. In comparison with the dual set winding, the copper loss is found to be reduced by 50 % in case of BCW.

(v) A drive system has been designed and simulated for the BSRM with BCW to investigate the torque and radial force production using power converters. The following are the key findings of the simulation with the drive system.

a) Asymmetric bridge power converters have been designed and simulated in the commercial software package Ansoft SIMPLORER[c], for both main current and the bridge current supplies. The switching topology has been established for both positive torque and radial force production for the proposed motor design.

b) The proposed motor has been simulated with a controlled drive system comprising of a PI speed controller and a hysteresis current controller for a speed controlled operation of the motor. The capability of the bridge current to produce radial force without affecting the normal torque production has been established under no load and zero eccentric conditions.

c) A model has been developed in MATLAB/SIMULINK to demonstrate the radial force or levitation control in the BCW scheme. A current command is generated using a current controlled converter for the bridge current to create an actuating force in the opposite direction. For this purpose a PID controller has been used to reduce the displacement error.

d) An attempt has been made to mimic the radial force generation due to static eccentricity of rotor. A steady state analysis of the motor has been carried out by simulating the FE model with the drive system in Ansoft Simplorer. The main currents and the radial forces have been calculated at a constant speed operation by considering a radial displacement of 7.2 % of the air-gap length.

e) Subsequently, the radial force obtained due to the static eccentricity is controlled by injecting controlled bridge currents to produce an equal and opposite force and suppress the net radial force. The displacement error has been minimized by using a PID control. The injection of bridge current in the desired direction reduces the static eccentricity by shifting the rotor towards the centre. This concept is validated experimentally in Chapter 5. The effect of bridge currents in torque production under static eccentric condition is found to be negligible.

f) In order to independently control the main currents and bridge currents, a current control algorithm has been developed to obtain a constant radial force at every rotational position. The main current and the bridge current required for the levitating force and torque are calculated individually according to an analytical method and verified by only FE analysis. The control of displacement by using current controller has been experimentally demonstrated in Chapter 5.

(vi) Two experimental test rigs have been developed to verify the analytical and the numerical findings. The following objectives have been fulfilled experimentally.

a) The SRM as designed analytically in Chapter 3 has been fabricated and used in experiments. Two test motors have been fabricated where one motor is wound with the conventional stator winding and the other with BCW.

b) A hardware of a 3-phase asymmetric bridge converter of 300 W for the main current has been fabricated.

c) The test motor I with conventional winding has been tested for only torque production with the main converter circuit. The capability of the converter and the proposed switching topology to produce positive torque at a constant speed operation has been demonstrated.

d) The test motor II with BCW has been verified for normal torque production by supplying only the main current. A comparison of torque and phase currents

is presented to show the difference in the winding configuration of normal SRM and BCW SRM.

e) The test motor II is tested for radial displacement present in the motor. The bridge currents have been utilized to reduce radial displacement using two methods, firstly a passive control method is employed where the bridge terminals in each phases are connected directly with each other or in other words the bridge terminals are short circuited. Secondly, a closed loop controller is implemented for real-time operation in controlling the radial displacement. A significant amount of reduction in the displacement is achieved.

f) It has been experimentally demonstrated that, with controlled bridge currents a significant reduction in radial displacement can be obtained using the same set of stator winding. The levitation force is calculated from the measured phase winding currents and it has been found that an average levitation force which is sufficient to lift the rotor is obtained with the supplied currents. The experimental work in this thesis builds an important significance in further developing a robust controller for the complete bearingless operation of the motor.

6.3 Scope for future work

Based on the work presented in this thesis, the following work can be suggested to extend the work in future,

(i) The practical development of a robust controller using adaptive control method is suggested for the complete bearingless operation of the proposed motor.

(ii) The proposed method of bridge current supply using the same winding can also be used for active vibration control of the motor.

(iii) The effect of the bridge currents in SRMs can be studied from the view point of minimization of torque ripple, vibration and noise so that SRMs become an attractive option in electric vehicles (EVs).

References

[1] N. M. Dumitru, "Electromagnetic flux monitoring for detecting faults in electrical machines," Ph.D. dissertation, Helsinki University of Technology, Teknillinen, 2006.

[2] W. Amrhein, S. Silber, K. Nenninger, G. Trauner, M. Reisinger, and R. Schoeb, "Developments on bearingless drive technology," *JSME International Journal Series C Mechanical Systems, Machine Elements and Manufacturing*, vol. 46, no. 2, pp. 343–348, 2003.

[3] R. Krishnan, *Switched Reluctance Motor Drives: Modelling, Simulation, Analysis, Design, and Applications*. CRC Press, 2001.

[4] H. Mitterhofer, B. Mrak, and W. Gruber, "Comparison of high speed bearingless drive topologies with combined windings," in *2014 International Power Electronics Conference (IPEC-Hiroshima 2014 - ECCE ASIA)*, 2014, pp. 1701–1706.

[5] A. Chiba, T. Fukao, O. Ichikawa, M. Oshima, M. Takemoto, and D. G. Dorrell, *Magnetic bearings and bearingless drives*. Elsevier, 2005.

[6] M. Sokolov, W. Gruber, S. E. Saarakkala, and M. Hinkkanen, "Modeling of a bearingless synchronous reluctance motor with combined windings," in *2019 IEEE Energy Conversion Congress and Exposition (ECCE)*, 2019, pp. 7084–7090.

[7] P. Vijayraghavan, "Design of Switched Reluctance Motors and Development of a Universal Controller for Switched Reluctance and Permanent Magnet Brushless DC Motor Drives," Ph.D. dissertation, Virginia Polytechnic Institute and State University, the Netherlands, 2001.

[8] T. Higuchi, H. Kawakatsu, and T. Iwasawa, "A study on magnetic suspension of switched reluctance motor," in *in Proc. Conf. Rec. IEEJ Annu. Meeting, Tokyo, Japan*, 1989, pp. 6–122.

[9] A. C. M. Takemoto, K. Shimada and T. Fukao, "A design and characteristics of switched reluctance type bearingless motors," in *Proc. Int. Sym. Magn. Suspension Technol.*, 1998, p. 49.

[10] M. Takemoto, H. Suzuki, A. Chiba, T. Fukao, and M. A. Rahman, "Improved analysis of a bearingless switched reluctance motor," in *IEEE International Electric Machines and Drives Conference. IEMDC'99. Proceedings (Cat. No.99EX272)*, May 1999, pp. 773–775.

[11] M. Takemoto, A. Chiba, H. Akagi, and T. Fukao, "Radial force and torque of a bearingless switched reluctance motor operating in a region of magnetic saturation," *IEEE Transactions on Industry Applications*, vol. 40, no. 1, pp. 103–112, Jan. 2004.

[12] Y. Yang, Z. Liu, Z. Deng, and X. Cao, "Design and characteristic analysis of a novel bearingless srm considering decoupling between torque and suspension force," *Mathematical Problems in Engineering*, vol. 2014, 2014.

[13] Li Chen and W. Hofmann, "Analytically computing winding currents to generate torque and levitation force of a new bearingless switched reluctance motor," in *2006 12th International Power Electronics and Motion Control Conference*, Aug. 2006, pp. 1058–1063.

[14] W. K. S. Khoo, "Bridge configured winding for polyphase self-bearing machines," *IEEE Transactions on Magnetics*, vol. 41, no. 4, pp. 1289–1295, Apr. 2005.

[15] E. Severson, R. Nilssen, T. Undeland, and N. Mohan, "Dual-purpose no-voltage winding design for the bearingless ac homopolar and consequent pole motors," *IEEE Transactions on Industry Applications*, vol. 51, no. 4, pp. 2884–2895, Jul. 2015.

[16] W. K. S. Khoo, K. Kalita, and S. D. Garvey, "Practical implementation of the bridge configured winding for producing controllable transverse forces in electrical machines," *IEEE Transactions on Magnetics*, vol. 47, no. 6, pp. 1712–1718, Jun. 2011.

[17] M. Oshima, S. Miyazawa, T. Deido, A. Chiba, F. Nakamura, and T. Fukao, "Characteristics of a permanent magnet type bearingless motor," *IEEE Transactions on Industry Applications*, vol. 32, no. 2, pp. 363–370, 1996.

[18] A. Chiba, T. Deido, T. Fukao, and M. A. Rahman, "An analysis of bearingless ac motors," *IEEE Transactions on Energy Conversion*, vol. 9, no. 1, pp. 61–68, 1994.

[19] C. C. X. Sun and Z. Yang, "Overview of bearingless induction motors," *Mathematical Problems in Engineering*, vol. 2014, 2014.

[20] T. Reichert, T. Nussbaumer, W. Gruber, and J. W. Kolar, "Bearingless permanent-magnet motor with 4/12 slot-pole ratio for bioreactor stirring applications," *IEEE/ASME Transactions on Mechatronics*, vol. 16, no. 3, pp. 431–439, 2011.

[21] W. Gruber, T. Nussbaumer, H. Grabner, and W. Amrhein, "Wide air gap and large-scale bearingless segment motor with six stator elements," *IEEE Transactions on Magnetics*, vol. 46, no. 6, pp. 2438–2441, 2010.

[22] D. Steinert, T. Nussbaumer, and J. W. Kolar, "Slotless bearingless disk drive for high-speed and high-purity applications," *IEEE Transactions on Industrial Electronics*, vol. 61, no. 11, pp. 5974–5986, 2014.

[23] J. Asama, D. Kanehara, T. Oiwa, and A. Chiba, "Development of a compact centrifugal pump with a two-axis actively positioned consequent-pole bearingless motor," *IEEE Transactions on Industry Applications*, vol. 50, no. 1, pp. 288–295, 2014.

[24] H. Sugimoto, S. Tanaka, A. Chiba, and J. Asama, "Principle of a novel single-drive bearingless motor with cylindrical radial gap," *IEEE Transactions on Industry Applications*, vol. 51, no. 5, pp. 3696–3706, 2015.

[25] Y. Okada, N. Yamashiro, K. Ohmori, T. Masuzawa, T. Yamane, Y. Konishi, and S. Ueno, "Mixed flow artificial heart pump with axial self-bearing motor," *IEEE/ASME Transactions on Mechatronics*, vol. 10, no. 6, pp. 658–665, 2005.

[26] W. Li, K. T. Chau, T. W. Ching, Y. Wang, and M. Chen, "Design of a high-speed superconducting bearingless machine for flywheel energy storage systems," *IEEE Transactions on Applied Superconductivity*, vol. 25, no. 3, pp. 1–4, 2015.

[27] H. Mitterhofer, W. Gruber, and W. Amrhein, "On the high speed capacity of bearingless drives," *IEEE Transactions on Industrial Electronics*, vol. 61, no. 6, pp. 3119–3126, 2014.

[28] T. Miller, *Switched Reluctance Motors and their Control*. Magna Physics Publishing and Clarendon Press, Oxford, 1993.

[29] S. A. Nasar, "Dc switched reluctance motor," in *Proc. IEE*, ser. 6, vol. 116, 1969, p. 1048.

[30] J. Byrne and J. C. Lacy, "Electrodynamic system comprising a variable reluctance machine," May 11 1976, uS Patent 3,956,678.

[31] P. J. Lawrenson, J. M. Stephenson, P. T. Blenkinsop, J. Corda, and N. N. Fulton, "Variable-speed switched reluctance motors," *IEE Proceedings B - Electric Power Applications*, vol. 127, no. 4, pp. 253–265, Jul. 1980.

[32] R. Krishnan, R. Arumugan, and J. F. Lindsay, "Design procedure for switched-reluctance motors," *IEEE Transactions on Industry Applications*, vol. 24, no. 3, pp. 456–461, May 1988.

[33] R. Arumugam, D. Lowther, R. Krishnan, and J. Lindsay, "Magnetic field analysis of a switched reluctance motor using a two dimensional finite element model," *IEEE Transactions on Magnetics*, vol. 21, no. 5, pp. 1883–1885, Sep. 1985.

[34] J. Corda and J. Stephenson, Eds., *Analytical estimation of the minimum and maximum inductances of a double salient motor.* Proc. of the International Conf. On Stepping Motors and Systems, 1979.

[35] P. Materu, "Design and Steady-state Analysis of the Switched Reluctance Motor Drive," Ph.D. dissertation, Virginia Polytechnic Institute and State University, 1989.

[36] A. V. Radun, "Design considerations for the switched reluctance motor," *IEEE Transactions on Industry Applications*, vol. 31, no. 5, pp. 1079–1087, Sep. 1995.

[37] R. M. Davis, W. F. Ray, and R. J. Blake, "Inverter drive for switched reluctance motor: circuits and component ratings," *IEE Proceedings B - Electric Power Applications*, vol. 128, no. 2, pp. 126–136, Mar. 1981.

[38] M. Barnes and C. Pollock, "Power electronic converters for switched reluctance drives," *IEEE Transactions on Power Electronics*, vol. 13, no. 6, pp. 1100–1111, Nov. 1998.

[39] S. Mir, I. Husain, and M. E. Elbuluk, "Energy efficient c-dump converters for switched reluctance motors," in *Proceedings of Applied Power Electronics Conference. APEC '96*, vol. 2, Mar. 1996, pp. 968–973 vol.2.

[40] S. M. Mahmoud, M. Z. El-Sherif, E. S. Abdel-Aliem, and M. N. Nashed, "Studying different types of power converters fed switched reluctance motor," *International Journal of Electronics and Electrical Engineering*, vol. 1, no. 4, pp. 281–290, 2013.

[41] N. R. Garrigan, W. L. Soong, C. M. Stephens, A. Storace, and T. A. Lipo, "Radial force characteristics of a switched reluctance machine," in *Conference Record of the 1999 IEEE Industry Applications Conference. Thirty-Forth IAS Annual Meeting (Cat. No.99CH36370)*, vol. 4, Oct. 1999, pp. 2250–2258 vol.4.

[42] F. Lin and S. Yang, "An approach to producing controlled radial force in a switched reluctance motor," *IEEE Transactions on Industrial Electronics*, vol. 54, no. 4, pp. 2137–2146, Aug. 2007.

[43] C. R. Morrison, M. W. Siebert, and E. J. Ho, "Electromagnetic forces in a hybrid magnetic-bearing switched-reluctance motor," *IEEE Transactions on Magnetics*, vol. 44, no. 12, pp. 4626–4638, Dec. 2008.

[44] N. Takahashi, X. Wang, B. Ge, and J. Wang, "Mathematical modeling of a novel bearingless switched reluctance motor," *COMPEL: The International Journal for Computation and Mathematics in Electrical and Electronic Engineering*, 2014.

[45] H. Chen, Z. Liu, Y. Yang, X. Cao, and X. Wu, "A novel bearingless switched reluctance motor and its control method," in *2018 IEEE International Power Electronics and Application Conference and Exposition (PEAC)*, Nov. 2018, pp. 1–6.

[46] Y. Yuan, Y. Ma, J. Xu, F. Yang, and K. Xie, "Full-period suspension force accurate modelling for a novel bearingless switched reluctance motor," *Electronics Letters*, vol. 55, no. 21, pp. 1119–1121, 2019.

[47] I. Husain, A. Radun, and J. Nairus, "Unbalanced force calculation in switched-reluctance machines," *IEEE Transactions on Magnetics*, vol. 36, no. 1, pp. 330–338, Jan. 2000.

[48] I. Chindurza, D. G. Dorrell, and C. Cossar, "Vibration analysis of a switched-reluctance machine with eccentric rotor," in *Second International Conference on Power Electronics, Machines and Drives (PEMD 2004).*, vol. 2, Mar. 2004, pp. 481–486 Vol.2.

[49] L. Chen and W. Hofmann, "Analysis of radial forces based on rotor eccentricity of bearingless switched reluctance motors," in *The XIX International Conference on Electrical Machines - ICEM 2010*, Sep. 2010, pp. 1–6.

[50] X. Wang, B. Ge, J. Wang, and F. J. T. E. Ferreira, "Radial force analytic modeling for a novel bearingless switched reluctance motor when considering rotor

eccentricity," *Electric Power Components and Systems*, vol. 42, no. 6, pp. 544–553, 2014. [Online]. Available: https://doi.org/10.1080/15325008.2014.880968

[51] X. Wang, Q. Tan, X. Liu, and B. Ge, "Improved radial force modeling and rotor suspension dynamics simulation studies for double-winding bearingless switched reluctance motor," *Electric Power Components and Systems*, vol. 45, no. 1, pp. 111–120, 2017. [Online]. Available: https://doi.org/10.1080/15325008.2016.1236852

[52] Jinghua Ji, Yukun Sun, Huangqiu Zhu, and Wenxiang Zhao, "Magnetic field analysis of bearingless switched reluctance motor using finite element method," in *2005 International Conference on Electrical Machines and Systems*, vol. 3, Sep. 2005, pp. 2121–2123 Vol. 3.

[53] H. Zhang, J. Zhang, and R. Gao, "Radial force reduction for switched reluctance motor with skewed slot structure based on fem," *Journal of Scientific Industrial Research*, vol. 69, pp. 594–599, 2010.

[54] Jingjun Zhang, Lili Wang, Haijun Zhang, and Ruizhen Gao, "Non-linear radial force simulation of switched reluctance motors based on finite element model," in *2008 IEEE International Conference on Robotics and Biomimetics*, Feb. 2009, pp. 1678–1682.

[55] Haijun Zhang, Ruizhen Gao, Jingjun Zhang, and Lili Wang, "Vibration analysis for switched reluctance motor system based on finite element and fft," in *2009 International Conference on Mechatronics and Automation*, Aug. 2009, pp. 4257–4261.

[56] M. Takemoto, A. Chiba, and T. Fukao, "A new control method of bearingless switched reluctance motors using square-wave currents," in *2000 IEEE Power Engineering Society Winter Meeting. Conference Proceedings (Cat. No.00CH37077)*, vol. 1, Jan. 2000, pp. 375–380.

[57] A. C. M. Takemoto and T. Fukao, "A method of determining advanced angle of square-wave currents in bearingless switched reluctance motors," in *Conference Record of the 2000 IEEE Industry Applications Conference. Thirty-Fifth IAS Annual Meeting and World Conference on Industrial Applications of Electrical Energy (Cat. No.00CH37129)*, vol. 1, Oct. 2000, pp. 241–248.

[58] M. Takemoto, A. Chiba, and T. Fukao, "A method of determining the advanced angle of square-wave currents in a bearingless switched reluctance motor," *IEEE Transactions on Industry Applications*, vol. 37, no. 6, pp. 1702–1709, Nov. 2001.

[59] B. Choi and M. Siebert, "A bearingless switched relunctance motor for high specific power applications," in *42nd AIAA/ASME/SAE/ASEE Joint Propulsion Conference & Exhibit*, 2006, p. 4804.

[60] Feng-Chieh Lin and Sheng-Ming Yang, "Instantaneous shaft radial force control with sinusoidal excitations for switched reluctance motors," in *Conference Record of the 2004 IEEE Industry Applications Conference, 2004. 39th IAS Annual Meeting.*, vol. 1, Oct. 2004, p. 430.

[61] F. Lin and S. Yang, "An approach to producing controlled radial force in a switched reluctance motor," *IEEE Transactions on Industrial Electronics*, vol. 54, no. 4, pp. 2137–2146, Aug. 2007.

[62] F. C. Lin and S. M. Yang, "Radial force control of a switched reluctance motor with two-phase sinusoidal excitations," in *Conference Record of the 2006 IEEE Industry Applications Conference Forty-First IAS Annual Meeting*, vol. 3. IEEE, 2006, pp. 1171–1177.

[63] X. Cao, Z. Deng, G. Yang, and X. Wang, "Independent control of average torque and radial force in bearingless switched-reluctance motors with hybrid excitations," *IEEE Transactions on Power Electronics*, vol. 24, pp. 1376–1385, 2009.

[64] Y. Yang, F. Liu, and Chengwei Liu, "A new bearingless switched reluctance motor with wide rotor pole arc," in *2014 9th IEEE Conference on Industrial Electronics and Applications*, Jun. 2014, pp. 374–378.

[65] D. Lee, H. Wang, and J. Ahn, "Modeling and control of novel bearingless switched reluctance motor," in *2009 IEEE Energy Conversion Congress and Exposition*, Sep. 2009, pp. 276–281.

[66] T. Park, J. Liang, D. Lee, H. Wang, and J. Ahn, "Suspending force control scheme for bearingless srm," in *INTELEC 2009 - 31st International Telecommunications Energy Conference*, Oct. 2009, pp. 1–5.

[67] H. Wang, J. Liu, J. Bao, and B. Xue, "A novel bearingless switched reluctance motor with a biased permanent magnet," *IEEE Transactions on Industrial Electronics*, vol. 61, no. 12, pp. 6947–6955, Dec. 2014.

[68] Y. Huang, S. Shi, Y. Yuan, Y. Sun, and J. Xu, "Direct suspension force control of hybrid stator bear-ingless switched reluctance motor based on quasi-continuous three-order sliding mode," *Progress In Electromagnetics Research*, vol. 80, pp. 157–167, 2019.

[69] P. Liu and X. Cao, "Control method for single-winding 12/4 bearingless switched reluctance motor," in *2019 14th IEEE Conference on Industrial Electronics and Applications (ICIEA)*, Jun. 2019, pp. 2087–2091.

[70] R. Torres and E. Severson, "Decoupled control for parallel drive no-voltage bearingless motors," in *2018 IEEE Energy Conversion Congress and Exposition (ECCE)*. IEEE, 2018, pp. 1688–1695.

[71] Y. Jiang, R. Torres, and E. Severson, "Current regulation in parallel combined winding bearingless motors," *IEEE Transactions On Industry Applications*, vol. 5, no. 5, pp. 4800–4810, Sep/Oct. 2019.

[72] M. A. Preston, J. P. Lyons, E. Richter, and K. Chung, "Integrated magnetic bearing/switched reluctance machine," Jun. 13 1995, uS Patent 5,424,595.

[73] G. Yang, Z. Deng, X. Cao, and X. Wang, "Optimal winding arrangements of a bearingless switched reluctance motor," *IEEE Transactions on Power Electronics*, vol. 23, no. 6, pp. 3056–3066, Nov. 2008.

[74] L. Chen and W.Hofmann, "Design procedure of bearingless high-speed switched reluctance motors," in *SPEEDAM 2010*, Jun. 2010, pp. 1442–1447.

[75] L. Chen and W. Hofmann, "Modelling and control of one bearingless 8–6 switched reluctance motor with single layer of winding structure," in *Proceedings of the 2011 14th European Conference on Power Electronics and Applications*, Aug. 2011, pp. 1–9.

[76] L. Chen and W. Hofmann, "Speed regulation technique of one bearingless 8/6 switched reluctance motor with simpler single winding structure," *IEEE Transactions on Industrial Electronics*, vol. 59, no. 6, pp. 2592–2600, 2011.

[77] L. Zhao, Z. Deng, and X. Cao, "Mathematical model of single-winding bearingless switched reluctance motor considering two-phase coupling," in *IECON 2013 - 39th Annual Conference of the IEEE Industrial Electronics Society*, Nov. 2013, pp. 2971–2976.

[78] X. Cao, J. Zhou, C. Liu, and Z. Deng, "Advanced control method for a single-winding bearingless switched reluctance motor to reduce torque ripple and radial displacement," *IEEE Transactions on Energy Conversion*, vol. 32, no. 4, pp. 1533–1543, Dec. 2017.

[79] X. Wu, Y. Yang, and Z. Liu, "Analysis and control of a novel bearingless switched reluctance motor with wider rotor teeth," in *IECON 2017 - 43rd Annual Conference of the IEEE Industrial Electronics Society*, Oct. 2017, pp. 1796–1801.

[80] Y. Y. Q. W. Xiang, M. Fang and Y. Yu, "A novel hybrid excitation double-stator bearingless switched reluctance motor," *Progress In Electromagnetics Research M*, vol. 69, pp. 37–49, 2018.

[81] Q. W. Xiang and L. Feng, "Optimization and analysis of 24/16/8 hybrid excitation double stator bearingless switched reluctance motor," *Progress In Electromagnetics Research C*, vol. 89, pp. 191–205, 2019.

[82] K. Raggl, J. W. Kolar, and T. Nussbaumer, "Comparison of winding concepts for bearingless pumps," in *2007 7th Internatonal Conference on Power Electronics*, 2007, pp. 1013–1020.

[83] D. Dietz and A. Binder, "Comparison between a bearingless pm motor with separated and combined winding for torque and lateral force generation," in *2019 21st European Conference on Power Electronics and Applications (EPE '19 ECCE Europe)*, 2019, pp. P.1–P.10.

[84] T. Holenstein, T. Nussbaumer, and J. W. Kolar, "A bearingless synchronous reluctance slice motor with rotor flux barriers," in *2018 International Power Electronics Conference (IPEC-Niigata 2018 -ECCE Asia)*, 2018, pp. 3619–3626.

[85] E. Severson, S. Gandikota, and N. Mohan, "Practical implementation of dual-purpose no-voltage drives for bearingless motors," *IEEE Transactions on Industry Applications*, vol. 52, no. 2, pp. 1509–1518, Mar. 2016.

[86] F. Ahmed, G. Kumar, M. D. Choudhury, and K. Kalita, "Bridge configured wounded switched reluctance motor," *Procedia Engineering*, vol. 144, pp. 817–824, 2016.

[87] F. Ahmed, M. D. Choudhury, G. Kumar, and K. Kalita, "Modeling and analysis of bearingless switched reluctance motor equipped with specialized stator winding," in *2016 IEEE International Conference on Power Electronics, Drives and Energy Systems (PEDES)*, Dec. 2016, pp. 1–6.

[88] M. D. Choudhury, F. Ahmed, G. Kumar, K. Kalita, and K. Tammi, "Design methodology for a special single winding based bearingless switched reluctance motor," *The Journal of Engineering*, vol. 2017, no. 7, pp. 274–284, 2017.

[89] G. Kumar, K. Kalita, and K. Tammi, "Analysis of bridge currents and ump of an induction machine with bridge configured winding using coupled field and circuit modeling," *IEEE Transactions on Magnetics*, vol. 54, no. 9, pp. 1–16, Sep. 2018.

[90] W. Amrhein, S. Silber, and K. Nenninger, "Levitation forces in bearingless permanent magnet motors," *IEEE Transactions on Magnetics*, vol. 35, no. 5, pp. 4052–4054, 1999.

[91] A. Radun, "Analytically computing the flux linked by a switched reluctance motor phase when the stator and rotor poles overlap," *IEEE Transactions on magnetics*, vol. 36, no. 4, pp. 1996–2003, 2000.

[92] R. Krishnan, *Electric motor drives: modeling, analysis and control*. Prentice Hall, 2001.

[93] International Electrotechnical Commission, "Dimensions and output ratings for rotating electrical machines - frame numbers 56 to 400 and flange numbers f 55 to f 1080," International Electrotechnical Commission, Geneva, Switzerland, Standard IEC 60072 -1, 1971.

[94] F. Ahmed, K. Kalita, and H. B. Nemade, "Torque and controllable radial force production in a single winding bearingless switched reluctance motor with a speed controlled drive operation," *International Transactions on Electrical Energy Systems*, p. e12312. [Online]. Available: https://onlinelibrary.wiley.com/doi/abs/10.1002/2050-7038.12312

[95] S. Shelke, "Controllability of radial magnetic bearing," *Procedia Technology*, vol. 23, pp. 106–113, 2016.

List of publications

Journal Publications

1. **F. Ahmed**, G. Kumar, M. D. Choudhury, and K. Kalita, "Bridge configured wounded switched reluctance motor," *Procedia Engineering*, vol. 144, pp. 817–824, 2016.

2. M. D. Choudhury, **F. Ahmed**, G. Kumar, K. Kalita, and K. Tammi, "Design methodology for a special single winding based bearingless switched reluctance motor," *The Journal of Engineering*, vol. 2017, no. 7, pp. 274–284, 2017.

3. **F. Ahmed**, K. Kalita, and H. B. Nemade, "Torque and controllable radial force production in a single winding bearingless switched reluctance motor with a speed controlled drive operation," *International Transactions on Electrical Energy Systems*, vol.30, no. 5, pp. e12312, 2019.

4. **F. Ahmed** and K. Kalita, "Controllability of radial displacement in bearingless switched reluctance motor using bridge configured winding," *International Journal of Applied Electromagnetics and Mechanics*, vol. 63, no. 1, pp. 133-152, 2020.

5. **F. Ahmed**, K. Kalita, and H. B. Nemade, "Design and Implementation of a Bridge Configured Winding Switched Reluctance Motor for Self-Bearing Operation using low power supply," (manuscript to be submitted).

Conference Publications

1. **F. Ahmed**, M. D. Choudhury, G. Kumar, and K. Kalita, "Modeling and analysisof bearingless switched reluctance motor equipped with specialized stator winding," *IEEE International Conference on Power Electronics, Drives and Energy Systems (PEDES)*, Dec. 2016, pp. 1–6.

2. **F. Ahmed** and K. Kalita, "Controllability of radial displacement in bearingless switched reluctance motor using bridge configured winding," *Proceedings of the International Symposium on Magnetic Bearings (ISMB 16)*, Aug. 2018.